High Voltage DC-biased Oil Type Medium Frequency Transformer

A Green Solution for Series DC Wind Park Concept

MOHAMMAD KHAREZY

Department of Electrical Engineering
CHALMERS UNIVERSITY OF TECHNOLOGY
Gothenburg, Sweden 2023
www.chalmers.se

THESIS FOR THE DEGREE OF DOCTOR OF PHILOSOPHY

High voltage DC-biased oil type Medium Frequency Transformer

A green solution for series DC wind park concept

MOHAMMAD KHAREZY

Department of ELECTRICAL ENGINEERING

CHALMERS UNIVERSITY OF TECHNOLOGY

Gothenburg, Sweden 2023

High voltage DC-biased oil type Medium Frequency Transformer
A green solution for series DC wind park concept
MOHAMMAD KHAREZY
ISBN: 978-91-7905-861-6

Doktorsavhandlingar vid Chalmers tekniska högskola.
Ny serie nr. 5327
ISSN0346-718X

Department of Electrical Engineering
Chalmers University of Technology
SE-412 96 Gothenburg
Sweden
Telephone + 46 (0)31-772 1000
www.chalmers.se

Cover:
The designed, manufactured, and tested Novel prototype oil-immersed
125 kV HVDC insulated, 5 kHz, 0.42 kV/5 kV Medium Frequency Transformer.

Printed by Chalmers Digital Printing
Gothenburg, Sweden, May 2023

To my father

Abstract

The electric energy generated by remote offshore wind parks is transported to the consumers using high voltage submarine cables. On the generation site, such transmissions are realized today by collecting the energy produced by several wind turbines in a bulky and expensive transformer placed on a dedicated platform. An alternative solution has been proposed recently, which allows to reduce the installation and maintenance costs by eliminating such a platform. It is suggested to equip each wind turbine in the wind park by an individual DC/DC converter and connect them in series to reach the DC voltage level required for an efficient HVDC energy transportation to the shore. The DC/DC converter is supposed to be a Dual Active Bridge (DAB) converter, which can be made reasonably small to be placed on the wind turbine tower or even in its nacelle. The key element of the converter defining its size and mass is a special transformer, which operates at voltages comprising a high (switching) frequency component superimposed on a high DC offset voltage. DC insulation design of such a transformer and investigation of the effects of a high DC insulation level on the other electromagnetic properties of the transformer is the subject of the present research.

In order to verify the concept a prototype of the transformer was built, and its evaluation presented. The unit has been manufactured for the rated power of 50 kW and rated voltages 0.4/5 kV including DC offset of 125 kV and square-shaped oscillations with the frequency of 5 kHz. The magnetic system was made of ferrite material and consisted of 10 shell-type core segments. The magnetic properties have been verified by measuring magnetization and losses at various frequencies in the range 1-10 kHz to cover the operational range of the DAB. The types and dimensions of the windings and their conductors were chosen to minimize the proximity and eddy current effects at higher frequencies. To reduce the size of the transformer and to allow for its efficient cooling, the active part was immersed in oil and cellulose-based materials (paper and pressboard) were used to build the high voltage insulation system.

The principles for dimensioning the insulation of the transformer are discussed. The criteria used for selecting insulating distances were based on the consideration of the electric field strength obtained from FEM simulations and using the non-linear Maxwell-Wagner model accounting for local variations of the electric field caused by accumulation of interfacial charges induced by DC stresses. The properties of the materials needed for the calculations were obtained by measuring their dielectric constants and electric conductivities. The methodology used for the measurements conducted for conventional mineral oil and eco-friendly biodegradable transformer oils and, respectively, for oil-impregnated paper/pressboard, is presented.

The methodologies used for obtaining parameters of the built transformer prototype needed for its integration in the power electric circuit of the DAB are introduced. A method developed for accurate calculations of the leakage inductance for the shell-type multi core transformers with circular windings is described. Two innovative methods for evaluations of parasitic capacitances based on high frequency equivalent circuits of the transformer are presented. The results of their verifications against performed Frequency Response Analysis measurements and FEM calculations as well as their accuracy are discussed.

Thermal performance of the developed transformer prototype is analysed based on the results of computer simulations of heat transfer in its active part under rated load. Identified hot spots and solutions for their elimination are presented.

Finally, the expected dimensions, weight, and efficiency of an actual DC/DC converter with the rated parameters corresponding to a 6 MW, 1.8 kV real wind turbine having a 250 kV offset DC voltage are estimated assuming that the developed transformer prototype is scalable. It is shown that the proposed solution allows for installing the full-scale converter having 2.2 Tons in weight and 1.8 m^3 in volume on the bottom of the wind turbine's tower.

Keywords: High voltage DC, Insulation design, Medium-frequency power transformer, Dual active bridge, Leakage inductance, Parasitic capacitance, High power isolated DC/DC converter, Offshore wind farm, HVDC.

List of Publications

This thesis is based on the work contained in the following publications:

Journal articles

I. **M. Kharezy**, H. R. Mirzaei, Y. Serdyuk, T. Thiringer and M. Eslamian, "A Novel Oil-immersed Medium Frequency Transformer for Offshore HVDC Wind Farms," *IEEE Transactions on Power Delivery, November 2020*

II. **M. Kharezy**, H. R. Mirzaei, Y. Serdyuk and T. Thiringer, "Green Solution for Insulation System of a Medium Frequency High Voltage Transformer for an Offshore Wind Farm," *MDPI Energies, March 2022*

III. **M. Kharezy**, M. Eslamian, T. Thiringer and Y. Serdyuk, "Determination of Parasitic Capacitance of High- Power Medium Frequency Transformers: Case study of a high voltage DC biased transformer for wind power application," *IEEE Transactions on Power Delivery, August 2023*

IV. M. Eslamian, **M. Kharezy** and T. Thiringer, "An Accurate Method for Leakage Inductance Calculation of Shell-Type Multi Core-Segment Transformers with Circular Windings," *IEEE Access, August 2021*

V. M. Eslamian, **M. Kharezy** and T. Thiringer, "An Accurate Analytical Method for Leakage Inductance Calculation of Shell-Type Transformers with Rectangular Windings," *IEEE Access, Maj 2021*

VI. M. A. Bahmani, T. Thiringer, **M. Kharezy**, "Design Methodology and Optimization of a Medium-Frequency Transformer for High-Power DC–DC Applications," *IEEE Transactions on Industry Applications, October 2016*

VII. B. Khanzadeh, T. Thiringer and **M. Kharezy**, "Multilevel Dual Active Bridge Leakage Inductance Selection for Various DC-link Voltage Spans," *MDPI Energies, January 2023*

Conference articles

VIII. **M. Kharezy**, M. Eslamian, and T. Thiringer, "Core Loss Evaluation of MFTs with Square-wave Voltage Excitation," *26th Soft Magnetic Materials Conference, SMM2023, Prague, Czech Republic, Submitted in April 2023*

IX. **M. Kharezy**, H. R. Mirzaei, T. Thiringer 2, J. Rastamo, M. Svensson, T. Nieminen and Y. Serdyuk, "Performance of Insulation of DC/DC Converter Transformer for Offshore Wind Power Applications," *Conference on Electrical Insulation and Dielectric Phenomena, CEIDP2020, NJ, USA, October 18-22, 2020*

X. **M. Kharezy**, M. Eslamian, and T. Thiringer, "Estimation of the winding losses of Medium Frequency Transformers with Litz wires using an equivalent permeability and conductivity method," *22stEuropean Conference on Power Electronics and Applications, EPE2020, Lyon, France, September 7-11, 2020*

XI. **M. Kharezy**, M. Eslamian and T. Thiringer, "Insulation design of a medium frequency power transformer for a cost-effective series high voltage DC collection network of an offshore wind farm," *International Symposium on High Voltage Engineering, ISH2019, Budapest, Hungary, August 26-30, 2019*

XII. M. Eslamian, **M. Kharezy** and T. Thiringer, "Calculation of the leakage inductance of medium frequency transformers having rectangular-shaped windings using an accurate analytical method," *European Conference on Power Electronics and Applications, EPE2019, Genova, Italy, September 2-6, 2019*

XIII. B. Khanzadeh, T. Thiringer and **M. Kharezy**, "Optimum Leakage Inductance Determination for a Q2L-Operating MMC-DAB with Different Transformer Winding Configurations," *International Symposium on Power Electronics, Ee2019, Novi Sad, Serbia, October 23 - 26, 2019*

XIV. **M. Kharezy** and T. Thiringer, “Challenges with the design of cost-effective series DC collection network for offshore wind-farms,” *Wind Integration Workshop on Large scale Integration of Wind Power into Power Systems as well as on Transmission Networks for Offshore Wind Power Plants, WIW2018, October 17-19, Stockholm, Sweden, 2018*

XV. M. A. Bahmani, T. Thiringer and **M. Kharezy**, “Optimization and experimental validation of medium-frequency high power transformers in solid-state transformer applications,” *IEEE Applied Power Electronics Conference and Exposition (APEC), USA, 2016*

XVI. M. A. Bahmani, T. Thiringer and **M. Kharezy**, “Design Methodology and Optimization of a Medium Frequency Transformer for High Power DC-DC Applications,” APEC, USA, 2015

Acknowledgment

This work has been carried out at RISE Research Institutes of Sweden and the Department of Electrical Engineering at Chalmers University of Technology. The financial support given by the Swedish Energy Agency (Energimyndigheten) within the project 44983-1 and 43048-1, as part of the research program “Forskning och innovation inom vindkraftsområdet VindEL 2017” and “Forskning och innovationsprogrammet SamspEL 2016” is gratefully acknowledged.

First, I express my sincere thanks to my examiner and main supervisor Prof. Torbjörn Thiringer and my co-supervisor Prof. Yuriy Serdyuk. Without their continuous help, the initiation and realization of this project would be impossible. My supervisor from RISE, Dr. Per-Olof Hedekvist is gratefully acknowledged for his continuous support. In addition, while conducting this project, I had the unconditional support of the guest researchers Dr. Morteza Eslamian and Dr. HassanReza Mirzaei from University of Zanjan, Dr. Babak Khanzadeh from Chalmers University of Technology and my former colleague Behrooz Bayat from Iran Transfo Company. I thank them wholeheartedly.

A very special thanks goes to Dr. Raik Orbay at Volvo Car Corporation for his very fruitful cooperation with me which made it possible to investigate the thermal behaviour of the prototype transformer. I also would like to thank my M. Sc. Thesis student Oriol Guillén Sentís, for his very nice cooperation when he conducted his thesis work "Feasibility of sea-based wind park” during spring 2020 and likewise, Joakim Rastamo and Marcus Svensson for their effective contribution to time-demanding conductivity measurements.

I need also to thank all my colleagues at RISE whose warm technical help was invaluable; among them, Dr. Anders Bergman, Dr. Alf-Peter Elg, Tatu Nieminen, Andreas Nilsson, Mathias Nordlund, Daniele Usai, Dr. Joni Klüss, Karl-Erik Rydler, Claes Wingqvist, Reine Weijmer, Andreas Andersson, Fredrik Arrhén and my former colleague Johan Söderbom.

I would also thank my former supervisor Dr. Mohammad Amin Bahmani for his kind support with the application to funding and the knowledge transferred to me at the stating stage of this project. Special thanks go to Dr. Seyed Ali Mousavi for his help for the core loss measurements, Kim Bolleter from Weidmann Electrical Technology AG, and Dr. Espen Doedens from Nexsans Subsea Energy Systems for providing insulation material samples and to Energimyndigheten for sponsoring the rest of the materials needed in the thesis work. I would also like to thank Dr. Xiangdong Xu for his effective help for buying formed insulation parts and his guidelines for conductivity measurements.

Eventually, my heartfelt gratitude goes to my family for all their patience, support, and love.

Mohammad Kharezy
Gothenburg, Sweden, 2023

Abbreviations

DC	Direct Current
AC	Alternating Current
BDV	Breakdown Voltage
CR	Conductivity Ratio
DAB	Dual Active Bridge
DDM	Drift-Diffusion Model
HV	High Voltage
LMW	Linear Maxwell Wagner
LV	Low Voltage
MFT	Medium Frequency Transformer
MW	Maxwell Wagner
MWM	Maxwell Wagner Model
NLMW	Non-Linear Maxwell Wagner
OIP	Oil Impregnated Pressboard
PD	Partial Discharge
PB	Press Board
PWM	Pulse Width Modulator
ZVS	Zero Voltage Switching

Contents

1 Introduction

1.1 Background

Offshore wind power has an enormous potential for global electricity production according to the International Energy Agency IEA [1]. It is a potential that needs to be exploited to counteract the trend of rising CO_2 emissions from electricity generation worldwide. IEA estimates that over 120 GW of offshore wind power will be available in Europe by 2040. With a capacity factor that generally is better than that of onshore wind power stations and better than solar power, offshore wind contributes to the security of supply and a stable electricity system. In addition to having stable policy frameworks and the ever-increasing size and number of wind turbines, continued technology development is needed in all parts of the wind energy chain to reduce costs. There is an extensive installation of wind energy parks taking place in the North Sea, as well as at other offshore areas. The main reason is that wind condition is better at sea as well as the fact that it is becoming more and more difficult to find locations on land where wind turbines can be installed without causing environmental disturbances.

Today, when a sea-based wind park reaches a size of some hundreds of MWs or more, a platform (or several ones), acting as the hub in the collection grid and a point of connection for the cable to land, is needed. Among other equipment the platform carries a transformer (typically 30/130 kV), an example is the Lillgrund (110 MW) wind park, south of the Öresund bridge. Since ordinary AC cables becomes inefficient over approximately 100 km [2], it has become necessary to move over to DC-transmission for some of the new wind parks, an example is the Borwind wind park north-west of the German North sea coast. However, within the wind park, still a collection grid running at 50 Hz AC is used and two platforms of gigantic sizes are needed for 50 Hz AC/AC and AC/DC conversion increasing the cost substantially for the wind energy installation.

A possibility here is to use the DC-technology also for the energy collection grid within the wind park. To do that, a key component is missing, the high-power DC/DC converter, that can produce a DC output voltage from the wind turbines of sufficient voltage level. Such a device can transform the voltage from the wind turbine to a high DC voltage using a much smaller converter unit compared to a 50 Hz transformer. An idea is to fit the converter system into a container on the outside of a wind turbine, thus utilizing the existing foundation out in the sea (Figure 1-1); however, a location inside the tower or nacelle is also an option.

Figure 1-1: Wind turbine- mounted DC/DC converter

A highly interesting solution is then to connect the output of the wind turbines in series, and in this way making the voltage level to reach 100 or even 200 kV. The idea would then be to continue the connection directly to shore without the need of a large transformer platform. A cable can transport up to 2000 A, and using a bipolar set-up, 800 MW can be reached without a platform, for the 200kV case. This is a huge investment saving. However, here comes a highly important factor: The wind turbine that is located closest to the DC-transmission cables going away to shore must take up the full insulation on its high-voltage side, and the duty falls on the output DC/DC converter. Today, the DC/DC converter technology including the transformer is far away from such capabilities. This is where the conducted research comes in.

In this study the prerequisites of an 800 MW farm having 133, 6 MW turbines with up to 200 kV HVDC insulation ability from the HV winding to ground, will be utilised as hypothesis for a future implementation in the conducted research.

A design approach for a high frequency medium voltage transformer, however, with a more crude DC -bias inclusion, was introduced earlier in a Ph.D. work [3] where it was applied on two down-scaled 50 kW, 1/3 kV, 5 kHz prototype Medium-Frequency Transformers (MFTs). These designs have later been manufactured, and successfully tested, fulfilling the efficiency, power density and leakage inductance requirements that the prototypes were designed for [4]. The efficiency has been verified experimentally to be 99.67 % and a power density of 12.2 kW/l which is nearly 13 times more than that of a normal 50 Hz transformer.

1.2 Previous work & research gap

1.2.1 MFT for high voltage applications

Heinemann et al. (ABB) in their work published in 2002 [5] have presented a prototype 350 kW, 3/3 kV, 10 kHz transformer with a shell type coaxial windings. The transformer is designed to be integrated into a multilevel converter and to be coupled to a 15 kV, 16 2/3 Hz line. A 95 kV Lightning Impulse (LI) test has been also performed. This transformer is not claimed to withstand HVDC voltage to ground. Moreover, its PD-free insulation level at AC 50 Hz is 28 kV to ground for a one-minute application of the voltage. This is an example of the highest voltage that a dry type MFT can deliver for a PD-free application.

Steiner et al. (Bombardier) in their work published in 2007 [6] have presented a design for a dry, core type and hollow conductor windings 350 kW, 1/1 kV, 8 kHz prototype transformer. The transformer is designed to be used in a multilevel converter and be coupled to a 15 kV, 16 2/3 Hz line. A 100 kV Lightning Impulse (LI) test has been performed. The high voltage DC insulation to ground was not investigated and even at the AC 50 Hz, its PD-free insulation level is 33 kV. This design also has the same PD inception level as the previous dry type transformer.

STS Transformers in 2015 has presented a design for a core type cast resin windings 450 kW, 1.8/1.8 kV, 8 kHz prototype transformer to be used in a multilevel converter and to be coupled to a 15 kV @ 16 2/3 Hz & 25 kV @ 50 Hz. At AC 50 Hz its PD-free insulation level is 37 kV to ground [7]. However, no information regarding the performance of the transformer under HVDC stress is presented.

Bahmani (Chalmers) has in his work published in 2016 [9] presented a shell type prototype transformer with coaxial windings rated for 666 kW, 1/2 kV for use in one stage of 15 series connected DC/DC converters. The total rating of the turbine is 10 MW, the turbine's output voltage is 1 kV, and the

output voltage of the farm is 30 kV (Figure 2-2). The insulation level of the high voltage side to ground was designed to be 60 kV. However, the insulation design is only based on a kV/mm high voltage strength figure of the insulation materials used as coil-former and a safety factor of 2. Another prototype was manufactured for 50 kW, 1/3 kV, 5 kHz which has not been designed or proved to withstand a high DC voltage to ground needed to be applied to the winding in a series DC wind farm configuration. Other parameters like insulation design for a combined insulation systems and non-uniform electric fields were not included in the scope of the study.

Jaritz et al. (ETH) in their paper published in 2017, have reported the design of an MFT 0.4/14.4 kV, 10 kHz having a high voltage isolation of 115 kV [8]. The unit is designed to be used in a system of 8 series 14.4 kV converters (totally 115 kV DC to ground). It has passed a 110 kV r.m.s. (136% of 115 kV/√2) 5 minutes AC PD test inside a synthetic Ester oil. However, its insulation has been designed for an AC stress and only based on a kV/mm high voltage strength and a capacitive voltage division based on the permittivity values of the material used. No information about the long-term effects of oil on plastic materials used as coil-formers and barriers are presented. Furthermore, no study has been done regarding the behaviour of the transformer under HVDC stress.

Gradinger et al. (ABB) in their work published in 2017 [9] have presented a design of a prototype transformer with core type cast resin winding with rated parameters 240 kVA, 0.6/0.9 kV, 10 kHz. A 150 kV Lightning Impulse (LI) test has been performed on this transformer. Also, it is claimed to withstand 50 kV HVDC voltage to ground, but this has not been considered in the design process. Furthermore, a DC test has not been performed on the manufactured prototype. Even at AC 50 Hz, the transformer's PD free insulation level has been found to be only 35 kV.

Only few publications reported studies of winding configurations considering high voltage stresses. Huang et al. [10] have compared the foil type winding with the litz windings and explained how an interleaved winding structure can lower the maximum electric field intensity and what is the limitations to do this. Jaritz et al. (ETH) in their paper published in 2017 [8], have explained how different winding configurations can help with achieving minimum insulation stress. However, none of these have considered the effect of the high frequency square wave regime on lowering the breakdown strength and accelerating aging of the insulation.

According to Ortiz [11], there is a research gap in isolation strategies implemented in designing. There are other challenges regarding the insulation design of an MFT and some of them are mentioned in a tutorial given by Dujic in [12].

There are only few works that have claimed a capability of MFT insulation to withstand a high voltage to ground on transformer HV side. Insulation designs is based on a kV/mm high voltage strength value of the insulation materials. In most of the cases a safety factor of 2 is used. None of the papers have presented an HVDC voltage to ground design.

Jaritz has presented a list of possible solid insulation materials that can be used as barriers in different places in the transformer [8]. However, the comparison is limited to the AC situation based on permittivity of the materials whereas the voltage distribution at DC steady state is to be based on conductivities.

Figure 1-2 summarized the presented prototypes of MFTs reported in the literature.

350 kW, 3/3 kV, 10 kHz
Heinemann et al. (ABB), 2002 [5]
Claimed HV insulation to ground 15 kV @16 2/3 Hz
PD free AC 50 Hz 28 kV

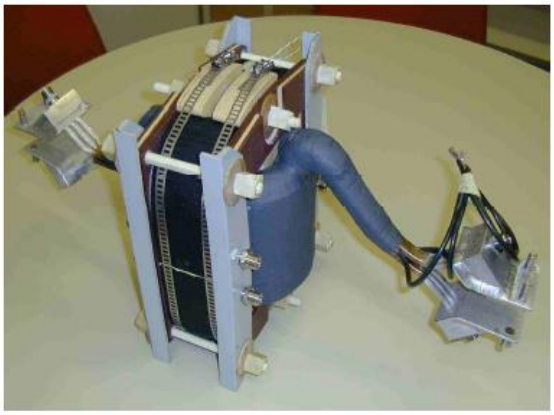

350 kW, 1/1 kV, 8 kHz
Steiner et al. (Bombardier), 2007 [6]
Claimed HV insulation to ground 15 kV @16 2/3 Hz
PD free AC 50 Hz 33 kV

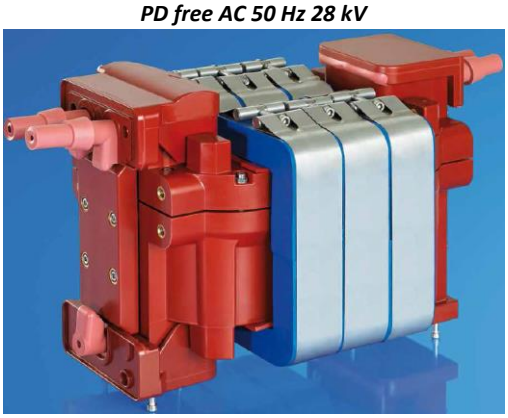

450 kW, 1.8/1.8 kV, 8 kHz
STS Transformers, 2015 [7]
Claimed HV insulation to ground 15 kV @ 16 2/3 Hz
PD free AC 50 Hz 37 kV

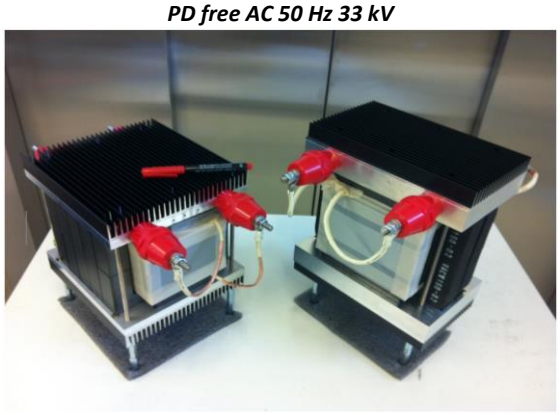

50 kW, 1/3 kV, 5 kHz
Bahmani, Kharezy (Chalmers), 2014 [4] & [13]
Claimed HV insulation to ground 3 kV DC
No information about PD test

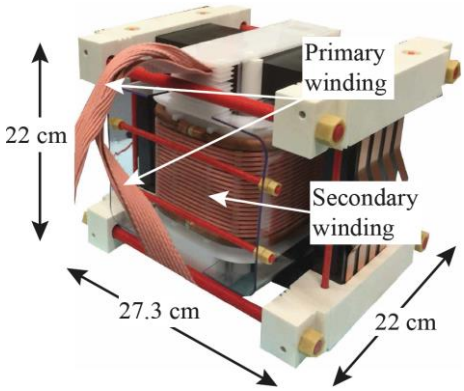

0.4/14.4 kV, 10 kHz
Jaritz et al. (ETH), 2017 [8]
Claimed HV insulation to ground 115 kV DC
PD free AC 50 Hz in oil 110 kV

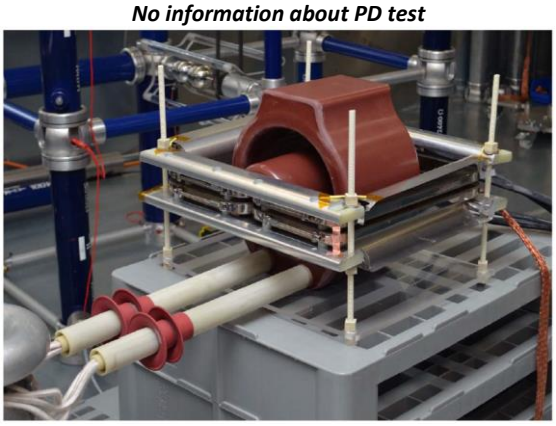

240 kVA, 0.6/0.9 kV, 10 kHz
Gradinger et al. (ABB), 2017 [9]
Claimed HV insulation to ground 50 kV DC
PD free AC 50 Hz 35 kV

Figure 1-2. Examples of MFTs having high HV to ground withstand strength

Based on the abovementioned literature review, it is clear that a very important research question that needs to be tackled for the series DC wind turbine concept to be realised, is how an insulation that can handle both AC and a very high DC stress, could be realised.

1.2.2 High voltage insulation under HVDC stress

Hybrid insulation systems made of different materials (e.g., oil and paper) experience excessive charge accumulation on materials interface when exposed to combined DC and AC stresses. This makes the

design criteria and rules to be different from those applied for insulation of conventional transformers. To reveal the influences of the interfacial changing on the electrical stresses in a composite oil/paper insulation system in the converter transformers, Gäfvert et al. [14] used an ion Drift-Diffusion Model (DDM) and compared it with the traditional Maxwell-Wagner model (MWM). They also used the optical Kerr effect measurement technique to verify the accuracy of the models. By comparing the measured electric fields inside a test object with the ones obtained by simulations, they have deduced that the ion drift diffusion model results in a better estimation of the electric field compared with the Maxell-Wagner model [14]. In particular, they have noticed a polarity effect in the electric field distribution that was not considered in the MWM. They found also that the simulation results have a relatively tight coincidence with the measurement [15].

In the DDM, different physical parameters are used as input, such as mobilities of positive and negative ions, their diffusion constants, particles dissociation and recombination rates, etc. However, the uncertainties when quantifying such parameters for specific simulations tasks as well as the complexity of the model itself are obstacles limiting the use of the DDM for engineering applications [14, 16]. Therefore, a relatively simple method allowing for quick estimations of the stresses acting on the insulation is highly desirable. After performing experimental verifications on oil/paper insulation structures that resemble real transformers it is concluded in [14] that the traditional MW model delivers reasonable results for steady state conditions and can be used for transformer dielectric design, although it cannot represent the physical phenomena that take place inside the dielectrics.

The MWM has been further verified and tested in several studies. Thus in [17], Kerr electro-optic technique have been applied to analyse electric field distribution between two electrodes immersed in oil insulations. They have observed a time and polarity dependent stress in oil/paper composite dielectrics. They have also observed that the electric field distribution is uniform for fresh oils and non-uniform for aged oil, having a maximum value close to the electrodes. Although these facts show the non-linear behaviour of the dielectrics, they have used a Linear Maxwell-Wagner (LMW) model which is based on the material's dielectric constants and conductivities. In a LMW model, the voltage distribution at the instant of the DC voltage application is capacitive, which gradually changes to resistive distribution. The rate of change in electric fields depends on the time constants of the dielectric materials. Although MWM cannot represent the non-linear behaviour of dielectrics, but the model has been the prevalent method in the HVDC dielectric design of transformers [17-22].

A summary of some important activates regarding oil-Barrier insulation system under HVDC stress is presented in Table 1-1.

Table 1-1. A summary of research activities regarding oil-Barrier insulation system under HVDC stress

Authors	Theoretical Method	Validation Method	Modelling
U. Gäfvert, O. Hjortstam Y.V. Serdyuk	Ion drift Method (Onsager theory)	Kerr effect measurement, Maxwell-Wagner simulation	Transformer Oil-barriers system
A. Küchler, M. Libschner F. Schober	Equivalent RC circuit	PDC measurement, Maxwell-Wagner simulation	Transformer Bushing Oil-barriers system
H. Okubo, K. Kato R. Nakane	Maxwell-Wagner	Kerr effect measurement, DC Breakdown, Maxwell-Wagner simulation	Transformer Oil-barriers system
G. Chen, B. Huang M. Hao		PEA space charge, Maxwell-Wagner simulation	Oil-barriers system
K. Backhaus, T. Gabler R. Fritsche H. P. Öftering	Ion drift Method (Poisson-Nernst-Planck)	DC Breakdown PDC	Oil-barriers system
Y. Ebisawa S. Yamada	Linear Maxwell- Wagner	DC Breakdown	Transformer Oil-barriers system

The presented review reveals that a DC insulation design method which is based on the traditional MW method but considers the non-linear behaviour of the insulation materials is missing in the literature. Therefore, to fill this gap, it would be very valuable to conduct research and build knowledge with the target of a modified form of the Maxwell-Wagner model.

Conventional AC insulation design methods are based on the control of safety factors in the oil gaps and creepage paths. This is performed by separate control of the *E* curves of the oil gaps and creepage paths. In this research it is shown that the *E* curve of the combined path is greater than the E curves of the oil gap and creepage paths. Consequently, the E_{av} curves of the combined path is higher compared to that of the oil gap and creepage paths and this can lead to a lower minimum SF for the combined path with respect to the SFs of its forming oil gap and creepage paths. Therefore, knowledge building is also needed regarding the *E*-curves related to the combined oil gaps and creepage paths.

1.2.3 Importance of measurement of electrical conductivity

The physical performance of insulation oils under HVDC stress cannot be explained just by their conductivity features. Ion drift and diffusion, and space charge have a great influence on the voltage distribution in this case and can be of use when analysing the time dependent conductivity values [19, 23].

When an HVDC voltage is applied to the MFT's HV winding, the voltage stress over the insulation layers is not simply calculatable considering constant conductivity figures for the materials. Among others, parameters like temperature of oil and paper, field strength, prestressing of insulation system and duration of application of voltage should be considered [24]. These parameters affect the ion mobility and density and consequently change the resistivity of the materials and the time of stabilization of the insulation system when HVDC is applied.

Additives like inhibitors, pour-point depressants, antioxidants or antistatic agents are added to the mineral or synthetic oils to make them as a reliable medium for a long-time application of power transformers as possible. Dissolution of these additives, or oil and cellulose oxidation products has a considerable effect on the conductivity of insulating oil or oil immersed cellulose [25]. That is why, even for the same type of oil, there is a vast spreading in the conductivity values depending on difference in producers, production facilities, markings or even periods of production.

Wahlström [26] and Beletsky [27] have suggested expressions respectively for the temperature and field dependencies of the resistivity of transformer oil and paper board. However, one cannot rely completely on these expressions and as mentioned earlier, there are several parameters that can affect conductivity values at the same time.

To sum up, for a successful insulation design, a set of measurements on oil and OIP electrical conductivity values are required. Several standards have presented methods for surface or volume conductivity of liquid or solid insulation materials (IEC 61620 1998, IEC 60247 2004, ASTM D1169 2011, IEC 62631-3-1&2 2016 or ASTM D257 2014). A comparative table is prepared, and the strong and weak points of the measuring methods are summarized in a Cigré publication [28]. The result of this comprehensive study shows that none of these standard methods guarantee both reproducible and comparable results with the conductivities under HVDC test or service conditions. Therefore, efforts will be made in this upcoming research work on how to prepare a reliable setup and perform a proper pre-conditioning process, in order to obtain repeatable and reliable values for the biodegradable insulation materials, which due to environmental ambitions are proposed to be used in a transformer for the series DC wind park application.

1.2.4 High voltage insulation under high frequency stress

Not only an MFT, but also 50Hz power transformers designed to be used as step-up transformers in wind farms are subjected to high frequency transients and high voltage stresses which is a result of resonances. At the moment, to design an MFT, one can rely on insulation materials datasheets for 50-60 Hz frequencies and use a conservative safety factor, however in this way the final design can be far from optimized, and also the failure rate will be unknown and finally the designs will not be comparable with each other. The importance of paying attention to the effect of the voltage wave form is explained by Heinemann in [5].

Nowadays, wind farm transformers are designed and manufactured according to IEC 60076-16. In his PhD thesis [29], Khanali concentrates on the effect of the rate of rise and repetition frequency of high voltage impulses on insulation of transformers. Although the study is on 50 Hz transformers, the same challenges exist for insulation design of MFTs, which operate under square wave voltages and in the kHz range.

IEC 60851-5, IEC 60243-1, or ASTM D149 specify tests of electrical properties of insulations at frequencies lower than 60 Hz. The standards which are referred to by insulation material suppliers like the withdrawn standard IEC 60250: 1969 or its replacement IEC 62631-2-1: 2018, or ASTM D150 only present guidelines for the determination of dielectric properties of insulating materials, and no information is given about withstand testing methods of insulation materials at frequencies higher than 60 Hz.

For power transformers, IEC 60076-11 and IEC 60076-16 together with IEC 60076-3 cover dielectric tests only at power frequencies and IEC 60664 and IEC 61558 series are about safety measures for transformers only up to 25 kVA. In the rotating machine field, valuable information can be found in IEC 60034-18-41 concerning the qualification testing of rotating machines fed from voltage converters under high frequency stress. However, neither standardization nor defined test methods specifically addressed the insulation materials for an MFT, which typically runs at medium frequency (<20 kHz) square wave shape with rise times in the microsecond range. Therefore, a series of insulation tests should be performed using a repetitive impulse voltage and the results should be compared with the data presented in high voltage materials' specification sheets.

Koltunowicz [30] demonstrated the influence of frequency and rise time on the breakdown voltage (BDV) and partial discharge inception voltage (PDIV) of grid transformers. A summary of results published in [31] clearly shows how an increase in the repetition frequency and/or a decrease in the rise time can affect the breakdown voltage causing its reduction. As claimed, the breakdown occurs after a certain number of impulses.

Kiiza [32] has described how a long PD activity combined with high voltage impulses can degrade an oil-paper insulation system. He has used AC 50Hz voltage and High Voltage (HV) impulses to demonstrate how this combination, results in insulation destruction. Morshuis [33] has published his findings on degradation of solid dielectrics, originating from an internal PD. In case of an MFT, instead of sinusoidal 50Hz, a medium frequency square wave can be used to create the partial discharge.

To sum up, very limited activities have focused on insulation design requirements of high voltage MFTs operating under a medium frequency square wave regime. The missing gap extends from an insulation material selection stage to reliable long-time operation. For example, the material data sheets which are developed for DC or power frequency applications do not present the breakdown strength under medium frequency square wave stress.

This work will not contribute to research regarding the high-frequency tension, but will try to demonstrate some measures that can be taken to reduce the risk for failure of insulation systems due to this type of stress.

1.2.5 The leakage inductance of circular shell-type MFTs considering the effect of core

To achieve the lowest loss by the Zero-Voltage Switching of a Dual Active Bridge converter, it is crucial to precisely calculate the embedded Leakage Inductance of the used Medium Frequency Transformer.

A Dual Active Bridge (DAB) can benefit from the MFT's leakage inductance (L_s) to transfer the power between the input and output bridges, and this will result in a high power-density unit. By controlling the switching on the two sides, the square wave voltage from the primary and the secondary converters will be adjusted to have a defined phase shift relative to each other. Such a transformer serves as an inductance, in addition to its natural duty of voltage adoption between the primary and secondary bridges (Figure 2-2b). In other words, the design of the transformer should fulfil the criteria of having a determined leakage inductance in addition to keeping the specified isolation, efficiency and the thermal requirements [34].

The lowest loss is achieved when Zero-Voltage Switching (ZVS) is stablished, which among other factors depends on the phase shift, $\varphi_{\min}$ between the primary and secondary bridges. The core loss is also highly dependent on the duty cycle and the rise time of the wave shapes [35], which can be affected by the leakage inductance of the transformer. It would thus be of great importance to accurately evaluate and implement the leakage inductance value of such a transformer in the design stage.

Different analytical methods have been used for the leakage inductance calculation in literature. In the classical approach (which can be found in [36-38], it is assumed that the leakage flux inside windings and in gaps between windings is completely axial while the effect of the radial leakage flux is considered by applying the Rogowski factor to the average height of the windings to obtain a higher equivalent winding's height [37]. The simulations performed in this paper show that although the classical approach is suitable for calculating the leakage inductance of conventional power

transformers, it may be inaccurate in the case of shell-type MFTs. In [39], the superposition of the axial and radial components of the leakage field is used to reduce large errors of the classical method.

The leakage inductance calculation using the double Fourier series extension of the leakage field is developed in [40]. The method is originally proposed for the first time by Roth in 1928 and applied for the calculation of the leakage inductance per unit length in 2-D planar coordinates in [41-44].

The method of images with an analytical 2-D solution of the magnetic vector potential is used for the calculation of leakage inductance in [45]. It is also concluded that the classical approach can lead to a considerable error when the windings have unequal heights. The method of images based on an expression of the magnetic vector potential for a rectangular conductor is also used in [46] for the computation of the static leakage inductance of HF transformers. The leakage inductance of toroidal transformers using the classical approach is presented in [47]. A review of the analytical methods of transformer's leakage inductance calculation is also presented in [48].

The Finite Element Method (FEM) has been extensively used for the leakage inductance calculation in literature [49-51]. The FEM formulation is independent of the geometrical details and thus it is more accurate than the analytical methods however, it takes substantially more time to evaluate. In addition, a FEM software or a specifically developed FEM program is also needed.

For calculating the leakage inductance using the conventional method, first, the inductance per unit length is calculated using a field analysis method, and then by multiplying the inductance per unit length by the Mean Length of Turns (MLT), the total leakage inductance is obtained [48, 52]. There is no definitive method for determining the MLT in the literature. Furthermore, an important issue is to incorporate the effect of the boundary conditions caused by the core walls in the leakage inductance calculation which has been less considered in the previous studies.

In a previously published article [44], the authors focused on the leakage inductance calculation of shell-type MFTs with rectangular windings. The leakage inductance per unit length is calculated by a double Fourier series analysis in 2-D planar coordinates. A new method for determination of MLT considering the distribution of Ampere-turns inside individual layers of the windings is also presented. The current thesis presents an accurate procedure for the leakage inductance calculation of shell-type MFTs with circular windings.

Unlike Rabins method [53], in the new analysis developed in this study, the core window is assumed to be bounded to the core wall from outside. It means that, the effect of the core's return leg is considered on the leakage inductance calculation of the shell-type transformer. Here, knowledge must be gained regarding if the differences in geometry and boundary conditions, will affect the vector potential and the mutual inductances. In case of a successful outcome, time-consuming FEM simulations can be avoided. Accordingly, the research issue here is how to accurately calculate the leakage inductance for a transformer which has a circular form, a segmented core structure and high isolation distances between the parts.

1.2.6 Determining parasitic capacitances for MFTs

Determination of parasitic capacitances is a necessary step in the design process of transformers to be used in power electronic devices. At high switching frequencies, these capacitances together with

inductive elements of the circuit cause unwanted oscillations during fast transients such as sharp fronts of square voltage waves appearing in a dual active bridge converter.

When a high frequency voltage is applied to a transformer, it is distributed along its winding. At lower frequencies, the voltage distribution is close to linear, and it is defined mainly by the inductances in the circuit whereas at higher frequencies the effect of parasitic capacitances becomes dominant that makes the distribution to be non-linear and been defined by the values of the capacitances. At high switching frequencies, these capacitances together with inductive elements cause unwanted oscillations during fast transients of sharp fronts of square voltage waves appearing in a dual active bridge converter [54].

Equivalent circuits for modelling electrical behaviour of the transformer in a wide frequency range have been proposed in [55] and [56]. To identify the elements in the circuit models, input data are required which can be obtained when a manufactured transformer is available for the related measurements. This limits the applicability of the equivalent circuit approach for the transformer's design stage, where many factors are needed to be considered to obtain feasible results. Estimations of parasitic capacitances have been attempted e.g., in [57] based on the geometrical symmetry of the winding design and static capacitance measurements. The scope of the calculations covered only static layer to layer capacitances of the windings due to the complexity of the capacitive network within the transformer. In addition, the influence of the core on the equivalent capacitance calculations was ignored. An attempt to account for the effect of the core has been undertaken in [58], but this study was only based on 2D analytical calculations and thus cannot be generalized to practical cases when asymmetric transformers' structures are common. In [59], FEM simulations were used for obtaining parasitic capacitances of a transformer, but this study covered only a winding and not considered any effect of the core. Thus, there is a lack of a general method for deriving an equivalent circuit for an MFT which is demanded since it could be further integrated into a power electronic circuit simulation tool to enable an analysis of the whole component. Such an option has been suggested in [60], where an implementation of a lumped parameter circuit based on finite element simulations was considered, but the analysis was limited by the condition assessment of 50 Hz power transformers.

There is a limited information in the literature about several important issues including the implementation of inductive elements in the equivalent circuit models, determination of capacitances between both ends of the windings and ground, effects induced by fast transients causing non-linear voltage distributions along transformer windings [55-60]. Therefore, it would be of high interest from a research point of view to compare various modelling approaches, to build knowledge regarding the influence of parasitic capacitances of the MFTs.

1.2.7 Importance of determining transformer losses

The information about the losses which produces heat inside the transformer is valuable for designing an HVDC MFT in two ways. First since MFTs have high power densities [61] and heat dissipation is extra important and second, because the DC insulation design has a direct dependence on the electrical conductivity values of the insulation materials which are themselves, temperature dependent parameters [28, 62]. In other words, energising and loading the transformer results in temperature changes in core and coils and consequently distresses the multilayer insulation system of the transformer. In addition, to achieve the highest efficiency of a DAB converter, it is crucial to accurately calculate the winding losses of the used MFT.

The main origins of the losses in a transformer are the losses in the cores when an alternatively changing flux having a certain density is induced in it and losses is in the windings when the high frequency current passes through them. These losses produce heat which warms up the environment which the active part is placed in (in this project transformer oil). The amount of heating will be varying during the transformer operation depending on the excitation voltage level and loading current level. Normally the losses are calculated and measured for the worst case when the transformer is supplied at its rated voltage and the rated current.

Winding losses are caused by ohmic loss in the current carrying windings and additional losses due to proximity and skin effect and core losses, consisting of static hysteresis losses, classic eddy current losses and excess eddy current losses [36]. Additional losses are because of induced capacitive/inductive currents in the adjacent construction conductive parts.

In addition, the losses will contribute to the warming up of the transformer oil which will affect the conductivity and consequently the voltage stress distribution under an HVDC high voltage application [28]. The amount of produced heat is used to design the oil circulation and cooling system of the transformer.

At high frequencies, the losses in the copper MFT winding conductors will drastically rise because of the skin effect in the conductors, and the proximity effect to the adjacent conductors. The winding losses are calculated using linear superposition of the losses caused by different harmonic contents of the applied AC current [63]. The voltage and current waveforms can be observed in Figure 2-1a.

Having access to a set of precise formulas and methods, for the calculation of winding losses with an acceptable accuracy, is of high importance. Wide frequency range, possibility of having a free selection of number of layers, and number of turns per layer are among the features that should be considered during the development of new methods. Previous works [64-67] propose formulas to calculate the AC resistance of the conductors under high frequency switching conditions. These proposed analytical methods for calculation of winding losses are based on empirical relations originally developed for foil windings, which have been modified by researchers to be applicable for the litz wires. However, these methods are approximate, and their application is time consuming, Furthermore, many simplifying assumptions are required in order to solve the problem. Accordingly, to conduct research in order to find a fast and accurate method for loss calculation of the windings made of litz wires, would be of great value.

Dielectric losses cause heating of the insulation material which is dependent to the frequency and magnitude of the applied voltage, and on the capacitance and loss angle of the insulation material as explained in [36], is negligible at 5 kHz compared with the core and winding losses [3] and is not included in the scope of this work.

1.2.8 Required information on oil type MFT's components

The liquid insulation is used for different purposes in a transformer. The most important functions of transformer oil are isolation (alone and as a saturating material for cellulosic barriers), cooling, absorbing the humidity of solid insulations and an arc-quencher [68]. In this research, two oil types are considered, the mineral oil which has the most well-known characteristics for AC and HVDC applications and is used for large converter transformers [69] and synthetic ester oil which is biodegradable [70, 71]. Because of their nonlinear electrical behaviour, a high volume of the research is concentrated on characterizations of these types of oil for HVDC applications [28, 72, 73]. However,

reliable electrical conductivity results at high voltage levels especially for ester OIP are missing in literature. The use of ester oil for designing high voltage DC transformers are not investigated thoroughly in the literature as it is done for mineral oil for the last decades. Consequently, it is valuable to build further knowledge about the application of ester oil in comparison with the mineral oil and to evaluate its effects on performance of the insulation system when an HVDC stressed transformer is under consideration.

A comprehensive review about environmental impacts of using natural ester is presented by Asano [70]. This type of oil is an environment-friendly replacement for mineral oil which has widely been in use in power transformers. References [74] and [75] are two important sources which present guidelines for the use of ester oils in electrical equipment. Natural ester has different chemical composition in comparison with other insulating fluids like synthetic esters or silicone fluids that have high fire points [74].

Solid barriers act as insulation when AC or DC voltage is applied to an oil filled transformer. In addition, barriers act as separators to reinforce the electrical strength of long oil gaps [76]. Both volume and surface (creepage) dielectric strength of the solid insulation are important. This study has concentrated on withstand strength of the insulation under HVDC stress. The conductivity of solid insulation which is a non-linear function of applied voltage, temperature and the time of application of voltage [28] is studied. Solid insulations are polarised and contribute to concentration of space charges in its interface with the insulation oil which shall be considered for a successful HVDC insulation system design.

Two types of solid insulation materials are used for manufacturing power transformers; cellulosic and Nomex materials [69]. Cellulosic transformer board is made of unbleached sulphate cellulose from slow and dense growing tree woods [76]. Nomex transformer board is made of synthetic crystalline aramide. The most important advantage of Nomex is its thermal stability, and its very high resistance to aging. Its disadvantage is its tendency to attract the particles if it is statically charged [24] and also no water absorption capability.

The main research question in this project is to increase knowledge of a special transformer for usage in a series DC wind park. In order to accomplish this, the reliable design aspects are investigated using a 50 kW, 0.4/5 kV, 5 kHz prototype transformer with the HVDC insulation to ground of 125 kV, which is designed and manufactured using off-the-shelf materials. Furthermore, to conduct verification tests on it and compare theory and simulation result.

1.3 Purpose & contributions

The purpose of this research effort is to generate scientific as well as practical knowledge required for bringing the DC series concept of an offshore wind park one step closer to pre-commercialization.

The following contributions were reached during the research work:

- Based on literature search, interviews, and research investigations, developed the procedure and set-up, in particular the pre-conditioning, to reliably determine the properties of the eco-friendly biodegradable ester-based transformer oil and OIP for high DC-voltage biased, insulation applications,
- Provided the scientific society with electrical conductivity values of synthetic ester OIP, including their temperature and field variations usable for HVDC insulation design,
- Demonstrated the implementation possibility of introducing non-linear properties of materials in the Maxwell-Wagner model, also applied in a simulation software,

- Proposed a novel combined-path method for designing oil-paper insulation systems which ensures a higher design safety level in comparison to the traditional oil-gap and OIP stress controls and demonstrated its usability,
- Formulated a procedure in order to reach a safe insulation structure which guarantees the adequacy of the proposed design to withstand the DC stress at the energization moment, during the whole transition from AC to DC, and at the final electrified and loaded condition,
- Experimentally proved a high accuracy analytical method for calculation of the leakage inductance for a wide range of segmented designs of shell-type transformers with circular windings, which considers the effect of core walls as well as the number and dimensions of the core segments,
- Derived and experimentally proved an accurate and practical method for calculating parasitic capacitances to achieve a high frequency equivalent circuit of an MFT. The circuit can be used on the converter design stage to predict the effect of these parasitic elements on the operation of power electronic devices,
- Proposed a simple, fast and accurate method for loss calculation of the windings made of litz wires and demonstrated its validity,
- Shown the effect of reduced breakdown voltage when exposing insulation media to frequencies much higher than 50 Hz and proposed precautions that shall be taken for a reliable high frequency insulation design by performing characterisation tests,
- Designed and manufactured an innovative prototype oil type transformer using off-the-shelf materials and in-house equipment and facilities, addressing the issue of a high voltage DC bias, resulting in a round transformer design, furthermore, conducted a series of verifying experiments utilizing the prototype transformer. In addition, provided details of the design as well as design procedure in order to make it possible for other researchers to verify and reproduce the results,
- Established what the pros and cons with ester versus mineral oil for an HVDC transformer application is and presented a comprehensive and unique set of comparisons between mineral and ester oil for high voltage DC insulated transformer, and
- Utilising the knowledge acquired from the prototype, demonstrated the resulting size and weight of the DC-biased wind turbine DC/DC converter. Brought forward efficiency characteristics for a proposal for a real-scale unit of the series DC wind turbine DC/DC converter.

Finally, based on the knowledge gained by abovementioned contributions a novel design method of an oil type power transformer with a high-voltage DC offset is introduced and validated, through both a theoretical analysis as well as a prototype that has been built.

1.4 Thesis layout

The thesis is structured as theory, simulations and characterisations, and manufacturing set-ups. Later, verification and analysis sections are presented, and the research is finalized by a real scale system design proposal.

The research questions are formulated utilising a literature review and the research gaps are highlighted in Section 1.2. Research activities regarding the DC insulation design are presented in Sections 2.2, 4.2, 5.1.6, and 5.3. The leakage inductance is studied in Sections 2.4, 4.3, and 5.1.1 and the parasitic capacitance in Sections 2.5, 4.4, and 5.1.2.

As explained in 1.2.3, another important research target is to find a reliable method for determining the conductivity of the materials used in the design. This aspect is described in Section 2.2, and 3.

In addition, the proposed methods for determination of the core and winding losses are introduced in Section 2.6, 4.5, and 4.6 which are followed by verification tests in Section 5.1. Finally, a real scale transformer design is presented in Chapter 6, utilising the generated knowledge in previous Chapters.

2 Theory

2.1 HVDC MFT for series DC integration layout

The Dual Active Bridge (DAB) topology is easy to control, has wide Zero Voltage Switching (ZVS) region without a need for snubber circuits in contrast to the single active bridge converters (SAB) which have the disadvantage of hard switching on the output diodes. Moreover, it can operate at a higher frequency and power level compared to full bridge converters (FBC) and has no need for high voltage and current resonant capacitors. A final advantage is that is has no need for a large resonant inductor as compared with Series Resonant Converters (SRC). The leakage inductance of the MFT is used as a resonant inductor inside a DAB and this, results in higher efficiency and lower volume and price. Although a Dual Half Bridge (DHB) has a lower number of parts, the circulating reactive current in the MFT is lower in the case of DAB [3]. As explained, the Dual Active Bridge (DAB) is a promising converter topology candidate to be used as part of an isolated DC/DC converter for sea-based wind-farm application.

An MFT is in a DAB set-up operated using square wave voltage stress as connected between two H bridges in the DAB DC/DC converter (Figure 2-1).

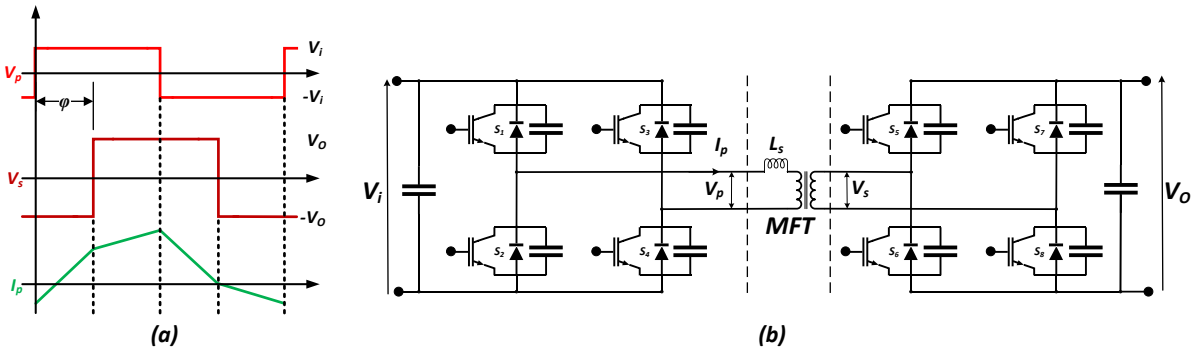

Figure 2-1. An MFT having an embedded inductance inside a DAB: voltage & current wave-shapes (a), and an MFT between two stages of a DAB acting as a series inductance (b)

In the series DC concept, DC voltage supplied by series connected converters will be directly transferred to a suitable grid connection point on land where it is feed into the main electrical system (Figure 2-2).

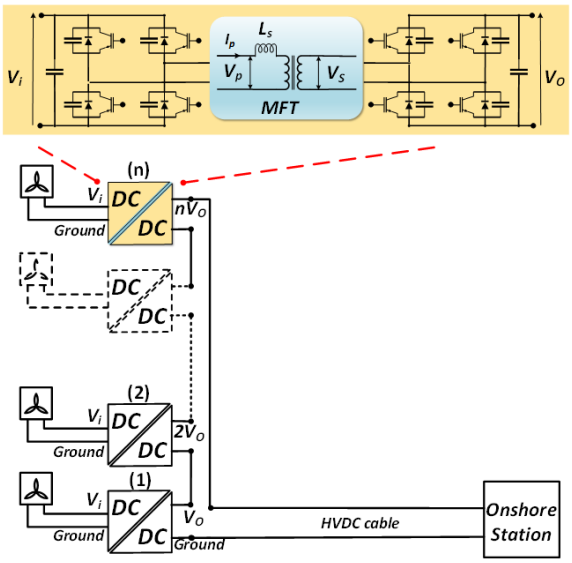

Figure 2-2. MFT inside a DAB as part of a series connected bridges

The DC/DC converter which have the highest place (highest potential to ground) in the series connected wind farm concept (number n) can experience a high DC voltage (nV_o) superimposed with a medium frequency square voltage of the secondary (V_s) of a few kilovolts to ground while the primary side, have the symmetrical voltage of V_p to Ground (Figure 2-3).

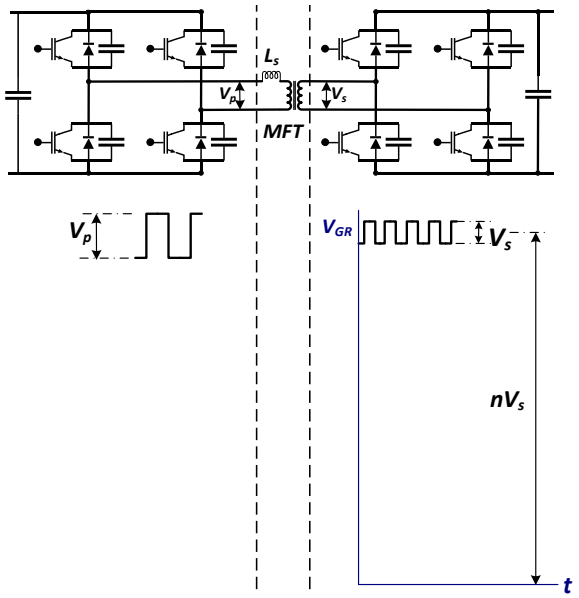

Figure 2-3.Voltage to Ground (VGR) at Secondary side of the MFT

This means that the transformer secondary winding – core, secondary winding – primary winding and secondary winding – body insulations should be dimensioned for a High DC Voltage (HVDC insulation concept).

At the same time, the primary winding – core, primary winding – body and turn-turn insulations both for LV and HV windings should be dimensioned for a medium frequency square wave voltage.

As an example, in the ideal case, if 30, 1:3 kV DC/DC converter be coupled in series, the voltage at the secondary terminals of the transformer number 30 will be 87kV<V_{GR}<90kV. If each turbine delivers 5 MW, the total deliverable power will be 150 MW at the voltage of 90 kV. In practice there needs to be a certain over installation of turbines to handle the varying power of the turbines as well has to handle the situation when some turbines are out of operation. In contrast to a normal shunt connected set of turbines that feeds out current to a common DC voltage, here the current between the two DC-voltage buses is the same for all turbines in a series connection.

In order to realise this system, the key issue is to have a transformer within the wind turbine DC/DC converter that apart from transmitting the power from the wind turbine to the collection radial, also is able to handle a very high common mode DC voltage to ground.

2.2 HVDC MFT's insulation design challenges and methods

The key challenges with the design of a high voltage insulation system of MFT are introduced in [61]. There is an important research question which will be addressed in this section. A transformer, for which a DC-bias of 100-300 kV is applied on top of a 10-20 kV AC; will that be a realizable object? When combining different aspects, for instance an energizing transient caused by the applying of an HVDC step, ensuring proper safety factors at all locations in the transformer, etc, which kind of process should be formulated? In this section the issues related to this question is highlighted.

2.2.1 Oil type high voltage transformers

Oil filled high voltage power transformers have been operating successfully for the past century in AC substations. For high power and voltage applications, mineral oil impregnated paper and pressboards have been the dominant technology in use [77]. A thick steel tank protects the active part from external contaminations, a metal core is surrounded by the windings and the oil is used as a reliable component in the insulation system and as a cooling medium (Figure 2-4).

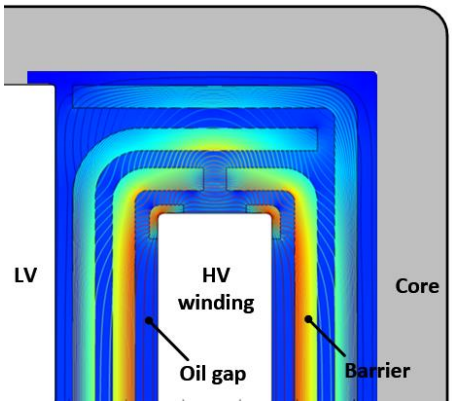

Figure 2-4. The core window filled with the oil, the distance between HV winding is divided to smaller gaps by barriers

For a DC design, the thickness of the solid barriers is important. The position, form, and overlapping of the solid barriers must be carefully taken into consideration. Local temperature, electric stress, humidity and oil flow inside the insulation system can change the conductivity of the insulation materials and should also be considered for a successful DC design process.

2.2.2 Transformer insulation under AC stress

Under AC stress, the voltage distribution is determined by the permittivity of the insulation materials constituting the insulation system. At steady state DC it is the conductivity of the insulation materials which determines the voltage distribution. For an oil paper insulation system, the low permittivity oil which experiences a high voltage potential difference under AC will take less voltage drop then under DC due to the higher conductivity compared with solid paper or pressboard insulation. When a DC voltage is applied to the transformer, first it is the permittivity values which determine the voltage distribution and at the steady state condition, the distribution is based on conductivity values [78].

The permittivity values have a weak dependence on the temperature while the conductivity values of both oil and paper, may change significantly. In addition, conductivities can change depending on the magnitude and duration of electrical stress applied as a function of time which varies based on the time constant related to the polarisation and relaxing of the insulation materials [28].

2.2.3 Effect of solid barriers at oil type transformers

Barriers can introduce physical improvements to an insulation system operating under AC regime and it is better to have a finer division in an insulation distance in transformer oil to gain more withstand voltage (Figure 2-4) [76]. For an oil volume between two electrodes, the insulation strength is influenced by gap distance, oil volume, electrode surface form and isolation coating of electrodes. The lower the gap distance, the higher the breakdown voltage per millimetre [77]. Therefore, the electric strength of a space between two electrodes in oil increases by inserting insulated barriers. Such a barrier has an influence both on discharge initiation process at the electrode surface and on discharge growing process at the oil gap.

2.2.4 Voltage distribution under AC stress

For an oil gap between two conductors divided into several gaps by solid barriers, the average permissible electric stress can be calculated by [77]

$$\frac{V}{d} = \frac{(n+1)\frac{\varepsilon_{\text{Oil}}}{\varepsilon_B} d_{\text{B}} + n d_{\text{Oil}}}{(n+1) d_{\text{B}} + n d_{\text{Oil}}} E_0 \left[\frac{d_{\text{Oil}}}{1mm} \right]^{-a} \quad \textbf{(2-1)}$$

where V is the applied voltage, d is the total distance between the conductors that shall be minimized, n is the number of oil gaps, ε_{Oil} and ε_{B} are the permittivity of oil and barrier respectively, d_{Oil} and d_{B} are the thicknesses of the oil gaps and barriers respectively, E_0 is the PD inception field strength for a 1 mm gap [76] and a is slope of the straight lines of the PD inception field strength-oil duct width in log-log curves [76].

For an AC non-uniform field distribution, e.g., at the ends of the winding or at the high voltage lead exits, the local average field stress $E_{\text{av}}(z)$ for each path length can be calculated from the following relation

$$E_{\text{av}}(z) = \frac{1}{z} \int_0^z E(z')dz' \quad \textbf{(2-2)}$$

For each critical insulation pass, the resulting field must be compared with the maximum permissible (partial discharge free) field strength $E_{\text{bd}}(z)$, which is based on a set of empirical measurements [77] and is given as

$$E_{\text{bd}} = E_0 d^{-0.37} \quad \textbf{(2-3)}$$

where E_{bd} is the strength of an oil gap of length of d mm; E_0 is equal to 17.5 and 21.5 kV_{rms}/mm for bare and covered electrodes, respectively.

Finally, a safety factor is calculated as

$$SF(z) = E_{\text{bd}}(z) / E_{av}(z) \quad \textbf{(2-4)}$$

which should be higher than 1 along the length of the selected path. This process should be repeated for all suspected critical insulation regions in the transformer.

Figure 2-5 demonstrates a selected critical path, absolute value of the local stress, averaged field stress curves along the paths, the maximum permissible field strength and safety curves under 125 kV AC for a sample transformer.

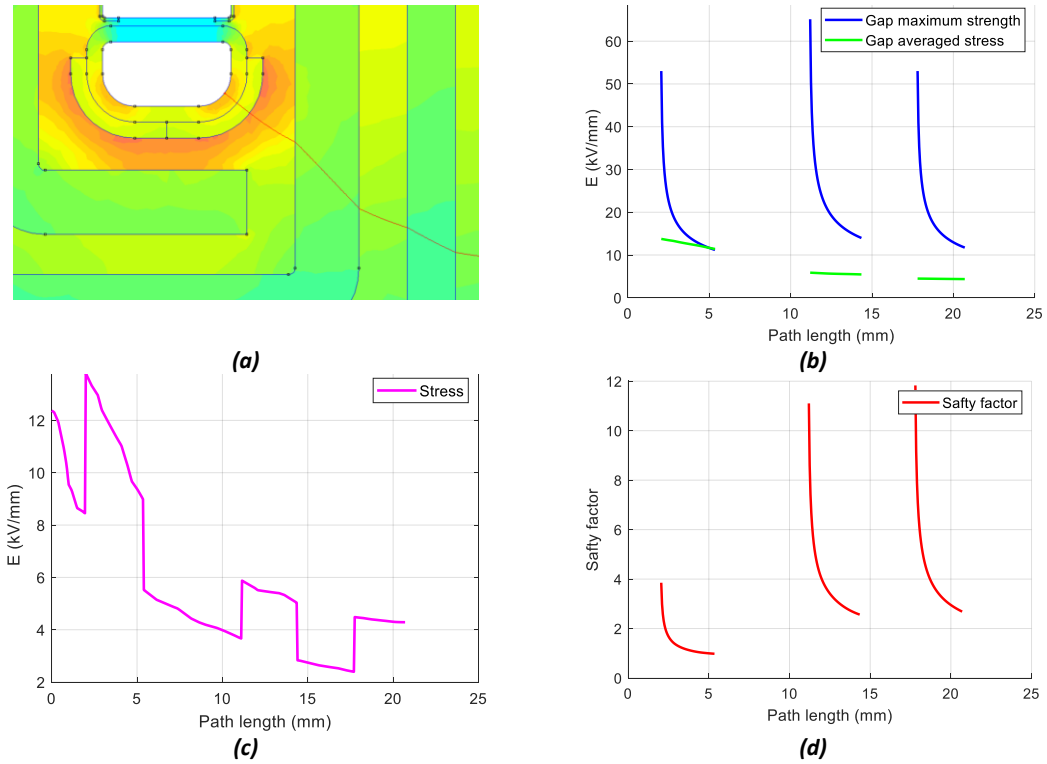

Figure 2-5. Sample critical path curves for an oil gap: a streamline pass from HV winding shield to the core body (a), comparison of the maximum and averaged field curves in the respective oil gap lengths (b), absolute value of the local stress along the field line(c), and the safety factor curves per oil gap (d)

2.2.5 AC design, creepage distances

The same evaluation method as for the oil gap is applied when the electric strength over the materials' interface is under consideration. First along the creepage path, the tangential field strength values shall be rearranged to a steadily ascending profile [77]. Then an averaging shall be performed on a path length between two points where the tangential stress is higher than 0.1 kV/mm [22]. On the interface between the transformer board and oil, the maximum permissible creepage strength is 30% lower than the permissible strength for an oil gap of the same length [77]. Figure 2-6 demonstrates a selected critical path, sorted values of the tangential local stress, averaged field stress curves along the path and the maximum permissible field strength curves under 125 kV AC on a sample transformer.

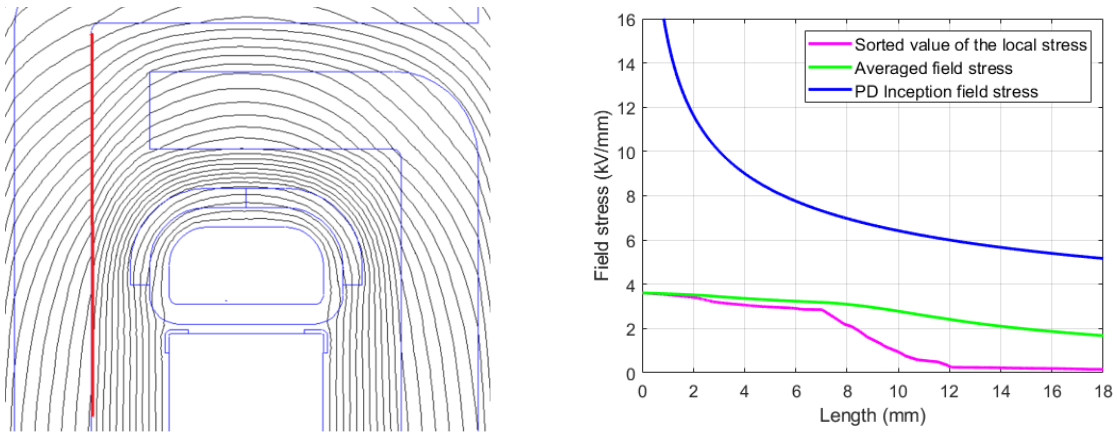

Figure 2-6. Sample creepage path curves on an insulations' interface

2.2.6 Insulation under DC stress

To handle a high DC voltage applied to the high voltage winding, the insulation should withstand induced AC voltage from the low voltage winding and the superimposed DC voltage applied from its

HV terminals. Steady state DC and repeated pulsed AC voltage stress is present. A combined HVDC and AC insulation design of the MFT is discussed in [78]. The study shows that for a dry-type MFT, it is difficult to accomplish this with a relatively high voltage to ground insulation. Oil-type insulation is thus more suitable for an AC design, the long oil gaps shall be divided by a number of solid barriers.

Figure 2-7 demonstrates an electrical circuit equivalent diagram of an three-layer insulation system when a DC step voltage is applied on it. The voltage distribution under AC stress is based on permittivity values of the insulation materials, i.e., capacitive properties. At the moment of application of DC voltage, the distribution is similarly based on permittivity values. Later it is a transition time, when the frequency dependent polarisations which have started with the voltage change, ends and finally the voltage distribution is based on the conductivities of insulation materials i.e., resistive properties.

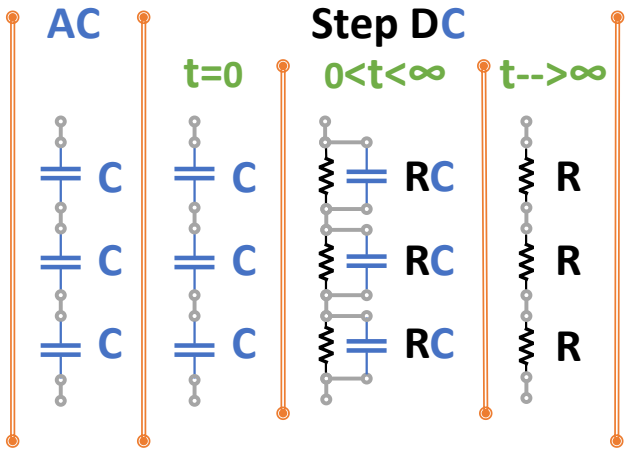

Figure 2-7. Behaviour of an insulation layer stressed with DC step voltage

2.2.7 Oil-paper insulation system under DC stress

For AC voltage stress, the electric field is higher in the oil gap having a lower permittivity than in the barriers which have a higher permittivity, and it is the oil gap which has a dominant effect on the AC voltage withstand strength. However, for DC voltage stress, the electric field is lower in the oil gap having a higher conductivity than in the barriers which have a lower conductivity, and it is the barrier thickness which has a dominant effect on the DC voltage strength. As a result, a proper design for an HVDC MFT should include both a high volume of oil and thick solid paper insulation.

Directly after switching on the high HVDC voltage, the capacitive field is charged to a certain HVDC voltage level and as explained, it is the permittivity of the materials which determines the voltage drops over the layers of the combined insulation system. After a long time following the applying of HVDC, the resistively divided field is supplied with HVDC voltage, and it is the conductivity of the materials which determines the final voltage drops over the layers of the combined insulation system. This is demonstrated by the FEM simulations presented Figure 2-8.

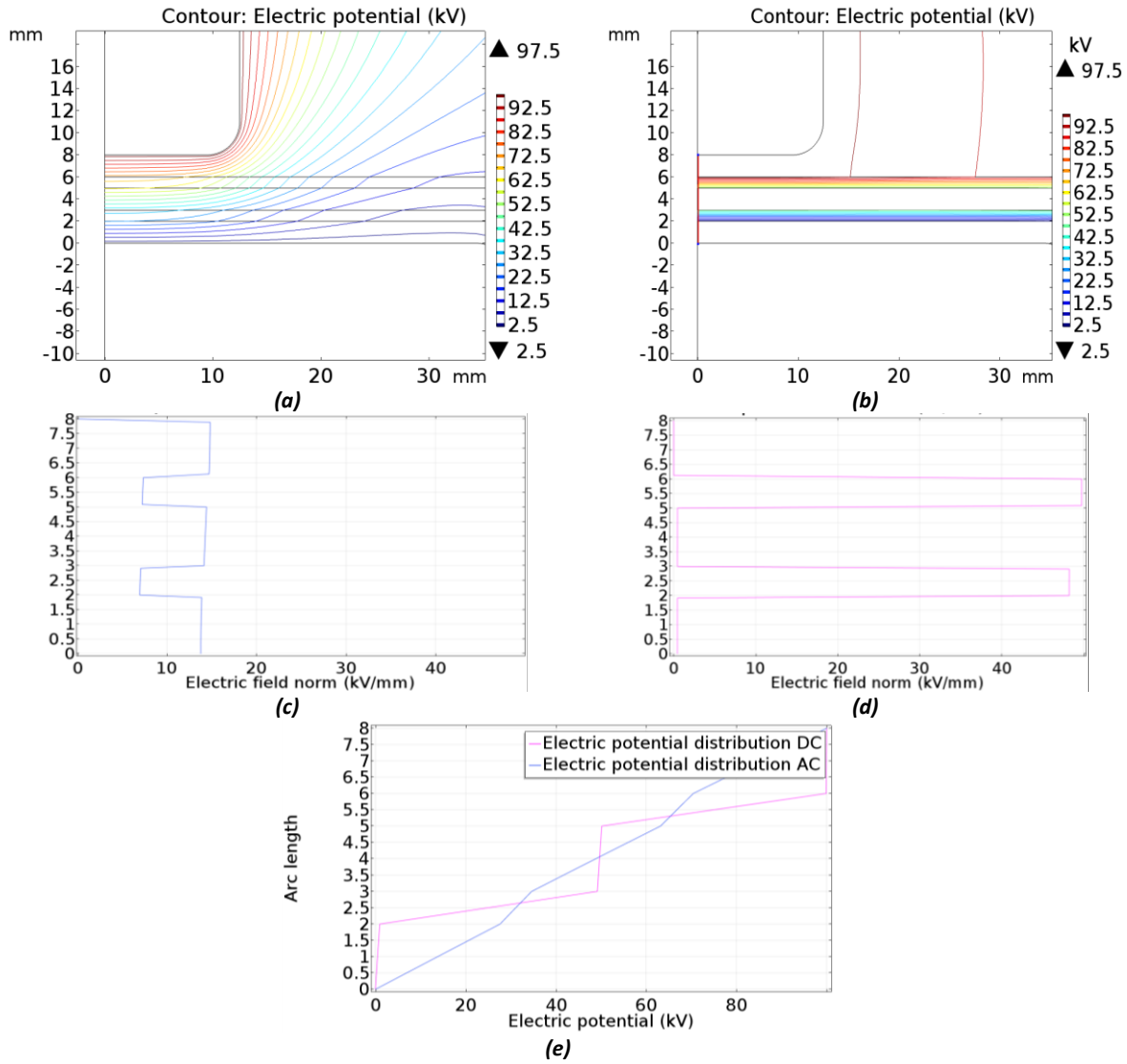

Figure 2-8. Two electrodes having the cylindrical geometry supplied with 100kV to ground, and two 1mm board barriers inside mineral transformer oil, demonstrating the difference between AC (blue) and DC (red) voltage distribution and effect of solid barriers: equipotential lines distribution under AC supply (a), equipotential lines distribution under DC supply (b), AC stress profile along the 8mm axis between two electrodes (c), DC stress profile along the 8mm axis between two electrodes (d), and the electric potential distribution (e)

2.2.8 Effect of unequal conductivities on varying voltage distribution under DC stress

Figure 2-9 demonstrates an insulation system consisting of three different insulation layers. On the interface of the two dielectrics, the change of electric charge densities, *D*, with time is equal to the difference on current densities *J* following the relation

$$J_2 - J_1 = \frac{d}{dt}(D_1 - D_2) \qquad \textbf{(2-5)}$$

Therefore, for a three-layer configuration as presented in Figure 2-9, the following system of differential equations is valid,

$$\sigma_2 E_2 - \sigma_1 E_1 = \frac{d}{dt}(\varepsilon_1 E_1 - \varepsilon_2 E_2)$$

$$\sigma_3 E_3 - \sigma_2 E_2 = \frac{d}{dt}(\varepsilon_2 E_2 - \varepsilon_3 E_3) \qquad \textbf{(2-6)}$$

$$d_1 E_1 + d_2 E_2 + d_3 E_3 = V$$

where E is the electric field intensity, V is the applied voltage, σ is the conductivity and ε is the permittivity.

$$\begin{bmatrix} \varepsilon_1 & -\varepsilon_2 \\ \frac{\varepsilon_3 d_1}{d_3} & \varepsilon_2 + \varepsilon_3 \frac{d_2}{d_3} \end{bmatrix} \begin{bmatrix} \frac{dE_1}{dt} \\ \frac{dE_2}{dt} \end{bmatrix} = \begin{bmatrix} -\sigma_1 & \sigma_2 \\ \frac{-\sigma_3 d_1}{d_3} & -(\sigma_3 \frac{d_2}{d_3} + \sigma_2) \end{bmatrix} \begin{bmatrix} E_1 \\ E_2 \end{bmatrix} + \begin{bmatrix} 0 \\ \frac{\sigma_3}{d_3} \end{bmatrix} V(t) + \begin{bmatrix} 0 \\ \frac{\varepsilon_3}{d_3} \end{bmatrix} \frac{dV(t)}{dt} \qquad \textbf{(2-7)}$$

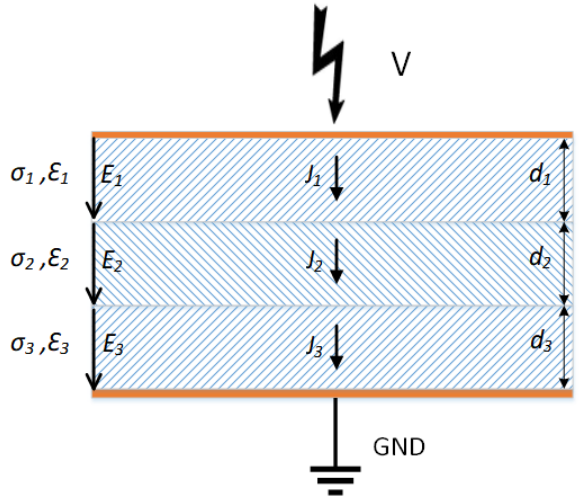

Figure 2-9. An insulation system combined of materials having three different electrical properties

The solution of this system yields time dependencies of the electric field intensity in the insulation system under applied DC voltage.

As an example, Moser and Dahinden [24] present typical values for permittivity and conductivity of the oil and the oil saturated transformer board and how the applied voltage waveform modifies the voltage distribution between two metal electrodes of defined configuration (Table 2-1).

Table 2-1. Example of 100kV AC versus DC voltage drop over a combined oil paper insulation system

DC at the instant of switching (AC) 100kV	DC steady state 100 kV
upper and lower layers 9 mm transformer oil	Middle layer 4 mm transformer board barrier
Relative permittivity $\boldsymbol{\varepsilon_r}$ Mineral oil 2.2, Transformer board 4.4	DC conductivity $\boldsymbol{\sigma}$ (S/m) Mineral oil 10^{-13}, Transformer board 10^{-15}
$E_i = \frac{V}{\varepsilon_i \left[\frac{d_{oil}}{\varepsilon_{oil}} + \frac{d_{board}}{\varepsilon_{board}} + \frac{d_{oil}}{\varepsilon_{oil}} \right]} \quad i = 1, 2, 3$	$E_i = \frac{V}{\sigma_i \left[\frac{d_{oil}}{\sigma_{oil}} + \frac{d_{board}}{\sigma_{board}} + \frac{d_{oil}}{\sigma_{oil}} \right]} \quad i = 1, 2, 3$
Voltage over 3 layers of insulation (kV) 45|10|45	Voltage over 3 layers of insulation (kV) 2|96|2
Electric field over 3 layers of insulation (kV/mm) 5|2.5|5	Electric field over 3 layers of insulation (kV/mm) 0.2|24|0.2

Undoubtedly it is thus interesting to consider how much the electric fields can deviate when the applied AC voltage is changed to a DC form. The electric field distribution at the instant of switching will be based on a capacitive division and finally based on a resistive division. During the time, before reaching the steady state condition which takes nearly 2 hours for this example, the voltage distribution will be according to Figure 2-10a. The electric field inside oil layers decreases from the initial value of 5 kV/mm to the final value of 0.2 kV/mm. At the same time the electric field inside the board increases from the initial value of 2.5 kV/mm to the final dramatic value of 24 kV/mm. It is obvious that a transformer designed to withstand 100kV AC only will never withstand if the same DC voltage is applied to it.

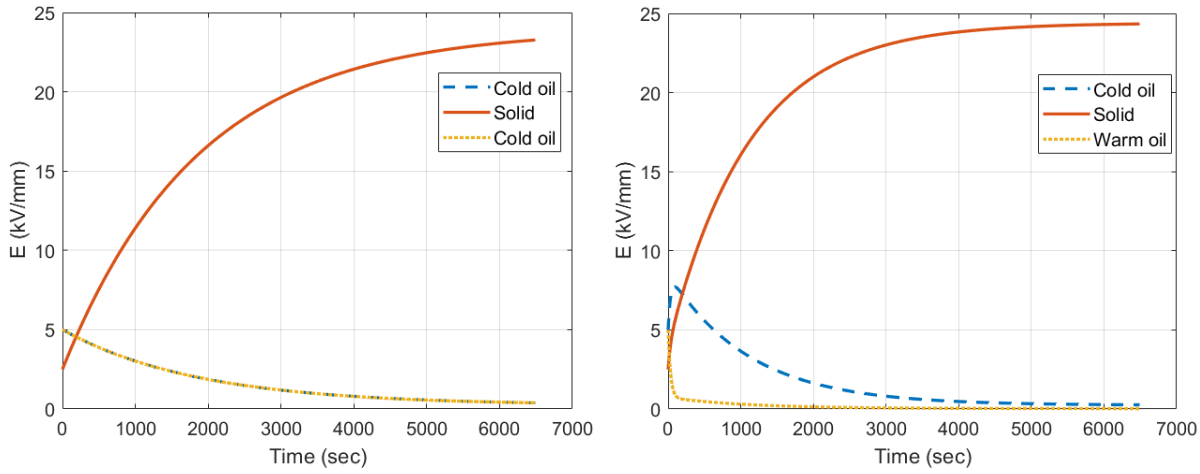

Figure 2-10. Electric field during transient state inside two similar oil layers and one transformer board layer: Two similar oil and a solid insulation layer electric field distribution under 100 kV DC (a), and a cold oil, a solid and a warm oil insulation layer electric field distribution under 100 kV DC (b)

The situation becomes even more complicated if for example, the conductivity of one of the oil layers has a slight difference from the conductivity of the other layer. Figure 2-10b presents an example, when this difference is in the order of 10, which is not unusual and can be a result of different temperature, humidity, even for an oil of the same type, but with a different production process [77]. Such a condition can happen when during a sudden load change the temperature of the oil near the winding becomes higher than the temperature of the oil in the successive oil ducts (DC conductivity of 10^{-12} S/m instead of 10^{-13} for example) or when the paper layers having more distance from the winding are colder, have a lower conductivity and experience more electrical field stress. The electric stress inside the oil layer goes higher than the value which is supposed to be highest at the moment of applying the voltage (5 kV/mm based on a capacitive division) and reaches a top value of 7.8 kV/mm.

2.2.9 Creepage under HVDC stress

Creepage stress under the HVDC regime should be prevented by a proper overlapping of insulation layers. The barrier arrangements will affect the distribution of the equipotential lines on the neighbouring interfaces. A uniform distribution of tangential electric field is favourable. However, in some cases a non-uniform distribution can increase the DC creepage strength. Thus Figure 2-11 demonstrates a space between two horizontal parallel electrodes. The upper electrode is charged with a positive HVDC, and the lower electrode is connected to ground.

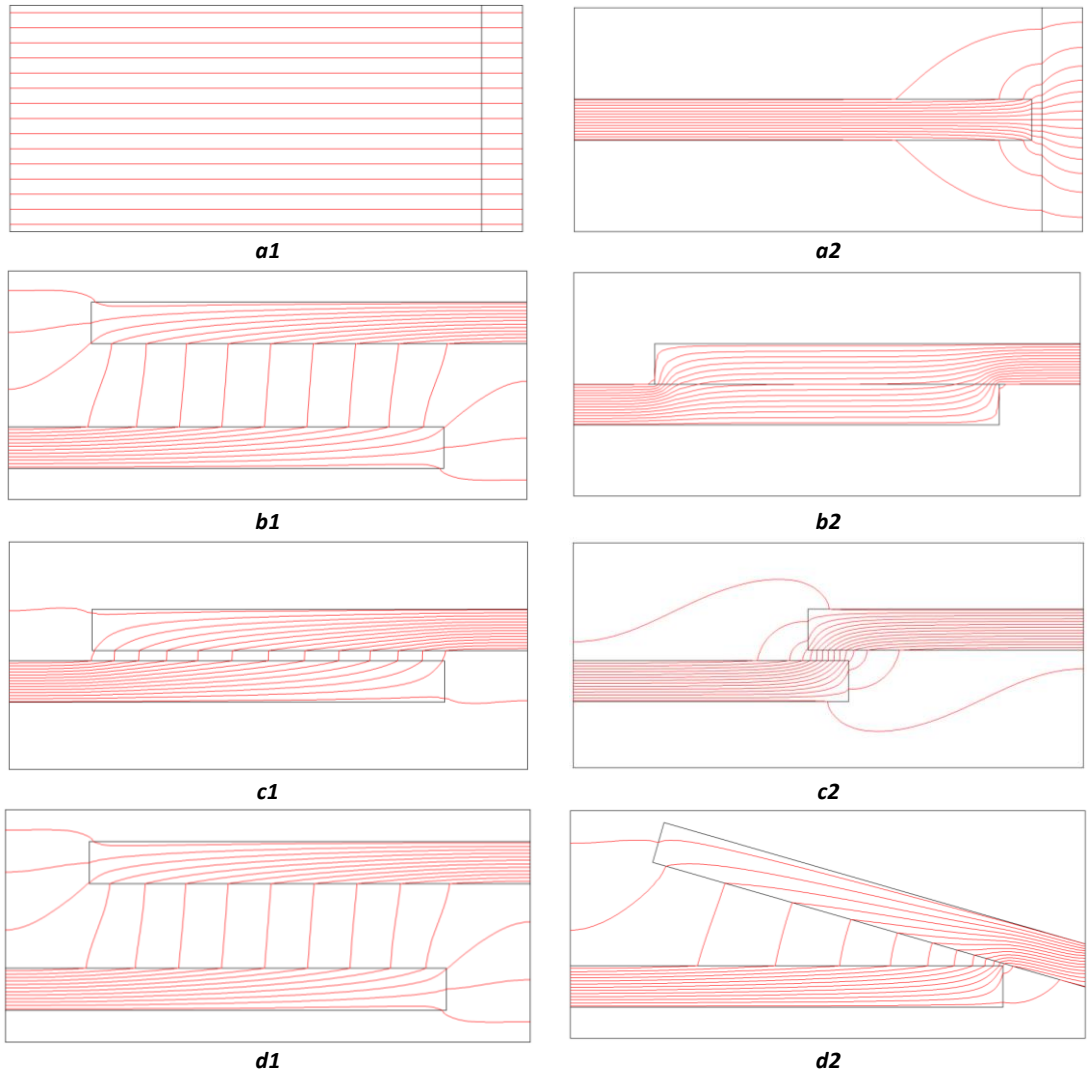

Figure 2-11. Effect of physical positioning of pressboards on creepage stresses on the interfaces: Equipotential lines are shown, the two horizontal parallel electrodes are supplied with DC voltage, the space between electrodes are filled with transformer oil

Figure a1 demonstrates a vertical barrier with uniform tangential stress. In Figure a2, positioning of a horizontal barrier causes a non-uniform creepage field distribution on the interface of the vertical barrier. Due to higher creepage stress in the middle of the barrier, at a first glance this seems unfavourable. However, the results of experimental creepage discharge tests unveil the positive effect of reduction of the vertical stress at the positions where the barrier meets the electrodes. The test results show a higher creepage withstand for Figure a2 setup compared with the test result for a1 [20]. A comparison of Figures b1 and b2 shows how an overlap (which is very normal to be used for an AC insulation design) causes a highly non-uniform voltage distribution on the barriers' interface which can lead to a creepage discharge.

Figures c1 and c2 demonstrate how a reduction in the overlapping area can lead to a very high creepage stress in the boards' surface and spreads even onto the vertical surfaces. At Figures d1 and d2, the angle between the boards causes a non-uniform voltage distribution which in turn can exceed the maximum permissible DC creepage strength of the OIP-oil interface.

The creepage distances could be treated by averaging as done in case of AC. However, because of an unknown charge carrier related process it is recommended to hold a high safety factor for instance 2. Averaging length in case of creepage strength under AC voltage will be from a point on the surface of

the solid dielectric having the electrical field higher than a threshold value of 0.1 kV/mm [22] to the point the strength drops down to a value lower than the threshold value. (Note: In some point the tangential field changes the polarity from positive to negative.)

Experimental creepage breakdown test results which are presented by Ebisawa [20] can be used as reference to extract acceptance criterion for allowable DC creepage stress. The reference gives DC creepage breakdown voltages and strength of three different test setups. As a rule of thumb, a low breakdown probability requires much lower stress levels, at least having a factor of two. For a simple model (a surface between two electrodes), the DC creepage strength values are half the AC breakdown value of an oil gap of the same length. The stresses are strongly dependent on oil and OIP properties and on the field distributions caused accordingly. The breakdown results might be dependent on the individual material properties during the tests. It is also shown that where the bare electrodes are involved the breakdown strength is half of the one where the creepage is on a surface with no direct contact to bare electrodes.

2.2.10 DC insulation design and non-linear conductivity

The topic for this section is the establishing of the applicability of the simplified engineering method for evaluations of electrical stresses in hybrid insulation systems based on a non-linear MW model.

Four main methods to analyse the effect of conductivity of the insulation material for the purpose of DC insulation design are presented in Figure 2-12.

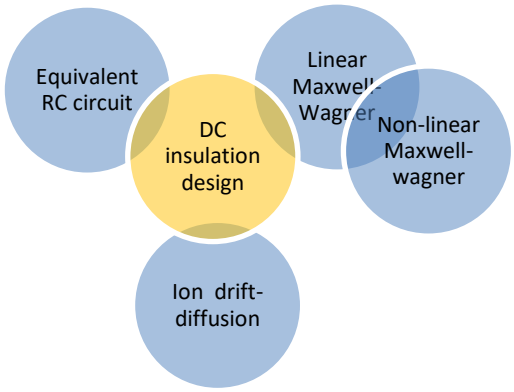

Figure 2-12. Different modelling methods for the study of insulation system under DC voltage stress

2.2.10.1 *Linear Maxwell-Wagner method*

In the simplest case, the Maxwell-Wagner (MW) model describes the current flow in a simple structure formed by two dielectrics with finite electric conductivities when a DC voltage is applied. It is simple and can predict the dynamics of charge transport as well as interfacial charge accumulation which affect the resulting field distribution in the insulation system. The equations describing the process and included in the MW model are

$$\mathbf{E} = -\nabla U \tag{2-8}$$

$$\mathbf{J} = \sigma \mathbf{E} \quad \text{Ohm's law} \tag{2-9}$$

$$\nabla \cdot (\varepsilon \mathbf{E}) = \rho \quad \text{Gauss's law} \tag{2-10}$$

$$\nabla \cdot \mathbf{J} = -\partial \rho / \partial t \quad \text{Continuity equation} \tag{2-11}$$

$$d\rho_s / dt = J \quad \text{Surface charge accumulation} \tag{2-12}$$

where U is the applied potential distribution; **E** and **J** are the vectors of the electric field and current density, respectively; σ is the electrical conductivity; ε is the dielectric permittivity; and ρ is the space charge density, ρ_s is the interfacial charge density and J is the current density.

According to the Linear MW (LMW) model, after applying a step DC voltage to the oil/paper dielectrics, the initial electric field distribution is based on material dielectric constants ratios (2.2 for oil and 4.4 for paper for example), and therefore the electric field intensity in the oil has a value nearly twice its value inside the paper. But at the final steady state, which may last up to several hours, it is the conductivity of materials that determines stress; a material with lower conductivity will take larger field intensity, and vice versa [78]. Since the ratio of the oil to paper conductivity may vary from 10 to 1000 or higher [28, 79], the paper will be more stressed than the oil at steady state. Therefore, the conductivity plays a crucial rule in an insulation system which is stressed by a HVDC voltage.

2.2.10.2 *RC network modelling based on equivalent electrical circuit elements*

One can simulate an insulation system using equivalent electrical circuit elements. Liebschner [80] has used this method to describe the temperature and voltage dependent behaviour of different combinations of oil-paper insulation systems. A simple example is a two-layer oil-paper system where a step voltage is applied between two bare electrodes (Figure 2-13).

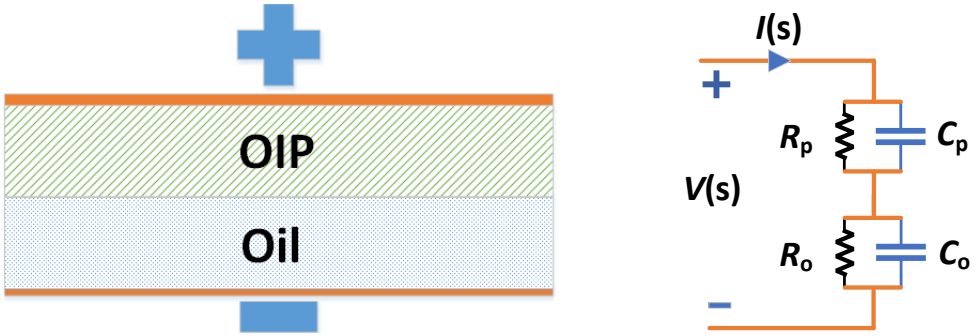

Figure 2-13. The equivalent circuit diagram of a two-layer insulation system

In this figure, R_p and R_o are the equivalent resistances of OIP, and oil and C_p and C_o are the equivalent capacitances of OIP and oil respectively. In a normal case σ_p is much lower than σ_o, where σ is the conductivity of the insulation layer. The following well-known equations relates the physical properties of the insulation layers to the elements of the equivalent circuit.

$$C = \varepsilon_0 \varepsilon_r \frac{A}{d} \tag{2-13}$$

$$R = \frac{1}{\sigma}\frac{d}{A} \tag{2-14}$$

Assuming a zero state for the circuit (zero set initial condition) and using a system of first order differential equations, the voltage and currents of the elements can be calculated having

$$V_p = \frac{C_o}{C_p + C_o} V_s e^{-t/\tau} + \frac{R_p}{R_p + R_o} V_s (1 - e^{-t/\tau}) \tag{2-15}$$

where

$$\tau = \frac{R_p R_o}{R_p + R_o}(C_p + C_o) \tag{2-16}$$

This method assumes having a constant (not variable with time or the applied voltage for example) conductivity values for the oil and OIP which is not true. However, the method is a simple tool for preliminary insulation design activities.

2.2.10.3 *Charged particles generation, drift and diffusion method*

In 1980, ASEA researchers applied an ion drift-diffusion model for simulations of the conduction process in transformer oil. The current transport equations, the continuity equations and the Poisson equation are adopted in this model. This model can predict the density of the ions of different polarities as a function of time and their position. ABB later has used the Kerr electro-optical measuring technique to verify the model. It was shown by experiments that the oil has a non-linear behaviour, especially at lower electric fields [14].

In [81] it is stated that a higher electric field intensity near the bare electrodes cannot be evaluated by the conventional MW method, in which the electric fields are estimated using the materials conductivities. Therefore, a charge carrier-based model using the Poisson-Nernst-Plank (PNP) equations is used. This model can predict the charge accumulation in front of the electrodes as well as the solid dielectric barriers. This model considers the charges injection from electrodes, oil intrinsic charge, charges movement inside the oil due to Coulomb forces and the diffusion process, recombination of charges and also their absorption into electrodes. Various combinations of oil/paper dielectrics are investigated to find electric field distribution using this method. The findings are different from the MW model results which is based on the materials conductivities ratio. However, the PNP model parameters like ion mobility and its dependence on oil contamination, the charge injection rate and its dependence to electric field intensity and polarity are not fully known and determined yet [82, 83]. It can be deduced from the results reported in [81] that at the final state after applying HVDC, the electric field intensity inside the paper obtained from the PNP model is somewhat lower than what is obtained from the MW model. This fact suggests that the stress in the paper will be overestimated in the MW model. Therefore, we will use the MW model to determine the geometry of the insulation and the safety factor for the paper will be higher in this case. At low stress levels (≈ 2 kV/mm) MW model can be used but at higher stress levels (≈ 20 kV/mm) PNP model shall be implemented.

2.2.10.4 *Non-Linear Maxwell-Wagner Method*

After explaining the physical phenomena of the non-linear dependence of the oil conductivity to change in applied voltage, temperature, etc. it is explained why the Maxwell Wagner method is still a reliable tool for insulation design on an HVDC transformer. However, in a Linear Maxwell-Wagner (LMW) model, the electrical parameters of the oil and paper are supposed to be constants. Although this assumption is nearly true for permittivity, it is known that conductivity is highly dependent on different parameters like temperature, electric field, water content, time, Oil Impregnated Pressboard (OIP) density, electrode materials and their dielectric coating and cover [28, 84, 85].

To consider the nonlinear dependence of the oil and OIP to the applied voltage and temperature, in this work a Non-Linear Maxwell-Wagner (NLMW) method is presented and employed. This is crucial to be able to design a compact transformer, and thus accurate calculations of the dynamic behaviour of the electric fields will be done. The NLMW model is adopted for MFT insulation design in this report, which accounts for (at least) field and temperature dependencies of the electric conductivity of the constituting materials and its results is compared with LMW.

2.2.10.5 *Effect of electrodes coatings*

According to Weidmann design curves [76], for an AC design, the bare metal electrodes should be coated with solid insulation to increase the total withstand strength and to prevent partial discharge originating from sharp corners. In contrary to AC voltage applications, for DC voltage there should be

a pass for to the leakage current. This means that an insulation cover should not totally cover all the electrodes [77].

Figure 2-14 demonstrates how covering of a high voltage electrode – which is common for a safe AC insulation design – can cause a very high stress on the covered OIP and lead to an unwanted discharge inside it. In Figure 2-14c, the charge carries have a pass to flow and a resistive voltage division based on the conductivities of the materials involved is in place. In Figure 2-14b, the current pass is barred. Therefore, the voltage-drop over the oil gap is close to zero and all the voltage difference between the electrodes stresses the covering barrier. This can lead to a stress much higher than the withstand stress of covering barrier.

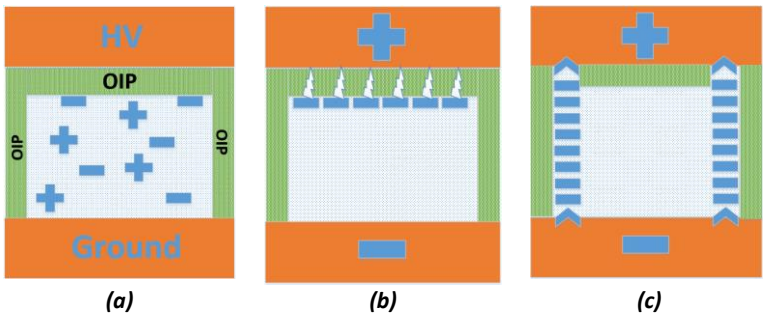

Figure 2-14. The effect of covering electrodes on the discharge in the insulation layer: an oil/OIP system between two electrodes not supplied by voltage (a), the positive electrode totally covered by OIP (b), and the positive electrode partly covered by OIP (c)

Investigations made by Okubo et al. [19] and Gabler et al. [86] show that there is more charge injections from the cathode compared to the anode. According to Okubo, the electric field near the cathode drops down much faster compared to the field near the anode. According to Gabler the setup with a covered cathode has a higher DC breakdown voltage. The reason might be that the injected electrons from the cathode move inside the oil and accumulate on the surface of the OIP (negative charge affinity). This leads to a lower stress at the cathode side and a higher stress at the anode side. As a direct result, the LV winding of the transformer as well as the grounded parts should be covered for a higher isolation purpose.

2.2.11 Conductivity measurements in time domain

If a step DC voltage is applied to a liquid or solid sample (Figure 2-15a), the current directly after application of voltage is mainly a superimposed polarisation and conduction current for solids and conductive for liquids. After a relatively long time the polarisation process ends, and a current based on the conductivity of insulation material will flow (Figure 2-15b). After short circuiting the electrodes (removing the voltage source), only a depolarisation process will take place (Figure 2-15a), resulting in a discharge current, slowly declining towards 0.

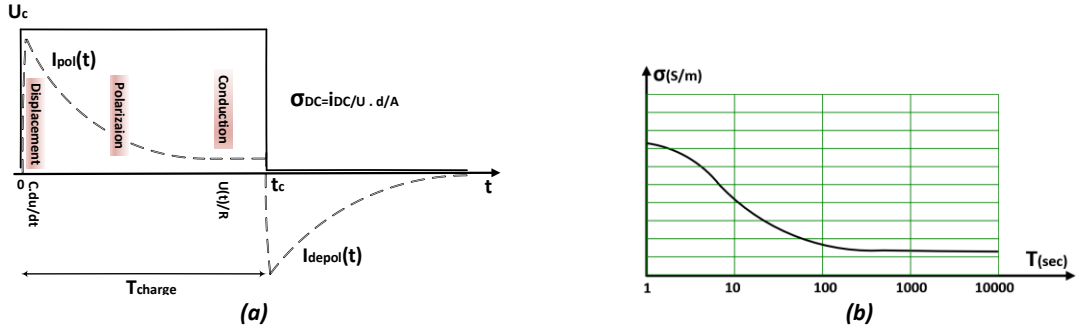

Figure 2-15. Polarisation, Depolarisation Current (PDC) measurement concept: the applied step DC voltage, short circuiting the object, and the resulting polarisation, conduction, and depolarisation currents (a), and the apparent conductivity versus time of application of the step voltage (b)

For a new HVDC transformer application, the oil and OIP conductivities measured at different conditions (depending on transformer operation condition after energisation) should be used for the insulation design of a transformer (Table 2-2). The transformer design should be repeatedly checked at different physical positions in the tank, applied voltage, time of application of voltage and loading conditions. In addition, for a transformer in service, the humidity, particle contamination, aging or the thermodynamic oil flow, have considerable effects on the conductivity figures and consequently on the predicted stresses on an HVDC transformer. However, these effects are not considered in the scope of this study.

Table 2-2. Different conditions during oil conductivity measurements

Conductivity	At the instant of energization	After energization and before loading	At steady state after long time of loading
Time	Short time	Relatively long	Long
Temperature	environment temp.	Low	Medium or High

2.2.12 Conductivity measurement system set-up

Many standards have presented measurement methods for surface or volume conductivity of liquid or solid insulation materials (IEC 61620 1998, IEC 60247 2004, ASTM D1169 2011, IEC 62631-3-1&2 2016 or ASTM D257 2014). A comparative table is prepared, and the strong and weak points of the measuring methods are summarized in a Cigré publication [28]. The result of this comprehensive study shows that none of these standard methods guarantee both reproducible and comparable results with the conductivities under HVDC test or service conditions. However, the measurement method proposed in this report refers to the guidelines from the same standards to be implemented at different measurement stages. The research question here is how to obtain useful and reliable conductivity values for the biodegradable insulation materials which are proposed to be used for design and manufacturing of an offshore high voltage DC module. To perform a reliable conductivity measurement procedure the following should be considered:

- Test object cell and temperature chamber
- Current measuring and data acquisition system and its protection
- High voltage application system and safety
- Mitigation of noises
- Preparation and testing of oil samples
- Preparation and testing of solid insulation samples

2.2.13 High voltage conductivity measurement test cell

The test cell for performing the measurements is essentially a guarded three-electrode system and the same as introduced in IEC 93, 1980 & IEC 62631-3-1, 2016 [87] with some improvements suggested in Cigré report 646 [28] to make it suitable for measurements at higher stress voltages (Figure 2-16).

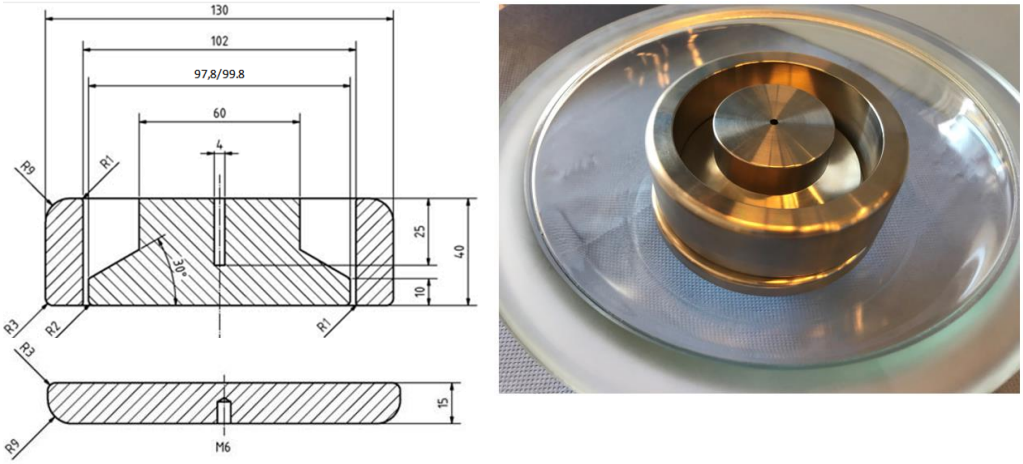

Figure 2-16. The test cell for performing the conductivity measurements

To calculate the volume conductivity of the insulation, the effective area of the guarded measuring electrode is calculated from the following equations considering precautions explained by Lisowski [88] and given by ASTM D257-14 [89]

$$A_{\text{eff}} = \pi \frac{(d_1 + Bg)^2}{4} \tag{2-17}$$

where d_1 is the diameter of the measuring electrode (99.8 mm), g is the gap width between the measuring and guard electrodes (1.1 mm), and B is the factor for accounting for the diameter enhancement by spreading the electrode margin

$$B = 1 - \frac{4}{\pi}\frac{h}{g}\ln\left(\cosh\left(\frac{\pi}{4}\frac{g}{h}\right)\right) \tag{2-18}$$

2.2.14 OIP conductivity values calculation using charge difference method

If a DC step voltage is applied to a liquid insulation (e.g., mineral transformer oil), a decreasing current will be observed in most of the cases. In contrast to solid insulation, this current is dominated by the conduction current component, and the polarization current component is negligible from the very beginning (after a few seconds). Thus, the conductivity can be calculated from the ratio of the polarization current and the voltage. Yet, the result is time-varying and strongly dependent on many other parameters (e.g., electrical stress and temperature). In the case of using oil impregnated pressboard, the conduction current is low, and the polarization current is relatively high. Therefore, the charge difference method [90] can be used, which is less sensitive to noise signals and gives a good estimate of the conductivity value in short measuring times. In this method

$$Q_{\text{pol}}(t) = \int I_{\text{pol}}(t)dt \tag{2-19}$$

$$Q_{\text{depol}}(t) = \int \left| I_{\text{depol}}(t) \right| dt \tag{2-20}$$

$$Q_{\text{dif}}(t) = Q_{\text{pol}}(t) - Q_{\text{depol}}(t) \tag{2-21}$$

$$Q_{\text{dif}}(t) \approx at + b \tag{2-22}$$

$$\sigma = \frac{a}{E\, A_{\text{eff}}} \tag{2-23}$$

where, I_{pol} and I_{depol} are the polarization and depolarization currents respectively, Q_{pol} and Q_{depol} are the polarization and depolarization cumulative charges, Q_{dif} is the charge difference, a is the slope of the

Q_{dif} *curve*, A_{eff} is the effective area of the measuring electrode and E is the applied field intensity.

2.2.15 Using the Arrhenius law

At lower temperatures, the stabilization of the current can take long time. In addition, the signal to noise ratio can be unacceptably low. To achieve the conductivity values in these conditions, the measurements can first be done at 50 °C and 90 °C and later the conductivity in 30 °C can be calculated according to the Arrhenius law [52]

$$\sigma_{DC}(T) = \sigma_{DC,ref} e^{-\frac{W_a}{kT}} \quad \textbf{(2-24)}$$

where, $\sigma_{DC,ref}$ is the reference value of conductivity at two different temperatures, T (K) is the target temperature, W_a (J) is the activation energy, and k (J/K) is the Boltzmann's constant (see Figure 3-16 as an example of application of this method).

2.3 Magnetic design input parameters

The overall dimensions of the insulation system are limited by the geometry of the magnetic core. In the magnetic design, the parameters and characteristics like the duty cycle, the relative rise time, and the frequency of the square wave as well as the amplitude of the applied voltage and the number of turns should be identified to find the core cross section. The duty cycle of the applied rectangular wave, D is assumed to be 0.5, which is defined as

$$D = \frac{t_{on}}{T} \quad \textbf{(2-25)}$$

where t_{on} is the conduction (on) time of the switch and T is the time period of the wave.

The relative rise time of the wave as is assumed to be 0 for the design, which is defined as

$$R = \frac{t_r}{T} \quad \textbf{(2-26)}$$

where t_r is the rise time of the wave.

The core cross section calculated for the square wave shape can be calculated as

$$V = N\frac{d\varphi}{dt} \quad \textbf{(2-27)}$$

$$\varphi = \frac{1}{N}\int_0^T v dt \quad \textbf{(2-28)}$$

and

$$\varphi_m = \frac{V_{DC} D T/2}{N} = \frac{V_{DC}}{4Nf} \quad \textbf{(2-29)}$$

and

$$A_c = \frac{\varphi_m}{B_m} = \frac{V_{DC}}{4Nf B_m} \quad \textbf{(2-30)}$$

where B_m is the maximum working flux density of the core (nearly 80% of the saturation flux density), K_c is the core filling factor (the ratio of effective to physical cross sections which is 1 for Ferrite), N is the number of turns for a winding and f is the switching frequency. A_c is the effective cross section of the transformer core and φ_m is the amount of flux in the core.

The core cross section for sinus wave shape can be calculated as

$$A_c = \frac{V_{rms}}{4.44 N f B_m} \quad \textbf{(2-31)}$$

2.4 Leakage inductance

The research question here is establishing analytical expressions, for highly time-efficient calculations of leakage inductance, and demonstrating how accurate such a procedure can be for a shell-type transformer with circular windings and a segmented core structure.

2.4.1 The effect of the leakage inductance on the transferable effective power of a DAB

As the inductance data is needed for the optimum design of a DAB converter, the leakage inductance of the MFT shall be determined in the design stage. A low leakage inductance negatively affects the soft switching process and consequently the converter efficiency. On the other hand, a higher leakage inductance causes an excessive reactive power circulation within the converter [34].

To have a higher leakage inductance, the number of turns of a MFT, the distance between the windings, the mean turn length, the core window height, all shall be increased, or the core window width shall be decreased. The inductance can be lowered by the reverse operations.

The voltage wave forms applied to the MFT in a DAB converter are not sinusoidal as in a conventional low frequency transformer (Figure 2-1b). Therefore, in case of this type of transformer, the leakage inductance and its related phase shift are under consideration and the transformer leakage inductance, L_σ corresponds to the value calculated according to

$$L_\sigma = V_{DC1} V_{DC2} \phi_{min} (\pi - \phi_{min}) / (2 P_{out} \pi^2 f_s n) \quad \textbf{(2-32)}$$

where, P_{out} is the output power of the DAB converter, V_{DC1} is the DC voltage of the LV side of the DAB converter, V_{DC2} is the DC voltage of the HV side of the DAB converter, n is the turns ratio of the transformer, f_s is the switching frequency and φ_{min} is the phase shift between the bridges which should be higher than a predetermined value to achieve Zero Voltage Switching (ZVS) [34].

2.4.2 The effect of frequency to the leakage inductance

The behaviour of the leakage inductance with respect to frequency in high frequency transformers (HFT) is studied up to 2 MHz in [34, 91-93], using Dowell method [94] or its improved form [95]. For high-power MFTs with rated frequencies less than 20 kHz, if litz wire is used, the change of leakage inductance due to the frequency variation is almost negligible [44].

2.4.3 Calculation of leakage inductance of rectangular shell-type E-core MFTs

In a previous work of the authors [44], an analytical method for calculating the leakage inductance of MFTs with rectangular windings was presented. The inductances per unit length, denoted by L_{in} and L_{out}, are calculated using a 2-D field analysis inside and outside the core window. A Mean Length of Turns (MLT) is employed which is equal to the perimeter of a hypothetical rectangle whose sides are located in the middle of the total width of the windings and the main gap on each side. Based on the part of the MLT which is surrounded by the core, the MLT is divided in two partial lengths, MLT_{in} and MLT_{out}. The total leakage inductance is then obtained by the summation of $MLT_{in}L_{in}+MLT_{out}L_{out}$. Good results were observed for this method compared to the measurement results. However, further research done by the authors showed that the proposed method was not general enough and by changing the dimensions of the windings or the core, the accuracy of leakage inductance may decrease. The results of multiple 3-D FEM simulations performed in the current work showed that despite the considerations made in calculating the leakage inductance per unit length, the determination of the MLT in the usual way is not accurate enough, resulting in errors in the total leakage inductance.

In a further study [96], an accurate analytical method for calculating the leakage inductance of shell-type E-core transformers with rectangular windings is presented. In that work, first, an analytical method based on a two-dimensional field analysis is provided for calculation of the leakage inductance inside the core window. Then, by applying the double Fourier series to the governing equation and considering the boundary conditions defined on the core walls, the vector potential relation for each coil is obtained in the form of infinite double series. Later, having the vector potential relation, the leakage inductance per unit length is obtained for any arbitrary arrangement of coils inside the core window. And finally, a new method for determination of the MLT based on the total energy stored in the axial leakage field is presented. In this method, the effect of the distribution of Ampere-turns in individual layers of the windings is considered in determining the MLT. Considering the boundary conditions exerted by the core walls, the MLT is divided into three partial lengths, and the total leakage inductance is derived from the combination of the leakage inductances calculated for three different core window arrangements.

The accuracy of the proposed method is confirmed by the 3-D finite element analysis. Moreover, the results of the proposed method are verified by measurements on two constructed MFTs with different core types and dimensions. A sensitivity analysis is also performed, and the results of the proposed method are compared with the results of the previous analytical methods as well as the results of the 3-D FEM for various case studies.

2.4.4 Calculation of leakage inductance of circular shell-type multi core-segment MFTs

The proposed method for the leakage inductance calculation is illustrated by a flowchart which is presented in Figure 2-17. The procedure includes the determination of the MLT according to the method presented in Section 2.4.4.1, the segmentation of the obtained MLT into three parts according to the method presented in Section 2.4.4.2 and calculation of the leakage inductance per unit length for each part based on the analytical approach presented in Section 2.4.4.3 and then obtaining the total leakage inductance by (2-101).

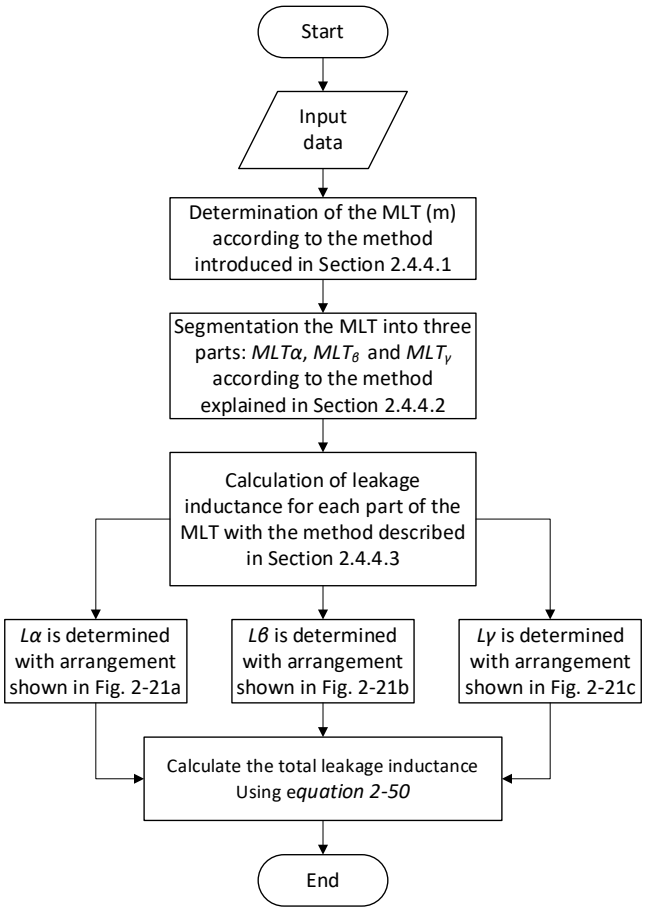

Figure 2-17. The flowchart of the proposed method used for calculation of the leakage inductance

2.4.4.1 *Determination of mean length of turns (MLT)*

The MLT is not essentially required for the leakage inductance calculation in cylindrical coordinates. However, in order to find the portion of the windings which is surrounded by the core segments, a method for the determination of the MLT in cylindrical coordinates is developed in this section. The method is similar to the one presented by the authors in [96] but it is adopted for circular windings. The method is based on the total energy stored in the axial leakage field.

According to Figure 2-18, the widths of the windings are different in general. It is assumed that the windings have the same height equal to h_w. In fact, h_w is the average height of the windings and is calculated as (h_{w1}+h_{w2})/2 where h_{w1} and h_{w2} are the heights of windings 1 and 2, respectively. The net Ampere-turns is zero and there is no leakage flux outside the windings. The magnetic flux density is calculated using Ampere's law, assuming an axial leakage field. The distribution of magnetic field strength, *H*, inside the windings and in the main gap is demonstrated in Figure 2-18. The magnetic field strength is constant inside the gaps while it changes linearly inside the windings

$$H_g = \frac{NI}{h_w} \tag{2-33}$$

$$H_1(x_1) = \frac{x_1}{T_1} H_g \tag{2-34}$$

$$H_2(x_2) = \left(1 - \frac{x_2}{T_2}\right) H_g \tag{2-35}$$

where *NI* is the absolute value of the Ampere-turns of each winding. T_1 and T_2 are the widths of windings 1 and 2 respectively. The coordinate parameters x_1 and x_2 are indicated in Figure 2-18.

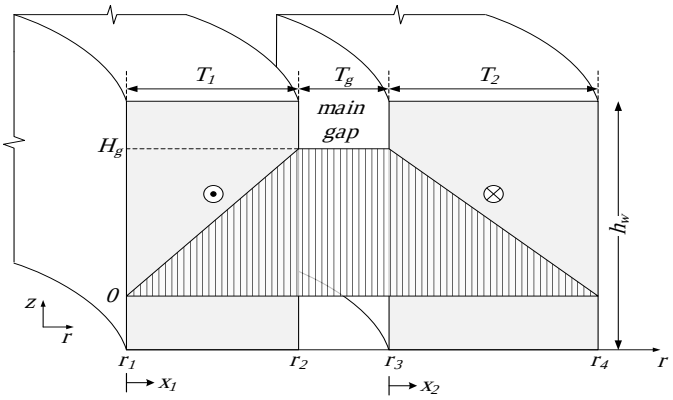

Figure 2-18. The distribution of leakage field inside windings

The field strength is constant in the main gap and thus the stored energy in the main gap is given by

$$W_{\mathrm{g}} = \int_{r_2}^{r_3} \frac{1}{2}\mu_0 H_{\mathrm{g}}^2 h_{\mathrm{w}} 2\pi r dr = \frac{1}{2}\pi\mu_0 H_{\mathrm{g}}^2 h_{\mathrm{w}} \left(r_2 + r_3\right) T_{\mathrm{g}} \qquad \textbf{(2-36)}$$

where T_g is the size of the main gap and r_2 and r_3 are the outer and inner radii of windings 1 and 2, respectively. The inner radius of winding 1 is r_1 and the outer radius of the winding 2 is r_4.

The stored energy in each winding is obtained as the volumetric integral of the magnetic energy density in cylindrical coordinates.

$$W_{\mathrm{i}} = \int_0^{T_{\mathrm{i}}} \frac{1}{2}\mu_0 H_{\mathrm{i}}^2\left(x_{\mathrm{i}}\right) h_{\mathrm{w}} 2\pi\left(r_{\mathrm{i}} + x_{\mathrm{i}}\right) dx_{\mathrm{i}} \quad , i = 1, 2 \qquad \textbf{(2-37)}$$

According to (2-37), the magnetic energy stored in windings 1 and 2 is individually obtained as

$$W_1 = \frac{1}{2}\pi\mu_0 H_{\mathrm{g}}^2 h_{\mathrm{w}} \left(\frac{1}{3}\left(2r_1 + \frac{3}{2}T_1\right)T_1\right) \qquad \textbf{(2-38)}$$

$$W_2 = \frac{1}{2}\pi\mu_0 H_{\mathrm{g}}^2 h_{\mathrm{w}} \left(\frac{1}{3}\left(2r_2 + \frac{1}{2}T_2\right)T_2\right) \qquad \textbf{(2-39)}$$

Now consider Figure 2-19. Each winding is substituted with an equivalent gap with a constant field intensity equal to H_g and an equivalent infinitely thin winding with the same Ampere-turns as before. H_g is the value of the field intensity in the main gap. The width of each equivalent gap is determined in such a way that the stored energy in the equivalent gap is equal to the energy stored inside the corresponding winding.

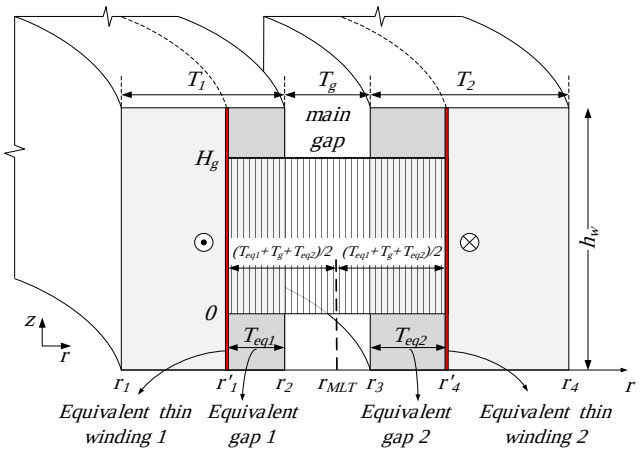

Figure 2-19. The windings are substituted with equivalent thin windings and equivalent gaps to create a gap with a uniform field intensity equal to the field intensity of the main gap and with an energy equal to the total energy of the leakage field

According to Figure 2-19, the energies stored in the equivalent gaps are given by

$$W_1 = \frac{1}{2}\pi\mu_0 H_g^2 h_w \left(r_2^2 - r_1'^2\right) \quad \textbf{(2-40)}$$

$$W_2 = \frac{1}{2}\pi\mu_0 H_g^2 h_w \left(r_4'^2 - r_3^2\right) \quad \textbf{(2-41)}$$

Equating (2-40) with (2-38) and (2-41) with (2-39), r_1' and r_4' are obtained as

$$r_1' = \sqrt{r_2^2 - \frac{1}{3}\left(2r_1 + \frac{3}{2}T_1\right)T_1} \quad \textbf{(2-42)}$$

$$r_4' = \sqrt{r_3^2 + \frac{1}{3}\left(2r_2 + \frac{1}{2}T_2\right)T_2} \quad \textbf{(2-43)}$$

Knowing r_1' and r_4', the radius of MLT, r_{MLT}, can be determined as

$$r_{MLT} = \frac{r_1' + r_4'}{2} \quad \textbf{(2-44)}$$

Once r_{MLT} is determined, the total stored energy i.e., the energy stored inside the windings and the main gap, can also be calculated as

$$W_T = \frac{1}{2}\mu_0 H_g^2 h_w \left(2\pi r_{MLT}\right)\left(T_{eq1} + T_g + T_{eq2}\right) \quad \textbf{(2-45)}$$

where T_{eq1} and T_{eq2} are the widths of the equivalent gaps of windings 1 and 2, respectively.

In most cases, r_{MLT} is close to the average radius $r_m = (r_1+r_4)/2$. However, as the difference in the widths of the windings increases, r_{MLT} deviates from r_m, resulting in a MLT different from the one conventionally used, which is a circular path in the middle of the total width of the windings and the main gap.

The method presented in this section can be developed for the cases where each winding needs to be modelled layer-by-layer. The method has been discussed in [96] for planar windings which can be extended for axisymmetric windings considering the approach provided in this section.

Using the total energy stored in the axial leakage field, W_T, it is possible to derive a relation for the leakage inductance similar to the relations presented in literature for conventional power transformers [36]. The leakage inductance considering the radial component of the leakage field using the Rogowski factor is given by

$$L_{leakage,classical} = k_r \frac{2W_T}{I^2} \quad \textbf{(2-46)}$$

where W_T is obtained from (2-45) and I is the current of the excited winding. The Rogowski factor, k_r, is obtained as [36]

$$k_r = 1 - \frac{1 - e^{-\frac{\pi h_w}{(T_1+T_g+T_2)}}}{\pi h_w / (T_1 + T_g + T_2)} \quad \textbf{(2-47)}$$

If the heights of windings 1 and 2, h_{w1} and h_{w2}, are different, then h_w can be calculated as the average height of the windings i.e., $(h_{w1}+h_{w2})/2$. It should be noted that the method described for determining h_w is dedicated only to the classical method developed in this section whereas in the method presented in Section 2.4.4.3 which is based on a field analysis, the height of each winding is accurately considered in the calculations.

The leakage inductance calculated according to (2-46) is referred to as the leakage inductance calculated by the classical method in this study.

2.4.4.2 *Segmentation of MLT*

Circular windings are preferred over the commonly used rectangular windings in shell-type MFTs with high isolation requirements for the HV winding. In addition to using circular windings, the core segments can also be distributed along the circumference of the winding region. The distribution of core segments is actually due to reasons such as overcoming the physical constraints, providing the permissible electrical clearances and the maximum use of the available space to create more symmetry in the geometry of the transformer. The leakage inductance of the transformer also increases with the distribution of the core segments. The reason is that the leakage flux is more affected by the core walls as the core segments are distributed, leading to a higher value of the leakage inductance. This necessitates the establishing of a new method, different from the one presented in the previous section, for calculating the leakage inductance of the shell-type transformers with n_c>2 which are referred to as the shell-type segmented-core transformers in this paper. n_c is the number of the core segments and is equal to 1 for the single core-segment transformer or equal to 2 for the double core-segment transformer.

A top view of a shell-type transformer with a regular polygonal core structure is shown in Figure 2-20. As can be seen, only some parts of the windings are surrounded by the core and thus the result of the leakage inductance calculation with the windings entirely situated inside the core window will exceed the real value. From another point of view, although each core segment geometrically surrounds a relatively small part of the windings, the entire winding region, including the parts which are not surrounded by the core, is magnetically affected by the core. This is essentially due to the high permeability of the core, which causes leakage flux to be absorbed by the core walls between the core segments. The vicinity of the core segments reinforces this effect. As a result, the leakage inductance will be underestimated if only those parts of the windings which are geometrically covered by the core segments are assumed to be inside the core window.

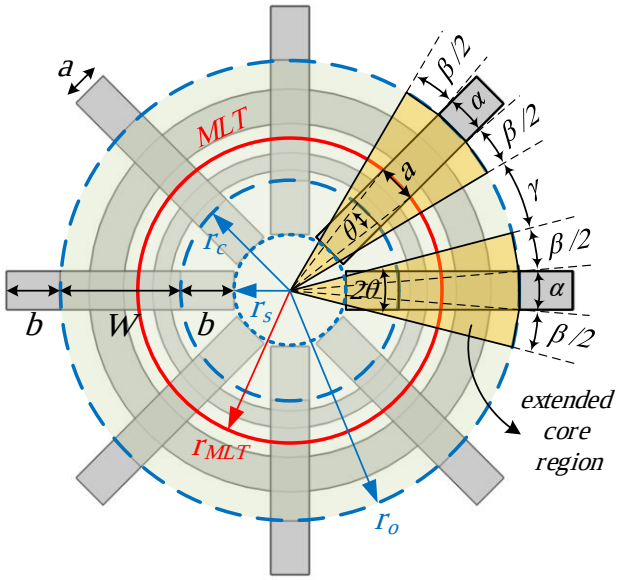

Figure 2-20. A top view of a shell-type Transformer with a regular polygonal core (segmented-core) structure

Therefore, an appropriate method is required for calculating the leakage inductance considering the core effect more accurately. A suitable solution was found by examining the core effect on the leakage flux through extensive investigations of multiple dedicated 3-D FEM simulations. An extended core region is considered around each core segment wherein the windings are strongly influenced by the core and thus it is assumed that the windings are completely surrounded by the top and bottom yokes

in this region (brown-coloured region in Figure 2-20). The equivalent angle of each extended core region is 2*Θ*, which is twice the angle of the core region used for the single and double core-segment transformers. *Θ* is illustrated in Figure 2-20 and is calculated by

$$\theta = 2arcsin\left(\frac{a/2}{r_{MLT}}\right) \quad \textbf{(2-48)}$$

where *a* is the thickness of the core segment and *Θ* is the angle of the core region wherein the windings are surrounded by the core yokes at top and bottom.

The angle of *Θ* can be considered as the summation of the two angles *α* and *β*. For *α*, the windings are adjacent to the core's return leg in the radial direction. The angle *α* is calculated as

$$\alpha = 2arcsin\left(\frac{a/2}{r_o}\right) \quad \textbf{(2-49)}$$

where r_o is the radius of the inner wall of the core's return leg. In the region equal to the angle of *γ* (outside the core region) the windings are outside the core window and are not surrounded by the core yokes.

According to the regions specified in Figure 2-20, the leakage inductance is calculated for three different core window arrangements, as shown in Figure 2-21. The total leakage inductance is calculated as a combination of the leakage inductance values obtained for these arrangements. The arrangement shown in Figure 2-21a is used to calculate the leakage inductance for those parts of the windings which are surrounded by the core and thus situated completely inside the core window (region with the angle of $\alpha \approx a/r_o$). To calculate the leakage inductance for those parts of the windings which are not adjacent to the core's return leg (region with the angle of $\beta = \Theta - \alpha$), the outer wall of the core window is displaced in the radial direction as shown in Figure 2-21b. The amount of displacement is the same as the width of the core window that is enough to neutralize the effect of the core's outer wall. In the region situated between two adjacent extended core regions (equal to an angle of $\gamma = 2\pi/n_c - \Theta$), the effect of the core is lower and thus, the core walls are assumed to be farther than the distance for the extended core region. The suitable displacement of the core walls for this region is demonstrated in Figure 2-21c.

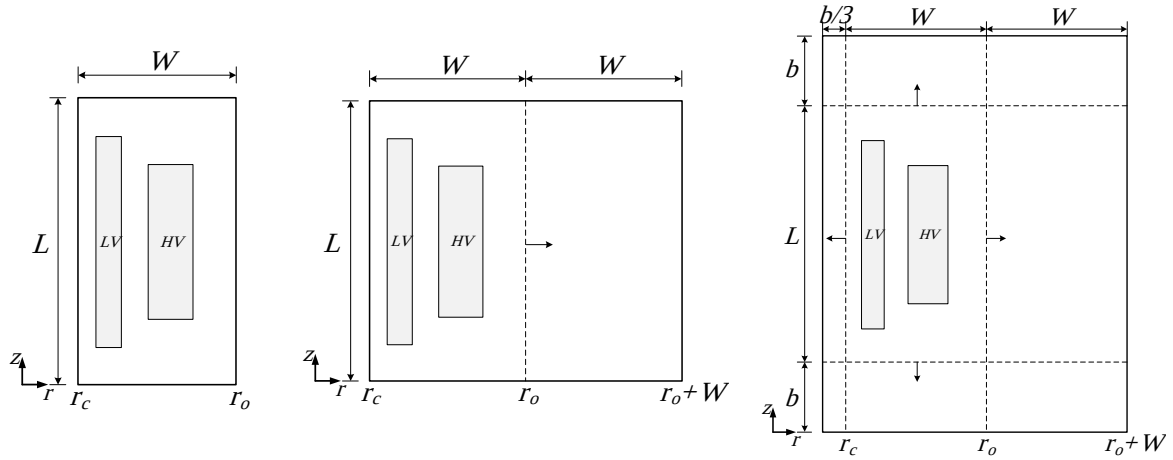

(a) α, L_α ***(b) β, L_β*** ***(c) γ, L_γ***

Figure 2-21. Core window arrangements and the relevant angles (in a sector equal to $2\pi/n_c$) and the corresponding leakage inductances for segmented-core transformers: the actual core window (a), the core window, unbounded from outside (b), and the core window, unbounded from outside, with displaced top and bottom core walls used for the region situated between two extended core regions (c)

Once the leakage inductances corresponding to the core window arrangements shown in Figure 2-21 are obtained, the total leakage inductance is obtained by

$$L_{leakage}^{total} = \frac{n_c}{2\pi}\left(\alpha L_{\alpha} + \beta L_{\beta} + \gamma L_{\gamma}\right) \quad \textbf{(2-50)}$$

where L_{α}, L_{β} and L_{γ} are calculated separately by

$$L_{\text{leakage}} = \frac{2W_{\text{m}}}{I^2} \quad \textbf{(2-51)}$$

with the relevant dimensions for the core window. I denotes the current in the side from which the leakage inductance is calculated and W_{m} is the total magnetic energy stored inside the core window obtained by

$$W_{\text{m}} = \frac{1}{2}\sum_{\text{i=1}}^{N}\sum_{\text{j=1}}^{N} L_{\text{ij}} I_{\text{i}} I_{\text{j}} \quad \textbf{(2-52)}$$

where N = 2 is the number of coils (with zero net Ampere-turns) with different dimensions and arbitrary arrangement inside the core window and L_{ij} is the mutual inductance of coils i and j.

The proposed method can still be used to calculate the leakage inductance of a shell-type transformer with an irregular polygonal core structure. For this purpose, first the transformer with irregular core structure is converted to a transformer with regular core structure with the same number of core segments and then the method is employed to calculate the total leakage inductance. The results of the FEM simulations confirming the validity of the procedure and sensitivity analysis results are presented in [97].

2.4.4.3 *Calculation of the leakage inductance based on the expressions for self and mutual inductances*

In this section, a method of calculation of the leakage inductance in cylindrical coordinates considering the core walls as the flux-normal boundary conditions, is presented. The method is based on the expressions for self and mutual inductances which is in turn a function of the vector potential in the region between a coil and the core, and the current density of the other coil.

The axisymmetric geometry is used for field analysis in cylindrical coordinates (Figure 2-22a). For two coils (with zero net Ampere-turns) with different dimensions and arbitrary arrangement inside the core window (Figure 2-22b), the leakage inductance is calculated using (*2-51*).

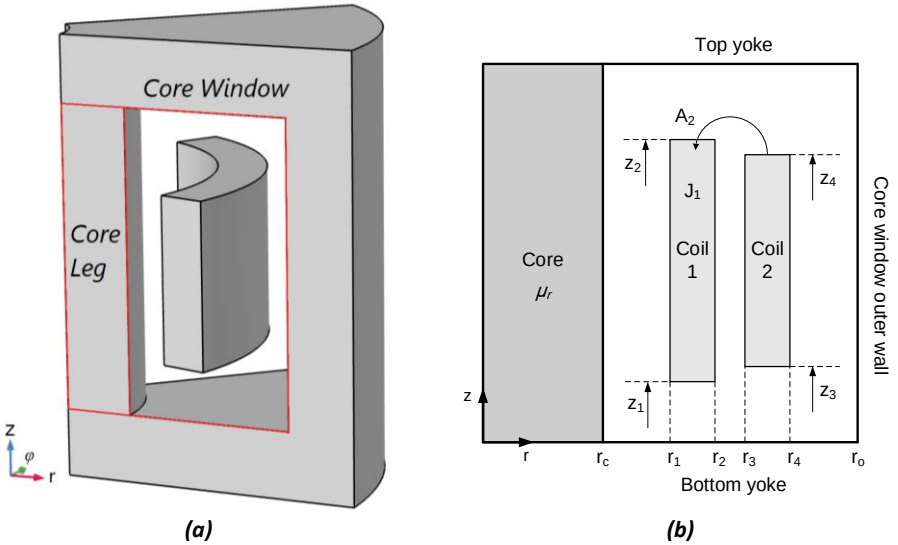

(a) *(b)*

Figure 2-22. The axisymmetric geometry used for field analysis (a), and the arrangement of two radially displaced coils inside the core window (b)

Using the solution of A inside the core window, the self and mutual inductances of a coil system can be obtained. The mutual inductance between coil 1 and coil 2 with currents I_1 and I_2 and uniform current densities J_1 and J_2 is given by

$$L_{12} = \frac{1}{I_1 I_2} \int_{V_1} A_2 J_1 dV_1 \qquad \textbf{(2-53)}$$

where A_2 is the vector potential in the region between the coil 2 and the core, and J_1 is the Fourier series expansion for current density of coil 1.

To obtain the mutual inductance of two radially displaced coils, first the vector potential should be achieved by a field analysis.

The solution space is divided into 4 regions as indicated in Figure 2-23.

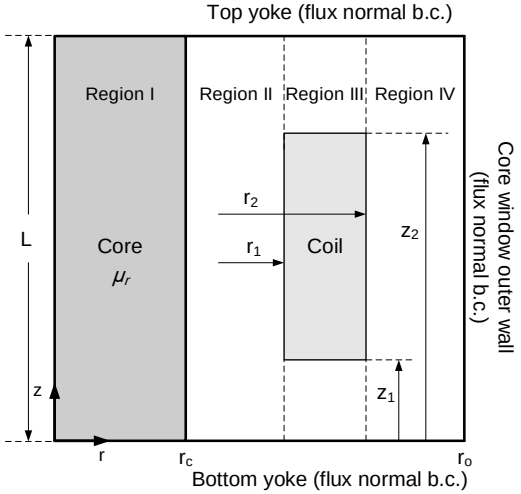

Figure 2-23. The geometry divided into solution regions

Radial and axial extensions of all regions are given in Table 2-3.

Table 2-3. The radial and axial extensions of regions in developed method

Region I	$0 \le r \le r_c$	$0 \le z \le L$
Region II	$r_c \le r \le r_1$	$0 \le z \le L$
Region III	$r_1 \le r \le r_2$	$0 \le z \le L$
Region IV	$r_2 \le r \le r_o$	$0 \le z \le L$

The following assumptions are made.

1. The coils are inside the core window and are surrounded by the core walls from all sides.
2. The coils have a rectangular cross section with a uniform current density. The arrangement of the coils is arbitrary.
3. The geometry is axisymmetric and the current density vector in the coils is azimuthal.
4. The permeability of the core leg could be of any finite value. Other walls of the core window are defined with the flux-normal boundary condition.

Because of the axisymmetric geometry, all the field quantities are independent of the φ coordinate. The vector potential equation in cylindrical coordinates can be expressed as

$$\frac{\partial^2 A_\varphi}{\partial r^2} + \frac{1}{r}\frac{\partial A_\varphi}{\partial r} - \frac{A_\varphi}{r^2} + \frac{\partial^2 A_\varphi}{\partial z^2} = -\mu_0 J_\varphi \qquad \textbf{(2-54)}$$

where A_φ and J_φ are the φ components of the vector potential and current density vector respectively. Note that the subscript φ is dropped for simplicity in the following equations.

The current density could be written as a Fourier series in terms of a fundamental spatial period of length *L* or window height.

$$J = J_0 + \sum_{n=1}^{\infty} J_n \cos\left(\frac{n\pi z}{L}\right) \quad \textbf{(2-55)}$$

where J_0 and J_n are the Fourier series coefficients.

Since it is assumed that the yoke material has infinite permeability, the magnetic flux density, **B**, must be perpendicular to the yoke surfaces. **B** is given by

$$\mathbf{B} = \nabla \times \mathbf{A} = -\frac{\partial A}{\partial z} a_r + \frac{1}{r}\frac{\partial (rA)}{\partial r} a_z \quad \textbf{(2-56)}$$

where a_r and a_z are unit vectors in the *r* and *z* directions, respectively. For **B** to be perpendicular to the top and bottom yokes, the a_r component of **B** must vanish at these yoke positions. If we consider a solution in the form of a series expansion with separated variables as

$$A = \sum_{n=0}^{\infty} R_n(r)\cos(mz) \quad , m = \frac{n\pi}{L} \quad \textbf{(2-57)}$$

then *∂A/∂z* will be zero at *z* = 0, *L*. Thus, this solution satisfies the flux normal boundary conditions at *z* = 0, *L*. R_n is a function which only depends on variable *r*.

Substituting (*2-55*) and (*2-57*) into (*2-54*) and equating corresponding coefficients on both sides of the resulting equation, using the orthogonality of cosine functions, the solution (*2-57*) is explicitly obtained as

$$A = Sr + \frac{T}{r} - \frac{\mu_0 J_0 r^2}{3} + \sum_{n=1}^{\infty}\left(C_n I_1(mr) + D_n K_1(mr) - \frac{\pi\mu_0 J_n}{2m^2} L_1(mr)\right)\cos(mz) \quad \textbf{(2-58)}$$

where *S*, *T*, C_n, D_n are unknown constants which should be determined using boundary conditions.

In regions *I*, *II* and *IV* the current density is zero and so the terms J_0 and J_n equal zero in these regions. In region *I*, the *T/r* term must be dropped since it approaches infinity as $r \to 0$. Also, since $K_1 \to \infty$ as $r \to 0$, D_n must be dropped too. Labelling the solution constants in this region with superscript *I*, *A* inside the core becomes

$$A^I = S^I r + \sum_{n=1}^{\infty}\left(C_n^I I_1(mr)\right)\cos(mz) \quad \textbf{(2-59)}$$

In region *II*, none of unknown constants in (*2-58*) are zero and *A* becomes

$$A^{II} = S^{II} r + \frac{T^{II}}{r} + \sum_{n=1}^{\infty}\left(C_n^{II} I_1(mr) + D_n^{II} K_1(mr)\right)\cos(mz) \quad \textbf{(2-60)}$$

In region *III*, the current density terms must be kept in (*2-58*). Also, like region *II*, none of unknown constants are zero. Thus, the solution in region *III* is given as

$$A^{III} = S^{III} r + \frac{T^{III}}{r} - \frac{\mu_0 J_0 r^2}{3} + \sum_{n=1}^{\infty}\left(C_n^{III} I_1(mr) + D_n^{III} K_1(mr) - \frac{\pi\mu_0 J_n}{2m^2} L_1(mr)\right)\cos(mz) \quad \textbf{(2-61)}$$

In region *IV*, the current density is zero and none of unknown constants are zero.

$$A^{IV} = S^{IV} r + \frac{T^{IV}}{r} + \sum_{n=1}^{\infty}\left(C_n^{IV} I_1(mr) + D_n^{IV} K_1(mr)\right)\cos(mz) \quad \textbf{(2-62)}$$

All region equations already satisfy the boundary conditions at *z* = 0, *L*. The unknown constants must be determined by satisfying the boundary conditions at $r = r_c, r_1, r_2, r_o$.

The vector potential must be continuous across the interfaces [36] at $r = r_c, r_1, r_2$, otherwise, the **B** given will contain infinities. Thus, at $r = r_c$, (2-59) and (2-60) must be equal for all *z.*

$$A^{I}(r_c) = A^{II}(r_c) \tag{2-63}$$

Two other similar equations using (2-60) and (2-61) and also using (2-61) and (2-62) can be written for continuity of A at $r = r_1$ and $r = r_2$ for all z.

In addition to the continuity of A at the interfaces between regions, the tangential component of **H** must be continuous across the interfaces. This means that the term B_z/μ_r must be continuous across all interfaces where μ_r is the relative permeability of the core for region *I* and it is equal to 1 for other regions. Hence, the following additional condition must be satisfied at $r = r_1$ for all z

$$\frac{1}{\mu_r r}\frac{\partial\left(rA^{I}\right)}{\partial r} = \frac{1}{r}\frac{\partial\left(rA^{II}\right)}{\partial r} \qquad \text{at } r = r_c \tag{2-64}$$

Two other similar conditions can also be written for continuity of H_z at $r = r_1$ and $r = r_2$. Moreover, to satisfy the boundary condition at the outer wall of the core window, the a_z component of **B** must vanish at $r = r_o$ i.e.

$$\frac{\partial\left(rA^{IV}\right)}{\partial r} = 0 \qquad \text{at } r = r_o \tag{2-65}$$

Solving for the S, T, C_n and D_n constants according to the above conditions and taking out the term $\mu_0 J_n/m^2$ as a common factor from C_n and D_n constants, the solutions in all 4 regions are obtained according to Table 2-4 where $x_c = mr_c$, $x_1 = mr_1$, $x_2 = mr_2$, $x_0 = mr_0$ and $x = mr$.

Table 2-4. Solution of A inside regions

Reg.	*Vector Potential (A)*	*Constants*	
I	$A^{I} = S^{I} r + \mu_0 \sum_{n=1}^{\infty} \frac{J_n}{m^2} C_n^{I} I_1(x)\cos(mz)$	$S^{I} = \mu_r S^{II}$	$C_n^{I} = C_n^{II} + D_n^{II}\frac{K_1(x_c)}{I_1(x_c)}$
II	$A^{II} = S^{II} r + \frac{T^{II}}{r} + \mu_0 \sum_{n=1}^{\infty} \frac{J_n}{m^2}\left(C_n^{II} I_1(x) + D_n^{II} K_1(x)\right)\cos(mz)$	$S^{II} = \frac{\mu_0 J_0 (r_2 - r_1)}{2}$ $T^{II} = r_c^2(\mu_r - 1)S^{II}$	$C_n^{II} = \frac{I_0(x_o)\int_{x_1}^{x_2} tK_1(t)dt + K_0(x_o)\int_{x_1}^{x_2} tI_1(t)dt}{I_0(x_o) - \alpha K_0(x_o)}$ $D_n^{II} = \frac{I_0(x_c) I_1(x_c)(\mu_r - 1)}{I_1(x_c) K_0(x_c)\mu_r + K_1(x_c) I_0(x_c)} C_n^{II} = \alpha C_n^{II}$
III	$A^{III} = S^{III} r + \frac{T^{III}}{r} - \frac{\mu_0 J_0 r^2}{3} + \mu_0 \sum_{n=1}^{\infty} \frac{J_n}{m^2}$ $\left(C_n^{III} I_1(x) + D_n^{III} K_1(x) - \frac{\pi}{2} L_1(x)\right)\cos(mz)$	$S^{III} = \frac{\mu_0 J_0 r_2}{2}$ $T^{III} = T^{II} - \frac{\mu_0 J_0 r_1^3}{6}$	$C_n^{III} = C_n^{II} + \int_0^{x_1} tK_1(t)dt$ $D_n^{III} = D_n^{II} - \int_0^{x_1} tI_1(t)dt$
IV	$A^{IV} = \frac{T^{IV}}{r} + \mu_0 \sum_{n=1}^{\infty} \frac{J_n}{m^2}\left(C_n^{IV} I_1(x) + D_n^{IV} K_1(x)\right)\cos(mz)$	$T^{IV} = T^{III} + \frac{\mu_0 J_0 r_2^3}{6}$	$C_n^{IV} = C_n^{III} - \int_0^{x_2} tK_1(t)dt$ $D_n^{IV} = \frac{I_0(x_o)}{K_0(x_o)} C_n^{IV}$

When the coils are radially displaced, one can assume that 1 is the inner and 2 is the outer coil (Figure 2-22b). The result will be independent of this assumption. Substituting for A_2 (region *II* solution for coil 2) and J_1 (Fourier series expansion for current density of coil 1) in (2-53), after some algebraic operations, the mutual inductance is obtained as

$$L_{12,\mathrm{rdw}} = \frac{\pi r_c^2 \mu_0 (\mu_r - 1) N_1 N_2}{L} + \frac{\pi \mu_0 N_1 N_2}{3L}(r_1^2 + r_1 r_2 + r_2^2) + \frac{\pi \mu_0 L}{I_1 I_2} \sum_{n=1}^{\infty} \left\{ \frac{J_{n,1} J_{n,2}}{m^4} \left[C_{\mathrm{n},2}^{II} \int_{x_1}^{x_2} x I_1(x) dx + D_{\mathrm{n},2}^{II} \int_{x_1}^{x_2} x K_1(x) dx \right] \right\} \quad \textbf{(2-66)}$$

where $L_{12,\mathrm{rdw}}$ is the mutual inductance of two radially displaced windings.

Note that when the coefficients C_n and D_n have a subscript 1, then the expressions given in Table 2-4 are evaluated using x_1, x_2. However, when the second subscript is 2, then x_3, x_4 must be substituted for x_1, x_2 in the formulas.

Since for the leakage inductance, the positive and negative Ampere-turns balance exactly, the terms related to the first term of inductances i.e., $\pi r_c^2 \mu_0(\mu_r\text{-}1)N_1N_2/L$ in (2-66) vanish in the total energy expression. Thus, this term can be dropped from the inductance relations when calculating the leakage inductance, and because of this fact, μ_r can also be taken as infinite (without having terms with infinite values in the energy equation), representing a flux normal boundary condition on the inner wall of the core window as well as the flux normal boundary condition on the other sides of the core window. It is noted that as $\mu_r \to \infty$ the parameter α in Table 2-4 approaches to $I_0(x_c)/K_0(x_c)$ that makes the constants of the solution simpler to evaluate.

The numerical techniques for solving of the integrals appeared in the formula (2-66) are given in the appendix of [97].

2.5 Parasitic Capacitance

This section will try to answer to the following research question: how to obtain and investigate nominated equivalent circuit set-ups, having different component configurations, for the prediction of the behaviour when accounting for MFTs parasitic capacitances in a power electronic application?

An MFT is an integral element of power electronic devices such as resonance or DAB converters. This type of transformer, especially a high voltage MFT, introduces relatively high parasitic capacitance and leakage inductance, which must be fairly known, correctly dimensioned and adjusted to ensure proper operation of the entire power electronic device. The calculation of the leakage inductance has been thoroughly studied in the earlier published article [97] whereas the determination of the capacitances of the MFT is the focus of the present study.

2.5.1 The frequency spectrum of the voltage waves of a DAB

For given voltage and power conditions, the optimal performance a DAB converter can be achieved within rather limited range of switching frequency 6-20 kHz [98]. In this work, the operating frequency is chosen to be 5 kHz and, therefore, the analysis of the parasitic capacitance should be performed considering signals with a rise time up to 20 µs that corresponds to the range >50 kHz in frequency domain. However, since the wave shapes produced by a DAB are close to square-like signals, rapid voltage variations comprising very high frequency components may exist. For this reason, frequencies up to few MHz will be considered.

2.5.2 The equivalent circuit of transformers

The commonly used equivalent circuit of power transformers operating at 50 Hz is shown in Figure 2-24. At such low frequencies, the capacitance of the transformer is negligible and is usually ignored [36]. However, it needs to be included to represent the MFT operating at high frequencies occurred due to switching waveforms.

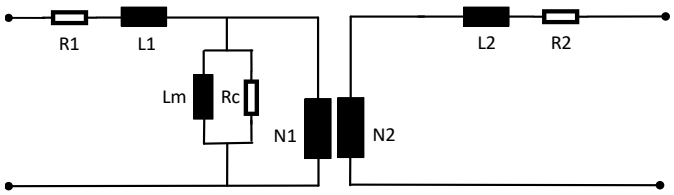

Figure 2-24. Equivalent circuit of 50 Hz transformers [36]. Elements: R1 & L1 are the series resistance and inductance of the primary and secondary sides, L_m is the parallel magnetizing inductance & R_c is a resistance representing the core losses

A comprehensive review of suitable equivalent circuits of transformers used in different applications is presented in [56]. Based on that analysis, a circuit shown in Figure 2-25, which combines the high and low frequency circuits, is seen as the most suitable for an MFT working as an element of a DC/DC converter. In particular, it reflects the features of the designs where one end of the windings is to be permanently grounded.

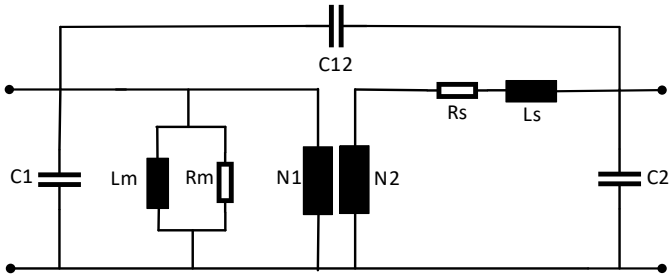

Figure 2-25. A combined wide frequency range equivalent circuit of transformer [56]. Elements: C12 is the capacitance between two windings, C1 = Cg1+Cs1 and C2 = Cg2+Cs2 where Cg is the capacitance to ground, and Cs is the series capacitance of each winding

The model in Figure 2-25 includes three capacitances resulting in a 2×2 admittance matrix. The relations between the capacitances of the equivalent circuit and the resonance frequencies for open and short circuits can be formulated as [56]

$$f_1 = \frac{1}{2\pi}\sqrt{\frac{1}{(C_1 + n^2 C_2 + (n-1)^2 C_{12})L_m}} \quad \textbf{(2-67)}$$

$$f_2 = \frac{1}{2\pi}\sqrt{\frac{1}{(C_2 + C_{12})L_s}} \quad \textbf{(2-68)}$$

$$f_3 = \frac{n}{2\pi}\sqrt{\frac{1}{(C_1 + C_{12})L_s}} \quad \textbf{(2-69)}$$

$$f_4 = \frac{1}{2\pi}\sqrt{\frac{C_1 + n^2 C_2 + (n-1)^2 C_{12}}{(C_1 C_2 + C_1 C_{12} + C_2 C_{12})L_s}} \quad \textbf{(2-70)}$$

Here, f_1 and f_2 are the first parallel and serial resonances; f_4 is the second parallel resonance frequency of the open circuit impedance; f_3 is the parallel resonance frequency of the short circuit impedance; n is the turns ratio of the transformer, and L_m and L_s are the magnetizing and leakage inductances respectively [56]. The latter can be determined from the linear part of a frequency dependent transformer impedance curves [55] using

$$L_m = \frac{|Z_m|}{2\pi f_{L_m}} \quad \textbf{(2-71)}$$

$$L_s = \frac{|Z_s|}{2\pi f_{L_s}} \quad \textbf{(2-72)}$$

Note that L_s can be calculated analytically or be extracted from standard measurements (e.g., frequency response analysis FRA), however, L_m needs to be measured due to the non-linear properties of the iron core.

2.5.3 The proposed models

In this section two equivalent circuits are proposed to model the parasitic capacitances of an MFT when it is integrated in a power electronic circuit. A combined analytical and numerical method is used to calculate the elements of the capacitances in the equivalent circuit network from the physical properties of the multidisc multilayer windings of the high-frequency high-voltage protype transformer.

2.5.3.1 *The Medium Frequency (MF) model*

Transformers implemented in power electronic circuits are not like power transformers concerning the terminal grounding. For conventional power transformers, one end of a winding is normally grounded and there is no capacitance to ground at that end. For MFT used in the DAB, both ends of the windings are subjected to an AC voltage stress. In this case, the capacitance to ground shall be considered on both ends of the winding that is implemented in the circuit in Figure 2-26. In addition to the capacitance between the two upper terminals, three additional capacitances shall be considered between four terminals of the transformer, each having the capacitance of *C*p/4.

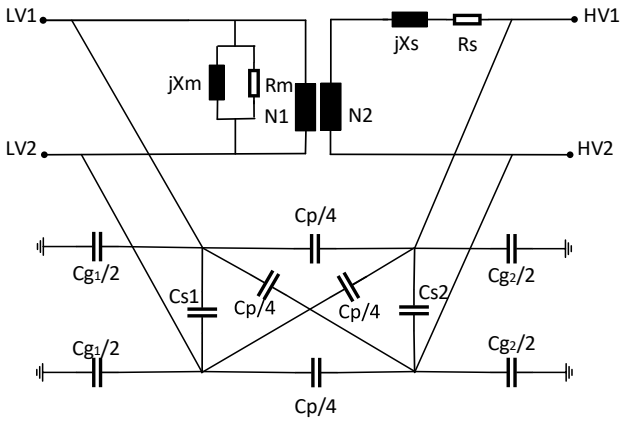

Figure 2-26. A high frequency equivalent circuit with not grounded terminals (MF model)

2.5.3.2 *The extended model*

The MF model inherently yields a linear voltage distribution along transformer's winding. This is not the case for transformers operating at power electronics as has been mentioned in the introduction. To deal with this shortcoming, an extended lumped elements model is suggested (Figure 2-27) where, in addition to capacitances, the inductances are also considered to reflect the fact that during high frequency rising spikes of the square wave, windings are paired by magnetic and electric fields. The self and mutual inductances have the major role in defining the voltage distribution at lower frequencies. At high frequencies, the inductances act as open circuit elements, and the impact of the capacitances becomes more pronounced. Using this circuit, a set of differential equations can be formulated and solved numerically. In this way, a lumped elements model is employed to convert an electromagnetic problem to a circuit model.

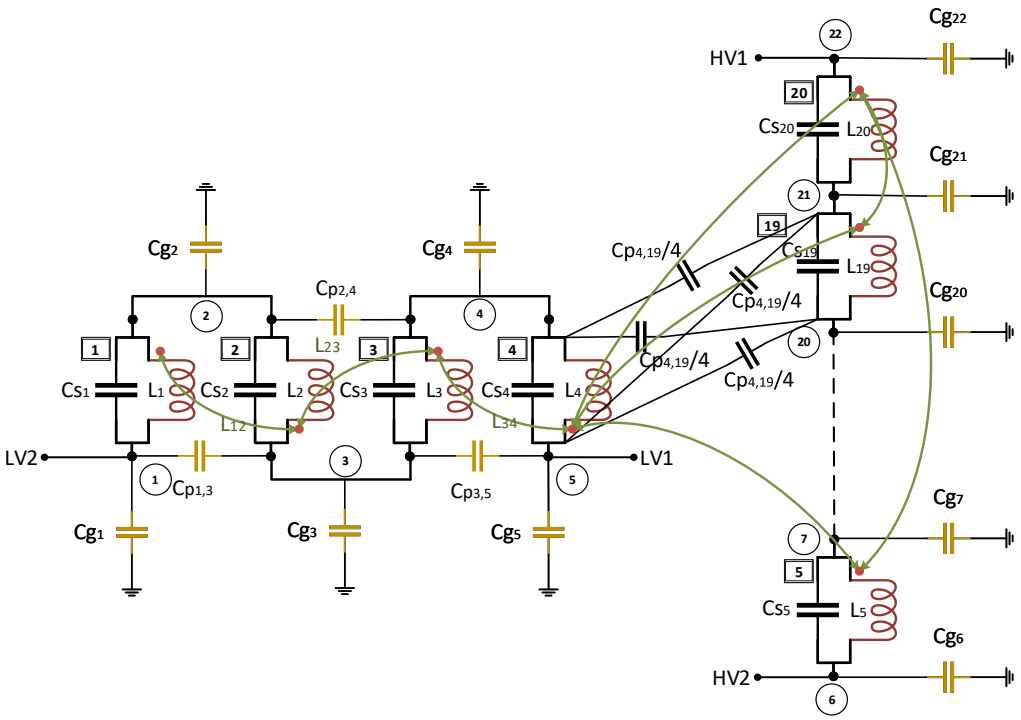

Figure 2-27. A lumped elements circuit including self and mutual inductances and capacitances of the layers and discs (for more clarity, not all indicators between windings capacitances and mutual inductance are shown)

To verify the proposed model, the prototype of MFT presented earlier in [99] is used as a study case. For the analysis, its windings were divided into smaller elements, specifically 4 layers for the LV winding and 16 discs for the HV winding. The voltage distribution over each element is assumed to be linear. Such representation results in 22 nodes and 20 branches in the equivalent circuit in Figure 2-27. The parameters of the elements of the circuit were identified by FEM simulations as described in the following section.

2.5.4 FEM simulations for obtaining capacitance and inductance matrices

To identify the lumped elements in the circuit in Figure 2-27, 3D simulations of the transformer were performed using Comsol Multiphysics. The full specification of the prototype of the MFT, used in this study, has been provided in [99] and [97]. In particular, the LV winding has 4 layers and 12 turns, and the HV winding has 16 discs and 128 turns as shown in Figure 2-28a.

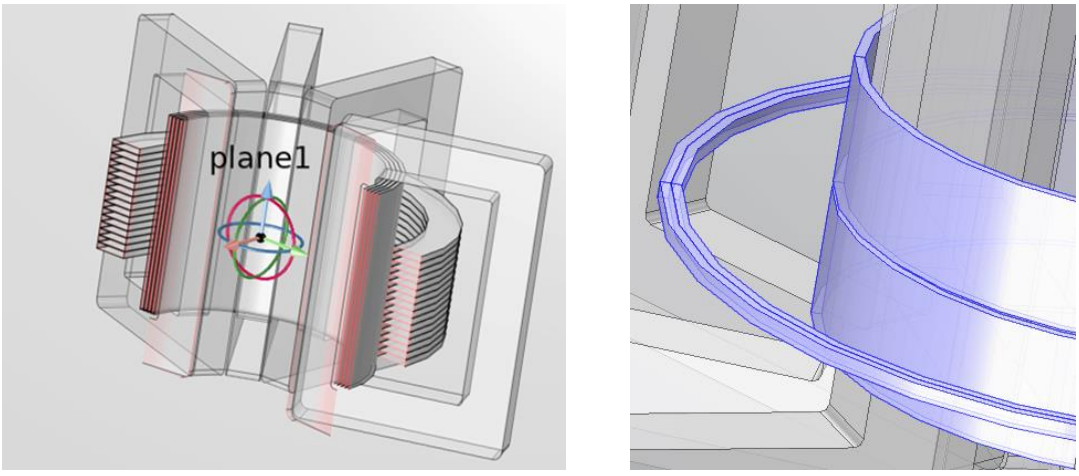

(a) *(b)*

Figure 2-28. The 3D FEM model of 4 layers of LV winding and 16 discs of HV winding in the core window (aa), and two turns of HV and two turns of LV for calculation of turn-to-turn capacitance of layer and disc winding

The Electrostatics interface of the Comsol's ACDC module was used, and the multi-terminal system of the transformer layers and discs was defined as excitation ports or terminals. The electrostatics interface solves the Poisson's equation to find the capacitances. A geometric layer was defined around the transformer and the Infinite Elements feature was assigned to the layer. In this way, the model produces more accurate quantities of capacitance.

The zero electric potential is assigned to most ultimate boundary and the core surfaces. To guarantee that the displacement currents at the outer edges do not diverge, the default Zero Charge condition was selected. The capacitance matrix was obtained by assigning Terminal conditions to the layers and implementing Port Sweep function to sweep the excitation over all ports. The Maxwell capacitance values were obtained from the Global matrix evaluation function [100]. This resulted in a 20×20 matrix of capacitances between 4 layers and 16 discs (Figure 2-28a).

The capacitance between two turns in a layer or disc winding were obtained considering the average diameter of the winding as shown in Figure 2-28b.

The self and mutual inductances of the elements of the transformer model (4 layers and 16 discs) were also obtained from the FEM model. For this case, a Magnetic Field interface was used to implement a stationary domain source sweep study [101]. An example of the solution demonstrating the current density at the last disc and the linkage flux of the disc to the other 19 current carrying elements is shown in Figure 2-29.

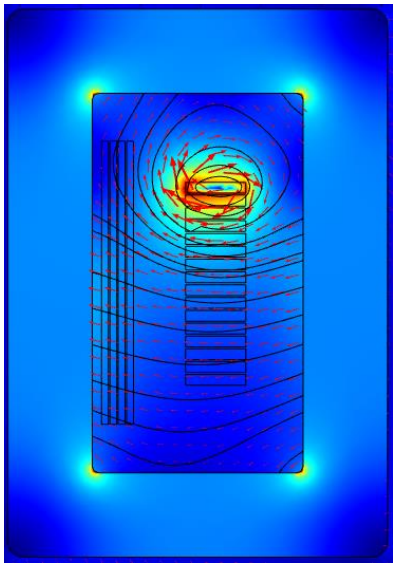

Figure 2-29. The current density plot showing a current at the last disc

2.5.5 Identification of capacitances for the equivalent circuits from fem simulations

In this section the analytical relations for calculation of the elements required for building the proposed medium frequency (Figure 2-26) and extended (Figure 2-27) models are presented. The values obtained from FEM simulations cannot be directly used for building the transformer equivalent circuit. In this section it is demonstrated how the elements of the capacitance and inductance matrices obtained from FEM simulations are used as input for those calculations.

2.5.5.1 *Calculation of the turn-to-turn capacitances*

The capacitance between two turns in a layer winding, C_{TL}, having an air layer between the turns is calculated as

$$C_{TL} = \varepsilon_0 \pi D_{ml} (w_l + t_e) / (t_e / \varepsilon_e + t_a / 1) \quad \textbf{(2-73)}$$

where ε_0 is the permittivity of air, ε_e is the relative permittivity of enamel isolation, D_{ml} is the average diameter of the layer winding, w_l is the bare width of the conductor in radial direction, t_e is the total enamel insulation thickness (both sides), t_a is the total thickness of air gap between two turns of a layer.

The capacitance between two turns in a disc winding, C_{TD}, is calculated as

$$C_{TD} = \varepsilon_0 \pi \varepsilon_e D_{md} (w_d + t_e) / (t_e / \varepsilon_e + t_a / 1) \quad \textbf{(2-74)}$$

where D_{md} is the average diameter of the disc winding, w_d the bare width of the conductor in axial direction, t_e is the total enamel insulation thickness (both sides) and t_a is the total air isolation thickness between two turns of a disc.

2.5.5.2 *Calculation of the winding's series capacitances for medium frequency model*

For a layer type LV winding, the series capacitance C_{SL} is determined as [36]

$$C_{SL} = \frac{C_{TL}}{N_{LW} N_L^{\,2}} (N_L - 1) + \frac{4(N_{LW} - 1)}{N_{LW}^{\,2}} C_{LR} \quad \textbf{(2-75)}$$

where N_L is the number of turns per layer, C_{TL} is calculated from (2-73), N_{LW} is the number of layers and C_{LR} is the inter-layer capacitance calculated as

$$C_{LR} = \frac{C_{LA}}{3} \quad \textbf{(2-76)}$$

where C_{LA} is the layer-to-layer capacitance calculated by (2-83) or can be directly obtained from FEM simulation.

For a disc type HV winding the series capacitance C_{SD} can be found as [36]

$$C_{SD} = \frac{C_{TD}}{N_{DW} N_D^{\,2}} (N_D - 1) + \frac{4(N_{DW} - 1)}{N_{DW}^{\,2}} C_{DR} \quad \textbf{(2-77)}$$

where N_D is the number of turns per disc, C_{TD} is calculated from (2-74), N_{DW} is the number of discs and C_{DR} is the inter-disc capacitance calculated as

$$C_{DR} = \frac{C_{DA}}{3} \quad \textbf{(2-78)}$$

where C_{DA} is the disc-to-disc capacitance calculated by (2-82) or directly obtained from 3D FEM simulation. The reason for having the factor 1/3 in (2-78), is the linear distribution of the voltage along two adjacent discs, which results in a linear voltage drop across the radial channel between discs, contributing to a reduced stored energy in between-discs area. More details in this regard can be found in [36].

2.5.5.3 *Calculation of the series capacitances for the extended model*

The series capacitances for the layer type LV winding, C_{S1} to C_{S4}, where there is a relatively high distance between the layers, are calculated as [36]

$$C_{S1-4} = \frac{N_L - 1}{N_L^{\,2}} C_{TL} \quad \textbf{(2-79)}$$

where N_L is the number of turns per layer and C_{TL} is calculated from (2-73).

The series capacitance of the disc type HV winding, C_{S5} to Cs_{20} are calculated as

$$C_{S5-20} = C_{T_{eq}} + \frac{2}{3} C_{D1} + \frac{2}{3} C_{D2} \quad \textbf{(2-80)}$$

where

$$C_{T_{eq}} = \frac{N_D - 1}{N_D^{\ 2}} C_{TD} \quad \textbf{(2-81)}$$

where N_D is the number of turns per disc and C_{TD} is calculated from (2-74).

The capacitances C_{D1} or C_{D2} in (2-80) are the capacitances between two adjacent discs and can be calculated from

$$C_{D1,2} = \varepsilon_0 \pi D_{md} (R + t_e) / (t_e / \varepsilon_e + t_a / 1) \quad \textbf{(2-82)}$$

where D_{md} is the average diameter of the disc winding, R is the disc winding radial depth, t_a is the total air isolation thickness between two discs as shown in Figure 2-30.

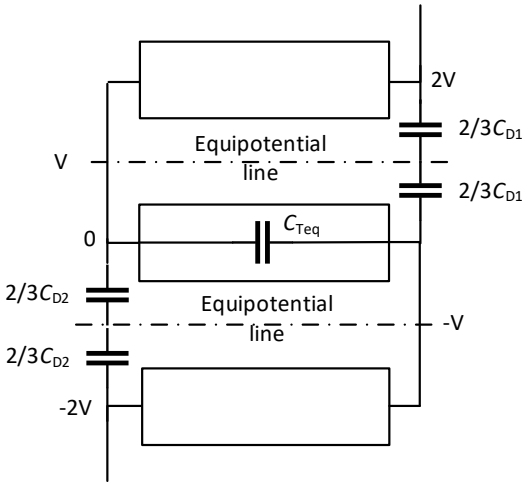

Figure 2-30. The elements for calculation of the series capacitance of the winding

2.5.5.4 *Calculation of inter-winding capacitance*

A transformer consists of at least three major conductive parts (electrodes) which are galvanically isolated (except autotransformers which are not in the scope of this study). At power frequency of 50 Hz, the windings are normally treated as inductive coils and have low DC resistances. There are capacitances between the secondary and primary windings and a magnetic (normally grounded) core, which are solely defined by the geometrical shapes and dimensions of these elements. Thus, the capacitance between two concentric circular windings is

$$C_{Cy1-Cy2} = \frac{2\pi\varepsilon_0 H}{\ln(b/a)} \quad \textbf{(2-83)}$$

where ε_0 is the permittivity of vacuum, b is the radius of the outer winding, a is the radius of the inter winding, and H is the average of the heights of the windings [36].

2.5.5.5 *Derivation of Z-curves from developed equivalent circuits*

As explained in the previous sections, the elements of the circuits are to be calculated based on the data extracted from 3D FEM simulations and analytical calculations. Knowing the elements, the equivalent circuits can be formed for the Medium Frequency (MF) model as in Figure 2-26 and for the extended model as in Figure 2-27.

For the circuit analysis of the extended model having n nodes and b branches, the system admittance matrix is determined using

$$\boldsymbol{Y = A' Z^{-1} A + Y_c} \quad \textbf{(2-84)}$$

where $\boldsymbol{Z} = j\omega\boldsymbol{L}$ is the impedance matrix representing the inductive elements, forming inductance matrix $\boldsymbol{L}$ ($b \times b$) of the winding; $\boldsymbol{Y_C} = j\omega\boldsymbol{C}$ is the admittance matrix, representing the capacitive elements $\boldsymbol{C}$ ($n \times n$) of the winding; $\boldsymbol{A}$ ($b \times n$) is the branch-node incident matrix.

For the open circuit test, a voltage source V_s is connected between the terminal nodes of transformers primary side, and the following parameters are calculated

$$\boldsymbol{Y}_a = \begin{bmatrix} \boldsymbol{Y} & \vdots & -\boldsymbol{y}' \\ \cdots & \cdots & \cdots \\ \boldsymbol{y} & \vdots & 0 \end{bmatrix} \quad \textbf{(2-85)}$$

$$\boldsymbol{I}_a = \begin{bmatrix} \boldsymbol{I} \\ \cdots \\ \boldsymbol{V}_s \end{bmatrix} \quad \textbf{(2-86)}$$

$$\boldsymbol{V}_a = \begin{bmatrix} \boldsymbol{V} \\ \cdots \\ \boldsymbol{I}_s \end{bmatrix} \quad \textbf{(2-87)}$$

where $\boldsymbol{Y}_a$ (n+1,n+1) is the augmented admittance matrix, $\boldsymbol{I}_a$ (n+1,1) and $\boldsymbol{V}_a$ (n+1,1) are augmented excitation and unknowns' vectors respectively. In (2-85), $\boldsymbol{y}$ is a (1×n) vector where $y_{i \neq k,l} = 0$, $y_k = 1$ and $y_l = -1$, if the positive terminal of the voltage source is connected to the node k and the negative terminal connected to the node l. $\boldsymbol{V}$ (n×1), is the vector of voltages of the branches, and $\boldsymbol{I}$ (n×1) is the vector of injected currents to the nodes. In (2-87), Is is the injected current from source to the node k.

The circuit's unknowns vector including nodal voltages and injected source current is obtained from

$$\boldsymbol{V}_a = \boldsymbol{Y}_a^{-1} \boldsymbol{I}_a \quad \textbf{(2-88)}$$

The input impedance is obtained by dividing the source voltage (V_s) with the source current (I_s). If the negative terminal of the voltage source (node l) is connected to ground, $y_l = 0$ is set to zero in $\boldsymbol{y}$.

The short circuit is simulated by connecting a voltage source having the amplitude of 0 towards the transformer's secondary side terminals. Later, equations (2-85)-(2-87) are solved assuming $V_s = 0$.

For the circuit analysis of the MF model, first, the admittance matrices of Y_L and Y_M are established

$$\boldsymbol{Y}_L = \frac{1}{R_s + j\omega L_s} \begin{bmatrix} a^2 & -a \\ -a & 1 \end{bmatrix} \quad \textbf{(2-89)}$$

$$\boldsymbol{Y}_M = \frac{1}{R_m + j\omega L_m} \begin{bmatrix} 1 & 0 \\ 0 & 0 \end{bmatrix} \quad \textbf{(2-90)}$$

where, R_s and L_s are the resistance and leakage inductance transferred to the secondary side, and R_m and L_m are the resistance and magnetizing inductance transferred to the primary side.

The admittance matrix of the system is then obtained as

$$\boldsymbol{Y} = \boldsymbol{A}' (\boldsymbol{Y}_L + \boldsymbol{Y}_M) \boldsymbol{A} + \boldsymbol{Y}_C \quad \textbf{(2-91)}$$

where $\boldsymbol{Y}_c$ (4×4) is the capacitive admittance matrix, and $\boldsymbol{A}$ (2×4) is the branch-node incident matrix of the circuit

$$\boldsymbol{A} = \begin{bmatrix} 1 & -1 & 0 & 0 \\ 0 & 0 & 1 & -1 \end{bmatrix} \quad \textbf{(2-92)}$$

For obtaining the input impedances at open and short circuit conditions, as it is explained for the extended model, voltage sources are connected between the related nodes and the circuits are solved using (2-85)-(2-88).

2.6 *Transformer losses*

2.6.1 Core losses

Basically, three methods have been developed for magnetic material's loss calculations [3]. First, the loss separation method, which includes calculation of static hysteresis losses, classic eddy current loss and excess eddy current loss and is usually too complicated to be used for engineering tasks (except in Fem analysis). Hysteresis loss is independent of the wave shape, and it is frequency and flux density dependent. This loss component can be calculated and verified by measurements. The classic eddy current loss can also be calculated but the excess eddy current loss should be included which is a function of frequency and maximum flux density, which needs to be determined by a series of measurements and parametrizations for the investigated magnetic material [102]. Second is the time domain approach which is the method used for loss calculations in FEM [3]. A third strategy is to use a set of empirical methods, all based on empirical measurements and on the formulation made by Steinmetz in 1892 [103]. In this work the samples to be used were available and measurement were chosen to be used for the loss determination.

A few types of core materials are popular among the researchers which work with medium frequency transformer designs. Ferrite and Nanocrystalline cores are previously used by the author to produce two 50 kW transformers [13]. The 'core losses – frequency' curves of Nanocrystalline cores from their datasheets are normally given at a very low operational working point (0.1-0.3 T for Nanocrystalline cores compared with 1-1.2 T as working point flux). In case of Ferrite cores, the data given in the core data sheet does not include the working point flux density of 0.3 T (Figure 2-31).

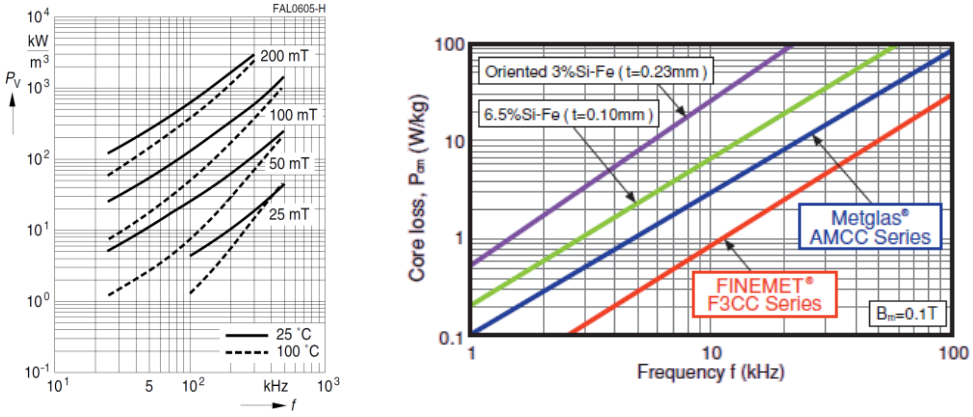

(a) *(b)*

Figure 2-31. Loss-frequency curves of sample N87 Ferrite and Finemet Nanocrystalline cores: Ferrite core [104] (a), and Nano crystalline core [105] (b)

2.6.2 Winding losses

The research question here is to validate the continuum representations of wound coils methodology in the context of multistrand winding wires of and to introduce a time-efficient method to calculate the winding loss, compared to previous methods. Therefore, in this part of the study an effective numerical method will be introduced and practically verified, for copper loss calculation of the MFTs with windings having litz wire conductors [106].

2.6.2.1 *MFT's current and the behaviour of the litz wire*

To calculate the current, in the transformer equivalent circuit, it is assumed that the real part of the complex impedance is ignorable compared with the imaginary part i.e. the leakage inductance [107]. With this assumption

$$I_p = (V_p - V_s) / X_L \quad \textbf{(2-93)}$$

where

$$V_p = 2\sqrt{2}V_i / \pi \quad \textbf{(2-94)}$$

The order h of the transformer's primary side r.m.s. value of the current is calculated from [13]

$$I_{ph} = \frac{2V_i\sqrt{1 - cos(h\varphi)}}{\pi^2 f h^2 L_s} \quad \textbf{(2-95)}$$

where V_i is the bus voltage of the primary, φ is the phase shift between the primary and secondary side voltages of the transformer, f is the frequency and L_s is the leakage inductance of the transformer.

For an MFT, the leakage inductance seen from the primary side can be calculated from [44]

$$L_s = \frac{2W}{I_p^2} MLT \quad \textbf{(2-96)}$$

where MLT is the mean length of the winding turns and W, the total magnetic energy stored inside the core window can be obtained from

$$W = \frac{1}{2}\int \mathbf{A} \bullet \mathbf{J} dv \quad \textbf{(2-97)}$$

Using Maxwell's equations and choosing the Coulomb gauge, the well-known equation for the vector potential **A** is obtained

$$\nabla^2 \mathbf{A} = -\mu_0 \mathbf{J} \quad \textbf{(2-98)}$$

where **J** is the current density vector in the z direction, and it can be assumed that all the field quantities of it are independent of z.

Losses caused by the current in a transformer are named Load losses [36]. Load losses consists of winding Ohmic resistance losses and additional losses. Winding DC resistance is calculated using

$$R = \rho \frac{l}{A} = \rho(MLT \times N) / (\pi r^2 n_S) \quad \textbf{(2-99)}$$

where R is the resistance of the winding, ρ is the resistivity of the copper wire, MLT is the mean length of the strands in each winding turn, N is the number of the turns of the measurement side, r is the radius of each wire strand, n_s is the number of the strands.

The additional or stray losses are produced by AC currents from the leakage field of windings and the field of high-current carrying leads. The additional losses are produced in the windings and structural parts. The losses in the windings are eddy current losses and circulating current losses.

Depending on the frequency, the presence of these additional losses will make the AC current losses higher than the equivalent DC current copper losses. Circulating current losses can be a result of having parallel conductors of different length or exposed to different electric field which leads to a different voltage drop over two parallel conductors of the same length. For the prototype transformer considered in this study parallel conductors are axially ordered and there are no circulating current losses in them. However, because of the relatively high frequency, eddy current losses are present and will be investigated.

Because of the high skin and proximity effects at high frequencies it is not economical to use normal wires to produce the windings. Copper foils are suitable alternatives for higher frequencies, but they need a great care during the production and for the termination when mounted in the transformer.

With the introduction of litz wires (bunch of individually insulated conductors), a higher flexibility in the production and lower losses can be gained [106].

A litz wire consists of a group of enamelled strands (Figure 2-32b). The enamel insulation of the conductor is normally modified polyurethane. At higher frequencies, increasing the number of strands together with the reduction of the strand's diameters, counteract the increase in the conductor resistance. The alternating current causes eddy currents in the conductor which acts to counteract the flow of the fundamental current. At higher frequencies, the effect of these eddy currents increases, and an AC resistance is added to the DC resistance. The eddy current loss in the middle of the conductor has a low value and increases when moving towards the outer part of the conductor. This causes the current to flow closer to the surface of the conductors instead of in the whole conductor (the skin effect). The skin depth [m] is a representation of the thickness of the conductor which is carrying the current and can be calculated from

$$\delta = \sqrt{\frac{2}{\omega\mu\sigma}} \qquad \textbf{(2-100)}$$

where ω is the radian frequency (rad/s), μ is the permeability of the conductor (H/m) and σ is the conductivity of the conductor (1/Ωm). For example, the skin depth for copper at the frequency of 5 kHz is 1 mm and this means that the current in the depth of 1 mm is reduced to 36.8% of the one at the surface [36]. Because of the proximity effect, the fields of the adjacent conductors increase the eddy current losses. The cross-sectional area of the single conductor is reduced to minimize these losses. Several conductors in parallel are used to carry the nominal current of a wire. To compensate for the effects of the fields on the individual strands, the conductors are twisted together so that, throughout the length of the wire, the position of one conductor transposes regularly. Because of the high capacitance effect of the conductor, litz wires can be used only up to 2 MHz. A typical diameter of each conductor as a function of frequency is 0.4 mm for 50-1000 Hz, 0.25 mm for 1-10 kHz or 0.032 mm for 1.5-2.8 MHz [108]. With an effective reduction of the skin effect, the litz wires have the best performance in high frequency circuits. Commercial production of several types and dimensions of the wire gives a good flexibility for getting the highest benefit in this project. Rectangular litz wires are estimated to be one of the best candidates for usage as the high and low voltage conductors in this project (Figure 2-32a). This arrangement helps for higher density and more mechanical strength of the winding. The available constructions from one of the leading litz wires manufacturers are presented in Reference [108].

(a) ***(b)***

Figure 2-32. A rectangular litz wire and its strands: A rectangular litz wire (a), and a bunch of enamelled strands (b)

2.6.2.2 *Evaluation of winding losses using equivalent permeability and conductivity method*

One method of calculating eddy current losses including skin and proximity effect losses is to make a finite element model, in which each turn in a winding is explicitly represented. By modelling each turn, the distribution of current density within each turn due to these effects, can be accurately determined. However, modelling every wire individually can be computationally expensive. An alternative approach is to replace a wound region composed by many wires with a region with proper equivalent complex-valued material properties.

Continuum representations of wound coils allow proximity and skin effect losses to be represented in numerical models without explicitly modelling each turn in the coil. Moreau et al. [109] described the use of a complex-valued magnetic permeability for representation of transformer windings with rectangular conductors, presenting closed-form expressions for frequency-dependent permeability. Gyselinck and Dular [110] presented a numerical method for obtaining equivalent properties of a round-wire winding with hexagonal packing. Dowell [94] replaced a winding composed of round wires with an "equivalent" foil winding that admits an analytical solution for proximity losses. Meeker [111] derived approximate but closed-form expressions for the equivalent conductivity and permeability of regions filled with hexagonally packed round wires, allowing proximity and skin effects to be included in 2D AC field computations. In this work the method developed in [111] is used for calculation of eddy current losses of MFT windings made by litz wires.

The effective material properties of the wound region can be expressed as [111]

$$\mu_{\text{eff}} = (1-c)\mu_0 + c\mu_{\text{fd}} \tag{2-101}$$

$$\sigma_{\text{eff}} = \frac{\sigma fill}{\frac{\mu_0}{\mu_{\text{fd}}} + \frac{(1-c)}{c} j\Omega - \frac{1}{3}\frac{\mu_{\text{eff}}}{c\mu_0} j\Omega} \tag{2-102}$$

where the parameter *c*, representing the fill factor of the equivalent foil geometry, is defined as

$$c = \sqrt{\frac{2\sqrt{3}}{\pi} fill} \tag{2-103}$$

where *fill* is copper fill factor, and the non-dimensional frequency is defined as

$$\Omega = \frac{\sqrt{3}\pi c\omega\sigma\mu_0 R^2}{8} \tag{2-104}$$

and the frequency-dependent permeability of a single equivalent foil is

$$\mu_{\text{fd}} = \frac{\mu_0 \tanh\sqrt{j\Omega}}{\sqrt{j\Omega}} \tag{2-105}$$

2.7 Converter Losses

The input power to the converter is the DC voltage of the source multiplied to the average or effective value of the source output current. The input power to the transformer is the mean value of the product of values of instantaneous voltage and current waves.

$$P_{\text{ave}} = \frac{1}{t_2 - t_1}\int_{t_1}^{t_2} i(t)v(t)dt \tag{2-106}$$

To calculate the effective value of the current (r.m.s.) for the calculation of winding losses, first, the Fourier transformation shall be used to find the harmonic components of the current and later each component together with the related frequency shall be used to calculate the loss components. Finally, the total winding loss will be the sum of loss components. A direct use of the r.m.s. value of a non-

sinusoidal current will lead to minor errors in winding loss calculations and here this error is ignored, and the losses are calculated from

$$I_{\text{rms}} = \sqrt{\frac{1}{t_2 - t_1} i^2(t) dt} \quad \textbf{(2-107)}$$

The semiconductor losses are consisting of the IGBTs and diodes losses when they are at the conducting state as well as when they are switching. The calculation methods are in principle the same both for an IGBT or a diode. It has been assumed that soft switching is achievable in all operating points, and thus the switching losses can be ignored.

Having the voltage and current wave shapes the total conduction loss will be

$$P_{\text{on}} = \frac{1}{T}\int_0^T V_{\text{SemiCond}}(t) i(t) dt = \frac{1}{T}\int_0^T (V_{\text{F}} i(t) + R_{\text{on}} i(t)^2) dt \quad \textbf{(2-108)}$$

One component of the conduction loss is consumed on the Collector-Emitter resistance of the semiconductor. While conducting, the power is consumed on the conduction resistance which can be calculated from I_C versus V_{CE} curves given in the specification sheets of a semiconductor. In this case the losses will be

$$P_{\text{on\_R}} = R_{\text{on}} I_{\text{RMS}}^2 \quad \textbf{(2-109)}$$

The other component is the average power dissipated while the semiconductor is at the on-stage. This loss is calculated as [112]

$$P_{\text{on\_F}} = V_{\text{F}} I_{\text{AVG}} \quad \textbf{(2-110)}$$

while V_F is the forward or on-stage voltage.

2.8 Insulation withstand strength under high frequency stress

During a long operation time for a high-voltage equipment under high frequency stress, both the voltage and the heat contribute to the degradation of the insulation material. Therefore, in this section it will be demonstrated how to extend datasheet information about DC and 50 Hz insulation abilities to high-frequency applications, in terms of insulation performance.

2.8.1 Voltage stress

Any insulation material has a withstand strength which is dependent on the applied voltage rate of rise, magnitude and duration. Three examples of voltage wave shapes which are standardized during the development of the power transformer's insulation design are AC at power frequency (50 Hz), Lightning Impulse (LI) and Switching Impulse (SI). As an example, for testing a power transformer, a switching impulse voltage can have a time to peak value down to 100 µs, a magnitude or peak value of 375 kV and a duration (time duration while the magnitude is higher than 90% of the peak value) of 200 µs and time to zero of minimum 1000 µs [113]. To design an insulation system for a power transformer, the Design Insulation Levels (DIL) should be determined first [36].

The following can be considered as additional sources for overvoltage stresses on the MFTs, which are in addition to the normal stresses that any low frequency power transformer (50 Hz) can stand for:

- Reflection of voltage pulses at the impedance mismatching terminals
- Resonance inside the converter
- Uneven distribution of voltage pulses along the windings

The following parameters are to be considered to ensure a reliable application of any insulation material for any MFT:

- Voltage magnitude
- Voltage frequency (or pulse repetition rate)
- Partial discharge
- Pulse rise time
- Pulse duty cycle and polarity

2.8.2 Effect of voltage amplitude

Because of transient over voltages or temporary overloads, the voltage on or temperature of an insulation part used in an MFT placed inside a DAB converter can be much higher than the calculated stresses values at steady state operation. The safety margins for the withstand strength at the rated values are presented in the materials' data sheets. Because of the accelerated aging, when the voltage magnitude increases, the lifetime of the insulation system decreases. Many investigations have concentrated on the effect of voltage magnitude to the acceleration of the insulation material aging. The most reliable relation has been presented in IEC 61251 [114] as

$$L = cE^{-n} \tag{2-111}$$

where, *L* is the time to breakdown, *E* is the electrical field and *c* and *n* are the parameters depending on temperature and other environmental effects. Investigation made by Stone et al. in 1992 demonstrates how an increase in the applied voltage magnitude decreases the time to failure of an epoxy insulation [115].

2.8.3 Effect of Frequency

In general, like for mechanical fatigue, regardless of frequency, the same number of voltage impulses or cycles in a period causes the same degradation of an insulation material. This is shown by Johnston in 1979 [116], during an extensive literature review where he has presented a table of summery for most of the efforts that has focused to the frequency acceleration of the voltage endurance. However, he has also referred to the works which reported a nonlinear acceleration result. This inconsistency can be because of humidity or a change of material temperature resulting from dielectric losses in a long-term test. According to Johnston, a linearity factor can be gained for every specific experimental setup, and it is shown that

$$f_1 t_1 = k(f_2 t_2) \tag{2-112}$$

where *k* is one, for most of the cases, if the temperature, humidity or test set-up effects are ignored.

2.8.4 Effect of partial discharge

Partial discharge is one of the physical processes which cause aging of insulation material. Chemical reactions, bombardment of cavity surfaces by charge carriers and local electrical field enhancement resulting from the discharge by-products, contribute to the creation of large holes and starting treeing activities [33].

Partial discharge inception voltage is the applied voltage when the electric field over an insulation material or system is higher than the required value for starting a PD activity. When an alternating voltage is applied, PD pulse trains can be repeated for each period (Figure 2-33). Compared with PD pulses that appears stochastically, discharges which occur at the voltages higher than the Repetitive Partial Discharge Inception Voltage (RPDIV) [117] are the main cause of the aging under square wave voltage regime.

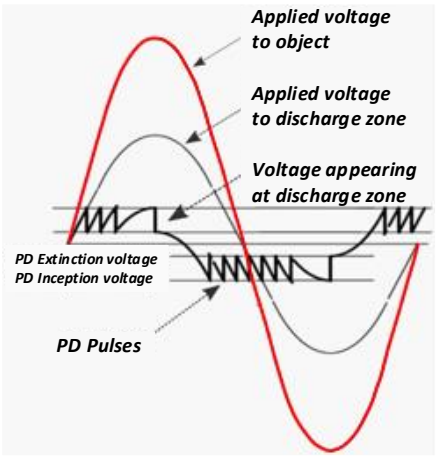

Figure 2-33. PD pulse train for each cycle of applied voltage [77]

2.8.5 AC standard breakdown test methods

To characterise the insulation materials, the main types of insulation tests are insulation withstand or breakdown (BD) test and Insulation aging test. The number of samples to undergo identical tests should be as high as possible to guarantee a reliable and repeatable result.

2.8.5.1 *For insulation oil*

IEC 60156 [118] describes a test method for the determination of AC breakdown voltage of transformer oil. Figure 2-34 demonstrates the electrode configuration for acquiring the insulation strength of transformer oil according to this standard.

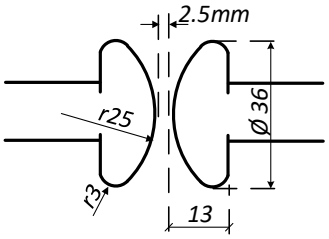

Figure 2-34 Standard electrode configuration for testing insulation strength of transformer oil [118]

2.8.5.2 *For insulated wires*

The tests samples are prepared according to a well-defined standard method of IEC 60851-5 [119]. For each sample, two wire strands are twisted several times. To secure a defined contact area for similar tests, a load is applied during twisting the pairs (Figure 3-26). The rate of voltage increase shall be defined (Figure 2-35).

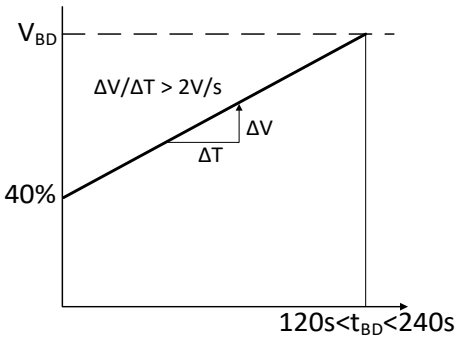

Figure 2-35. Voltage profile with a slow rate-of-rise test according to IEC 60243-1

2.8.5.3 *For insulation tapes, plates or films*

Regarding high voltage testing of insulation materials, a series of articles and standards exists. To achieve more reliable results in a shorter period, the standardized methods are preferable to the experiments that are presented in the scientific articles. The following is a list of standards which can be used:

- IEC 60243-1:2013, Test methods to determine the electric strength of insulating materials at power frequencies (50-60 Hz)
- ASTM D149:2004, Test methods for electrical insulation tests of solid insulating materials at power frequencies
- IEC 60505:2011, Evaluation and qualification of electrical insulation systems
- IEC 61251:2015, Electrical insulating materials and systems AC voltage endurance evaluation
- IEC 62539:2007, Guide for the statistical analysis of electrical insulation breakdown data

2.8.6 Testing combined insulations

Testing withstand ability of single type materials may not be a real representation of withstand strength of a combined solid insulation system. At the interface of two solid insulation materials, the breakdown strength is governed by size and pressure of the voids filled of different insulating material (in case of testing in air is according to Paschen curve [120]). This is also true for the interface of insulation and electrodes.

2.8.7 Mechanical electrode preparations

Here are some notes presented in IEC 60243-1:2013 [121] regarding a test set-up that can guarantee a reliable and repeatable series of the tests:

- The electrodes should be kept clean, smooth, and free from defects after each AC-BD test.
- For most of the materials, increasing the thickness of the test object will result in lower electric strength and the results of the tests for different thicknesses are not directly comparable. The thickness of the specimen, time of voltage application, duration, and intensity of surface discharges directly before a breakdown, affects the electric strength of most of the types of insulation materials [121].
- The leads to the high voltage electrodes shall not affect the electrode setup in any way, nor change the electric field near the breakdown position.

2.8.8 Handling of surrounding medium oil

When oil is used as a surrounding medium, any discharge will pollute the oil and should therefore be avoided. Practical tests show that this is not easily achievable especially if the discharge current amplitude and duration cannot be kept short enough.

2.8.9 Measuring voltage

It is well accepted in the high voltage industry that it is the peak value of the applied voltage which shall be adjusted during standard withstand tests. For all the frequencies, the same peak value is applied. The Partial Discharge (PD) is monitored.

2.8.10 Rate of rise of voltage

As the time of voltage application increases, the electric strength of most of the materials decreases with increasing the voltage application time [121]. Therefore, the rate of rise of AC voltage is important. One of the methods can be chosen; the rapid rise, the 20 s step-by-step or the slow rate-of-rise (120 s - 240 s) method.

According to ASTM D149-97a [122], the “Slow rate-of-rise test” is simpler and the preferable method to the “Short-time test” and “step-by-step test” method and gives more meaningful results when different materials (artificially contaminated in this case) are compared with each other. The test method is described in sub-clause 10-3, IEC 60243-1 [121].

2.8.11 Monitoring PD during an aging test or before an AC-BD test

Necessity of PD monitoring

The partial discharge (PD) measurement is an accepted test for qualification of insulation systems. During insulation test of materials or a complete transformer, recorded PD signals include useful information about any possible design, or manufacturing mistake or a sign of undesirable aging.

Proper PD measuring under square wave

When it comes to a square wave signal on the terminals of an MFT, the transformer insulation will be under repetitive impulses of high dv/dt stress. During the application of a square wave shape voltage to an MFT, as the PD signals become similar to the supply voltage signal, then it is very important to use a correct method to measure the PD signals [123].

Measured PD during a dielectric test

The existence of partial discharge should be controlled for a reliable and repeatable aging test. When increasing the applied voltage, the partial discharge (PD) starts at the PD Inception Voltage (PDIV). The PDIV depends on many parameters where just part of them are originating from the nature of a material under test. The remaining parameters such as voids between the material and electrodes, discharges at the edges of electrodes or the insulation material surface where the touching surfaces ends, have a parasitic nature during a high voltage insulation test.

3 Characterisation of Insulation Materials for HVDC MFT Application

The most important part of the insulation material specification data to be used for the DC insulation design of a HVDC MFT is the magnitude of its electrical conductivity. There is a lack of open data of conductive properties of esters and ester OIP and therefore one of the research objectives is to quantify electric conductivities of these materials including their temperature and electric field dependencies. As it is explained in Section 0 a conductivity magnitude is not a straightforward predetermined value which can be found in any data base. Therefore, a great effort in this work is devoted to conductivity measurement of mineral and ester transformer oil and Oil Impregnated Pressboards (OIPs).

The other aspect that should be considered regarding characterisation of the insulation material used for production of a medium frequency transformer which is subjected to high frequency pulses from fast rising square wave voltage signals (Figure 2-1a) is their voltage withstand strength under high frequency stress. This aspect is covered in Section 3.2 and guidelines to tackle this challenge is presented.

3.1 Electrical conductivity under high voltage DC stress

3.1.1 DC conductivity measurement setup

High voltage DC conductivity measurements are performed using the background information presented in Section 2.2.11. A complete test setup is developed which is demonstrated in Figure 3-1 and described in the following sections.

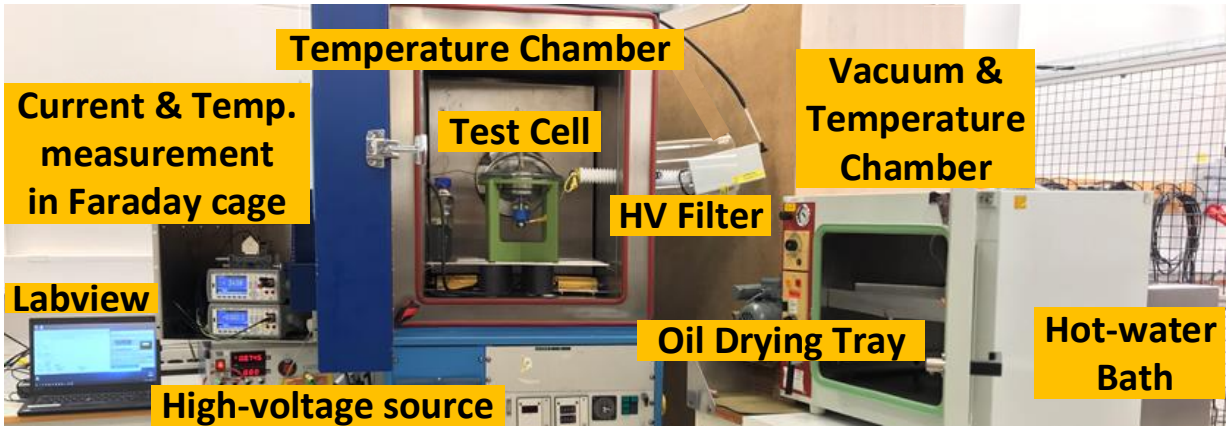

Figure 3-1. The test setup for conductivity measurements

The test cell for performing the measurements was manufactured based on the background information presented in Section 2.2.13. The middle part has been manufactured with two different sizes, one having D = 97.8 mm with $R2$ = 1 mm [28] and to handle higher voltages, one having D = 99,8 with $R2$ = 2 mm [124]. The other rounding dimensions are $R1$ = 1 mm, $R3$ = 3 mm and $R9$ = 5 mm.

In case of oil tests, a gap distance of 2 mm was held using dried and oil impregnated pressboard during the oil test. Stainless steel (EN 10020) having a maximum contact surface roughness of 4 µm was used. In case of solid dielectrics, a sample thickness of 1 mm was used in the set-up. A minimum pressure of 10-20 kPa (1-2 N/cm^2) [28] was held using epoxy coated round lead metal sheets (Figure 3-2).

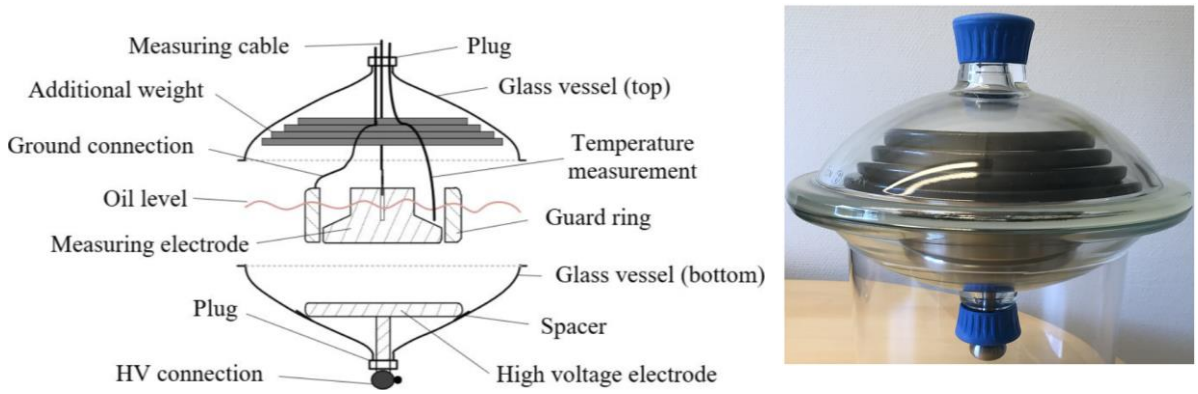

Figure 3-2. Electrode setup for high stress conductivity measurements under pressing metal sheets [28]

The setup was placed in a temperature chamber. Since the measuring system is very sensitive to the external electrical and mechanical noises, to stabilise the temperature of the chamber during the polarisation phase, a set of series-parallel connected high power resistors was used as a heating setup to keep a constant temperature of the chamber during the whole period of measurement (Figure 3-3).

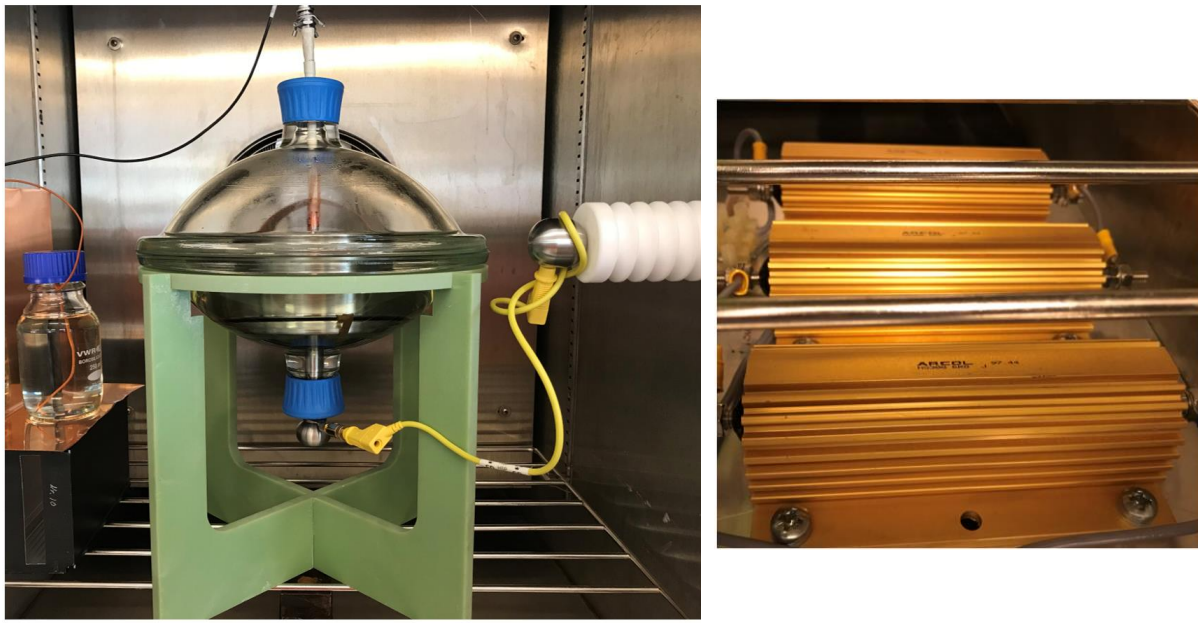

(a) *(b)*

Figure 3-3. Measurement vessel inside a temperature-controlled chamber connected to HV DC bushing (a), and temperature stabilising heating resistors (b)

3.1.1.1 *Current measuring and data acquisition system and its protection*

The current measuring circuit is as Figure 3-4 and similar to IEC 93, 1980 adopted for volume resistivity measurement.

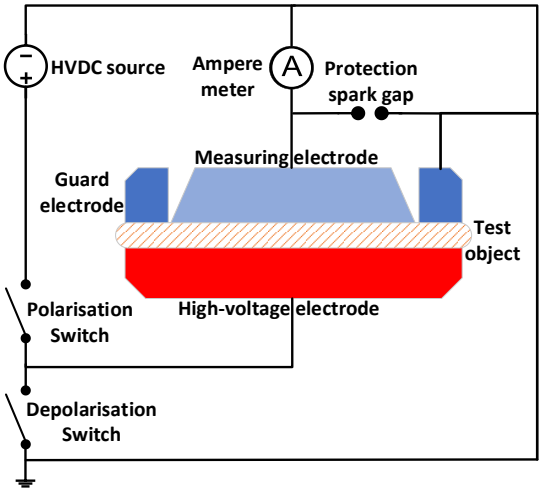

Figure 3-4. Conductivity measuring circuit diagram

The current measuring system consists of a Femto DLPCA-200 current amplifier having a current measuring range from 10 pA to 10 mA (Figure 3-5)and a Keysight 34470A Digital voltmeter.

Figure 3-5. FEMTO DLPCA-200 current amplifier

A Labview based control and data acquisition software is developed for automatic amplifier gain setting as well as recording of the measured data. All the test condition data have been entered via the interface before starting each measurement, and the measurement data file is automatically named and saved every minute.

The current measuring system should be protected against high applied voltage and high short circuit current. The protection against an input current higher than the maximum permissible 10mA of the Femto DLPCA-200 current amplifier, can usually be fixed using a high voltage high ohmic series resistance in the circuit. In this case it is done by setting the current limit of the high voltage DC power supply to a current lower than 10 mA and therefore no external current limiting series resistance is needed.

The protection against a possible high voltage transient has been done by a parallel connection of the following elements:

- A 2049-07 medium duty 2 electrode gas discharge tube having a 75 V DC sparkover@100 V/s
- Two parallel reverse-coupled 1N3595 small signal diodes with maximum reverse current of 1nA @150 V and a minimum forward voltage of 0.5 V
- A TransGuard multilayer ceramic transient voltage suppressor having minimum possible leakage current at the working voltage and a working voltage higher than the voltage at the input of Femto DLPCA-200 which is maximum 10 µA x 60 Ω = 0.6 mV. In this case a VC060314A300 is used.

The manufactured high voltage protection module is subjected to the maximum predicted input voltage of the current amplifier and the leakage current is measured using a precision source meter (Figure 3-6). The measured leakage current at 0.6 mV on the input, is less than 0.5 pA which is much less than the typical measured conductivity current of nearly 100 pA.

Figure 3-6. Test setup for verification of overvoltage protection system

Figure 3-7 demonstrates the current amplifier, voltage measuring device, test cell temperature meter, and a high voltage DC source with polarity reversing function.

Figure 3-7. Conductivity measurement setup inside a noise suppression cage

3.1.1.2 *High voltage application system and safety*

A Fug HCN 140M 0-35000 V High voltage DC power supply equipped with an adjustable current limiting system of 0-4 mA is used as a source. A low inductance ground connection has been prepared at the body of the high voltage DC source.

3.1.1.3 *Mitigation of noises*

A high voltage filter consisting of series resistors and parallel capacitors is connected to the delivery point of the high voltage DC to the chamber. The resistance is composed of ten 22 MΩ in series and the capacitance is combined of 6 series and 4 parallel capacitors. The selected parts were double metallized film pulse capacitors with a polypropylene dielectric PHE450 47 nF, 2000 V and Metal Glaze Film Resistors MGRF 22 MΩ, 2 W, 3500 V. Effort has been taken to avoid discharges because of low isolation distances and sharp high voltage conductors (Figure 3-8).

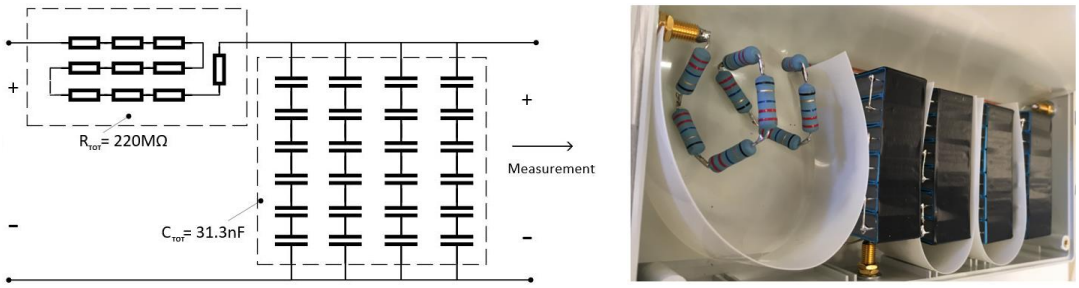

Figure 3-8. Designed and manufactured HV filter

The complete measuring setup is placed inside a grounded metal shielding box. The mains supply has been done using a 1:1 isolating transformer. The multi-meters and the current amplifier have been connected by a fibreoptic hub and cables to the computer.

3.1.2 Preparation and testing of samples

Oil samples and the oil in the container for testing pressboard samples were dried (down to 5 ppm) according to the method explained in [80]. A setup including a hot water bath (Figure 3-9a), a heating and vacuum chamber and a stainless-steel tray were used for this purpose (Figure 3-9b). The process, simply explained, is to warm up the oil to 80 °C, feed it into a vacuum chamber through a Swagelok severe-service union-bonnet needle valve, which is already warmed up to 80 °C, spread a thin layer of oil on the steel tray under a vacuum less than 1 mbar, collect the dried oil in the lower part of measuring vessel, turn off the heating and let the system cool down to room temperature. The vacuum level was constant during the whole process. This process takes minimum 72 hours.

(a) *(b)*

Figure 3-9. Dry oil preparation setup: A heating and vacuum chamber equipped inside with a steel tray for drying and collecting the dried oil (a), and the regulated hot water bath feeding the hot oil through a needle valve into a heating and vacuum chamber (b)

The mineral oil vapor-pressure curve [125] (Figure 3-10a) was used to adjust the temperature and vacuum level of the chamber for the most effective drying process of the samples. For example, applying 10 mbar and 60 °C will evaporate the water from a humid mineral transformer oil without evaporating the oil itself.

A Vaisala MM70 oil humidity meter was used to measure the humidity content of the oil samples (Figure 3-10b). The humidity content of the mineral oil before drying, before starting the conductivity tests and at the end of measurements were registered. The humidity content of the oil was checked after the processing, and it was found to be less than 5 ppm for the mineral oil and less than 30 ppm for the ester oil before the conductivity measurement tests were done.

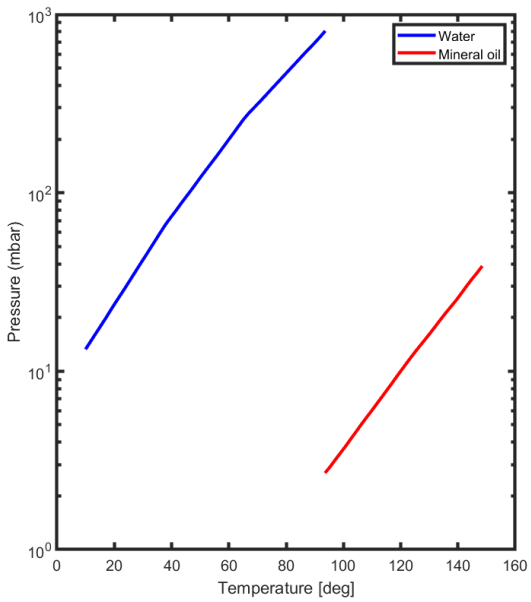

(a)

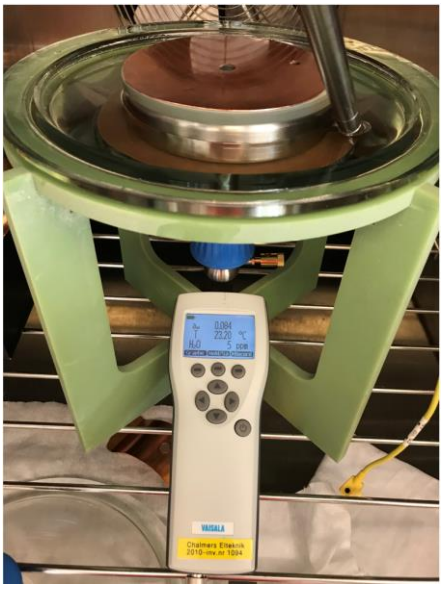

(b)

Figure 3-10. The vapor-pressure curve used and the humidity measuring equipment: the vapor-pressure curves to adjust temperature and vacuum during drying process (a), and the Vaisala meter showing the oil water-content after treatment (b)

The preparation of solid samples was done according to Section 20.3 of IEC60641-2. 2004 [126]. In this work, first the new and clean samples are placed with a 1 mm distance in the steel tray in the chamber. Later the temperature is increased to 80 °C and after stabilising the temperature, the objects is set under full vacuum for the next 72 hours. Finally, the same procedure as the one for the oil sample preparation was followed to impregnate the hot oil in the already dried cellulose solid insulations.

3.1.3 Conductivity measurement procedure

Each experiment was conducted by applying a high DC test voltage and recording the time variation of the current through the test object until it reached a steady state (polarization phase). Directly after, the test object was short-circuited for a time interval of at least twice of the polarization time, and the current was recorded again (depolarization phase). The process of a Polarisation, Depolarisation Current (PDC) measurement is demonstrated in Figure 2-15.

The conductivities were calculated in the range of the applied electric field of (1-6) kV/mm and (1-12) kV/mm for oil and OIP, respectively, and for a temperature range of (30-90) °C.

3.1.4 Conductivity measurement results

In this section, OIP refers to the cellulosic transformer board impregnated with the mineral or ester transformer oil. The tested mineral transformer oil is Nynas Nytro 10 XN and the ester transformer oil is Midel 7131 synthetic ester. The electrical permittivity values of mineral and ester oil and OIP are 2.2 & 4.4 and 3.5 & 4.6 respectively.

3.1.4.1 *Mineral oil and OIP*

Although in case of mineral oil, the conductivity data for high voltage DC applications are already given in literature [28, 124, 127, 128], the measurements have been done to support a reliable design of the measuring system.

Oil and OIP samples considered for the manufacturing of a prototype MFT were tested and the results are presented in Figure 3-11 and Figure 3-12 respectively.

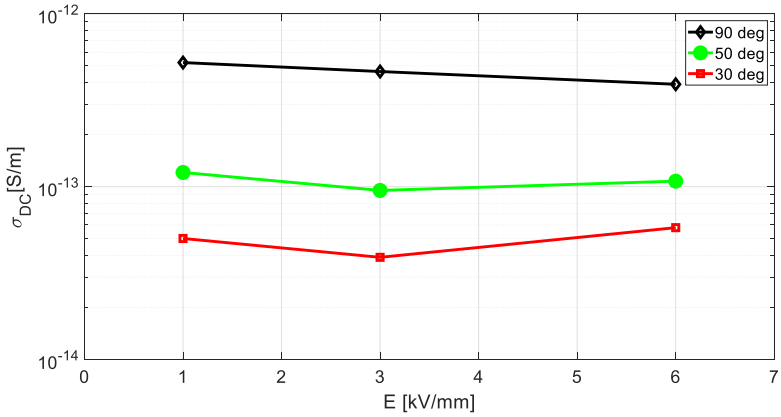

Figure 3-11. Conductivity measurement results of mineral oil

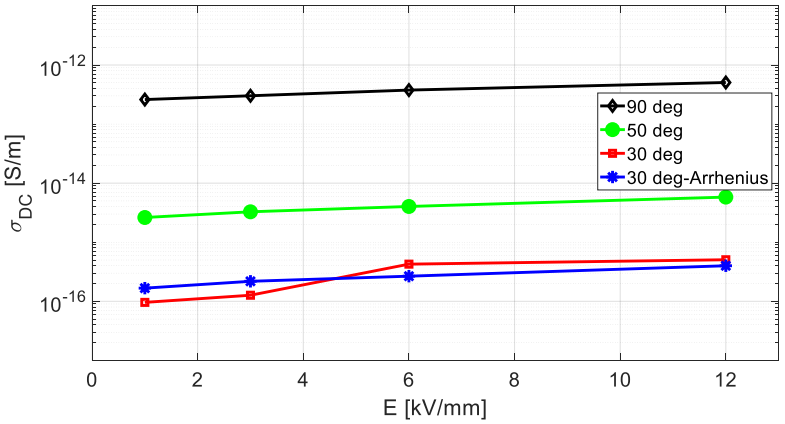

Figure 3-12. Conductivity measurement results of mineral OIP

The measured conductivity values, which are also summarized in Table 3-1, strongly depend on temperature, and a weak dependency to the electric stress can be observed as well. This reflects the impact of the thermal and electric stresses on the electro-chemical processes in the oil and on oil-pressboard interfaces, in particular charge injection and accumulation, ionic drift, recombination, etc. As explained in Section 2.2.9 these dependencies have an impact on the field dynamics in the insulation system and thus on the design of the HVDC MFT. The stress distribution on a simple series of insulation layers depends on the Conductivity Ratio (*CR*) of oil to OIP: $CR = \sigma_{Oil}/\sigma_{OIP}$. According to Table 3-1, the *CR* values have a large scatter ranging from 294 at 30 °C to 1 at 90 °C. The effect of *CR* on the electric field stress on the different points of the transformer will be discussed in Section 4.2.

Table 3-1. A summary of conductivity measurement results for mineral oil

		1 kV/mm	3 kV/mm	6 kV/mm	12 kV/mm
Oil	30 °C	5×10^{-14}	3.9×10^{-14}	5.8×10^{-14}	-
	50 °C	1.2×10^{-13}	9.5×10^{-14}	1.1×10^{-13}	-
	90 °C	5.2×10^{-13}	4.6×10^{-13}	3.9×10^{-13}	-
OIP	30 °C (Arrhenius)	1.7×10^{-16}	2.2×10^{-16}	2.7×10^{-16}	4×10^{-16}
	50 °C	2.6×10^{-15}	3.3×10^{-15}	4×10^{-15}	5.8×10^{-15}
	90 °C	2.6×10^{-13}	3×10^{-13}	3.8×10^{-13}	5.1×10^{-13}
CR	30 °C	294	177	215	-
	50 °C	46	29	27	-
	90 °C	2	1.5	1	-

The results have a good correspondence with one of the most reliable results presented by Küchler [124].

3.1.4.2 *Ester oil and OIP*

After a complete set of conductivity measurements on mineral oil and OIP which provided a series of results which are comparable with the previous literature, the method is applied to characterize the biodegradable synthetic ester oil under HVDC stress.

The preliminary measurements showed unstable and varying results for the polarisation current of ester oil. Therefore, to get stable current curves, it is decided that a conditioning is to be performed on the ester oil. In addition, the polarization time is increased from 1h (as was the case for mineral oil) to 3h for the ester oil. To reach repeatable results it is also decided to perform a set of conditioning stress applications before each measurement [73]. In case of ester OIP it is performed like the measuring method for mineral OIP, and a 3-hour measurement is performed. Figure 3-13 and Figure 3-14 demonstrate the test duration for ester oil and ester OIP respectively.

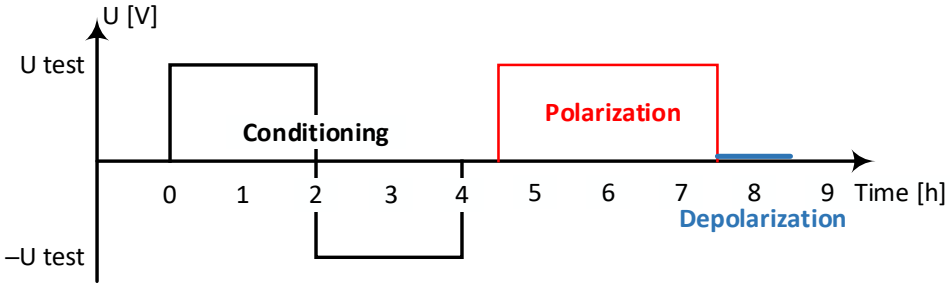

Figure 3-13. Measurement technique for ester oil

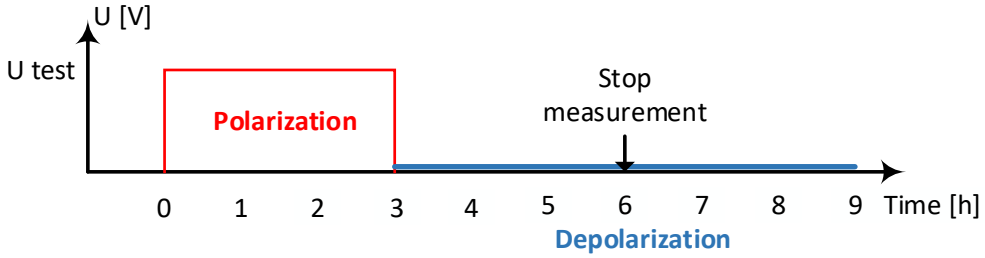

Figure 3-14. Measurement technique for ester OIP

For the ester OIP, the measurements at 30 °C showed that the depolarisation takes a longer time than expected. Therefore, the measurements were performed for a minimum of three hours during depolarisation (Figure 3-15).

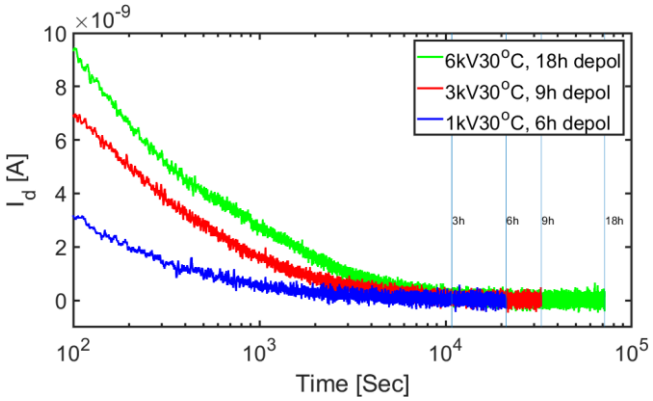

Figure 3-15. The minimum depolarisation time required at 30°C

A summary of measurements done on the ester oil is presented in Figure 3-16.

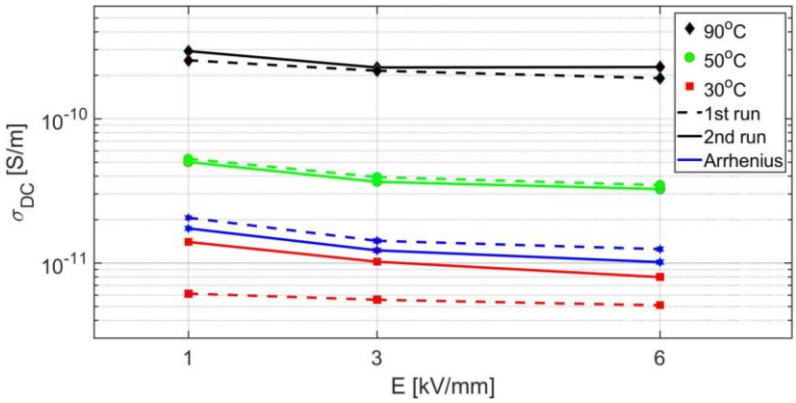

Figure 3-16. A summary of conductivity measurements of ester oil

The ester OIP measurements are presented in Figure 3-17.

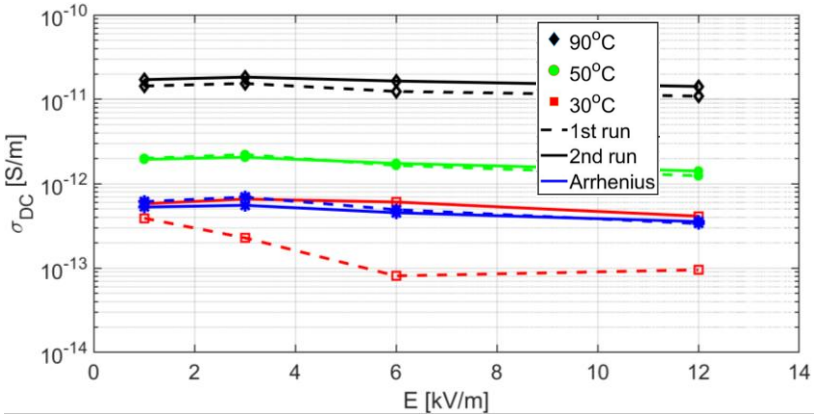

Figure 3-17. A summary of conductivity measurements of ester OIP

For both ester oil and OIP, the results show that, the conductivity values of the second run measured at 30 °C have good agreement with the Arrhenius calculations. For the first run, as the results of 50 and 90 °C were available, the Arrhenius method can be applied to determine the values of conductivity at 30 °C. The measured values on the first 30 °C run is not correct, and the results of the second run are reliable.

A summary of conductivity measurement results for ester oil and OIP is presented in Table 3-2. The results of the second series of ester OIP measurements together with the results of the first series of ester OIP measurements (with using Arrhenius results for 30 °C) can be preliminary used for the insulation design of an HVDC ester MFT prototype.

Table 3-2. A SUMMRY OF CONDUCTIVITY MEAUREMENT RESULTS for ester oil

		1 kV/mm	3 kV/mm	6 kV/mm	12 kV/mm
Oil	30 °C	1.4×10^{-11}	1.0×10^{-11}	0.8×10^{-12}	-
	50 °C	5.0×10^{-11}	3.6×10^{-11}	3.2×10^{-11}	-
	90 °C	2.9×10^{-10}	2.3×10^{-10}	2.3×10^{-10}	-
OIP	30 °C (Arrhenius)	6.1×10^{-13}	6.9×10^{-13}	4.9×10^{-13}	3.4×10^{-13}
	50 °C	2.0×10^{-12}	2.22×10^{-12}	1.6×10^{-12}	1.2×10^{-12}
	90 °C	1.4×10^{-11}	1.5×10^{-11}	1.2×10^{-11}	1.1×10^{-11}
CR	30 °C	23	15	16	-
	50 °C	25	16	20	-
	90 °C	20	15	18	-

Limited information about the conductivity of biodegradable ester oil under HVDC stress is accessible [72, 129] and in case of ester OIP there is even less information available [73]. Figure 3-18 demonstrates comparisons between the ester oil measurement results of this work with the measurements presented in literature.

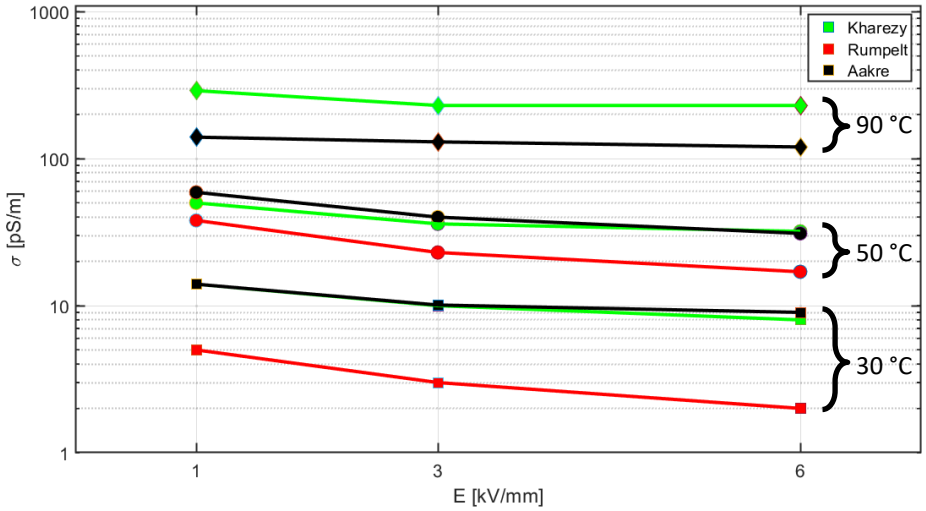

Figure 3-18. A comparison of measurement results of the conductivity of ester oil with the values given in literature; green: Kharezy, red: Rumpelt [129] and black: Aakre [72])

3.1.4.3 *Mineral oil/OIP versus ester oil/OIP*

Figure 3-19 is provided for the purpose of comparison of the measurement results on the mineral and ester oil and OIP.

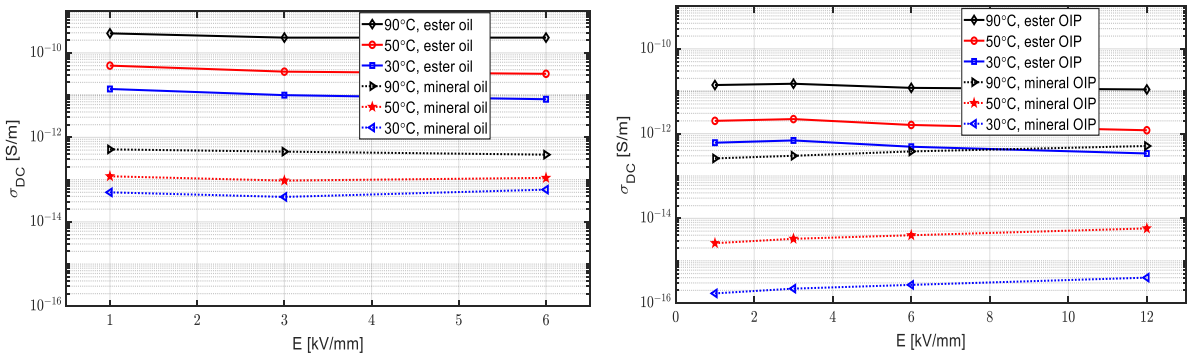

Figure 3-19. Comparison of the measurement results on the mineral and ester oil and OIP

The most important difference in the results is the higher values of conductivity for the ester oil. It is at 30 °C, 100-130 times, at 50 °C, 320-430 times and at 90 °C, 450-480 times higher.

In mineral OIP the moisture increased from 5 ppm to 16 ppm, and in ester OIP the increase level was from 46 ppm to 225 ppm. It seems that the ester OIP can absorb more water without significantly increase the conductivity values.

A simple comparison of the conductivity values of ester and mineral oil and OIP highlights that the *CR* values of ester oil/OIP are not as much temperature and voltage stress dependent as the mineral oil/OIP is. This reduces the dynamic stress level of the design in case of using ester oil and OIP. It is also noticeable that the ester oil/OIP conductivities are several hundred times higher than the mineral oil/OIP conductivities. This causes the time constants to be lower (Section 4.2) and consequently results in a shorter time for the transformer to reach the steady state condition (Figure 3-20b). The space charge accumulation time is much lower in the case of ester oil (Figure 3-20d).

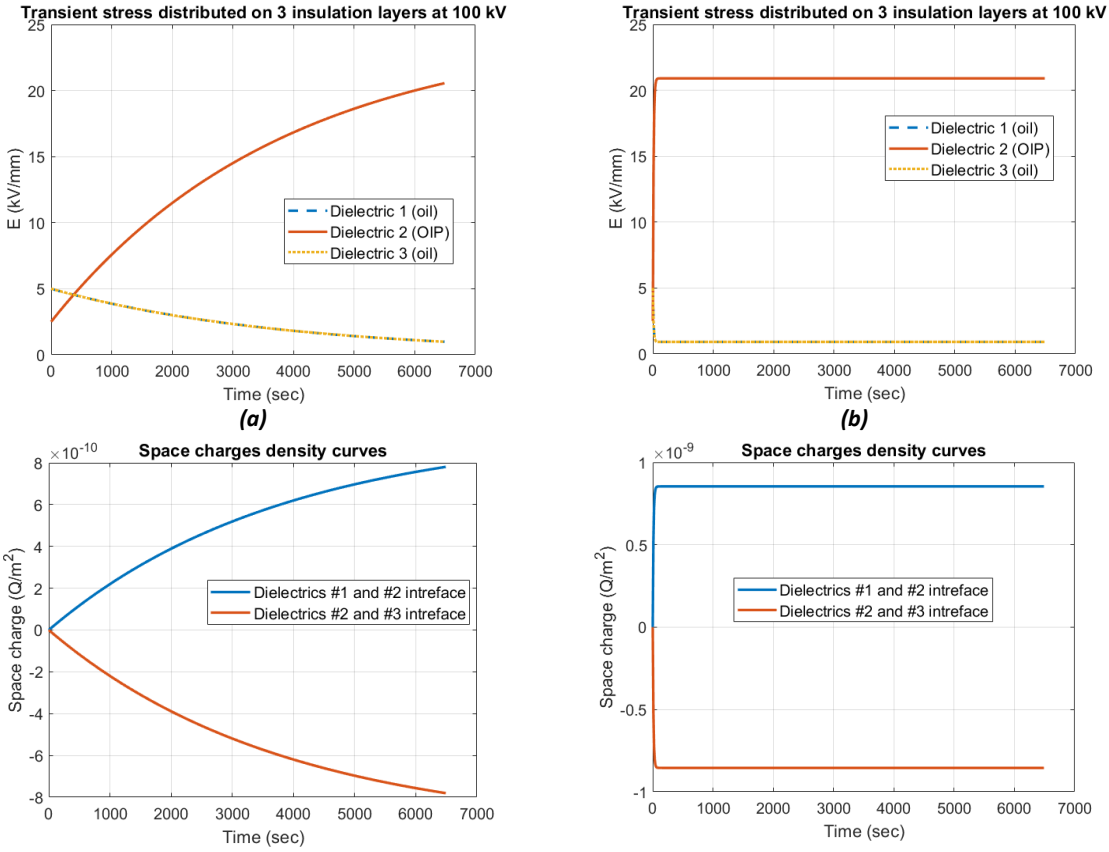

Mineral oil ($\sigma = 5\times10^{-14}$) and OIP ($\sigma = 1.7\times10^{-16}$) ***Ester oil ($\sigma = 1.4e^{-11}$) and OIP ($\sigma = 6.1e^{-13}$)***

Figure 3-20. Space charge accumulation curve in a three-layer, oil-OIP-oil insulation system at 30 °C and 1 kV/mm

3.2 AC breakdown simulations and test conditions

Based on the background information presented in Section 2.7 the following activities were performed in this work.

3.2.1 Effect of shape of electrodes and surrounding medium to the results of the tests

Application of an electric field should not be done in such a way that any other phenomena disturb the main purpose of the voltage application. The intention is to simulate the actual electric field only inside the insulation as it will happen during a real application of the insulation material. Any discharge on the surface of the material can create heat and gas bubbles which in turn destroys the material and the electric field distribution inside it. IEC 60243-1 has proposed the use of specially shaped electrodes for testing of electric strength of tapes (Figure 3-21).

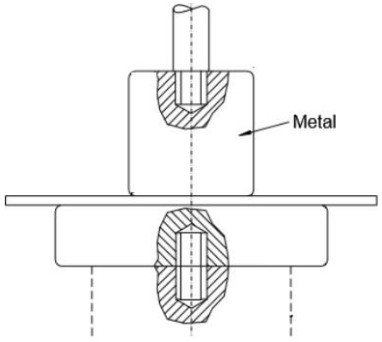

Figure 3-21. IEC 60243-1, proposed electrode setup [121]

Figure 3-22 demonstrates a FEM simulation of the IEC proposed electrode pairs stressed by 100 kV to ground for testing a 1 mm layer of insulation tape (Polyamide Kapton, ε_r = 7.0) in air. There will be a very high electric field in the air, 757 kV/mm for this example which will lead to an extensive corona discharge around the electrode. The discharge can destroy the material at the edges and a puncture or flashover can happen outside the electrode area instead of in the middle.

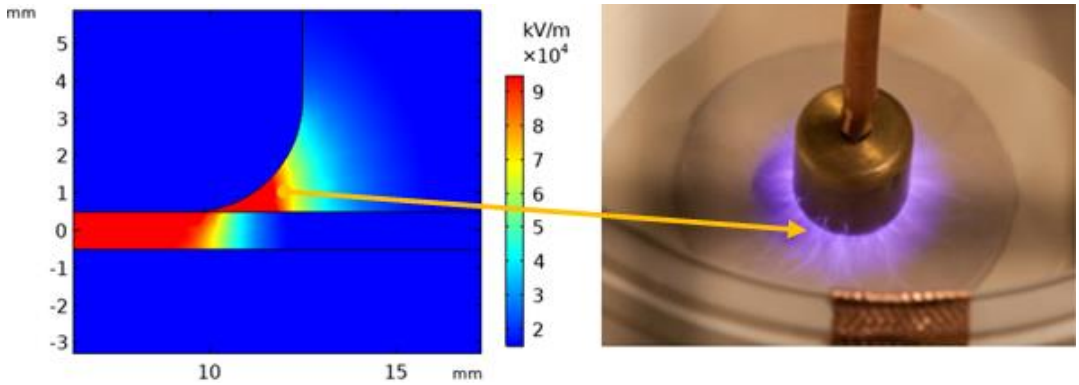

Figure 3-22. The effect of improper surrounding insulation material on the unwanted external discharges on the surface of the insulation material under test

Depending on the relative permittivity of the materials [77], the electrical field in the medium around a solid insulation material under a test can be higher than the electrical field within the test object. This causes surface discharge and partial discharges near the test object (Figure 3-22) which deteriorates the material around the electrode corners and can affect the breakdown voltage of the test setup [130]. During application of voltage, by placing the sample inside a suitable oil as a surrounding medium, depending on the strength of the dielectrics, there will be no external discharge at the edges of the electrodes, and an ACBD will happen inside the insulation material any discharge over the surface of the sample will be avoided.

Mineral transformer oil (IEC 60296), organic ester fluid (IEC 61099) and silicone fluid (IEC 60836) is proposed in IEC 60243-1 among the other suitable fluids [121] as a selection for surrounding medium.

3.2.2 High frequency strength tests on the litz wire

In this section the withstand tests on the Polysol 155 litz wire [106] used in this project is explained. An IGBT full bridge converter is used to supply the square wave voltage. The highest voltage available from the source was ±350 $V_{Peak\text{-}Peak}$. Figure 3-23 demonstrates the circuit diagram and specification of the converter.

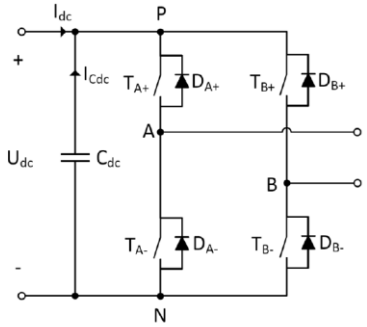

Component	#	Type	Rating
IGBT module	2	Semikron SKM 145GB066D, half-bridge	150 A, 600 V dc
Dc-link	2	1 mm copper plates	500 V dc
	2	1 mm plastic insulation	
Capacitors	2	EPCOS B43456A9688M,	6.8 mF, 400 V dc
	3	Vishay MKP1848622454P4	22 µF, 450 V dc
	2	WIMA MKP101G041006D	1 µF, 400 V dc
Gate driver	2	SKHI 23/17R, half bridge	1700 V dc
Heat sink	1	Semikron KL 285 P3 300 mm	
Control interface	2	Texas Instruments UCC275524	15 V dc

Figure 3-23. IGBT full bridge converter for production of square waves

Some points should be explained here:

- The ratio of step-up transformer is checked using an audio amplifier in the range of 50 Hz to 5 kHz. The measurement shows that the transformer has nearly the same ratio at this frequency range. If the applied voltage is a square wave signal it contains higher orders of voltage harmonics and the output voltage will not be a square wave signal but possibly more towards a voltage of near sinusoidal shape.
- The high voltage divider used should have a wide frequency range to truly transfer the wave shape at the high voltage primary to the scope's input.
- To do the insulation tests, it is not enough to have a high voltage source but there should be a current limiting facility to protect the converter every time the short circuit happens in the insulation material. The SKHI 23/12 (R) drive circuit for IGBTs is selected to have a short circuit turn-off protection by V_{CE} monitoring.

The following equipment was used in the test setup:

- IGBT full bridge converter, 10 kW, DC link 350 V, maximum switching frequency 45 kHz
- HILO-test, HVT 240 R/CR wide frequency band (7.3 MHz), high voltage divider Ratio 12440:1
- Step-up transformer: 600 V/22 kV, 333/9.1 A
- Pico, TA044, 70 MHz High-voltage differential probe

The circuit diagram for the 5 kHz insulation tests is presented in Figure 3-24 and the setup in Figure 3-25.

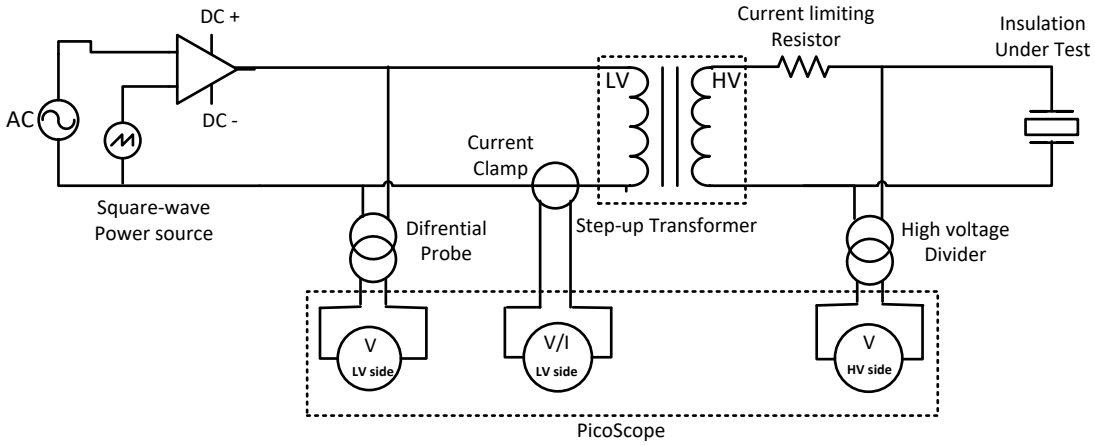

Figure 3-24. Circuit diagram for the 5 kHz insulation tests

Figure 3-25. IGBT full bridge converter, step-up high voltage transformer and high voltage wide band voltage divider

The test samples were prepared considering precautions given in IEC 60851-5 [119]. For each sample, two 400 mm wire strands are twisted 33 times. A load of 0.85 N was applied during the twisting of the

pairs. The rate of voltage increase was 100 V/sec. At least 5 test specimens were tested. Figure 3-26 shows the prepared samples according to precautions of IEC 60851-5.

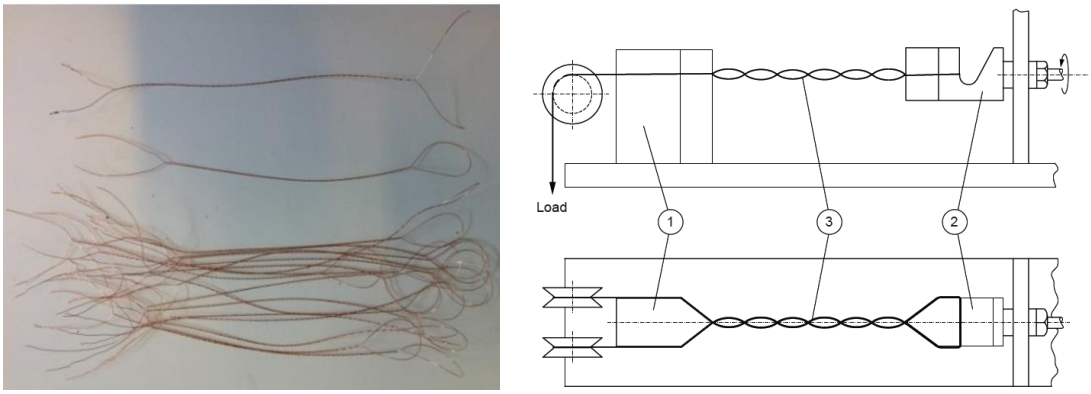

Figure 3-26. Insulated wire samples prepared according to precautions of IEC 60851-5

Elektrisola's typical value for 0.25 mm litz wire is 180 V/µm and no standard (IEC 60851-5 for example) is mentioned in the product specification. The producer has stated 2.5-3.0 kV as the breakdown voltage of the wire to ground. This can be interpreted as nearly 5 kV/ wire-wire insulation. The results of three types of the performed tests are presented in Table 3-3.

Table 3-3. Comparison of breakdown voltage (kV) at different frequencies on twisted strands of litz wires

DC	50 Hz r.m.s. sinus	5 kHz r.m.s. sinus
5.8	**3.3**	**1.1**

Compared with the value presented in the material's datasheet the following results can be presented:

- Nearly 5.8/5.0 = **1.2** times **higher** breakdown voltage for **DC**
- Nearly 5/3.3 = **1.5** times **lower** breakdown voltage for **50 Hz**
- Nearly 5/1.1 = **4.6** times **lower** breakdown voltage for **5 kHz** sinus wave form

The tests with 5 kHz square wave voltage can show much lower breakdown voltage results. It is shown in Table 3-3 how an increase of the frequency from 50 Hz to 5 kHz causes the withstand ability of the insulation material to be reduced from 5.8 KV under a DC excitation to 1.1 kV under a 5 kHz stress. The frequency spectrum of a square wave signal contains frequencies which are much higher than 5kHz. As explained in this section, the higher the frequency, the higher the stress on the insulation material (This is a subject of future research.).

The rate of voltage increase, and the time of application of a fixed voltage before reaching the breakdown voltage will affect the final recorded voltage at the time of breakdown. Partial discharge starts at a lower voltage level than the breakdown voltage. The corona sound was clearly noticeable even where the voltage was one third of the breakdown voltage. The discharge destroys the wires' insulation in the long run. Many efforts have been done to produce corona resistive motor winding wires [131], however corona resistivity does not mean corona free. The lifetime will be reduced anyhow. It is suggested to measure the partial discharge inception voltage for the actual conductor-insulation-ground physical combination. Insulation system models should be based on transformer design and the actual ambient condition. PD inception levels should be measured, and the transformer insulation design should be based on critical voltage obtained from the experiment. The designed transformer should not experience partial discharge at its rated operating condition.

To demonstrate the effect of application of a standard method (IEC 60851-5) compared with a simulated test procedure (presented earlier), a second series of tests were performed.

The samples were 25 cm long twisted litz wires. The voltage is applied between two bunches of twisted wires. The results are summarized in Table 3-4.

Table 3-4. Comparison of breakdown voltage (kV) at different frequencies on 25 cm of twisted litz wires

	DC	50 Hz sinus	5 kHz sinus
Maximum	4.1	2.0	0.92
Minimum	1.6	0.4	0.89
Average	2.9	0.8	0.90

Both series of results, obtained from a standard test and a simulated test, show that in a typical prototype transformer, the breakdown voltage can be several times lower than the figure presented in the material's technical specification. Therefore, it is suggested to do insulation tests on the simulated conductor-insulation-ground test setups, before attempting to start designing prototype transformers. The lower breakdown voltages of the simulated test can be described by a bigger contact area between two wires and a tighter contact which can lead to higher PD activity and consequently more destruction of the insulation layers covering the conductors.

4 Prototype HVDC MFT

At least one prototype is needed for making this work complete and prove the concept. Info regarding manufacturing an oil-paper type transformer suitable for high DC offset voltage in this size without any HVDC bushing is missing in available literature. As, the main research question in this project is to investigate reliable design aspects for a high HVDC insulation to ground of an industrial scale transformer, a prototype academic experimental transformer is designed and manufactured using off-the-shelf materials and in-house equipment. Verification tests are performed on it and the results are compared with the theory and simulations.

4.1 Prototype basic design

For the prototype transformer the design inputs of 50 kW, 0.4/5 kV, 5 kHz and with the HVDC insulation to ground of 125 kV are selected.

To have the best isolation possibility and avoiding sharp edges which are the weakest points to withstand high voltages, a circular design is selected. This design in addition, provides a better condition for the cooling of active part. The low voltage winding is very near to the central legs of cores and the HV winding is placed nearly at the same clearance from the LV winding and the grounded cores (Figure 4-1).

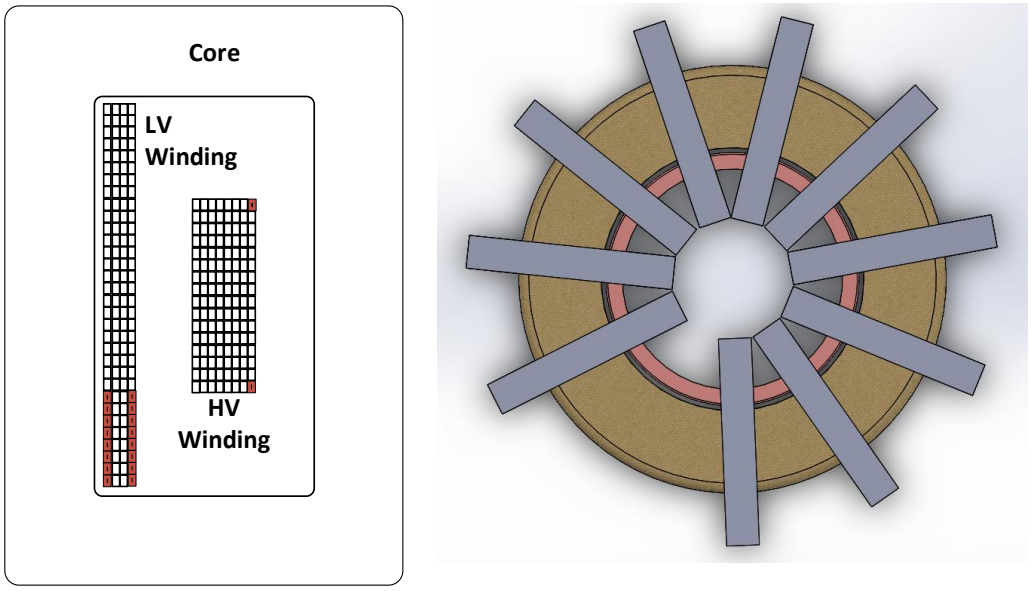

Figure 4-1. Protype transformer's basic design: the Core window (a), and the cores arrangement (b)

The transformer design starts with having the following basic design input:

- Output power, P_{out} = 50 kW
  - (The same as the two previous prototypes and adopted to the available California Instrument 4500LX AC, 50 kW, 5 kHz, 150/300 V single/three phase PWM converter)
- Voltage ratio, V_{LV}/V_{HV} = 0.42/4.5 kV
  - (The primary voltage adopted to the DAB bridge that will be available to connect the prototype transformer to it and the secondary voltage as an integer multiple of the primary voltage)
- Switching frequency, f = 5 kHz

- (According to [98] the highest power density of samples of medium frequency transformers are achieved at a frequency between 10-25 kHz. As the available California Instrument 4500LX source can only reach 5 kHz, this frequency is selected for the prototype transformer design)

- Duty cycle D = 0.5 and relative rise time R = 0
  - (Figure 2-1a)
- Isolation Level, V_{iso} = 125 kV DC
  - (The high voltage or secondary winding side DC insulation to ground)

The following design was used from the basic design idea using the equations earlier mentioned in Section 2.3):

- Rated primary current, I_{T1} (r.m.s.) = 50 kW / 421.8 V = 118.5 A
- Rated secondary current, I_{T2} (r.m.s.) = 50 kW / 4500 V = 11.11 A
- Maximum allowed current density, J_{max} = 3 A/mm^2
  - (According to the litz wire manufacturer's datasheet for operation at 95°C)
- Number of turns, N_1 and N_2 = 12 and 128
  - (As shown in Figure 4-3 the voltage difference between two adjacent discs of the high voltage winding will in this way be 4.5 kV/128 x 16 = 560 V which is less than 0.9 kV and safe enough according to the experimental verification tests presented in Section 3.2.2)
- The magnetic core cross section, from (2-32) calculated as 5493 mm^2 for Ferrite where
    - V_{rms1} is the rated voltage of the winding = 421.8 V
    - K_c is the core filling factor ≈ 1 for Ferrite
  - (k_c is the core filling factor or the ratio of effective to physical cross sections)
    - N_1 is the number of turns of the primary winding = 12
    - B_m is the maximum working flux density of the core ≈ 0.32 T for Ferrite
  - (≈ 80% of the saturation flux density [104])
    - f is the switching frequency = 5 kHz
- A core is selected having a core window of the highest dimensions achievable. The commercially available sample Epcos TDK type B67385U 126/91/20 (Figure 4-2) is selected which has 20 x 28 = 560 mm^2 as physical core area. This means that 10 core stacks including 20 U cores is suitable for the design. The maximum working flux density of the core will be 0.314 T.

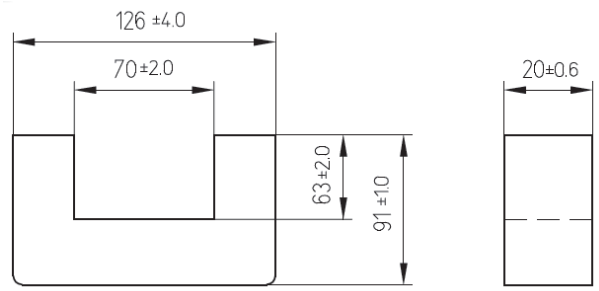

Figure 4-2. Dimensions of an Off the shelf Ferrite core which is used for HVDC MFT prototype

- For the primary winding, considering 118.5 A as rated r.m.s. current, the space that the primary winding occupy in the core window will have a height of h_{w1} = 3.8 (h_{b1}) x 8 (n_{p1}) x 4 (N_{l1}+1) = 121.6 mm (Layer type winding using the litz wire introduced in Section 2.6.2.1) and the width of W_1 = 2.5 (w_{b1}) x 4 (m_1) = 10 mm where h_{w1} is the primary winding height, h_{b1} is the litz wire

height used for the primary winding, n_{p1} is the number of parallel litz wires of the primary winding, N_{l1} is the number of the litz wires per layer of the primary winding, W_1 is the width of the primary winding, w_{b1} is the litz wire width and m_1 is the number of layers of the primary winding (Figure 4-3). Note that the ideal magnetic height of the winding will be 3.8 (h_{b1}) x 8 (n_{p1}) x 3 (N_{l1}) = 91.2 mm. From the manufacturer's datasheet for the 181 x 0.2 mm litz wire, the maximum current density is 3 A/mm^2. In this project a 30.4 x 2.5 mm^2 primary winding wire, having a filling factor 0.6 was used, resulting in a 118.5 A current corresponding to 2.6 A/mm^2.

- For the secondary winding, considering 11.11 A as rated r.m.s. current, 3 A/mm^2 as maximum current density and 0.6 as filling factor of the litz wire, the space that the secondary winding occupy in the core window will have a height of h_{w2} = 3.8 (h_{b2}) x 16 (N_{l2}) = 60.8 mm (Disc type winding) and the width of W_2 = 2.5 (w_{b2}) x 8 (m_2) = 20 mm where h_{w2} is the secondary winding height, h_{b2} is the litz wire height used for the secondary winding ,N_{l2} is the number of litz wires per layer of the secondary winding, W_2 is the width of the secondary winding, w_{b2} is the litz wire width and m_2 is the number of layers of the secondary winding (see Figure 4-3). In this project a 3.8 x 2.5 mm^2 secondary winding wire, having a filling factor 0.6 was used, resulting in a 11.1 A current corresponding to 1.95 A/mm^2.
-

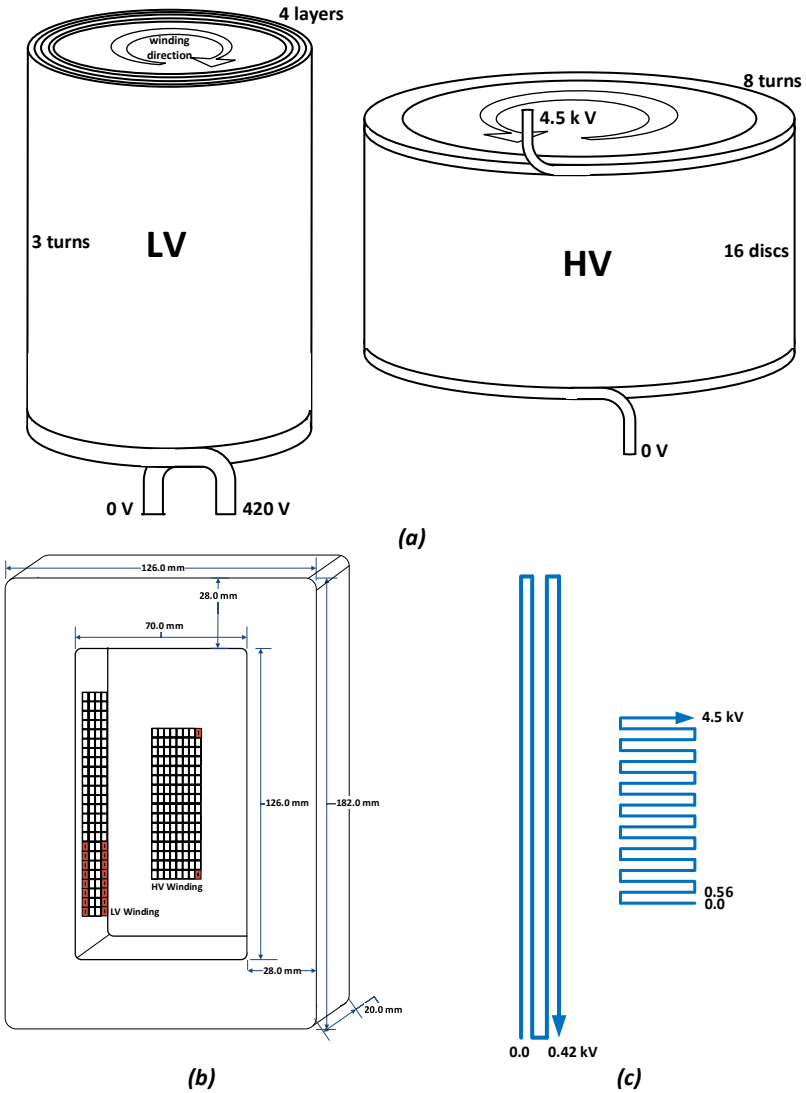

Figure 4-3. Windings in the core window and their connection type: the windings' directions (a), the position of the windings in the core window (b), and the connection type of the windings (c)

Before continuing with the other important magnetic design aspects which will be discussed from Section 4.3, it is necessary to be sure that the insulation of the transformer is safely designed to withstand a predetermined HVDC stress between the HV winding and the other conducting parts of the active part.

4.2 Prototype insulation design

The insulation design is mainly focused on the isolation of the high voltage (secondary) winding in the 70 x 12 mm^2 core window. The core is grounded, and the LV (primary) winding will be stressed only with 0.4 kV to ground which can be assumed as grounded focusing on the very high 125 kV DC which is going to be applied to the HV winding. The transformer tank is made of a plastic cylinder which has a suitable electrical insulation property. Therefore, considering the windings' dimensions in the core window, the main task is to check if the winding-core clearance is enough to fulfil the DC insulation criteria if a step of 125 kV DC voltage is applied.

A Non-Linear Maxwell-Wagner (NLMW) model is adopted for the MFT insulation design, which accounts for (at least) field and temperature dependencies of the electric conductivity of the constituting materials.

The 50 kW MFT operates at biased 422/4500 V AC (5 kHz) and 125 kV DC voltages as mentioned earlier in the introduction to the Chapter 4. Because of the availability of high quality mineral oil with a trustable data sheet in the market, the insulation system is built based on mineral transformer oil and Oil-Impregnated Pressboard (OIP) to fulfil the requirement of high DC voltage isolation to ground and a stabilized temperature condition.

To minimize the number of sharp corners and to provide a better heat transfer between the windings and the core stacks, a polygonal design is considered (Figure 4-4) instead of the previously used planar designs [13]. This structure allows for installing OIP barriers to achieve a high voltage withstand level in a minimum space. Justifications of the OIP thickness and oil gaps widths were performed by considering the withstand levels of the overall dielectric structure obtained from the FEM simulation. Precautions were made to achieve oil gaps of the same size to let a smooth flow of cooling oil through the entire insulation system.

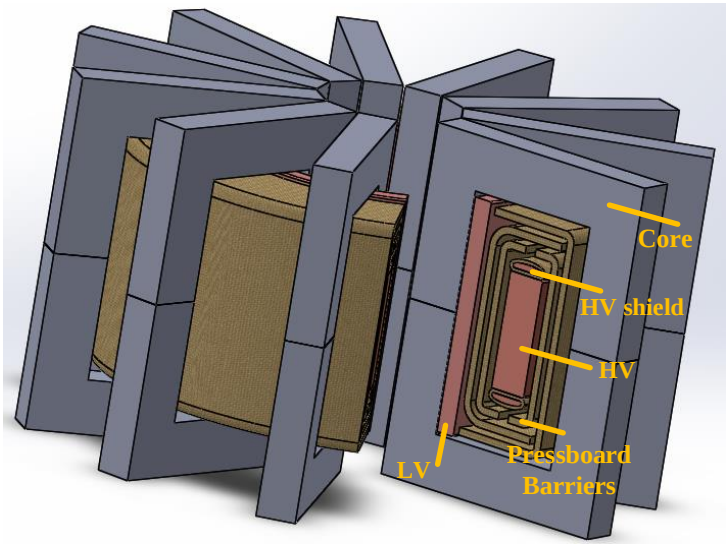

Figure 4-4. Polygonal transformer design

The NLMW model outlined in Section 2.2.10.4 was utilized to estimate the withstand levels of the insulation system of the MFT prototype. The transformer geometry including its insulation system was implemented in COMSOL Multiphysics (LiveLink to MATLAB was used). Three different sets of simulations were provided for 30, 50 and 90 °C, respectively. At each temperature, the related measured stress-dependent conductivities of the oil and OIP, presented in Section 3.1.4, were implemented in COMSOL as a local table. A piece wise cubic interpolation was selected to create a conductivity function with electric field as the independent variable, and in this way the NLMW model was established.

The calculations were performed assuming axisymmetric conditions that is rather close to the case when a single section of the core is considered. Time domain analysis was implemented to find the stresses at different time steps starting from the instant of applying a step DC voltage (1 s) to the final steady state (at 10^4 seconds). Figure 4-5 demonstrates the potential distribution and electric field on the insulation materials for the moment of application of voltage and after a long time.

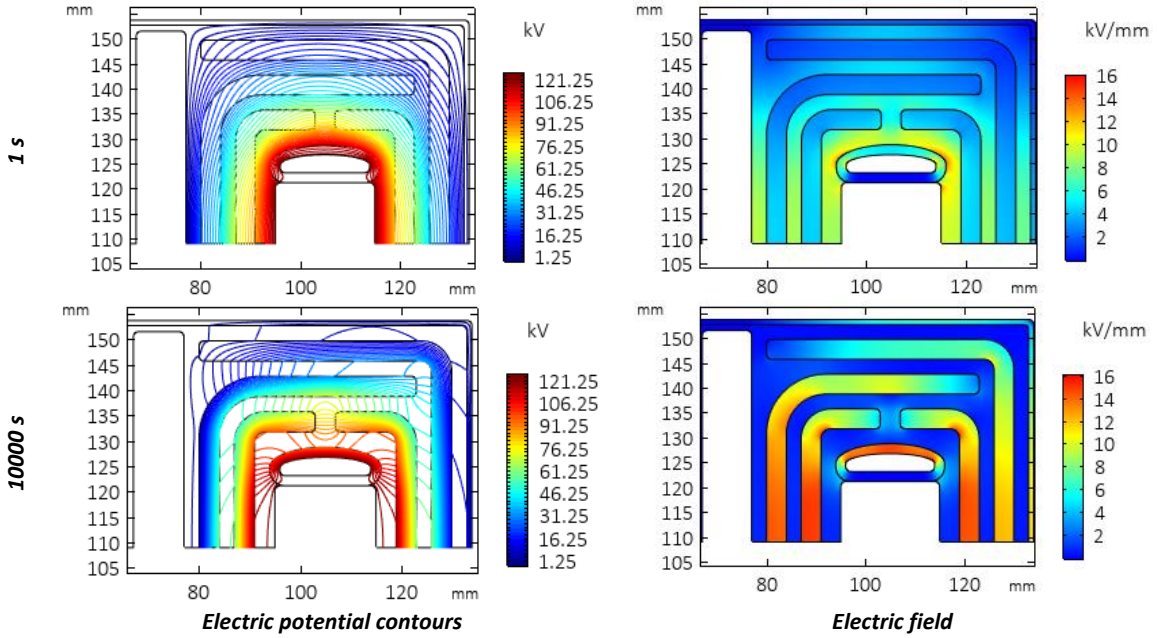

Figure 4-5. Electric potential and field distribution at 1 and 10000 seconds in the oil/OIP system

As an example, the electric field distributions in the cross-section of the winding at 50 °C at 1, 60 and 3600 seconds are shown in Figure 4-6. As expected, the results clearly indicate the high stress in the oil gaps at 1 s, which is gradually transferred to the OIP with time (compare with the plot for 1 hour).

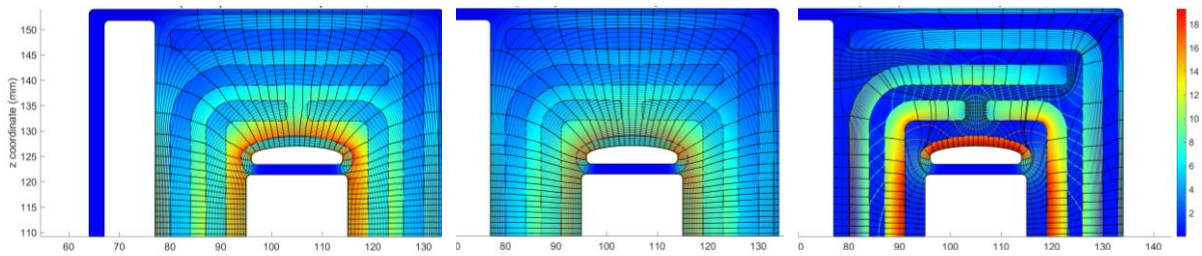

(a) One second ***(b) One minute*** ***(c) One hour***

Figure 4-6. Time domain analysis, electrical stresses at discrete time steps applying a step DC voltage. Surface: Electric field norm (kV/mm), Counter: Electric field potential, Streamline: Electric field

The time variation of the field strength at two points at the corner of the HV shield (one in the OIP and the other in the adjacent oil gap) is shown in Figure 4-7. The stress at the point in the OIP, has decreased after experiencing a clear maximum at about 950 seconds. Similar analysis of the electrical stress in the oil gaps, OIP barriers and along creepage paths has been performed.

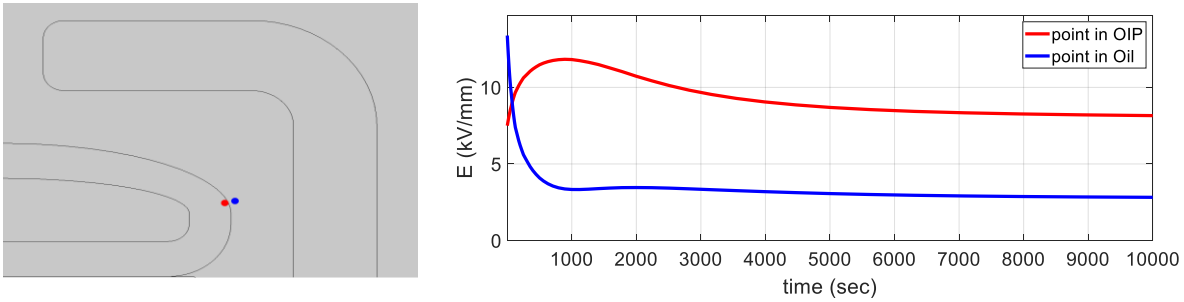

Figure 4-7. The time variation of the field strength at two points at the corner of the HV shield

The dynamic behaviour is characterized by the time constants $\tau_{Oil} = \varepsilon_{Oil}/\sigma_{Oil}$ and $\tau_{OIP} = \varepsilon_{OIP}/\sigma_{OIP}$. The relative dielectric permittivity of the materials can be assumed to be constant at the operational conditions of the transformer and equal to typical values of 2.2 and 4.4 for oil and OIP, respectively [78]. In contrast, the electric conductivities depend on temperature and electric stress as demonstrated in this work. According to Table 3-1, to cover all possible combinations of oil and OIP conductivity ratios, three different conditions were considered, namely, *CR* = 294 for 30 °C, *CR* = 29 for 50 °C, *CR* = 1 for 90 °C.

Seven different critical points were selected to represent the time dependent stress under these three conditions (Figure 4-8).

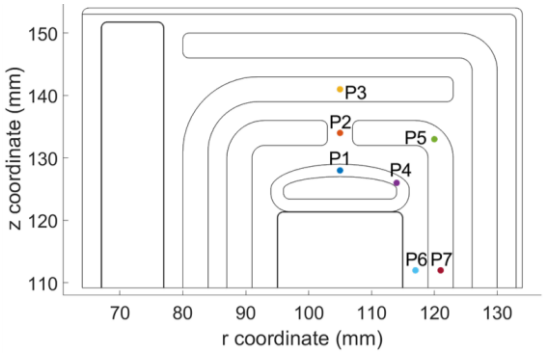

Figure 4-8. The geometry of the transformer and the points in which the electric field are obtained

As shown in Figure 4-9, the time to reach steady state at 30 °C with *CR* = 294 is about 10^5 seconds which is much longer than the stabilization time for 50 °C with *CR* = 29. Meanwhile, the time for 90 °C with *CR* = 1 is very short. In addition, a double exponential curve with a clear maximum occurs for both P1 and P4, which reveals that considering only the initial and final stress distribution is not enough for a practical insulation design method and such local maximus must be investigated carefully and limited by a design change as much as possible. The stresses on P6 and P7 at the lateral side of the HV winding indicate the stabilizing time of about 10^4 seconds for 30 and 50 °C. However, this time span is much longer than the 300 second value found for 90 °C. A single exponential stress variation can be observed for both locations.

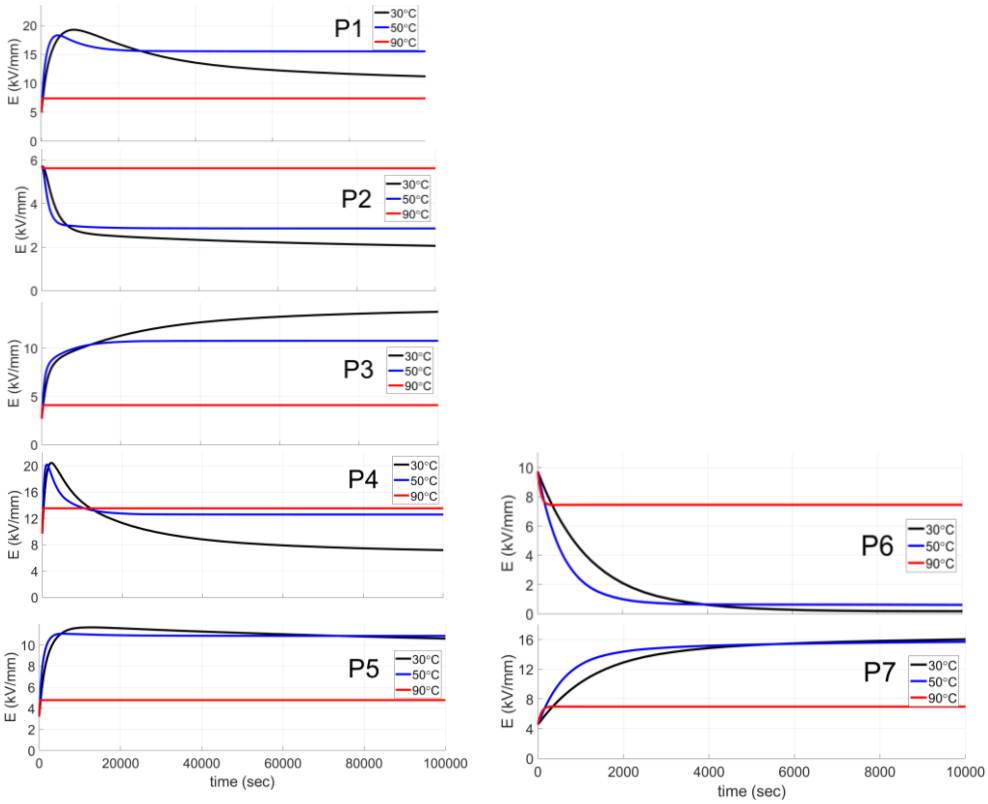

Figure 4-9. The electric field at P1 to P7 at different temperatures

4.2.1 Oil gaps and OIP barriers design

To identify the safety factor for each oil gap as well as the maximum stress at each OIP barrier, electric field streamlines originating from the points with the highest electric field in the transformer were utilized (Figure 4-10a). The field strength was obtained for every single streamline on each time step. Based on the streamline shown in Figure 4-10a by a thick red line, the field strength along the streamline is shown in Figure 4-10b. The variations of the values of E_{bd}, E_{sorted} *and* E_{av} are presented in Figure 4-10c. Further, the safety factors for the oil gaps were calculated using (2-2) to (2-4) and the SF curves of the oil gaps and presented in Figure 4-10d.

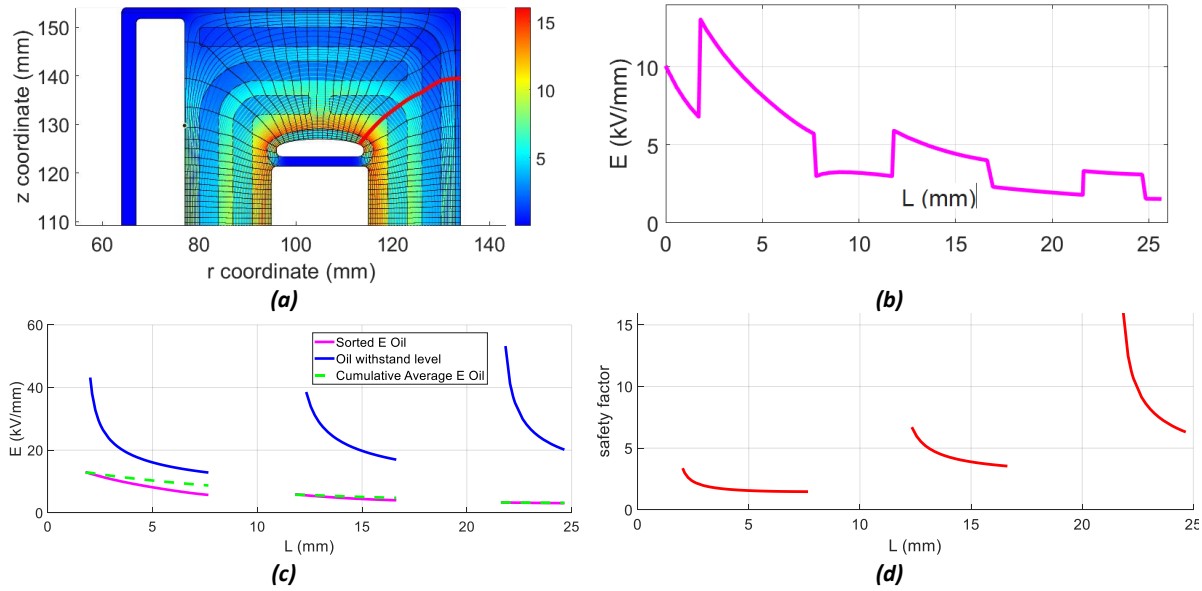

Figure 4-10. A sample simulation at 125 kV, 50°C: the streamlines originating from the points with the highest electric field and a red sample streamline (a), the field strength along the red streamline (b), the sorted stress E_{sorted}, cumulatively integrated E_{av} curves compared with gap withstand curves E_{bd} (c), and the Safety curves SF (d)

For the insulation design of conventional AC transformers, the safety factor of the oil gaps is considered to be *SF*>1.0 [77]. In this case, dependencies of the electrical conductivity of oil and OIP on moisture content, electrode materials and their coatings shall also be considered. In addition, as already explained in Section 2.2.9, the electric field distribution in the HVDC oil-paper insulation systems does not fully comply with the LMW model. For these reasons, higher safety factors are considered as acceptable in this study for the DC insulation design. For the same reason, for the paths in the 4 mm OIPs, the maximum stress of 20 kV_{rms}/mm are considered as critical [76].

A Matlab script has been developed to determine the oil gaps with low safety factors and OIP barriers with high stress for further repetitive manual optimization of the design. For example, in Figure 4-11 the critical regions of the oil gaps and OIPs for all time steps are presented for the applied voltage of 125 kV. It should be mentioned that for all time steps at temperatures 30°C, 50°C and 90°C, the minimum safety factor reached 1.67 in the oil gaps and the maximum local stress in the nonuniform field can be as high as 27.3 kV/mm in the OIP.

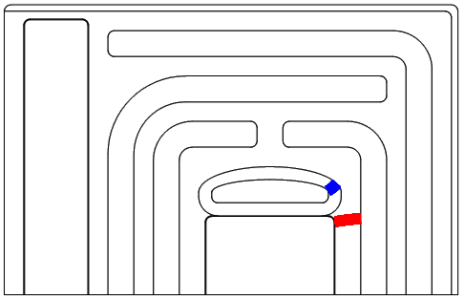

Figure 4-11. Critical regions for all the time steps at applied voltage 125 kV are shown for oil gaps (red) with minimum SF and OIP barriers with maximum stress (blue) for temperatures 30, 50 and 90 °C

4.2.2 Interface insulation design

To identify the safety factor for the oil-OIP interfaces, the effect of the tangential electric field on the existing creepage paths at all the time steps are considered. Figure 4-12 presents a summary of the simulations of the fields along a sample oil-OIP interface divided in segments with the same direction of tangential field at 125 kV, 50°C and 1 second performed with the NLMW model.

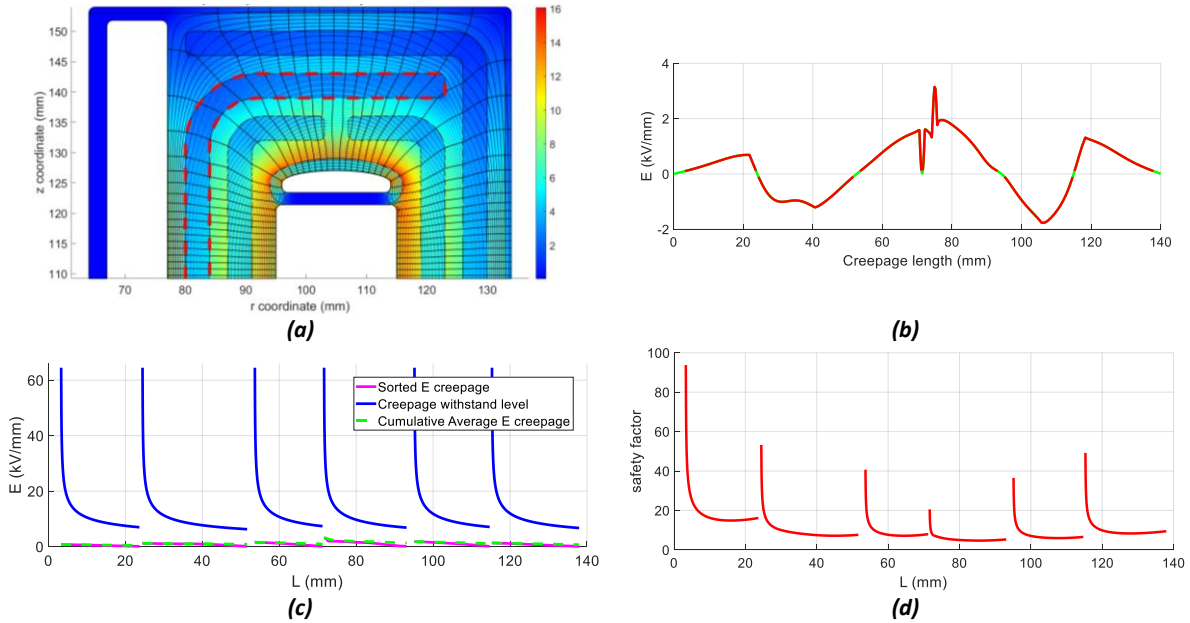

Figure 4-12. A sample simulation at 125 kV, 50°C and 1 second: a sample oil-OIP interface (dashed red) (a), kV/mm E-field along the creepage path (b), E_{sorted}, cumulatively integrated E_{av} and E_{bd} curves (c), and the safety curves SF (d)

The selected interface is highlighted by a red dashed line for further illustrations (Figure 4-12a). The electric field along the displayed oil/OIP interface (Figure 4-12b) shows how the tangential field changes from positive to negative and drops below 0.1 kV/mm at some locations (green pieces along the curve). It is assumed that when the tangential field drops under this value, the creepage path is discontinued, and a new path starts as soon as the field reaches a stress higher than 0.1 kV/mm [22]. In such a way, the abovementioned interface is cut to pieces and, for each piece, the E_{bd}, E_{av} and sorted E_{sorted} curves are displayed in Figure 4-12c by blue, green and pink curves, respectively. It is worth mentioning that the creepage withstand E_{bd} curves are assumed to be 0.7 times of the withstand level of an oil gap of the same path length [77], which is presented in (2-3). The creepage paths safety factor curves (Figure 4-12d) are calculated by dividing the withstand curves to the cumulative average curves. The safety factor curves have been considered for temperatures 30, 50 and 90°C, and for all time steps from the time of energizing the transformer until 10^4 seconds. The minimum safety factor for all time steps and all temperatures was 1.55. An output from the simulation demonstrating the critical creepage paths is presented in Figure 4-13, where the red lines indicate safety factors less than 1.6.

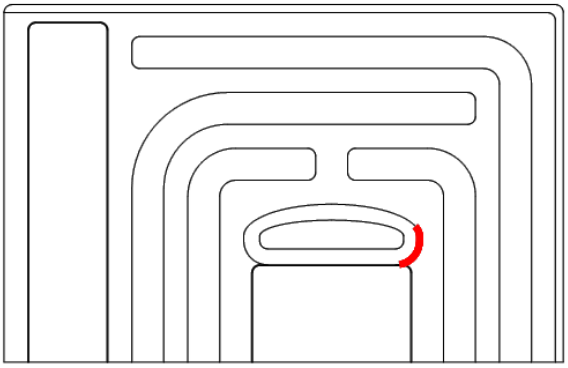

Figure 4-13. The critical paths for all time steps with minimum SF shown in red for temperatures 30, 50 and 90°C

As mentioned earlier in Section 2.2.12, three additional important design aspects are leakage inductance, core losses and winding losses.

4.3 Prototype leakage inductance

The leakage inductance of the prototype transformer is calculated by the method presented in Section 2.4.4 and with the details presented in [97] by the authors. COMSOL Multiphysics is also used for 3-D FEM analysis of the leakage field inside the MFT under study. The windings are modelled as stranded coils with uniform current densities. The net Ampere-turns of the windings is equal to zero to represent the short-circuit test condition used for the leakage inductance measurement. The core is modelled as a linear magnetic material with high relative permeability. The windings and surrounding medium are specified as non-magnetic materials with a relative permeability equal to 1. The electrical conductivity is defined to be zero for all materials. A stationary study is used. The outer surface of the domain is defined as the magnetic insulation (flux-parallel boundary condition). The result of the leakage field analysis using 3-D FEM is displayed in Figure 4-14a. The distribution of the leakage flux density inside the core window is also shown in Figure 4-14b. It is noted that the low value of the flux inside the core is due to the condition of the zero-net Ampere-turns of the windings. As can be deduced from Figure 4-14a and Figure 4-14b, the core changes the shape of the leakage flux, affecting the leakage inductance consequently. This implies the necessity of using more accurate analytical methods since the classical leakage inductance formulas may not be accurate enough in this case.

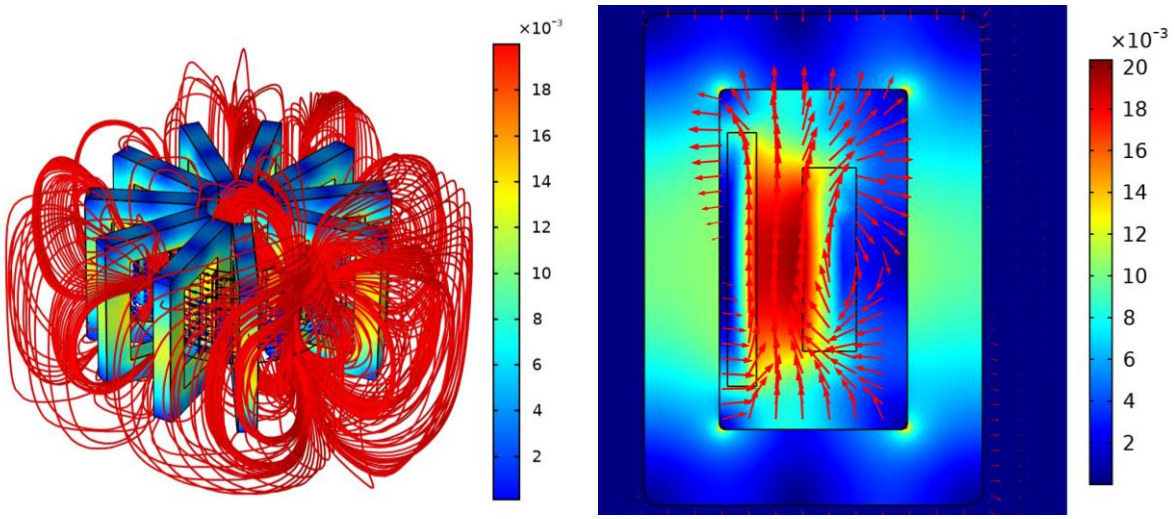

(a) *(b)*

Figure 4-14. The leakage field obtained by 3-D FEM simulation (a), and the distribution of leakage flux density inside the core window (b) both in Tesla

The leakage inductance calculated using 3-D FEM is 26.65 µH. The leakage inductance is calculated using the total magnetic energy stored in the leakage field which is the energy stored outside the core segments. The leakage inductance calculated by the proposed method in Section 2.4.4 is 26.67 µH.

4.4 Prototype parasitic capacitances

Based on the background theory presented in Section 2.5, to be able to compare the results for the capacitances of the MFT prototype, all other parameters in the equivalent circuits were adjusted. Thus, physical dimensions of the core, windings, etc. were used as the input to the models.

The verification against the measured data was performed using the values of the capacitances and L_m and L_s. The frequency dependencies of the impedances were obtained by introducing open and short circuit connections at the HV side. Note that the Z-curve of the circuit seen from the LV side were considered, that could be compared with the curves attained from the measurements. The acceptability of the models was defined by agreement of the four major resonance frequencies obtained from the equivalent circuit approach with the measured results.

4.4.1 The Medium Frequency (MF) method

The capacitive elements of the MF model are

- Cs_1 is the series capacitance of the layer type LV winding calculated from (2-75), where $N_L = 3$ and C_{TL} is found either from (2-73) or directly from 3D FEM model.
- Cs_2 is the series capacitance of the disc type HV winding calculated from (2-77), where $N_D = 8$ and C_{TD} is obtained from (2-74) or directly from 3D FEM model.
- Cg_1 is the sum of the capacitances of the layers to ground obtained from the capacitance matrix.
- Cg_2 is the sum of the capacitances of the discs to ground obtained from the capacitance matrix.
- Cp is the sum of capacitances between the outer layer and all discs.

The frequency dependencies of the impedance extracted from the model are presented in Figure 4-15 (here and on Figure 4-16 and Figure 5-6, the vertical scale is the impedance in Ω, and the horizontal scale is the frequency in Hz). The resonance frequencies obtained with the MF equivalent circuit are f_1 = 23.2 kHz, f_2 = 307 kHz and f_4 = 1.47 MHz for the open circuit conditions and f_3 = 1.44 MHz for the short circuit connection. The obtained model capacitances are Cg_1 = 153.2, Cg_2 = 31.5, Cp = 25.2, Cs_1 = 409.6 and Cs_2 = 74.6 (in pF).

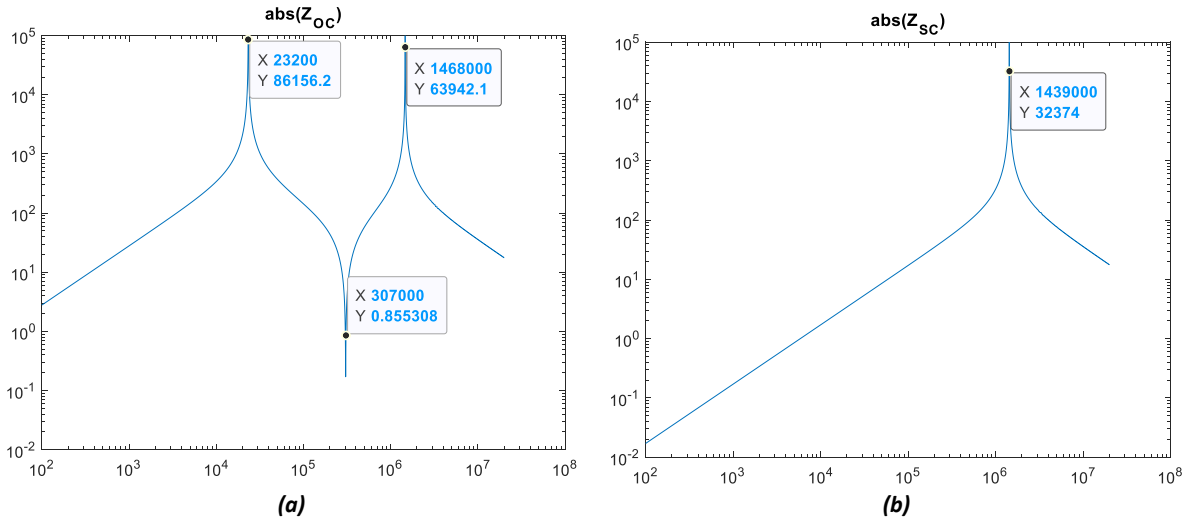

(a) *(b)*

Figure 4-15. The medium frequency model, Z curves achieved; Zoc (a) and Zsc (b)

4.4.2 The extended model

The capacitive elements of the extended model are

- Cs_1 – Cs_4 are calculated analytically from (2-79), where N_L = 3 and C_{TL} is achieved from (2-73) or from the 3D model considering the average diameter of the winding as in Figure 2-28b.
- $Cp_{1,3}$, $Cp_{2,4}$ or $Cp_{3,5}$ is 1/3 of the capacitance between two layers, achieved from the 3D model [12].
- Cg_1 or Cg_5 is the half of the capacitance of the layer to ground and Cg_2 – Cg_4 are the sum of the half of the capacitances of the adjacent layers.
- Cs_5 – Cs_{20} and C_t are calculated from (2-80), where N_D = 8 and C_{TD} is achieved from (2-74) or from the 3D model.
- Each *C*p is a capacitance between the outer layer and a disc (there are 16 *C*ps in total). Each *C*p which is obtained from 3D FEM simulation is divided into four capacitances each having the value of ¼ of *C*p. The capacitances are connected between two terminals of the outer layer and two terminals of each disc.

The frequency dependences of the impedance obtained from the model are presented in Figure 4-16. The resonance frequencies of this equivalent circuit are f_1 = 24.4 kHz, f_2 = 311 kHz and f_4 = 1.54 MHz for the open circuit and f_3 = 1.51 MHz for the short circuit configurations.

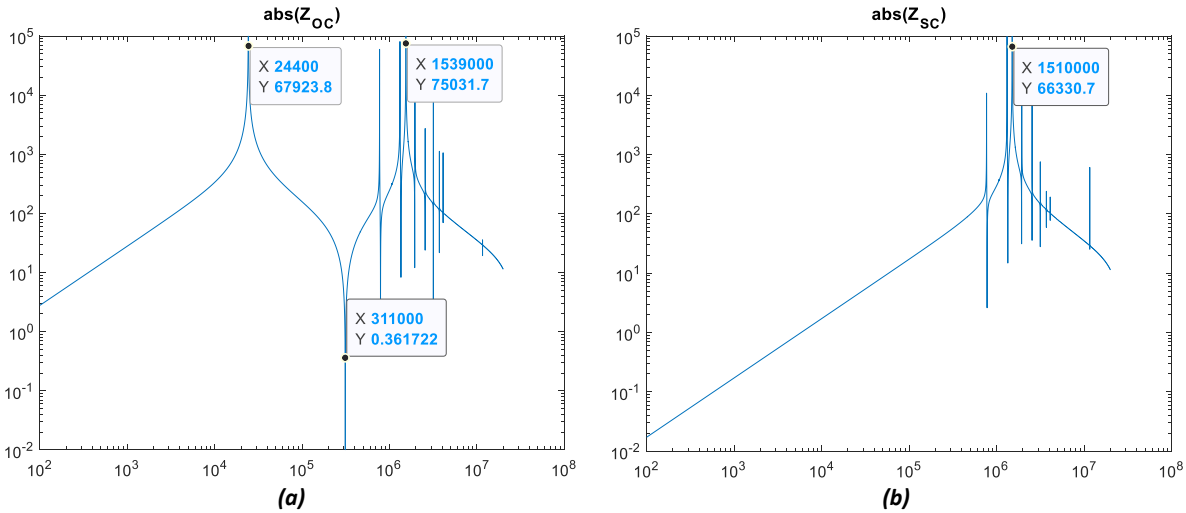

(a) *(b)*

Figure 4-16. The detailed model, Z curves achieved; Zoc (a) and Zsc (b)

Note several minor resonances on the curves in Figure 4-16 which originate from resonances between the distributed capacitance and inductance elements of the circuit. In a real transformer, the amplitude of these resonance components will have a very low amplitude due to the damping phenomena. These resonances are distinguishable from the main four resonances which are going to be used as criteria for the accuracy of the model, for representing the parasitic capacitances of the MFT under consideration. The secondary frequencies of minor resonances are those ones, for which the amplitude of the frequency response tends to continue its increasing or decreasing behaviour as it was before the resonance moment.

4.5 Prototype core losses

The suitability for the relatively high operating frequency is the first criterion for the selection of a core for a medium frequency transformer which experiences high frequency voltage harmonic components of the applied square wave from the DAB side (Figure 2-1a) [13]. Another crucial criterion for the selection of a core for manufacturing a prototype HVDC MFT is a large window size. This ensures an enough insulation clearance for the high DC voltage which is going to be applied to the HV winding.

Nanocrystalline cores can carry more flux which helps the reduction of the weight and size of the prototype. Because these finished cores can be produced from raw sheets of Nanocrystalline bands, there are several producers which can shape products suitable for individual needs. But the raw material is produced only by very few producers, and it is expensive, and the cost of post processing is high. Fortunately, Ferrite cores are relatively cheap and available from several commercial suppliers. Of course, it is possible to order cores of larger sizes; however, in order to keep the total cost of manufacturing low, it is decided to select the biggest off the shelf product available on the market.

As mentioned earlier, the prototype MFT's power is 50 kW, the voltage ratio is 421.9/4500 V, rated transformer currents are 118.5/11.11 A and the number of turns is 12/128 for the primary and secondary sides respectively. Using (2-30) a core consists of 10 core stacks of Epcos TDK type B67385U 126/91/20 made of the Ferrite N87 material [104] is selected (Figure 4-17). The physical core area is 20 x 28 = 560 mm^2 and for 10 core stacks including 20 U cores is 5600 mm^2 which is suitable for the design. The maximum working flux density of the core will be 0.31 T which gives 0.8 of saturation flux density of the core (0.39 T) at room temperature [104].

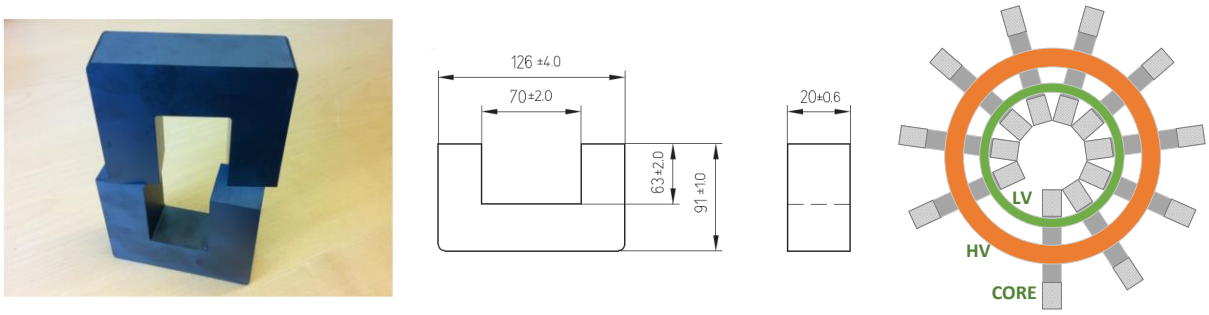

(a) *(b)* *(c)*

Figure 4-17. Ferrite core used for the HVDC MFT: the ferrite cores' shape (a), the core dimensions (b), and the HVDC MFT cores stacks (c)

In this work, instead of using the empirical equations based on characterization coefficients from the core suppliers earlier mentioned in Section 2.6.1, the selected core material is characterized by direct core loss measurement and an accurate no-load loss estimation for the prototype transformer are done based on the measurements results.

4.6 Prototype winding losses

In this work, a numerical method based on FEM simulations is presented, which is based on the equivalent permeability and conductivity of the stranded copper conductors. The method is applied to the model of a 5 kHz prototype MFT transformer equipped with the litz wires, and different simulations, with and without the usage of the equivalent model, are performed. Winding losses are calculated at different frequencies. Subsequently, the winding losses of the prototype MFT are measured at different frequencies and compared with the results of simulations. The results of simulations have an acceptable conformity with the presented measurements. Therefore, the proposed method can be used by designers of MFTs as an effective and quick way to easily estimate the winding losses of MFTs where litz conductors are used.

As shown in Figure 2-1a, the current wave form is similar to a sinusoidal shape and for any simulation or measurement experiment it seems enough to just apply the fundamental element of the medium frequency current wave to estimate the losses in the windings.

The complex permeability and conductivity defined by (2-101) and (2-102) are applied in simulations for the modelling of the litz wires as a continuum.

The finite element simulations were performed in FEMM, which uses approximate but closed-form expressions for the equivalent conductivity and permeability of regions filled with hexagonally packed round wires. These expressions allow the proximity and skin effects to be included with ease in 2D, AC field computations. Solutions were performed over a range of frequencies between 0 and 15 kHz. The value of losses and increase of losses in relation to DC losses are illustrated in Table 4-1 showing an increase of losses equal to 21% at 5 kHz, the fundamental frequency, and a value of 189 % at 15 kHz, the third harmonic frequency of the current waveform in the MFT. As explained in Section 5.1.4.3, these results agree with the actual measurements on the prototype MFT.

Table 4-1. Results of loss analysis with equivalent material representation method (see Section 5.1.4.3 for the loss measurement results)

Frequency (kHz)	Losses (W)	Increase of Losses to DC losses (%)
0	61.2	0
1	61.7	1
2	63.3	3
3	65.9	8
4	69.5	14
5	74.1	21
6	79.7	30
7	86.4	41
8	94.1	54
9	102.9	68
10	112.6	84
11	123.4	102
12	135.2	121
13	148.0	142
14	161.9	165
15	176.8	189

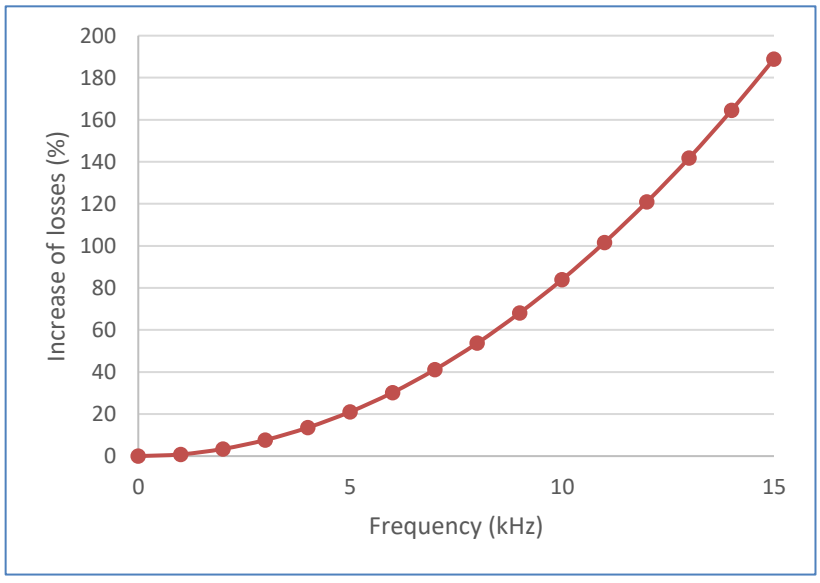

The validity of the method was investigated by a comparison of finite element solutions with an equivalent and explicit model of a wound coil. The model with explicit windings needs a fine mesh inside the wires in order to adequately model skin and proximity effects at high frequencies. Since an

analysis of a problem with all wires modelled with explicit litz strands is not possible due to the huge amount of required mesh elements at high frequencies, only one wire is modelled explicitly at each time and the total losses that occur inside its copper strands is extracted and compared with the one that is obtained from the equivalent material representation method. Each wire consists of 186 round copper strands wound in alternating layers of 16 and 15 strands in the columns.

The change of the current distribution inside the individual strands of a litz wire at different frequencies is shown in Figure 4-18. The results of the loss analysis for a litz wire are shown in Table 4-2 demonstrating that the equivalent material model provides good agreement with the explicit model over the whole frequency range from 0 up to 15 kHz.

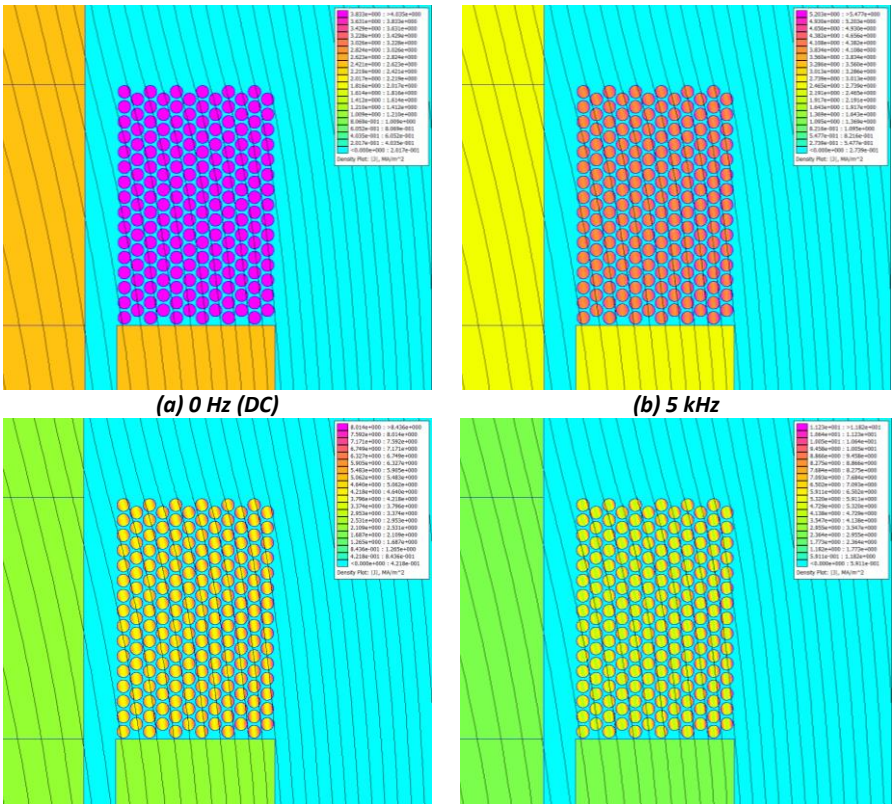

(a) 0 Hz (DC) ***(b) 5 kHz***

(c) 10 kHz ***(d) 15 kHz***

Figure 4-18. Current distribution inside individual strands of a litz wire at different frequencies

Table 4-2. Comparison of litz wire losses for explicit and equivalent material models

Frequency (kHz)	0	5	10	15
Exact Method	0.827109	0.951974	1.32653	1.95066
Equivalent Material Representation	0.827067	0.951871	1.32624	1.95008

Depending on the frequency, the presence of these additional losses will make the AC current losses higher than the equivalent DC current copper losses. Circulating current losses can be a result of having parallel conductors of a different length or exposed to a different electric field which leads to a different voltage drop over two parallel conductors of the same length. For the prototype transformer considered in this study, parallel conductors are axially ordered and there are no circulating current losses in them. However, because of relatively high frequency, eddy current losses are present and will be investigated.

4.7 Prototypes manufacturing

4.7.1 Transformer tank

The transformer tank and the active part support structure were made of extruded thermoplastic acrylic (Plexiglas) which has an excellent electrical insulation property and offers good chemical and thermal resistance to warm transformer oil. An oil circulation and cooling system together with an oil expansion cylinder all from off the shelf materials were connected to the oil tank to feed in the cold oil from bottom and to suck out oil from top. To make a better natural circulation and flow distribution, the oil inlet and outlet pipes were made both in pair and inlets and outlets placed in 90 degrees position. All the piping system were made of oil and heat resistant, electrically insulating plastics (Figure 4-19).

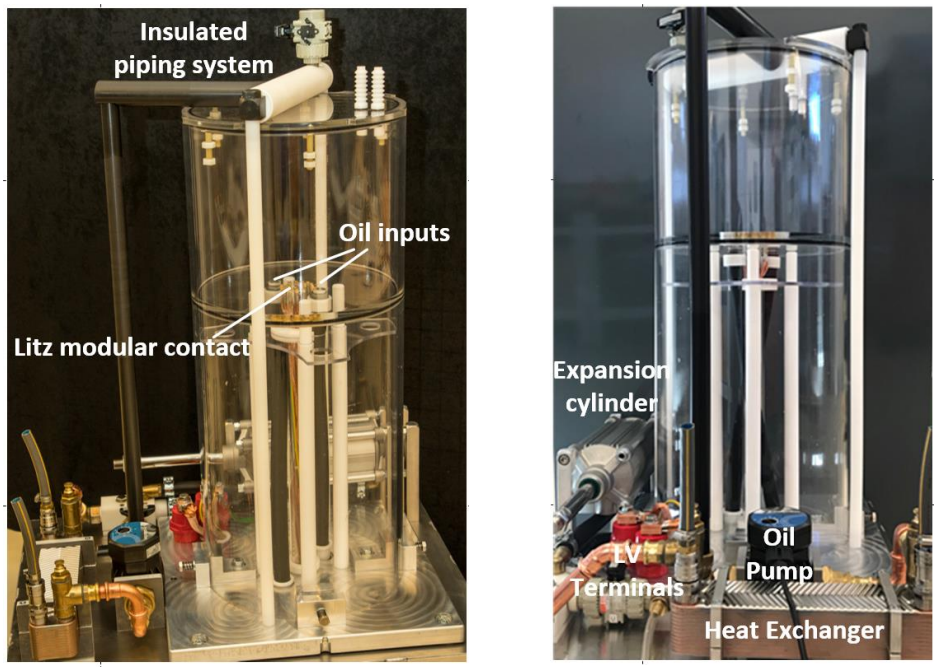

Figure 4-19. Transformer tank and active part mechanical structure

As the tank itself takes the role of the isolation of 125 kV DC to ground, the only isolation required is between two 5 kV winding terminals which were made of Teflon (Figure 4-20a). All the cores were grounded using copper strips (Figure 4-20b). 8+8+1 female banana contacts in the bottom plate of the tank are connected to the two LV terminals outside tank on the bottom plate using 17 litz wires.

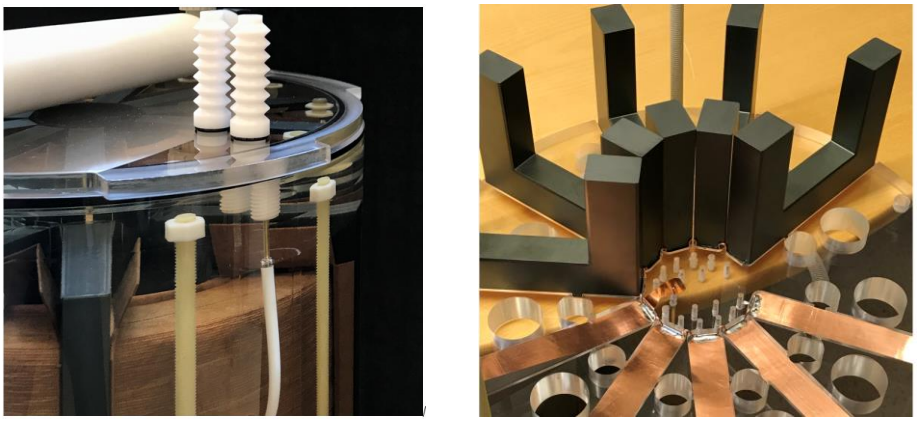

(a) *(b)*

Figure 4-20. HV bushings and core grounding strips: The HV bushings for isolation of 5 kV AC (a), and the grounding copper strips for Ferrite cores (b)

4.7.2 Active part

Each active part includes two round extruded thermoplastic acrylic (Plexiglas) discs which press the cores using epoxy threaded rods. There are enough holes in the discs to let a smooth flow of the oil through the insulated active parts and the core. The HV winding terminals are connected to the two banana contacts on the top pressing plate. Theses contacts are connected to the female contacts of the two home-made Teflon bushings which will deliver 5 kV AC voltage on the tank cover. The high-current LV terminals are terminated by 8+8 banana contacts at the bottom pressing plate which can sit directly on the female banana contacts at the bottom of the tank. The core-grounding plate is connected to one banana contact at the bottom of bottom pressing plate which can sit directly on a female banana contact at the bottom of the tank. Each litz wire of 8, has its own banana contact to reduce the extra losses in the external connections to a minimum. The low voltage and high voltage windings of the magnetic prototypes are of layer and disc type respectively as explained in Section 4.1. The LV winding has 8 parallel and the HV winding has one rectangular litz winding (Figure 4-21a).

(a) *(b)*

Figure 4-21. Two windings and magnetic active part module which sits inside the transformer tank: the HV and LV windings (a), and the magnetic prototype (b)

The dimensions of the built magnetic prototype are presented in Figure 4-22.

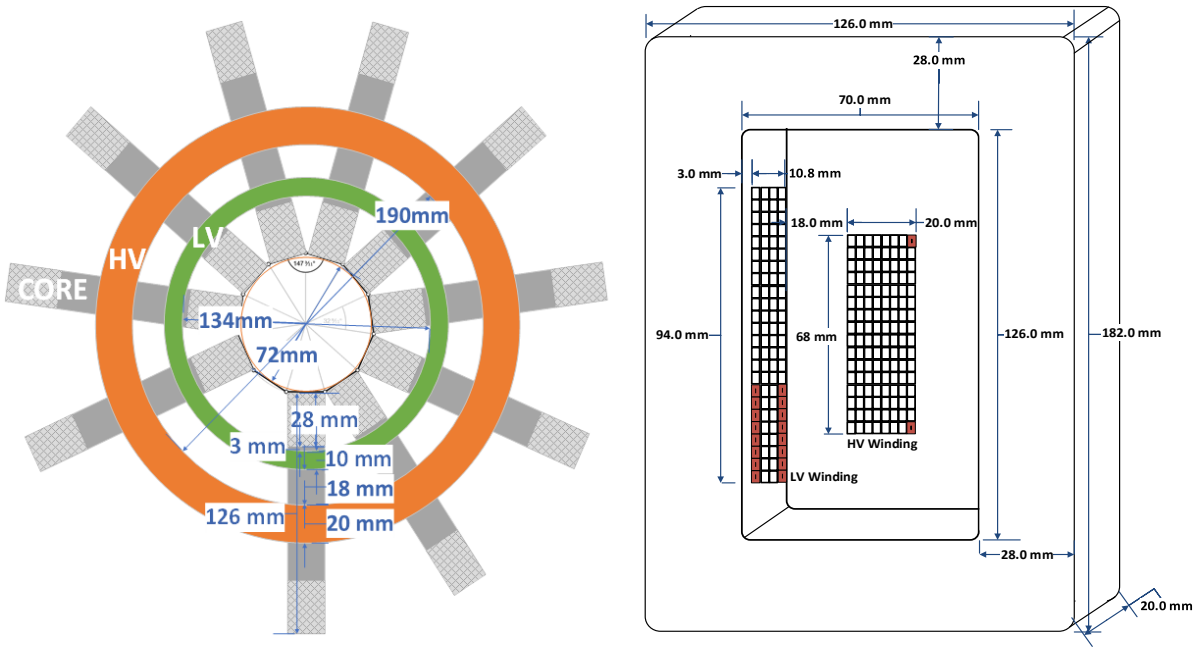

(a) *(b)*

Figure 4-22. Decagon MFT winding dimensions and their positions inside core window

4.7.3 Electrodes for HVDC test

The LV and HV electrodes of the insulation prototype were made of aluminium cylinders exactly replicating the windings (Figure 4-23).

(a) *(b)*

Figure 4-23. The replica of windings made for insulation prototype: the insulation prototype winding replicas (a), and the LV electrode with all 8+8 output litz wires (b)

4.7.4 OIP insulations

Main formed insulation barriers were ordered from a supplier. These parts are made of wood pulp clay mould and dried under special conditions [76] (Figure 4-24)

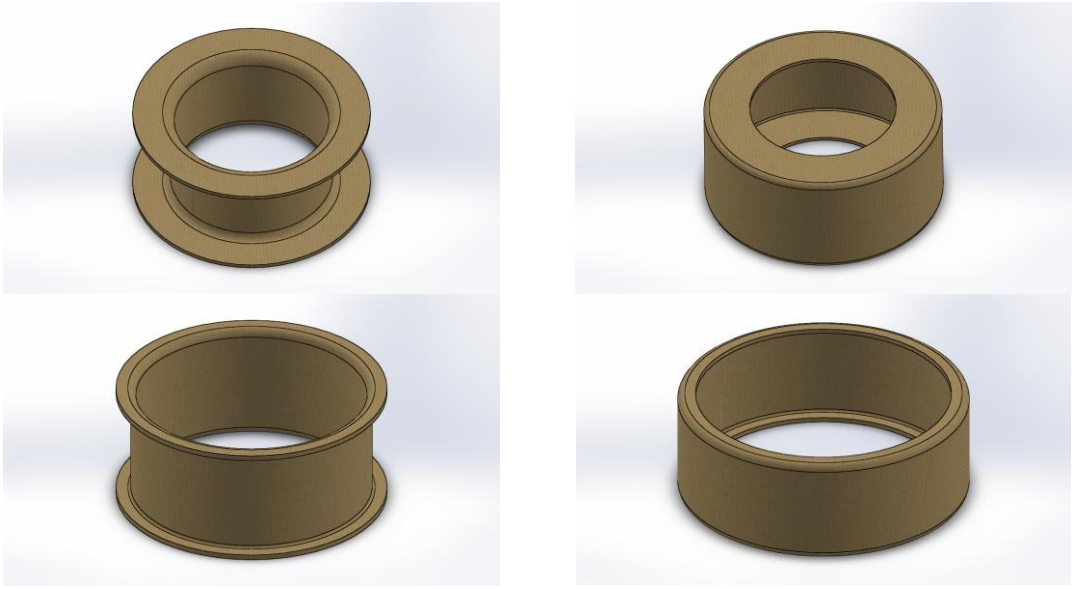

Figure 4-24. Formed insulation parts ordered to a supplier

Figure 4-25a shows the manufactured insulation prototype active part and Figure 4-25b demonstrates a model made by a 3D printer mantled in the active part before ordering the actual insulation parts from the supplier.

The other insulation parts needed are made of cellulose pressboards by the author. 1 mm pressboards are bent after making them damp on the edges and using dies to keep it in its form during drying (Figure 4-26).

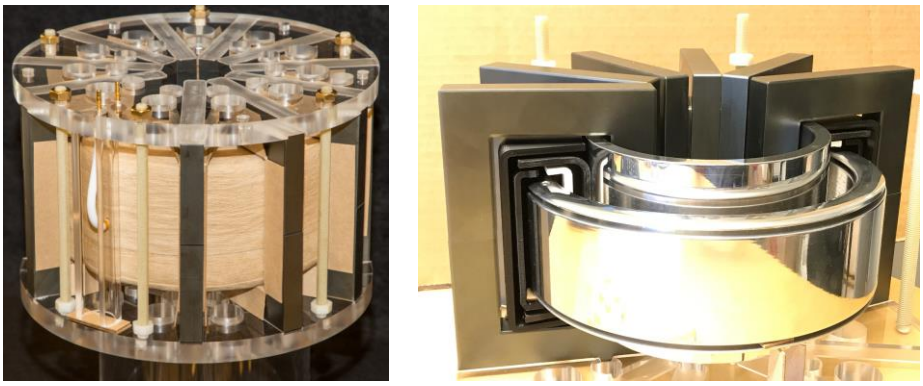

(a) *(b)*

Figure 4-25. A cut model of insulation parts mantled together with the made coil replicas and cores: the manufactured insulation prototype active part (a), and the 3D printed insulation barriers and test electrodes (b)

Ionized water, which has much less impurity of conductive particles compared with tap water, was used for damping the dry pressboard before bending (Figure 4-27b & c). A Lutron WA-2017 SD water conductivity meter is used to confirm the suitability of the water. 6 µS/cm (micro-Siemens) was measured for ionized water compared with 240 µS/cm which was measured for normal the tap water.

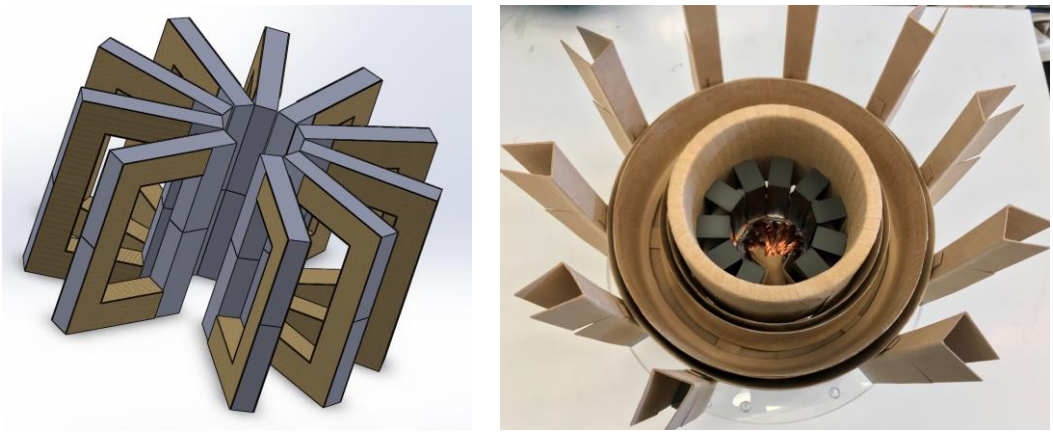

(a) *(b)*

Figure 4-26. The core barriers during setting up: a model of core protection boards (a), and the core protection boards, lower part of formed insulations and the LV winding mantled (b)

Two Teflon bushings to insulate 5 kV AC between two high voltage terminals are build and installed on the Plexiglass tank cover. To lead the high voltage out of the HV electrode to the HV bushing installed on the top of the transformer tank, a Teflon insulated copper cable is used (Figure 4-25a).

(a) *(b)* *(c)*

Figure 4-27. The tools used to form and dry pressboards to formed insulations (a), the conductivity (µs/cm) of ionized water (b), compared with the conductivity of tap water (c)

4.7.5 Oil filling

The active part was put in a stainless-steel container, and the container has been placed in 80 °C for 12 hours and later additionally under full vacuum for 96 hours. Later 80°C oil is led into the vacuum chamber trough a needle valve and filled the container from the bottom. After the oil filling, the heating was stopped, and the system was left under vacuum for 72 hours to cool down to room temperature.

At the same time the main transformer tank is prepared for receiving the active part. The valve on the top is connected to a 2 m empty pipe which was connected to a vacuum pump. The valve at the bottom is connected to a barrel of dried and degassed transformer oil at room temperature.

The active part container is taken out of the vacuum chamber, the humidity content of the oil is checked (Figure 4-28a), the active part raised and placed in the tank, the tank cover is closed, and vacuum is set to a proper value not over loading the transformer tank mechanical structure. The bottom valve was opened, and the tank was filled with transformer oil from the bottom (Figure 4-28b). Finally, the transformer is left for 72 hours before testing.

(a) *(b)*

Figure 4-28. The active part ready to be mantled in the transformer tank: the active part in the oil container after oil impregnation (a), and the transformer oil filling setup (b)

The three-stage oil-filling process after putting the active part in the transformer tank is demonstrated in Figure 4-29.

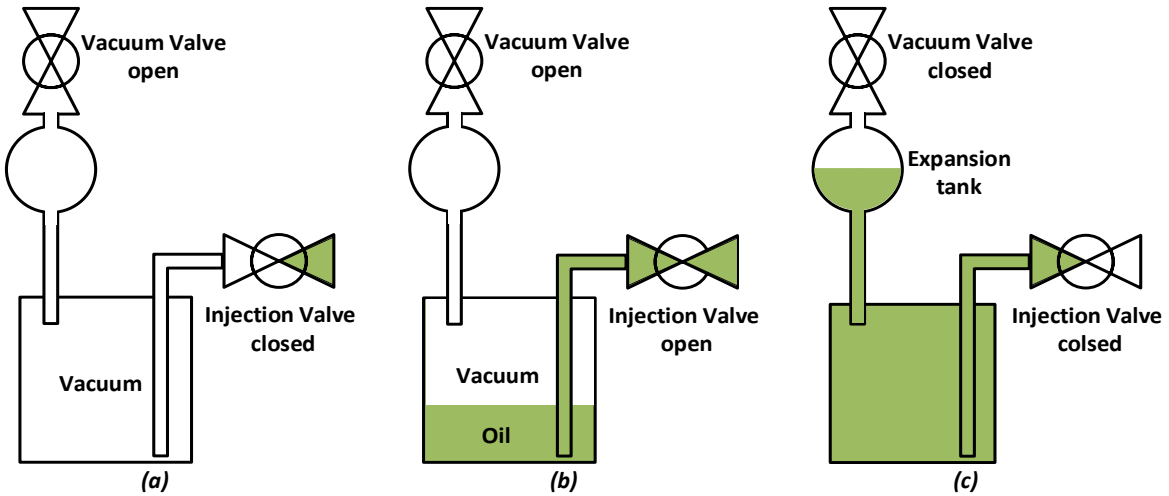

(a) *(b)* *(c)*

Figure 4-29. The three-stage oil-filling process after putting the active part in the transformer tank: the active part drying and degassing (a), the oil injection under vacuum (b), and the Oil filled tank (c)

4.7.6 Prototype MFT's cooling system

As explained in section 3.1.4 the conductivity of insulation materials is changing with temperature variations because of the heat generated by the core or coils. The heat will be generated inside the transformer tank by the core when the rated voltage is applied and by the winding when the rated current flows. An effective insulation system performance is dependent on a stable and predictable temperature around the active part components [132]. It is therefore, a very important task to design and implement an effective cooling system for the MFT. The cooling system considered for the oil type MFT in this study is an oil forced and directed circulation. The warm oil is cooled down by an oil-water heat exchanger (Figure 4-30). A hydraulic expansion cylinder is connected to the closed oil circulation system which can expand in case of expansion of the oil due to a change in oil temperature. To take the advantage of the weight of oil, the warm oil is fed from the top and drained out from the bottom of the transformer. To assure a balanced penetration of the coolant into the paper insulation material in the vicinity of the HV coil, two inlets are prescribed.

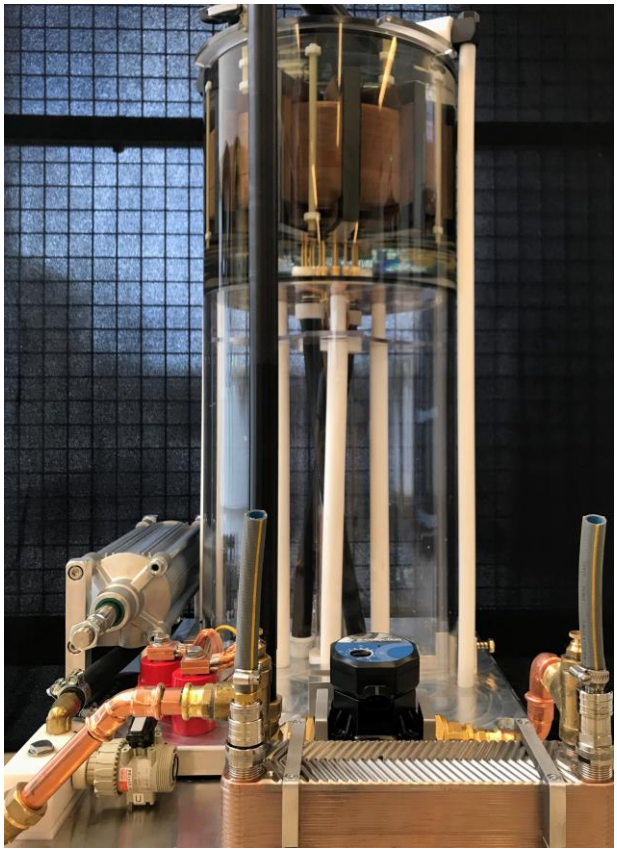

Figure 4-30. The cooling system of the prototype transformer including Plexiglas transformer tank (up), a hydraulic expansion cylinder (left) and an oil-water heat exchanger (front)

5 Design Verification and Analysis

5.1 Verification tests

5.1.1 Leakage inductance

Table 5-1 presents the dimensions of the constructed prototype transformer which will be used in this section.

Table 5-1. Dimensions of constructed prototype transformers (mm)

Number of core stacks	10
Core stack width	20
Core thickness	28
Core window height	126
Core window width	70
Primary winding number of layers x turns per layer	4 x 3
Secondary winding number of discs x turns per disc	16 x 8
Primary-Secondary isolation gap mean length (perimeter)	540
Part of MLT_{iso} inside the core window (ten 20 mm cores)	200
Part of MLT_{iso} outside the core window	340

To verify the calculation method, inductance measurements have been performed on the Decagon magnetic prototype MFT built in this project. Ferrite cores are used for the design (Figure 5-1a). The measurement of leakage inductance has been performed using an Agilent E4980A RLC meter. The measurements are performed from both sides. If the measurement is performed from the secondary winding terminals, the primary winding shall be short-circuited (Figure 5-1b).

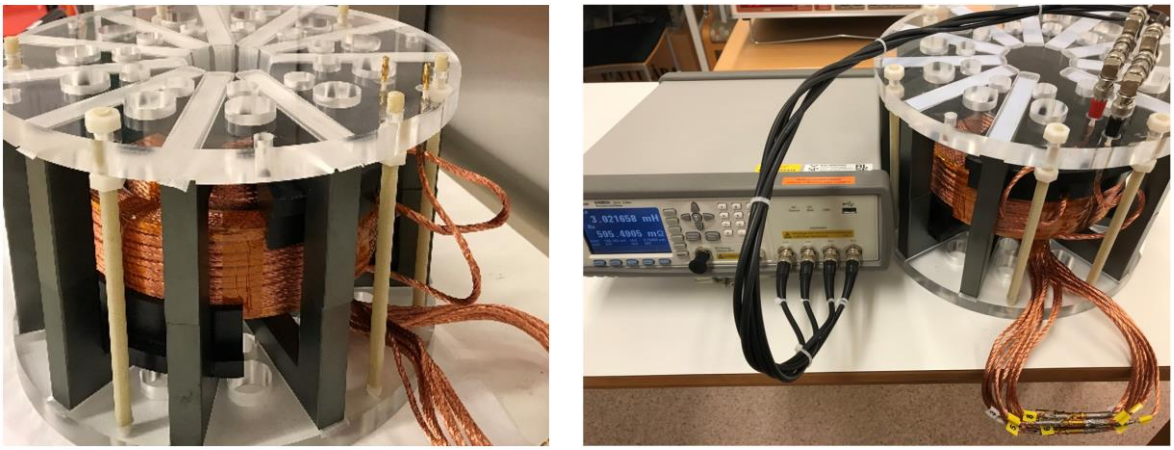

(a) ***(b)***

Figure 5-1. The constructed prototype transformers and leakage inductance measuring test setup: the Decagon MFT (a), and the leakage inductance measuring circuit (b)

The results of the measurements are presented in Figure 5-2 which indicates a value of 26.46 µH at 5kHz. The change of inductance with the applied frequency is not significant due to the use of the litz wire in the windings [44]. It is noticeable that the skin depth of copper at 10 kHz is about 0.73 mm (with σ = 4.74e^7 S/m at 75°C) while the diameter of each strand of the litz wire is only 0.2 mm. Therefore, no significant change is observed in the leakage inductance value in the frequency range of 100 Hz to 10 kHz.

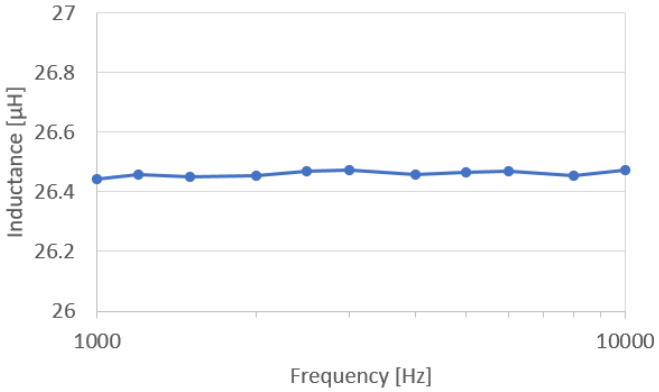

Figure 5-2. The leakage inductance measured as a function of frequency

The measured value for the leakage inductance is 26.46 µH. The result of the 3-D FEM and the proposed method in Section 2.4.4 are compared with the measurement in Table 5-2. The values of relative percent errors for 3-D FEM and the proposed method are both less than 1 percent, indicating a small deviation between measured and calculated leakage inductances.

Table 5-2. The results of leakage inductance calculation

Measurement (µH)	3-D FEM (µH)	Proposed Method (µH)	3-D FEM Absolute Error (%)	Proposed Method Absolute Error (%)
26.46	26.65	26.67	0.7	0.8

To verify the proposed method in this study, a sensitivity analysis is also performed on a shell type transformer similar to the prototype transformer in three cases and for different numbers of core segments. Assuming that the LV winding may get a higher total dimension for inserting the cooling channels inside, and the HV winding may be placed farther away from the LV winding because of a higher isolation distance, two additional cases are defined. The number of core stacks are also varied from 10, for the prototype, to 8, 6, 4 and 3 stacks. The number of the core segments is changed in such a way that the flux density inside the core remains constant (Figure 5-3). As the number of the core segments, n_c, is reduced, the total cross-sectional area of the core segments is increased proportionally.

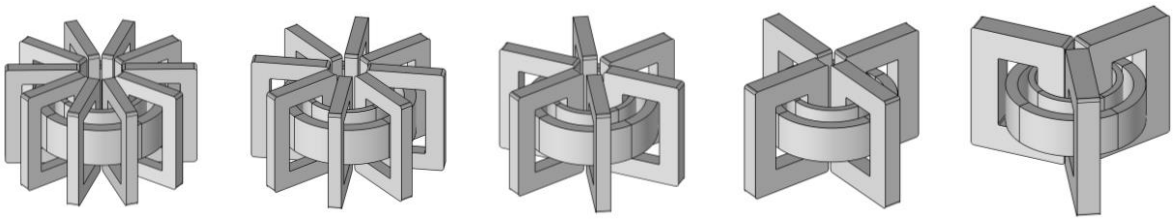

(a) 10 core segments **(b) 8 core segments** **(c) 6 core segments** **(d) 4 core segments** **(e) 3 core segments**

Figure 5-3. A shell-type transformer with different numbers of core segments

For case 1, the dimensions of the windings are equal to the dimensions of the windings of the transformer prototype under study in this paper. For case 2, the radial width of the LV winding is increased by 9 mm representing an addition of three cooling ducts, each with a width of 3 mm, between the LV layers, considering a uniform Ampere-turns model of the LV winding. As a result of increasing the LV width, the HV winding's inner diameter is increased accordingly, to keep the main

gap between the windings constant. The width of the core window is also increased proportionally to keep the HV winding's distance to the outer wall of the core window constant. For case 3, in addition to an increase in the LV winding's width equal to 9 mm, the width of the main gap is also increased by 6 mm to provide more clearances between the LV and HV windings. Similar to case 2, as a result of increasing the inner diameter of the HV winding, the width of the core window is also increased accordingly to preserve the distance between the HV winding and the outer wall of the core window. In both cases 2 and 3, the height of the windings, the height of the core window, the inner diameter of the LV winding and the width of the HV winding remain constant.

The results of the leakage inductance calculation using the proposed method and using the 3-D FEM as the reference method are shown in Table 5-3 for n_c>2. The accuracy of the proposed method is also compared with Rabins method [53] as well as the classical method. Equation (2-46) is used for the calculation of the leakage inductance according to the classical method. According to Table 3, the accuracy of the proposed method in all cases for different numbers of core segments is higher than the accuracy of the other methods (less than 1 % in all cases). It should be noted that although the parameter Θ is dependent on the dimensions of the core segments, the accuracy of the proposed method is independent of the value of this parameter. It can be seen from Table 5-3 that the error of Rabins method increases, especially as the number of the core segments decreases. Note that the number and dimensions of the core segments are not properly reflected in the geometry in Rabins method, leading to inaccurate results in the leakage inductance calculation. According to Table 5-3, the classical method produces inaccurate results in all cases. It should be noted that the core walls do not affect the value of leakage inductance in the classical method.

Table 5-3. The leakage inductance results from the sensitivity analysis for segmented-core transformers

		10 core segments			8 core segments			6 core segments			4 core segments			3 core segments		
		Case 1	Case 2	Case 3	Case 1	Case 2	Case 3	Case 1	Case 2	Case 3	Case 1	Case 2	Case 3	Case 1	Case 2	Case 3
Leakage Inductance (μH)	3-D FEM	26.71	31.19	37.56	26.54	30.94	37.22	26.25	30.55	36.69	25.78	29.92	35.83	25.44	29.48	35.22
	Proposed Method	26.67	31.09	37.43	26.47	30.83	37.07	26.21	30.48	36.60	25.83	29.99	35.93	25.61	29.71	35.55
	Rabins Method [34]	27.14	31.91	38.65	27.13	31.90	38.64	27.12	31.89	38.63	27.10	31.88	38.61	27.03	31.82	38.54
	Classical Method (31)	27.90	31.79	38.14	27.90	31.79	38.14	27.90	31.79	38.14	27.90	31.79	38.14	27.90	31.79	38.14
Absolute Relative Error (%)	Proposed Method	0.1	0.3	0.3	0.3	0.4	0.4	0.2	0.2	0.2	0.2	0.2	0.3	0.7	0.8	0.9
	Rabins Method	1.6	2.3	2.9	2.2	3.1	3.8	3.3	4.4	5.3	5.1	6.6	7.8	6.3	7.9	9.4
	Classical Method	4.5	1.9	1.5	5.1	2.7	2.5	6.3	4.1	4.0	8.2	6.3	6.4	9.7	7.8	8.3

The attracted reader can refer to [97] for more details regarding the transformers with n_c≤2 i.e., the single and double core-segment transformers.

5.1.2 Parasitic capacitance

The parasitic capacitances of the MFT were measured using an RLC meter and a network analyser. In the measurements with the network analyser, a frequency swept impedance measurements were performed from the LV side while the HV side was either open or short circuited.

5.1.2.1 *Measurement of interwinding capacitances*

Normally, as standard tests for power transformers, the capacitances between the windings and between a winding and ground are measured using an RLC meter while two terminals of each winding are short circuited. As the winding terminals are short-circuited during measurement, there is no possibility for direct measurement of the series capacitance of the winding *C*s. Only, *C*p, the capacitance between windings, and *C*g, the capacitance of winding to ground are measurable.

Measurements are performed using a GW Instek precision meter LCR-8000G. The measurement results are presented in Table 5-4.

5.1.2.2 *Measurement of magnetizing and leakage inductances*

The magnetizing and leakage inductances are calculated using (2-71) and (2-72) respectively [55] at the frequencies of f_L_m = 5 kHz and f_L_s = 100 kHz from impedance curve recorded using the RLC meter. The calculated values are L_m = 4.5e-3 mH and L_s = 27.5 µH which are comparable with the 4.4 mH and 26.6 µH respectively, achieved from direct measurements.

5.1.2.3 *Obtaining impedance curves by FRA measurements*

Frequency Response Analysis (FRA) is used to obtain the circuit impedance for two open and short circuit cases. This method is used to measure the transfer function or alternatively the input and output impedances of an electrical network. Every change in the transformer internal physical condition will cause the impedance characteristics or the frequency response of the transformer to be affected [15]. The impedance values are calculated using the measured FRA values in dB where dB = 20Log_{10} Z.

Although a programmable RLC meter can also be used for Z curve measurements on supplied terminals, measurement using a frequency response analyser is more convenient as the frequency response curves are displayed in real time at all the frequency range. In addition, the signal to noise ratio at lower frequencies is much better for a frequency response analyser.

The FRA measurements were performed using an Agilent Technologies E5061B vector network analyser (Figure 5-4) at two different conditions, when the transformer is open circuit and when it is short-circuited at the HV side (Figure 5-5).

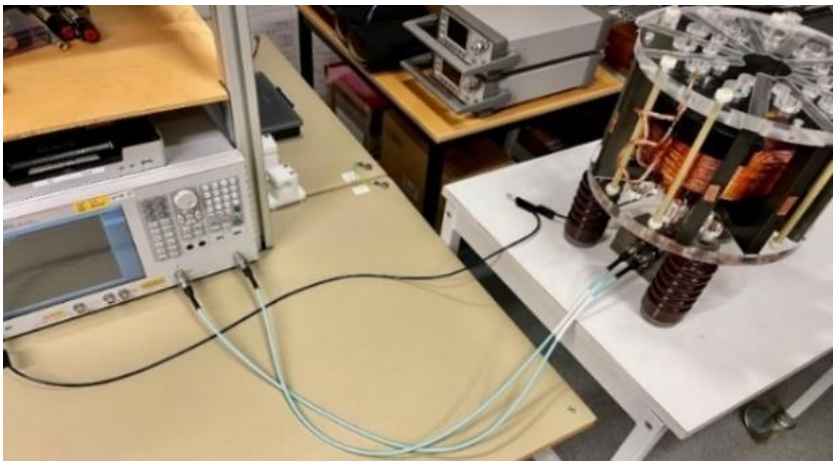

Figure 5-4. A network analyser used to measure the frequency response of the MFT

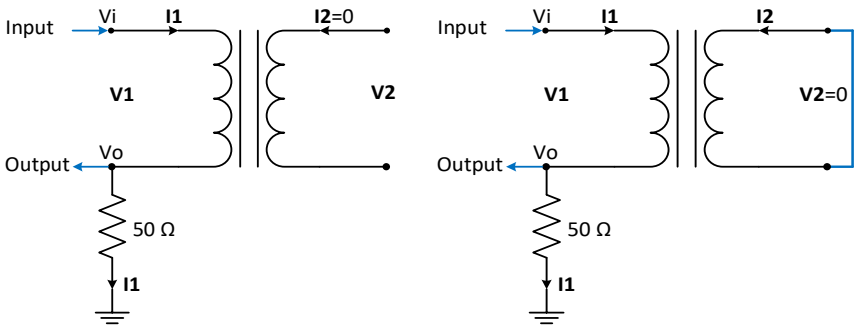

(a) ***(b)***

Figure 5-5. Two different conditions during FRA measurement when the transformer is open circuit (a), and when it is short-circuited (b)

To obtain the impedance curves from FRA measurement results, first, shall the magnitude (dB) and phase (rad) curves, (recorded during the FRA measurements) be converted to a Z (Ω) or impedance curve. For the circuits presented in Figure 5-5, $H = V_o/V_i$ and $Z = V_1/I_1$ and therefore

$$Z = \frac{V_1}{I_1} = \frac{V_i - V_o}{V_o / 50} = \frac{50(1-H)}{H} \qquad \textbf{(5-1)}$$

The impedance curves extracted from measurements are presented in Figure 5-6. These measurements result in the resonance frequencies of f_1 = 24.6 kHz, f_2 = 303 kHz and f_4 = 1.56 MHz when the HV side is open circuited and f_3 = 1.53 MHz when the HV side is short circuited.

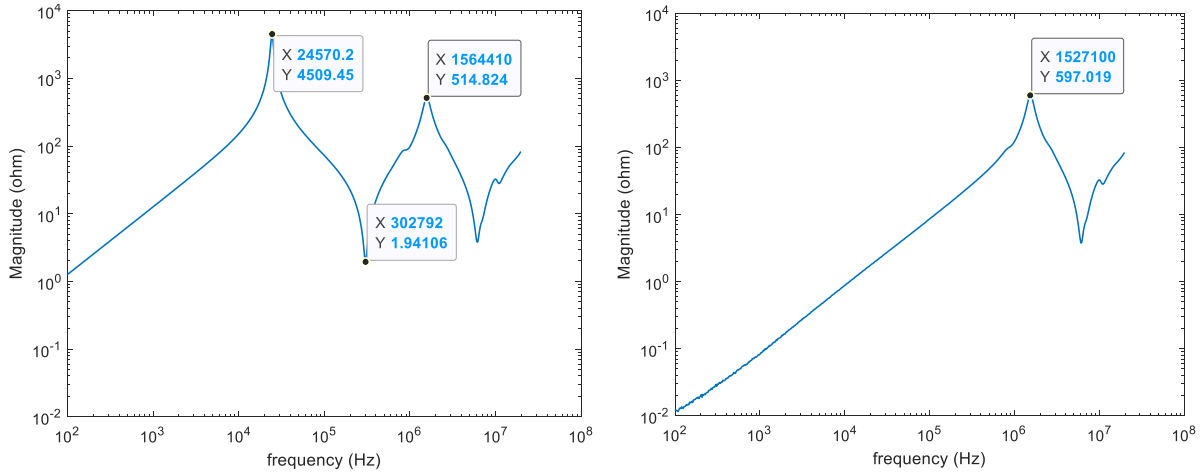

(a) ***(b)***

Figure 5-6. Frequency swept curves extracted from FRA measurements; Zoc (a) and Zsc (b)

5.1.2.4 *Comparison and validation of the proposed methods*

The calculation of the capacitance between the windings and core is not a straightforward task. The core is divided into several sections and has a varying and relatively long distance from the windings. A 3D FEM model is used for the calculation of the winding-core capacitances as well as the HV-LV inter-winding capacitance. To check the validity of the results, standard measurements are conducted. During a standard test both HV and LV winding terminals are short circuited to form an HV or LV electrode. There is an acceptable similarity between the simulation and measurement results (Table 5-4).

Table 5-4. Winding-core capacitances, measured and simulated (pF)

	Measured		FEM simulation	
Capacitance (pF)	LV	HV	LV	HV
LV	172	23	154.2	25.4
HV	23	33	25.4	31.8

Table 5-5 presents a comparison of the resonance frequencies obtained from the two different calculation methods compared with the actual measurement results as reference.

Table 5-5. A comparison between the resonance frequencies from different methods with the actual measurement results

	f_1 kHz	Deviation from measure. **%**	f_2 kHz	Deviation from measure. **%**	f_3 MHz	Deviation from measure. **%**	f_4 MHz	Deviation from measure. **%**	Total Deviation Sum of squares **%**
FRA measurement	24.6	-	303	-	1.53	-	1.56	-	-
MF method	23.2	-5.7	307	1.3	1.44	-5.9	1.47	-5.9	**5.1**
Extended method	24.4	-0.8	311	2.6	1.51	-1.3	1.54	-1.3	**1.7**

As can be noticed, both the extended and the MF methods are appropriate for transformers used in power electronic applications. The results are promising and sufficiently representative for transformer´s parasitic capacitances. The discrepancies with the measured resonance frequencies are in the range of 5%. In the extended method, the deviations are even smaller and are less than 2%. If only a simple equivalent circuit is needed, the MF method introduced for power electronic transformers can be compared with the method introduced in the literature [55, 56] (Figure 2-25). To do this, it should be assumed that the LV_2 and HV_2 terminals are grounded in Figure 2-26 and therefore, $Cg_1/2$, $Cp/4$ and $Cg_2/2$ capacitances will be short-circuited. In this way, the capacitances C_1, C_{12} and C_2 in Figure 2-25 will be $Cg_1/2+Cs_1+Cp/4$, $Cp/4$, and $Cg_2/2+Cs_2+Cp/4$. For the second run, the capacitances C_1, C_{12} and C_2 are supposed to be Cg_1+Cs_1, Cp and, Cg_2+Cs_2 which is the case for the model proposed in the literature.

Comparing the results with the extended model as the reference, reveals that for a similar circuit arrangement, (i.e., earthing condition of the winding terminals) the MF model is more precise in comparison with the model introduced in literature even for conventional transformers (Table 5-6).

Table 5-6. A comparison between the resonance frequencies from the MF and literature methods with the extended method results

	Extended method		MF method	Literature model
f_1 (kHz)	24.3		21.5	18.9
f_2 (kHz)	312		286	253
f_3 (MHz)	1.48		1.39	1.28
f_4 (MHz)	1.52		1.43	1.33
Total deviation Sum of squares (%)	-		**8.3**	**17.3**

5.1.3 Core losses

Core losses can be measured by two methods: using a power analyser or using a Volt-Ampere method.

5.1.3.1 *Volt-Ampere method*

The Volt-Ampere method is implemented by a Brockhaus MPG200 measuring unit (Figure 5-7a) which is used for a series of loss measurements in this work. This method is based on an instantaneous voltage-current sampling and integration method and uses the current signal sampled from the primary side (using an magnetising current from supply side) together with the voltage signal sampled from the secondary side (open circuit voltage which is equal to the magnetizing voltage from the primary side considering the transformation ratio) (Figure 5-7b).

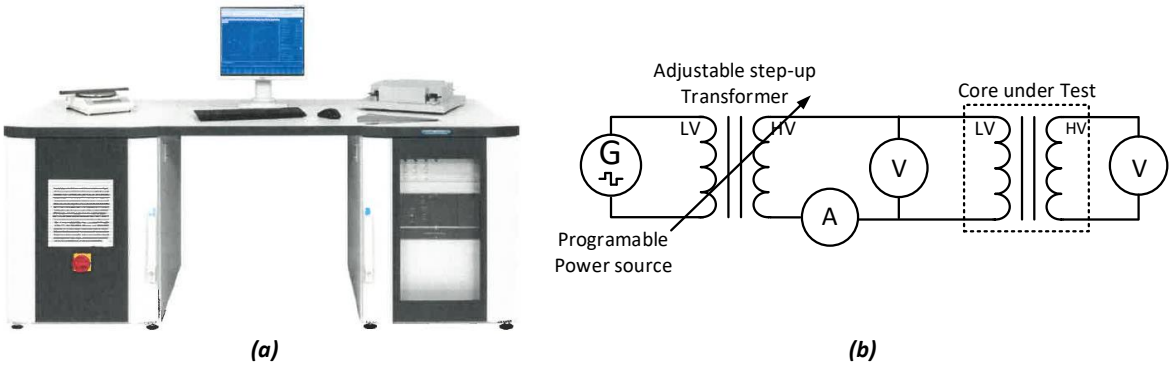

(a) ***(b)***

Figure 5-7. The circuit diagram for measuring core losses: Brockhaus MPG200 core test system (a), and the Volt-Ampere method circuit diagram (b)

The product of voltage and current samples are integrated over a set of measuring cycles using [133]

$$P_i = \frac{1}{w_e.T}\frac{N_1}{N_2}\int_0^T v_L i_L dt \qquad \textbf{(5-2)}$$

where w_e is the mass of the core, T is the time period, N_1 is the number of primary winding turns; N_2 is the number of secondary winding turns, v_L is the voltage on the open secondary side and i_L is the current at the primary side.

The tests have been performed applying a precise wave shape and frequency on a type of Nanocrystalline cores and a type of Ferrite core (Table 5-7).

Table 5-7. The core samples undergone the measurements

	Nano	Ferrite
Core type	Hitachi FINEMET ® F3CC Series Cut Core [105]	93/152/30 N87 [104]
Weight (kg)	2.2625	754.7 x 2
Mean magnetic length L_m (mm)	410.2	352.9
Filling factor k_c	693/(29.6 x 30) = 0.78	1
Density (kg/m^3)	7300	4850
Magnetic cross-section *Ac* (mm^2)	30 x 29.9 x 0.78 = 699.7	840
Operating temp (°C)	20-155	25-100

Demagnetization before each measurement has been performed. Measurements has been performed in room temperature. Four windings are wound to be used for supplying the magnetizing current and to pick up the voltage on the two core limbs. The limit of 100 V and 52 A from the unit has dictated the selected number of turns and type of connections of the windings (series or parallel) (Figure 5-8).

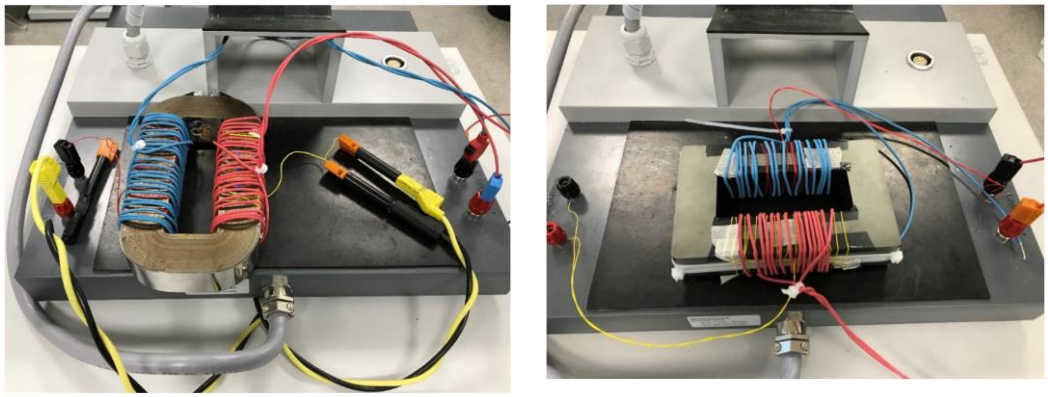

(a) ***(b)***

Figure 5-8. Voltage pickup and current supplying coils connected to the measuring circuits: The nanocrystalline core (a), and the ferrite core (b)

A sample recorded current, voltage and *B/H* curve at 5 kHz applying sinusoidal and square wave shapes are presented in Figure 5-9. The test results are summarized in Table 5-8. It is noticeable that at room temperature, the losses are not dependent of the wave shape change from sinusoidal to square wave shape at 5 kHz if the flux density is kept under 0.3 T. This becomes clearer comparing the recorded B/H curves at different excitation voltage shapes.

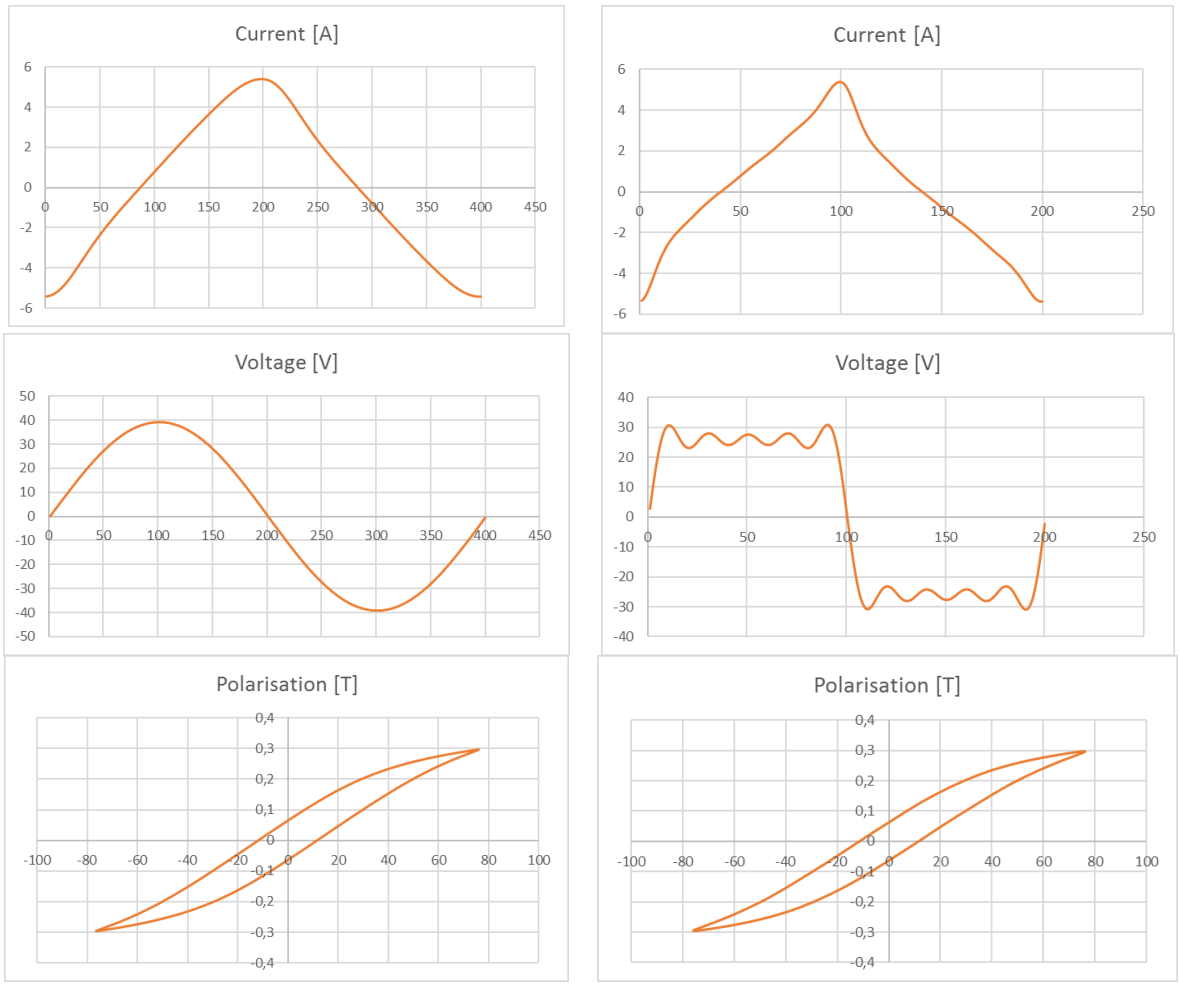

(a) Sinus 5 kHz, 0.3 T ***(b) Square 5 kHz, 0.3 T***

Figure 5-9. The recorded current, voltage and B/H curves applying different wave shapes

Table 5-8. Summary of loss density measurements (W/kg) on two high frequency core samples

	Nanocrystalline				Ferrite			
Flux density (T)	0.1 (Data sheet)		1.0 (= 1.23 x 0.8)		0.3 (= 0.38@100°C x 0.8)		0.4 (= 0.49@25°C x 0.8)	
f (kHz)	Square	Sinus	Square	Sinus	Square	Sinus	Square	Sinus
1	0.0108	0.0121	1.333	1.3096	2.2679	2.1599	4.2998	4.2147
2	0.0227	0.0283	2.937	3.2474	4.3549	4.4404	8.1522	8.6792
4	0.0561	0.0724	8.0898 (0.975T)	8.9581	9.0285	9.3601	17.4141 (0.39T)	17.8390
5	0.0788	0.0909	10.291 (0.96T)	12.292	11.6345	**11.6518**	21.4151 (0.38T)	22.6056
8	0.159 (8.3kHz, 0.093T)	0.2013	25.184 (8.3kHz)	24.773	20.4339 (8.3kHz)	19.6096	40.8608 (8.3kHz)	37.9127
10	0.181 (9.1kHz. 0.093T)	0.261 (9.5kHz)	33,383	31,025 (9.5kHz)	25.0809	25.2984	48.5436	49.0182

HVDC MFT core losses

First to verify the calculation, the measurement procedure is applied to recalculate the already measured core losses of the previously manufactured dry type planar Ferrite design MFT [13]. The total volume of the cores is 0.0030576 m^3 and their total weight 14.83 kg. Applying the same loss density of 11.65 W/kg (from Table 5-8), the total core losses will be 172.76 which is comparable with the measured value of 171.4 W at room temperature and the flux density of 0.32 T.

The measurements performed on the Ferrite cores used for HVDC MFT prototype at 0.3 T demonstrates that for each core the loss at 5 kHz square wave excitation is about 11.65 W/kg (Table 5-8). The density of core is 4870 kg/m^3 according to its datasheet. Consequently, the measured losses can be presented as 56.7 kW/m^3. The total volume of the cores is 0.002772 m^3 according to Table 5-9. Therefore, the total core losses for the transformer at 0.3 T will be approximately 160.1 W. Based on the cores technical data, at a working temperature 80 °C the core losses will be reduced by 33% for the prototype and will reach 107 W [104].

Table 5-9. The specification of the core used for manufacturing the prototype transformer

Core type	B67385U 126/91/20
A_c, Core cross-section (mm^2)	560
Weight of one U core (kg)	0.675
Volume of one U core (m^3)	0.0001386
Total weight of cores (kg)	13.500
Total volume of cores (m^3)	0.002772

5.1.3.2 *Direct power measurement method*

To determine the core losses, when it was not possible to use the Brockhaus test system, a simplified system was used. An audio amplifier is used to amplify the signals generated by a signal generator to the desired voltage level and the core loss measurement has been performed at supply terminals by a precision Power analyser (Figure 5-10).

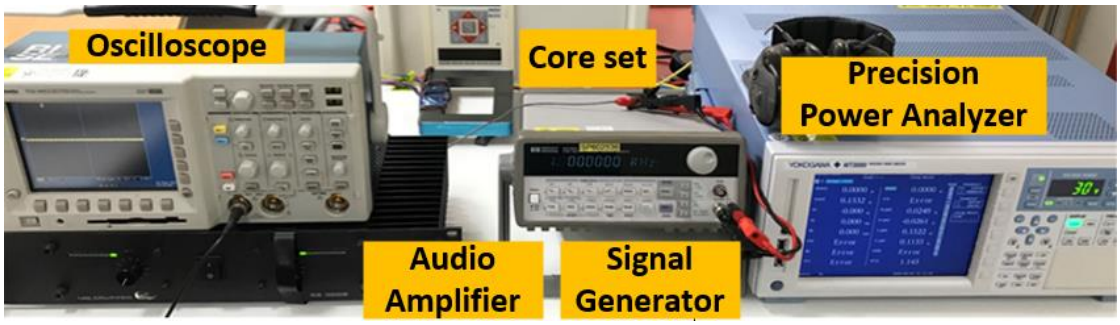

Figure 5-10. Core loss measuring test setup

The second series of core loss measurements are performed using a power analyser which is designed to handle the very low phase angles between the voltage and current. A Yokogawa WT3000, precision power analyser is used for the direct loss measurement. It is obvious that the voltage-drop in the supply winding due to magnetising current is also measured. As a result, the measured loss will be slightly higher than the real loss. To make a correction, a 4 turns coil was wound to pick up the supplied voltage to the primary while the supplied current is measured from the main winding. Table 5-10 demonstrates the calculations made to determine the voltage that should be set on a 4-turn winding around the core during a one core set loss measurement.

Table 5-10. Preliminary calculations to perform direct core loss measurements

Core type	B67385U 126/91/20
A_c Core cross-section (mm^2)	560
K_c Filling factor	1
Weight of one U core (kg)	0.675
Volume of one U core (m^3)	0.0001386
Total weight of cores (kg)	13.500
Total volume of cores (m^3)	0.002772
Flux density @421.9 V & 5kHz square (T)	0.32
Required test Square Voltage @0.32 T & 5 kHz (V)	421.90
Applied to 4 turns one core Square Voltage @0.32 T& 5kHz (V)	14.06
Required test Sinusoidal Voltage @0.32 T & 5 kHz(V)	468.86
Applied to 4 turns one core Sinusoidal Voltage @0.32 T & 5kHz (V)	15.63

The required voltage to achieve the rated flux density is calculated for both square and sinusoidal waves using (2-30) and (2-31) respectively. The required voltage to reach the same flux density for the sine wave feeding is higher than the voltage for the square wave. Table 5-11 shows the result of measurements for the sinusoidal- and square- wave-shapes at nominal flux densities of the core in the frequency range of 1 to 10 kHz at room temperature. The results show that the losses for sine wave is slightly higher than that of the square wave.

Table 5-11. Ferrite N87 core loss measurements results at room temperature using the simple setup

Frequency (kHz)		1	2	3	4	5	6	7	8	9	10
Square											
4 turns supply	Nom. Volt.	2.8	5.6	8.4	11.2	14.1	16.9	19.7	22.5	25.3	28.1
Voltage from Aux	App. Volt.	2.8	5.6	8.4	11.3	14.1	16.9	19.7	22.5	25.3	28.1
One UU core	Meas. Curr.	4.4	4.4	4.4	4.4	4.5	4.5	4.5	4.5	4. 6	4.57
	Meas. Loss	2.9	5.9	8.9	11.9	15.0	18.0	21.0	24.5	27.3	30.6
Ten set of ∩ U cores	Total Loss	29.0	59.0	89.1	119.3	**149.6**	179.7	210.5	244.6	273.5	306.0
Sinusoidal											
4 turns supply	Nom. Volt.	3.1	6.2	9.4	12.5	15.6	18.7	21.9	25.0	28.1	31.3
Voltage from Aux	App. Volt.	3.1	6.2	9.4	12.5	15.6	18.7	21.9	25.0	28.1	31.3
One UU core	Meas. Curr.	5.5	5.5	5.5	5.5	5.5	5.5	5.5	5.4	5.48	5.45
	Meas. Loss	3.0	5.9	8.8	11.9	15.0	18.1	21.5	25.0	28.4	32.1
Ten set of ∩ U cores	Total Loss	29.6	58.4	88.2	118.6	**150.0**	181.5	214.9	250.3	284.4	320.6

5.1.4 Winding losses

To verify the calculation method, measurements have been performed on the built prototype Decagon MFT (Figure 5-1a). Table 5-12 presents the dimensions data of the designed prototype.

Table 5-12. Dimensions data of the Ferrite prototype

	Sizes in (mm)
Primary winding	
Number of turns (4 layers)	12
Thickness	10
Thickness (built prototype)	10.8
Wire height (8 parallel conductors)	30.4
Magnetic height	91.2
Magnetic height (built prototype)	94
Physical height	121.6
Secondary winding	
Number of turns (16 discs)	128
Thickness	20
Wire height	3.8
Magnetic height	60.8
Magnetic height (built prototype)	68
Physical height	60.8

5.1.4.1 *DC resistance*

The resistances of the finished windings are measured using a precision HP 3458 multimeter at 20 °C. The cores' magnetizing circuits were open during the resistance measurement (Figure 5-11). This omits the possibility of measuring the core magnetizing current in addition to the resistive current, the current stabilizes very quickly, and the measurement time will be reduced dramatically.

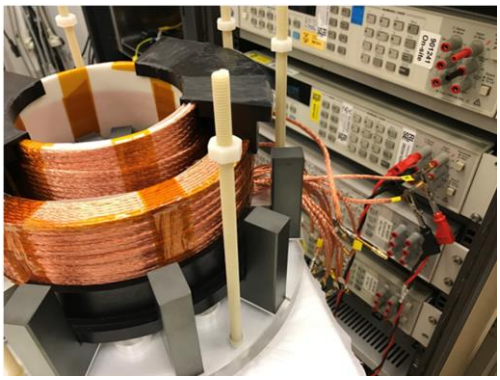

Figure 5-11. DC resistance measuring setup

The calculated DC resistances using (2-99) and the measured values are presented in Table 5-13.

Table 5-13. Comparison of calculated and measured DC resistances at 20 °C

Measured from	Secondary	Primary
Calculated	274.262	2.322
Measured	276.36	2.402

The RI^2 losses when a DC current is applied are calculated and presented in Table 5-14.

Table 5-14. Calculated and measured resistances and calculated RI^2 losses at 20 °C

	Secondary	Primary
Calculated R (mΩ)	274.262	2.322
Rated r.m.s current (A)	11.11	118.5
Calculated DC, RI^2 losses (W)	34	33
Transformer DC, RI^2 losses (W)	**66.46**	

5.1.4.2 *Short-circuited transformer AC resistance*

To evaluate the effect of frequency on the losses, the AC resistances are measured for the frequency range of 100 Hz to 10 kHz using an Agilent E4980A RLC meter. As it can be seen in Figure 5-12, the change of AC resistance is not significant below 1 kHz. It is shown in Table 5-17 that the losses calculated from the measured AC resistances agree excellently with the values resulted from FEM simulations.

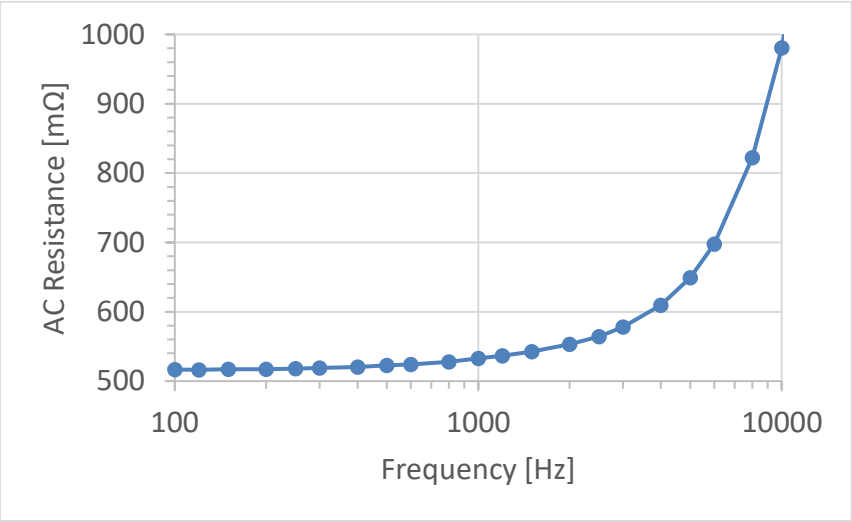

Figure 5-12. Series inductance and AC resistance measured from the secondary side while the primary side is short-circuited

5.1.4.3 *Load losses*

The winding loss measurement circuit is demonstrated in Figure 5-13.

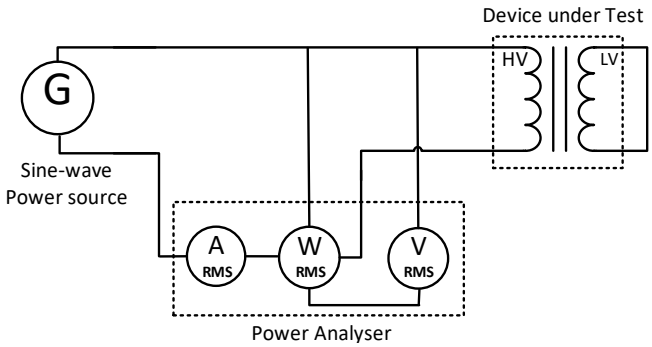

Figure 5-13. Windings loss measurement circuit diagram

The voltage, current and the power parameters were registered using a precision power analyser. The supply source used was a Chroma 61605 AC, 0-1000 Hz power supply (Figure 5-14). To measure the total losses in the primary and secondary windings, the rated current of the transformer shall be applied to the windings. At the secondary side, when the primary side is short-circuited (Figure 5-14), the voltage is raised until the maximum current, near to the rated current, passes simultaneously in both windings. The losses are measured as fast as possible to capture the losses at room temperature.

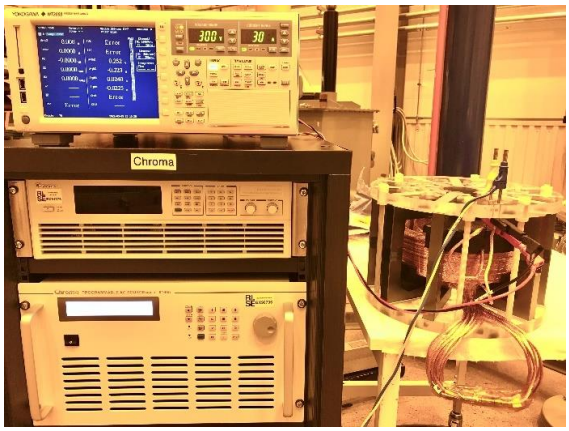

Figure 5-14. Windings loss measurement setup on prototype MFT

The load loss is measured at room temperature using the short circuit method and the DC resistance values at room temperature (20 °C) is used to estimate the load losses at the operation temperature (reference 80 °C). The load losses under full loading were calculated at rated current and reference temperature from the reduced current and room temperature measurements according to Table 5-15.

Table 5-15. Load losses at rated current and reference temperature (80 °C) at 1kHz from room temperature measurements

Total RI^2 losses at 20 °C	66.46
Calculated RI^2 losses at 80 °C	81.98
Measured Load losses at 20 °C and 1 kHz	67.52
Additional Losses (measured total losses minus calculated RI^2 losses at 20 °C)	1.06
Calculated Load losses at 80 °C (calculated additional losses plus calculated RI^2 losses at 80 °C)	**83.04**

The losses in the extra wires (between the winding turns and the terminals) are considered according to Table 5-16.

Table 5-16. The losses in extra wires

Extra wire	mm	mΩ	A	W
LV	400	0.159	118.5	2.23
HV	1800	5.724	11.11	0.71
Total				2.94

The numerically calculated values are corrected to include the losses in the extra wires out of the winding and the 4 % extra length of the litz wire strands. It means that the calculated value should be added with 2.94 and the result should be multiplied by 1.04. Table 5-17 demonstrates the rise of AC resistance measured from the secondary side while the primary side was short-circuited. The resulting increase in the calculated losses in comparison with the losses directly measured, and also calculated by the numerical method, are also presented in the same Table.

Table 5-17. The rise in AC resistance and calculated winding losses at 20°C compared with the measured value

Frequency (Hz)	Measured AC resistance from HV side (mΩ)	Losses calculated from AC resistance (W)	Losses Measured by Power Analyser (W)	Losses Calculated by FEM (W)
1000	533	65.8	67.5	67.2
2000	553	68.3	-	68.9
3000	578	71.3	-	71.6
4000	610	75.3	-	75.3
5000	649	80.1	-	**80.1**

Additionally, as demonstrated in Table 5-18, the total impedance of the short-circuited transformer calculated by the measured R and L values achieved from the RLC meter is comparable with the calculated impedance from the voltage and current values registered by the Power analyser.

Table 5-18. Comparison of the impedance measured by the RLC meter and during the winding loss measurements

1 kHz	Decagon
L (nH)	3023335
R (mΩ)	532.86
Z (Ω), RLC meter	**18.99**
U (V)	215.21
I (A)	11.34
Z (Ω) at rated current	**18.98**

As a direct supply of the rated current under short circuit condition at 5 kHz was not possible, putting all the above-mentioned data together, the load losses of the Decagon transformer at 80 °C, 5 kHz and at the rated current will be 95.6 W. This value is obtained by replacing the measured load loss at 1 kHz (67.52 W) in Table 5-15 with the load loss at 5 kHz (80.1 W) presented in Table 5-17.

5.1.5 Measurements on MFT installed in a DAB

As a DAB become available in the last stages of the project, an experimental setup is arranged to measure the actual wave forms of the voltage and current (Figure 5-15). The purpose of the test was to compare the measurement wave forms with the wave forms achieved from simulations when the actual parameters of the transformer and DAB are implemented in the simulation.

(a) ***(b)*** ***(c)*** ***(d)***

Figure 5-15. The DAB setup for recording the wave of the prototype MF: the DAB and control and recording setup (a), the MFT under test(b), the four-channel oscilloscope for recording the wave form (c) and the voltage and current probes for accurate acquisition of the waveforms (d)

A DAB built of Imperix PEB 8038 - Half-bridge SiC power modules is used [134] (Figure 5-16), which uses silicon carbide power switches. The maximum operating frequency was adjusted to 5 kHz for the test. The maximum ratings of the bridge were 800 V DC and 38 A r.m.s..

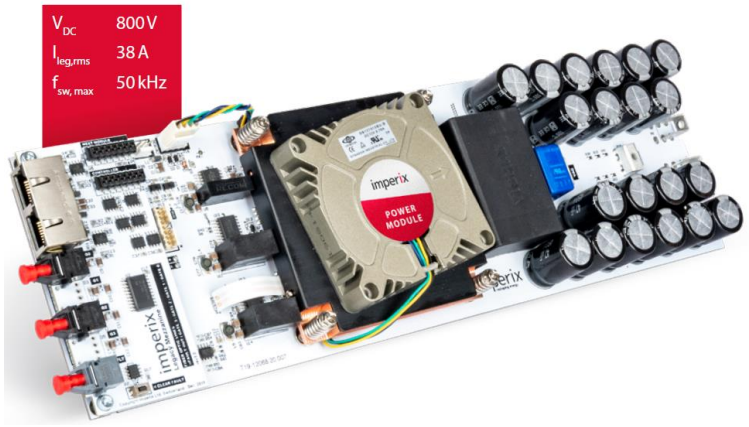

Figure 5-16. An Imperix PEB 8038 - Half-bridge SiC power module [134]

Figure 5-17 presents the Simulink model used for obtaining the current and voltage wave forms for comparison with the measurements.

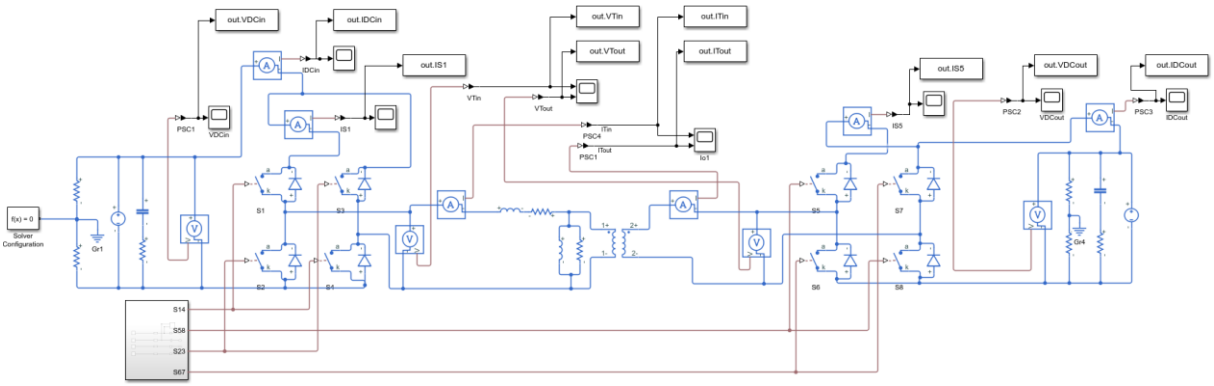

Figure 5-17. The Simulink model used for obtaining the wave forms

The transformer data is set in Simulink and the waveforms are obtained. The recorded wave forms and the wave forms obtained from the simulations are demonstrated in Figure 5-18 which shows the conformity of the simulation with the measurements.

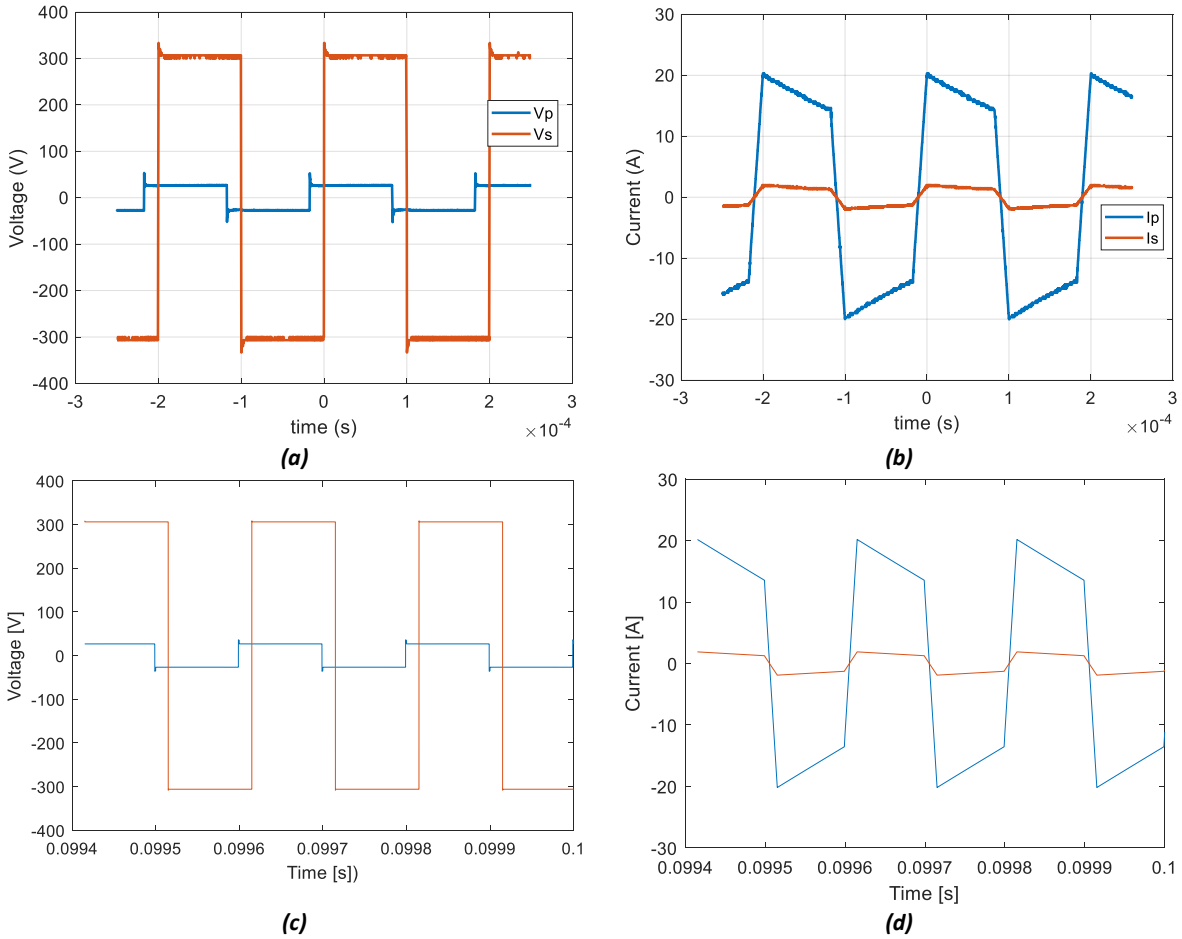

Figure 5-18. The recorded voltage (a) and current (b) wave forms, and the voltage (c) and current (d) wave forms obtained from the simulations

5.1.6 Insulation test

To verify the insulation design, the insulation prototype is subjected to a high voltage DC stress test. The duration of voltage application was determined by the results of the simulation showing that a dynamic voltage distribution can continue up to 4000 seconds (Figure 4-7).

The test circuit is shown in Figure 5-19. The applied voltage was measured by a precise 150 kV DC voltage divider and was registered using a data acquisition system (Figure 5-20). The transformer successfully passed the test and no breakdown occurred during HVDC application. The design voltage of 125 kV is applied. A final breakdown voltage could be determined by performing a repeated test procedure on the several similar test objects by a gradual increasing of the test voltage after each breakdown. This value can help the designer to investigate proper safety factors for the designs. Such investigation was not in the scope of this study.

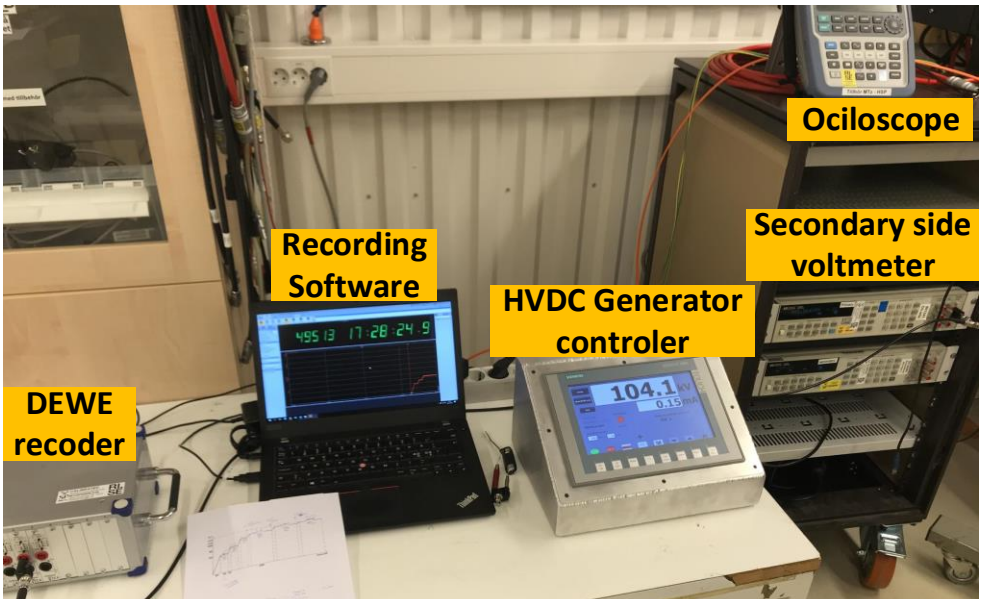

(a)

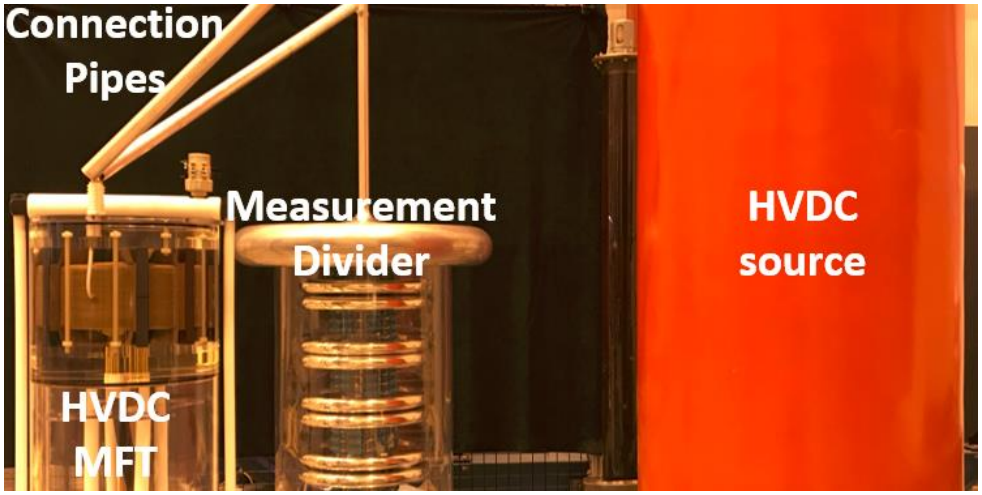

(b)

Figure 5-19. Insulation prototype HVDC testing setup: the HVDC voltage control & measuring setup (a), and the high voltage test setup (b)

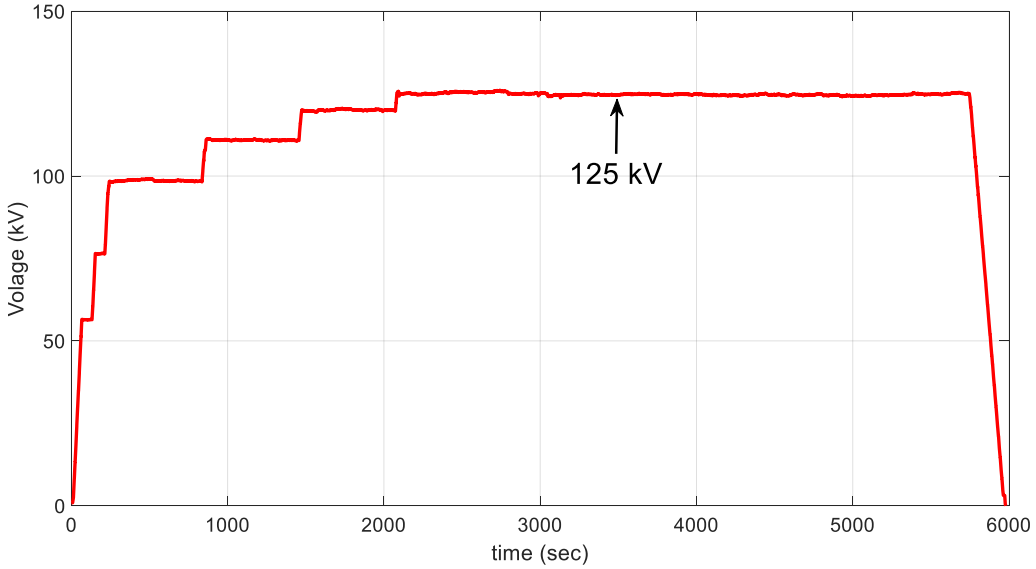

Figure 5-20. Applied voltage-time to HVDC MFT prototype

5.2 Non-suitability of dry insulations for high voltage DC transformers

Here motivations for using oil as insulation material for the targeted transformer is presented which is completed with a simple analysis. Insulation materials operating under HVDC conditions will absorb more contaminations compared to the case of AC operation. Under AC operation the net absorption effect is near zero. In addition, the electrical field distribution on the surface of the insulation material is purely resistive and therefore, several factors can change the field distribution along the discharge paths; among others, the nonlinear nature of surface resistivity, charge accumulation and surface contamination and humidity can be mentioned here [135]. In addition, as Figure 5-21 demonstrates, under AC excitation, with the application of few kVs there will be corners with an electric field easily exceeding the corona inception voltage in air.

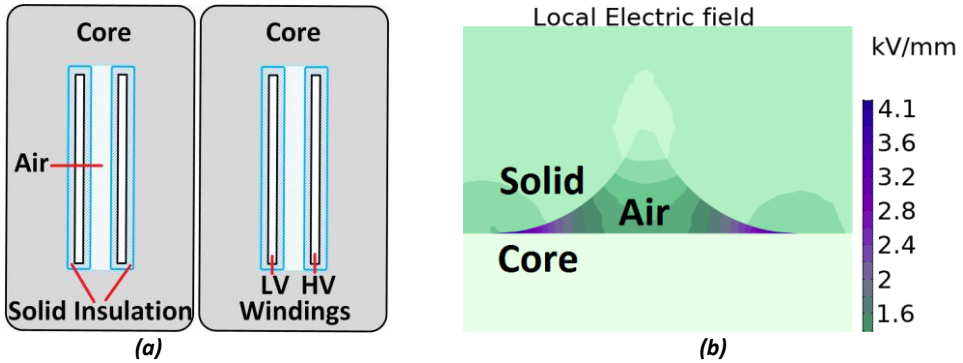

Figure 5-21. High electric stress in the air in the vicinity of solid insulation of windings: The previously build dry type MFT prototypes [13] (a), and the field stress at the corners (b)

5.3 Insulation design analysis of a biodegradable oil based MFT

In this section an important research question is answered: what the effects of switching from mineral oil to ester oil on the insulation design aspects under DC stress are. The insulation design of an HVDC MFT using biodegradable oil and OIP is analysed based on the method developed previously, which was verified by experimental testing. Consequently, the performance of the ester-based insulation system is analysed and compared with the case when mineral oil is used. Furthermore, in addition to the previously considered safety factors of the insulating oil gaps and creepage paths, a novel criterion based on the combined path is suggested.

The dielectrics of the MFT is under time varying electric field stresses, which change from the initial permittivity-based distribution to the final conductivity-based distribution, including the transient phase in-between. To find exact values of the stresses on dielectric materials, computer simulations were conducted utilizing time dependent electric current physics in the COMSOL Multiphysics software. Owing to the vertical symmetry at the core window section, only the upper part of the design is considered. A DC voltage is applied to the HV winding while both the LV winding and the core are supposed to be at ground potential (Figure 5-22).

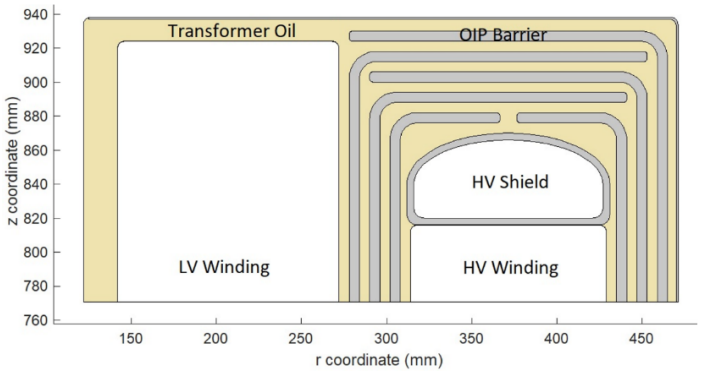

Figure 5-22. The dielectric structure of the oil-type MFT

For the combined AC and DC voltages on the HV winding of the MFT, the magnitude of the DC voltage (250 kV) is much higher than the AC voltage (18 kV). In this way, applying just a step of HVDC voltage to this winding can be considered enough to simulate the operational condition. The logarithmic time steps from t = 1 s (the instant of HVDC application) to t = 10000 s (when the steady state condition supposed to be reached) are considered to find the solutions. The conductivities of the ester oil/OIP and mineral oil/OIP materials depend on the temperature and the instantaneous electric field intensity. Therefore, as a basis for a Non-Linear Maxwell Wagner (NLMW) solution, explained in Section 2.2.10.4, three separate sets of simulations were performed for 30, 50 and 90 °C temperatures for ester oil/OIP, and similarly, for mineral oil/OIP. In each set, the measured results from Table 3-1 & Table 3-2 were used as two input local tables of stress dependent conductivities in COMSOL. The electric field distribution was investigated during three distinguished time periods: initial, final and transient stages. Subsequently, a smart algorithm for dielectric stress evaluation is applied.

5.3.1 Initial stress distribution

Figure 5-23 demonstrates the initial distribution of the electric stress at the insulation system immediately after the application of 250 kV DC which is based on the Permittivity Ratio (PR) of the oil to the OIP. The dielectric permittivity does not depend on temperature, and therefore, the initial distribution of the stresses is temperature independent. Since the permittivities of the oils are lower than that of the OIPs, in both ester and mineral oils, the stresses in the oil channels are higher than the stresses in the OIP barriers. However, since the PR of the ester oil to ester OIP (3.5 to 4.6) is lower than the PR of the mineral oil to mineral OIP (2.2 to 4.4), for the case of the ester oil, the initial stresses in the OIPs is higher than that in the mineral oil. As shown in Figure 5-23, the distribution of the streamlines is nearly the same for ester and mineral oils and the highest stresses in both cases are at the sides of the HV shields and in the oil. Moreover, as can be seen from the colour bars, the maximum stress in the mineral oil is slightly higher than that in the ester oil.

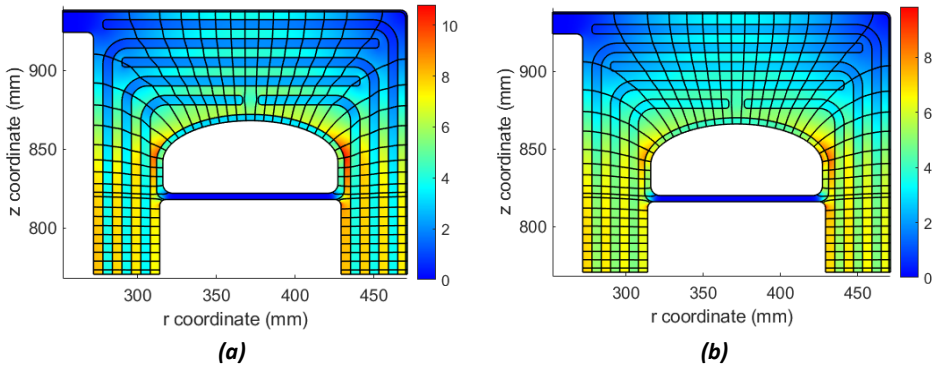

(a) ***(b)***

Figure 5-23. The initial permittivity-based stress distribution in kV/mm (the colour bar unit) and the electric field streamlines in the dielectric structure of the MFT using: the mineral oil (a), and the ester oil (b)

5.3.2 Steady state stress distribution

Figure 5-24 illustrates the final steady state stress distribution in the MFT insulation system by using both ester and mineral oils. It can be easily seen that they are temperature dependent due to the temperature dependence of the Conductivity Ratio (*CR*) of the oil to OIP. However, the temperature dependency of *CR* of the ester oil is weaker than that of the mineral oil, and hence, higher consistency of stress distribution regarding the temperature variation of the operation condition can be observed in the case of ester oil usage.

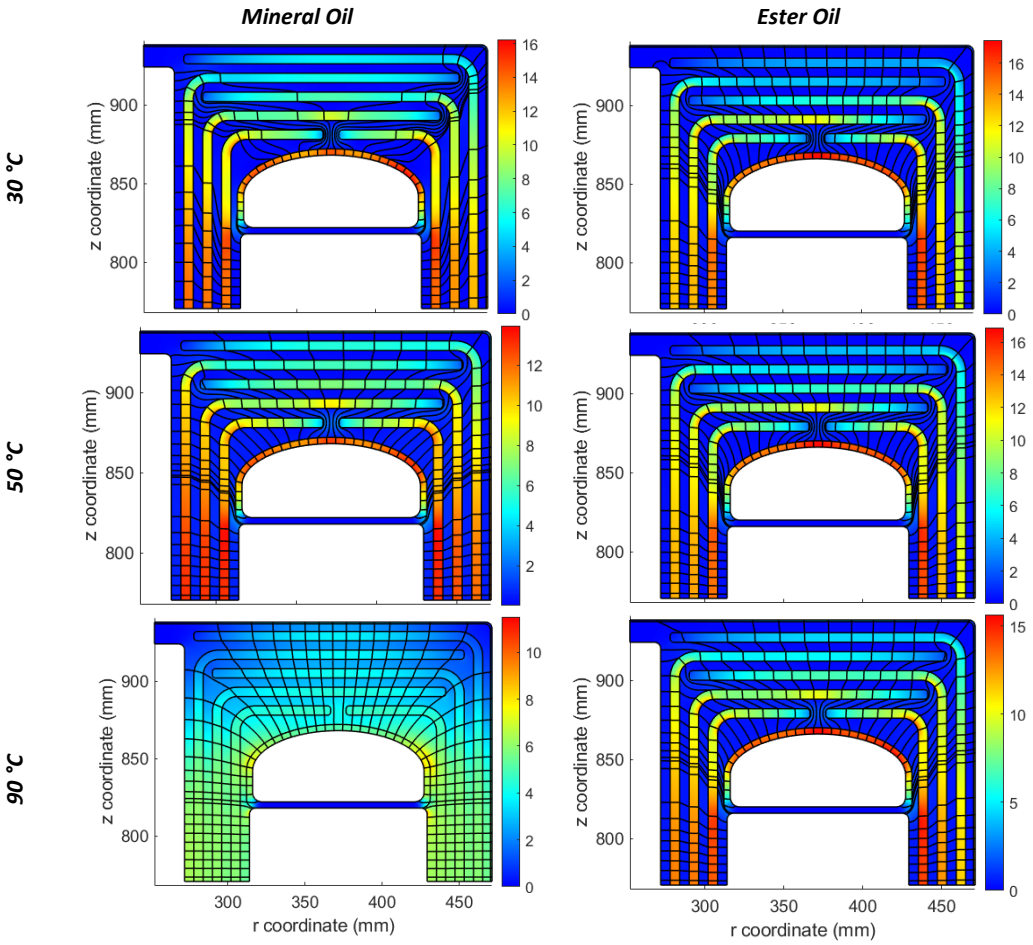

Figure 5-24. The final steady state stress distribution in kV/mm (the colour bar unit) and the electric field streamlines in the dielectric structure of the MFT at different temperatures using: the mineral oil (left), and the ester oil (right)

5.3.3 Transient stress distribution

The transient phase, which occurs between the initial and final states, may last for some hours. To investigate the time-dependent behaviour of the stress in the dielectric structure of the MFT, seven various typical points were selected in this structure as shown in Figure 5-25.

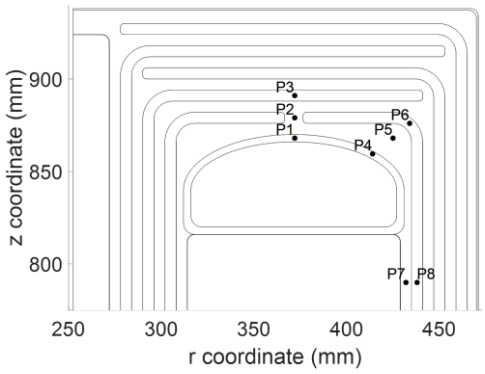

Figure 5-25. The position of typical points in the dielectric structure to investigate their stresses in time domain

The points P1, P3, P4, P6 and P8 indicate the locations inside OIPs and the other remaining points are in the oil channels. The curves presenting time dependent stresses at these points are demonstrated for each temperature (30, 50 and 90 °C) in Figure 5-26. The time axis is plotted up to 160 min for mineral oil and 2 min for the ester oil. It can be noticed that the major differences caused by using ester and mineral oils are in the duration of the transient phase, the location of the maximum stresses, the final steady state distribution, and the effect of the temperature.

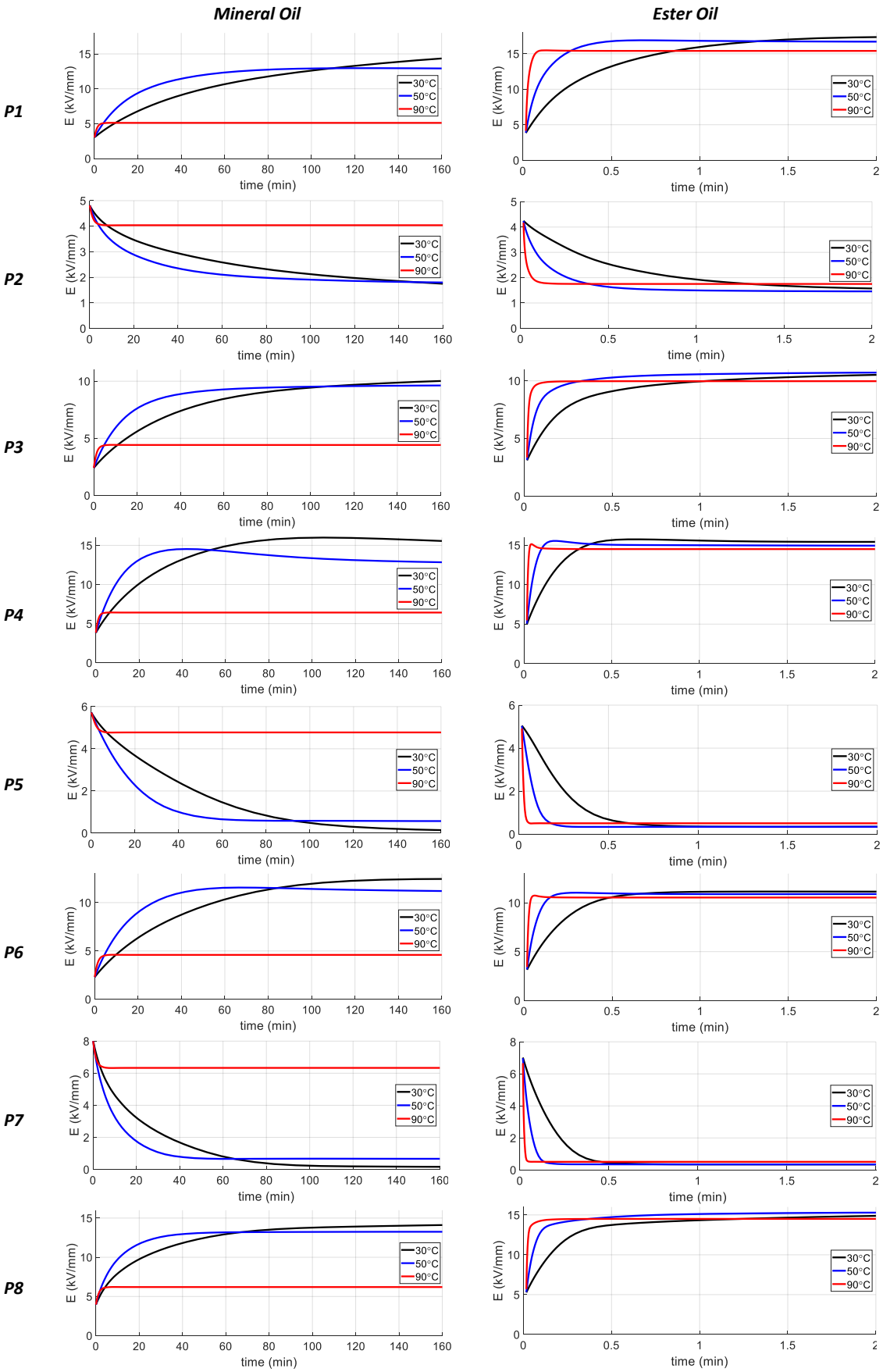

Figure 5-26. The time variation of stress curves of P1 to P8 using: the mineral oil (left), and the ester oil (right)

As mentioned previously, the initial stress distribution immediately after the HVDC application depends on the PR of the oil to OIP, and therefore, using ester oil causes higher stresses in OIPs with

respects to the mineral oil application. Moreover, using ester oil results in a shorter transient phase and faster transition to the steady state condition with respect to mineral oil. This is because of the lower time constants (the ratio of electrical conductivity to the permittivity of the insulation materials) when using the ester oil, which originates from its much higher conductivity with respect to the mineral oil. Additionally, an even faster transition can be observed at higher temperatures in both oils for the same reason.

For both oils, the stress in the OIPs at steady state is greater than their values at the initial state and the opposite is observed for stresses at oil gaps. Additionally, it can be noticed that the final steady state values for mineral oil at 90 °C differ considerably with respect to 30 and 50 °C, while this is not the case when using ester oil. This is caused by the fact that the *CR* of the oil to OIP has greater divergence with respect to the temperature in mineral oil than that for of the ester oil, see Table 3-1 and Table 3-2. Moreover, at points P1, P4 and P6, it can be observed that the local maximum stress can be higher than its initial and final values. This fact emphasizes that considering just the initial and final stress distribution is insufficient to obtain an accurate dielectric design evaluation, since the worst cases (in terms of stress in the dielectrics) may occur during the transient phase.

5.3.4 Dielectric design evaluation

Here, the dielectric design of the real scale MFT with application of ester oil/OIP is evaluated and investigated from the dielectric withstand viewpoint, and then the design is compared with mineral oil/OIP application. In order to evaluate the dielectric design automatically, COMSOL Live Link with MATLAB was utilized to identify the minimum safety factors in the oil gaps and creepage surfaces and maximum stress in the OIPs at various temperatures and for all the time steps. At every single time step of each time dependent FEM simulation, the maximum stress in the OIPs as well as the minimum safety factors in oil gap paths, creepage paths and combined paths were investigated.

5.3.4.1 *The maximum stress in OIP*

The OIPs bear a definite maximum permissible electric stress, below which they can work safely. This maximum stress is usually determined by experiments and is typically about 20 kV rms/mm according to [76]. Therefore, the maximum stress in the OIPs must be checked to be less than this value. For each streamline path of a FEM simulation and at each time step, the OIP path sections are extracted. The maximum electric field at all points of these sections are evaluated as a measure of the severity of the stress in OIPs. This procedure is illustrated in Figure 5-27.

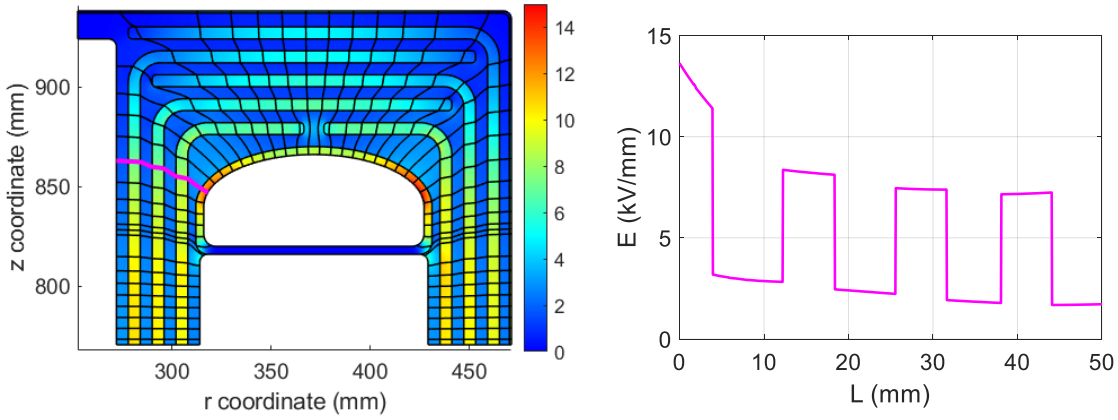

(a) *(b)*

Figure 5-27. The streamlines by using ester oil at 10 s and 30 °C: a sample streamline (thick pink line) (a), and the electric field curve along this streamline starting from the rightmost point (b)

5.3.4.2 *The safety factors in oil gaps*

Similarly, for each streamline path of the FEM simulation at each time step, the oil gap path sections are extracted (Figure 5-27), and then, the minimum safety factor (SF) for each path is calculated using the method described in [76, 99]. To obtain the SF for each oil gap path, the electric field curve along this path is extracted and rearranged in a descending order. Then, the cumulative stress curve, E_{av}, is obtained from (2-2) [76, 99]. Then the safety factor curve of the oil gap is calculated by dividing the cumulative stress curve to the breakdown strength curve of the oil (E_{bd}) from (2-3) and (2-4) [76, 99]. The safety factor of an oil gap is considered as the minimum value of the related safety factor curve. It is worth mentioning that the partial discharge inception voltage and breakdown voltages of synthetic ester oil is slightly higher than that for mineral oil [136], and therefore, (2-3) is assumed to be valid for ester oil with a safer margin.

5.3.4.3 *The safety factors in creepage surfaces*

The common surfaces of the oils and OIPs are disposed to creepage discharges created by the tangential field. According to [76, 99], the withstand level of such creepage surfaces can be considered as 0.7 of the oil gaps withstand level (E_{bd} or the partial discharge free field strength) . To investigate the creepage strength of the design, the tangential electric field on the creepage surface of each barrier is extracted. Then, its related curve along the surface path is divided into multiple sections at places where its value falls below 0.2 kV/mm [22] or its direction changes (Figure 5-28). Afterwards, the SF of each creepage path sections is calculated using a procedure like the one discussed for oil gaps; however, the factor 0.7 is introduced to account for the weakening of the strength at the surface due to possible creepage,

$$SF = \frac{0.7E_{bd}}{E_{av}} \tag{5-3}$$

As a replacement to (5-3), one can consider the same breakdown voltage for both the oil gap and creepage paths, and instead, the E_{av} stress curve shall be divided by 0.7, giving

$$SF = \frac{E_{bd}}{E_{av}/0.7} \tag{5-4}$$

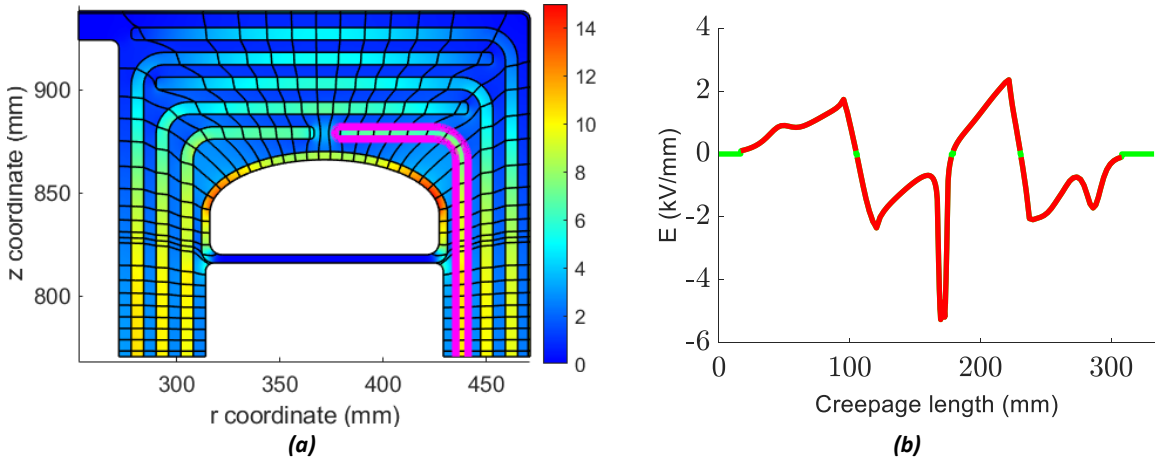

(a) *(b)*

Figure 5-28. The streamlines by using ester oil at 10 s and 30 °C: a sample creepage surface (thick pink line) (a), and the electric field curve along this creepage surface (accounted from the right bottom) (b)

5.3.4.4 *The safety factors in the combined oil gaps and creepage surfaces*

It is known that electrical discharges can be initiated in oil gaps and then continue their path on the creepage surfaces. Additionally, the breakdown in the oil gaps and creepage surfaces along the oil gaps may be considered to have a similar mechanism. Therefore, the oil gap strength and creepage strength

cannot be assumed to be completely independent. Thus, it is reasonable to calculate the safety factors in combined oil gaps and creepage paths. The research question here is how a formulation for the insulation structure could be framed for the combined oil gap and creepage path, rather than looking at them separately to ensure a safer design set-up.

To explain the case, consider a section of a streamline in an oil gap that is confined between two barriers as shown in Figure 5-29. This streamline can be extended from two ends on the barriers, in the same direction of the tangential electric field on both surfaces. These protractions would be extended along the barriers until the tangential electric field on the surface falls below 0.2 kV/mm or its direction changes. The stress curve on this path is obtained by the stress curve for an oil gap path combined with the tangential stress curves at both creepage paths. As shown in (5-4), the stress curves of creepage paths shall be divided by factor 0.7 before combination with the stress curve of the oil gap.

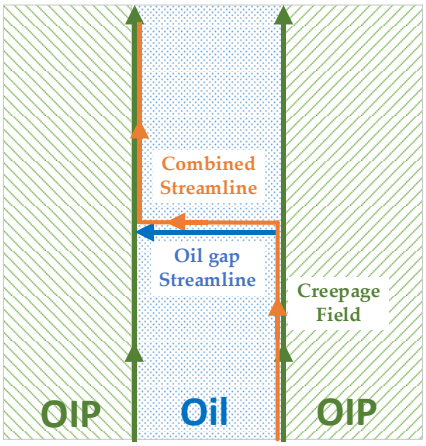

Figure 5-29. Extracting a combined path from an oil gap path and the linked creepage paths

Considering this procedure, one can perceive that the minimum SF of a combined path must be equal (in a good dielectric design) or less than to the minimum SF of its related oil gap path and the minimum SFs of the related two creepage paths. One can consider the combined path, which is illustrated in Figure 5-30a by a pink line, which is composed by two creepage paths connected to the two ends of an oil gap path. The stress curves along this combined path as well as on its forming sections in the oil gap and on creepage surface are shown in Figure 5-30b. The sorted electric field stress curves (*E* curve from (2-2) of the mentioned paths are depicted in Figure 5-30c. Since the E curves of oil path and creepage paths are the rearranged form of their stress curves in descending order, the maximum of stresses in each of these paths could be adhered together in the *E* curve of the combined path. Therefore, it can be clearly seen that the *E* curve of the combined path is greater than the *E* curves of the oil gap and creepage paths. Consequently, the E_{av} curve of the combined path will be higher compared to that of the oil gap and creepage paths. Consequently, according to (2-4), this can lead to a lower minimum SF for combined path with respect to the SFs of its forming oil gap and creepage paths (Figure 5-30d).

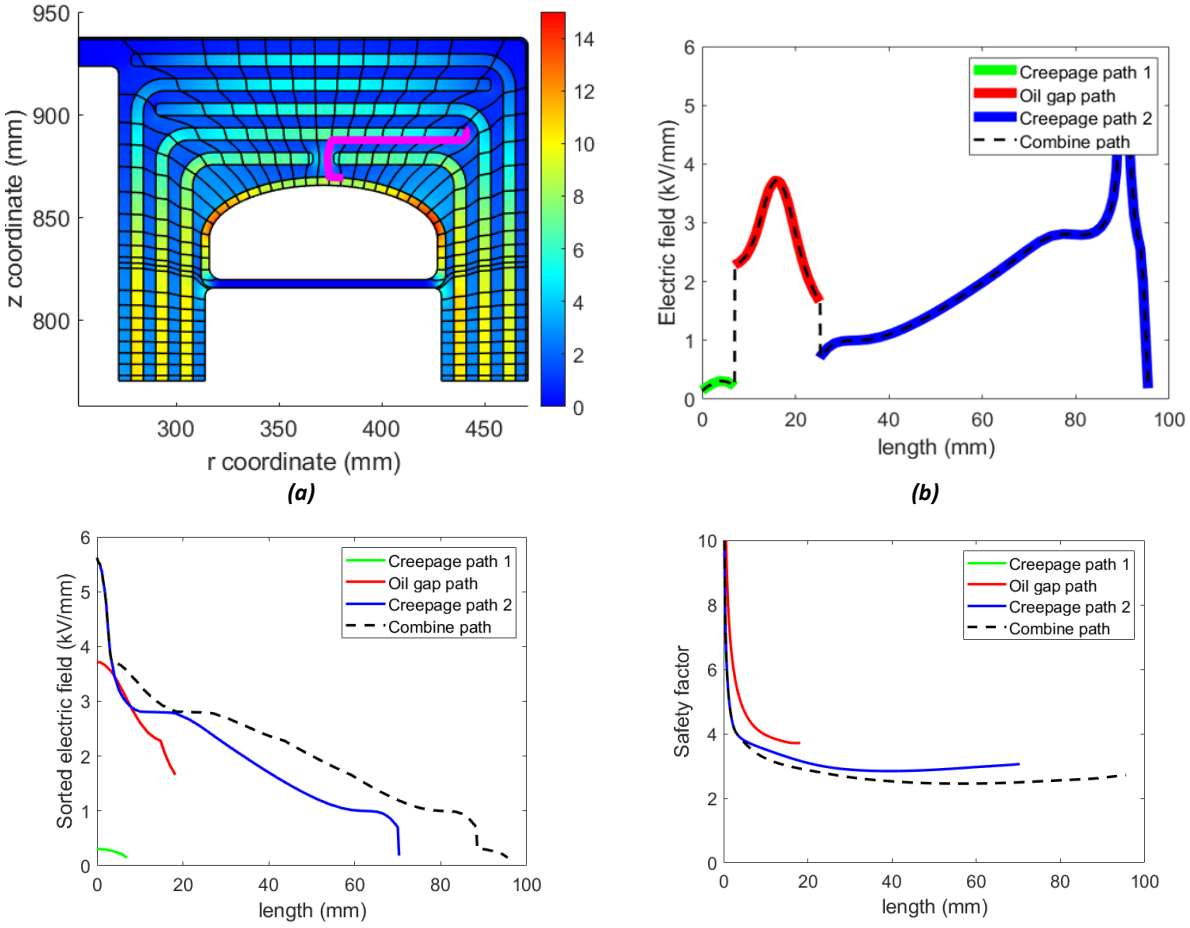

Figure 5-30. The streamlines by using ester oil at 10 s and 30 °C: a sample combined path in an oil gap and two creepage paths (thick pink line, creepage path 1 is on the insulation of the HV shield and creepage path 2 is on the oil duct barrier) (a), the electric field curve along this combined path (b), the sorted electric field curves (c), and the safety factor curves (the safety factor of the creepage path 1 is higher than 40 and that is why the green line is not shown) (d)

5.3.4.5 *The dielectric design evaluation*

The above-mentioned procedure for the evaluation of the dielectric strength is implemented to be run repeatedly in MATLAB using COMSOL Live Link and is clarified in the flowchart in Figure 5-31. The final results from this evaluation for ester and mineral oils at all time steps and all temperatures (30, 50 and 90 °C) are summarized in Table 5-19.

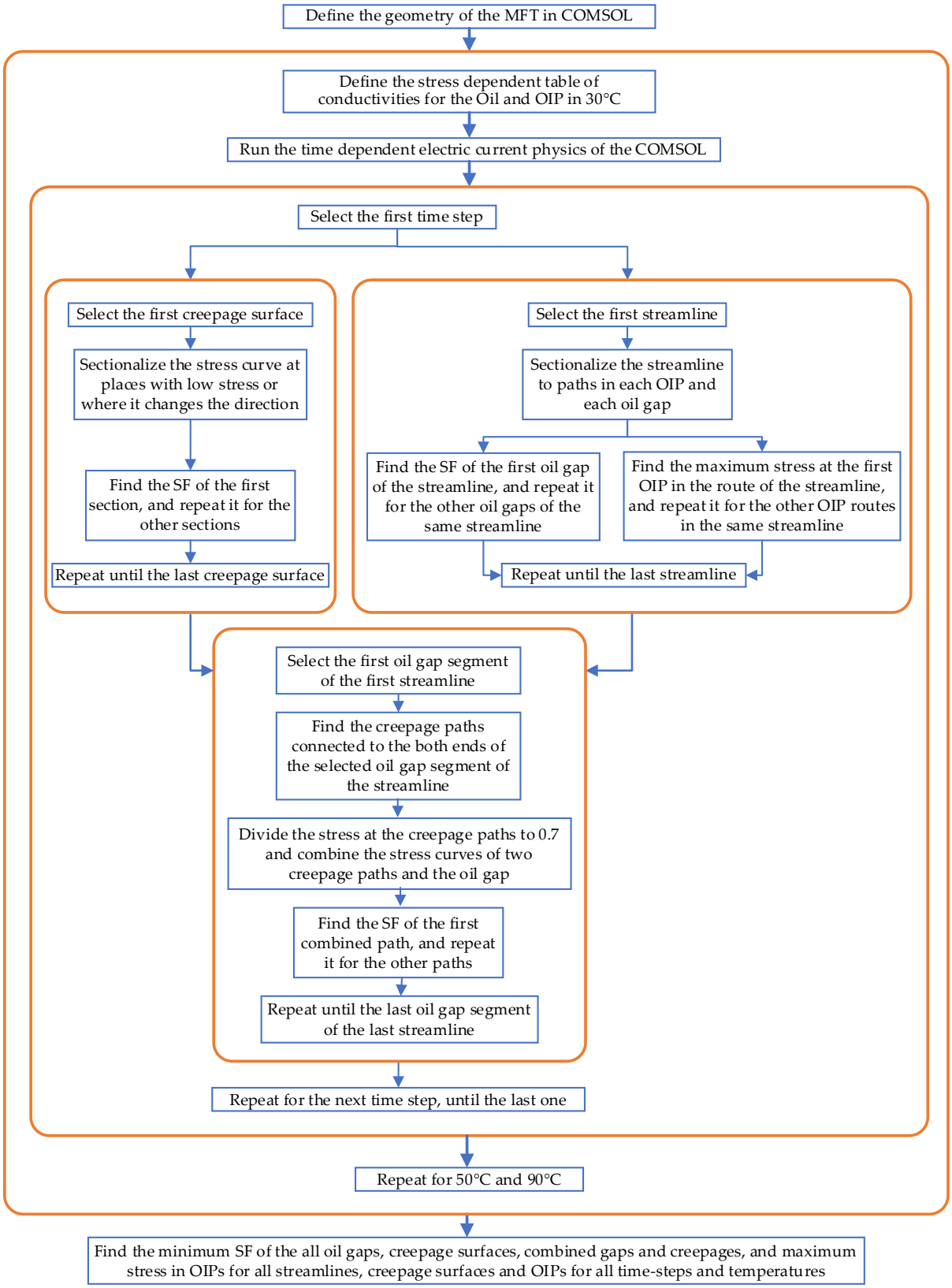

Figure 5-31. The flowchart of automatic insulation design evaluation applied in COMSOL Live Link with MATLAB

It can be seen in Table 5-19 that the maximum stresses in OIPs and minimum SFs in creepage paths occur not in the initial state nor in the final state, but rather in the transient phase. This fact again emphasizes the importance of the time dependent analysis of stresses in the dielectrics. The minimum SFs in the oil gaps happen right after the HVDC switching. The same is valid for the combined paths.

As was mentioned previously, the minimum SF of the combined paths will be equal or less than the minimum of the SFs of the oil gap paths and the SFs of a creepage paths. In Table 5-19, by comparing the minimum SFs of the oil gap paths, the creepage paths and combined paths and the time of their occurrences, it can be concluded that the SFs of the combined paths are generally determined by the oil gaps in the dielectric design of the real scale MFT. However, just in one of the simulations, using ester oil at 90 °C, the minimum SF of the combined path (1.7) is slightly lower than the SF of the oil gap paths (1.8).

Regarding the maximum stress in OIPs, it can be seen that by using ester oil instead of mineral oil, a slightly higher stress at 30 and 50 °C occurs. But at 90 °C, the maximum stress in the mineral OIP is not much lower than that of the ester OIP, even much lower than that of the mineral OIP at 30 and 50 °C. Therefore, this issue cannot be considered as a superiority for the mineral oil application.

As the final deduction from Table 5-19, it can be indicated that the SFs of all oil gaps, creepage paths as well as the combined paths at all temperatures and time steps are far higher than 1 and that the maximum stresses in OIPs are less than 20 kV/mm. Therefore, the merit of the dielectric design of the provided MFT using the biodegradable ester oil can be verified. Additionally, the minimum SFs of all oil gaps, creepage paths and nearly all combined paths by using ester oil are higher than that of the case when the mineral oil is used. In addition, the maximum stress at all temperatures and all time-steps in the case of ester oil (17.7 kV/mm) is only slightly higher than that in the mineral oil application (17.5 kV/mm). Therefore, from the viewpoint of the dielectric withstand level, there is no restriction for using ester oil instead of mineral oil.

Table 5-19. The maximum stresses in OIPs, the minimum SFs in the oil gaps, on the interface creepage paths and combined paths and the related time of occurrences

	Temp. (°C)	Max. Stress in OIPs (kV/mm)	Time (s)	Min. SF in Oil Gaps	Time (s)	Min. SF at Creepage Surfaces	Time (s)	Min. SF at Combined Paths	Time (s)
mineral oil	30	17.5	4467	1.5	1	2.4	2239	1.5	1
	50	16.2	1778	1.5	1	2.4	891	1.5	1
	90	8.3	398	1.5	1	2.5	158	1.5	1
ester oil	30	17.7	28	1.7	1	2.3	12.6	1.6	1
	50	17.7	8	1.7	1	2.4	4	1.6	1
	90	17.3	2	1.8	1	2.5	1.4	1.7	1

The following summary is presented as a comparison result between using a biodegradable ester oil instead of conventional mineral oil and also regarding the advantage of using a combined path method introduced in this study.

- The conductivity values of the ester oil/OIP are generally higher than the mineral oil/OIP, which causes lower time constants for ester oil/OIP and consequently faster convergence to the steady state condition (shorter transient phase) by using ester oil.
- For both ester and mineral oils, the lower the operational temperature, the lower the conductivity values. As a result, the transient state is longer at low temperatures.
- The temperature dependency of ester oil/OIP conductivities are lower, which causes the transformer to be less sensitive to temperature variations during energization or variable loading conditions. As a result, the transformer filled with mineral oil behaves completely different at 90 °C compared to the behaviour at lower temperatures.

- For a successful insulation design, it is insufficient to check the stress distribution only during the initial and steady state conditions, but check is necessary also during the transient state when instantaneous maximums in the field strength may occur.
- By using ester oil, the stress in the OIP at steady state condition is at the same level as for a similar transformer filled with mineral oil. Similarly, the minimum SFs at the oil gaps, creepage paths as well as the combined paths are almost at the same order for both ester and mineral oils applications.
- The introduced combined method for safety factor calculation can be used effectively in a transformer insulation design evaluation. The SF value of an insulation design discovered by this method is equal or lower than the minimum of the SF values found by conventional methods on the independent oil gaps and creepage paths. Therefore, the new proposed method can be considered as a conservative method for insulation design evaluation.

6 Design Proposal for a Real Scale Unit

An initial investigation was done regarding the feasibility of a series-connected wind park [137]. For different offshore wind parks of types of AC/AC, AC/DC and DC/DC, the life cycle cost and the energy efficiency were determined and compared. In addition, the energy losses and costs of the transmissions systems were evaluated.

Three cases were selected, and Life Cycle Cost (LCC) analysis was performed. Case1 and case 2 were 1000 MW and 500 MW offshore wind parks respectively, located at four different distances from suitable grid connection points, namely 60, 80, 100 and 120 km. Case 3 was a wind park similar to the 110 MW Lillgrund park having 48 wind turbines of 3 MW located at two different distances out in the sea, namely 9 and 60 km.

The findings from [137] show that the DC series also offers the highest electrical efficiency related to the AC/AC and AC/DC systems. Due to the high energy losses in the AC transmission system, i.e., in the cables, the AC/AC system is more expensive than the AC/DC case, when the farm was located at a longer distance to land than 80 km to 100 km. Subsequently, for large power capacities at long distances, the HVDC technology (AC/DC or DC/DC) is preferred [137].

In case of a park having the size of Lillgrund and is placed 9 km out in the sea an AC/AC system is more beneficial than the DC Series system. When the distance to the land increases (to 60 km for example), the DC Series will be more cost effective where the offshore platform needed, is omitted. In this case 85 M€ will be saved. The efficiency of the DC design is also higher, and the losses will be lower than the similar AC/AC design [137].

In [137], among other studies, todays classical system, shown in Figure 6-1, is compared with a real scale series DC system (Figure 6-2). The interested reader can also find more information in [138-142].

In the system study the prerequisites of a 1 GW farm having 100, 10 MW turbines with up to 200 kV HVDC insulation ability from the HV winding to ground is assumed. To realise this a series connection of 17, 10 MW, 1.8/18 kV DC/DC equipped wind turbine units with 250 kV DC to ground insulation will deliver up to 306 kV in series which has a good margin in case of uneven power production from the various turbines (due to the current series connection, the turbines add voltage in proportion to their power production) or having one of the several turbines out of operation. 250 kV HVDC insulation ability from the HV winding to ground could be a choice for a system operating at maximum 200 KV DC to ground. Below, thus, follows the design proposal for such a real scale unit.

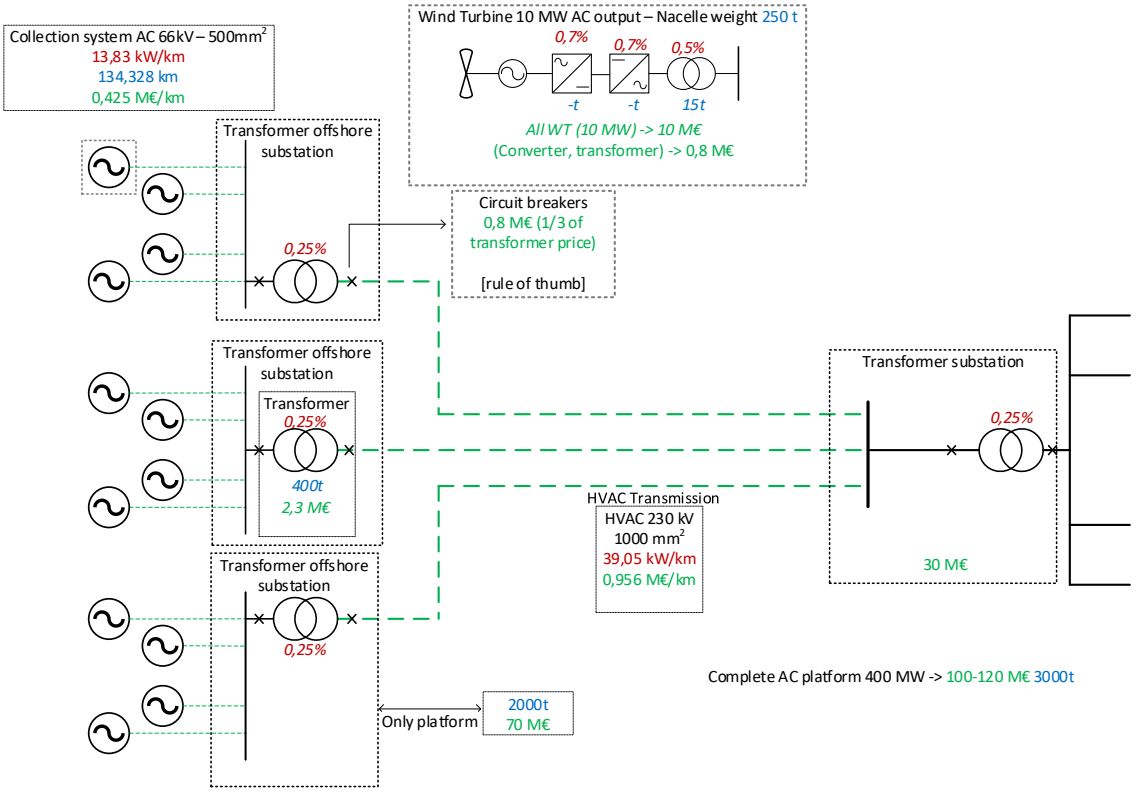

Figure 6-1. A detailed cost/Loss data of an AC/AC 1GW park having 100 WTs of 10 MW capacity [137]

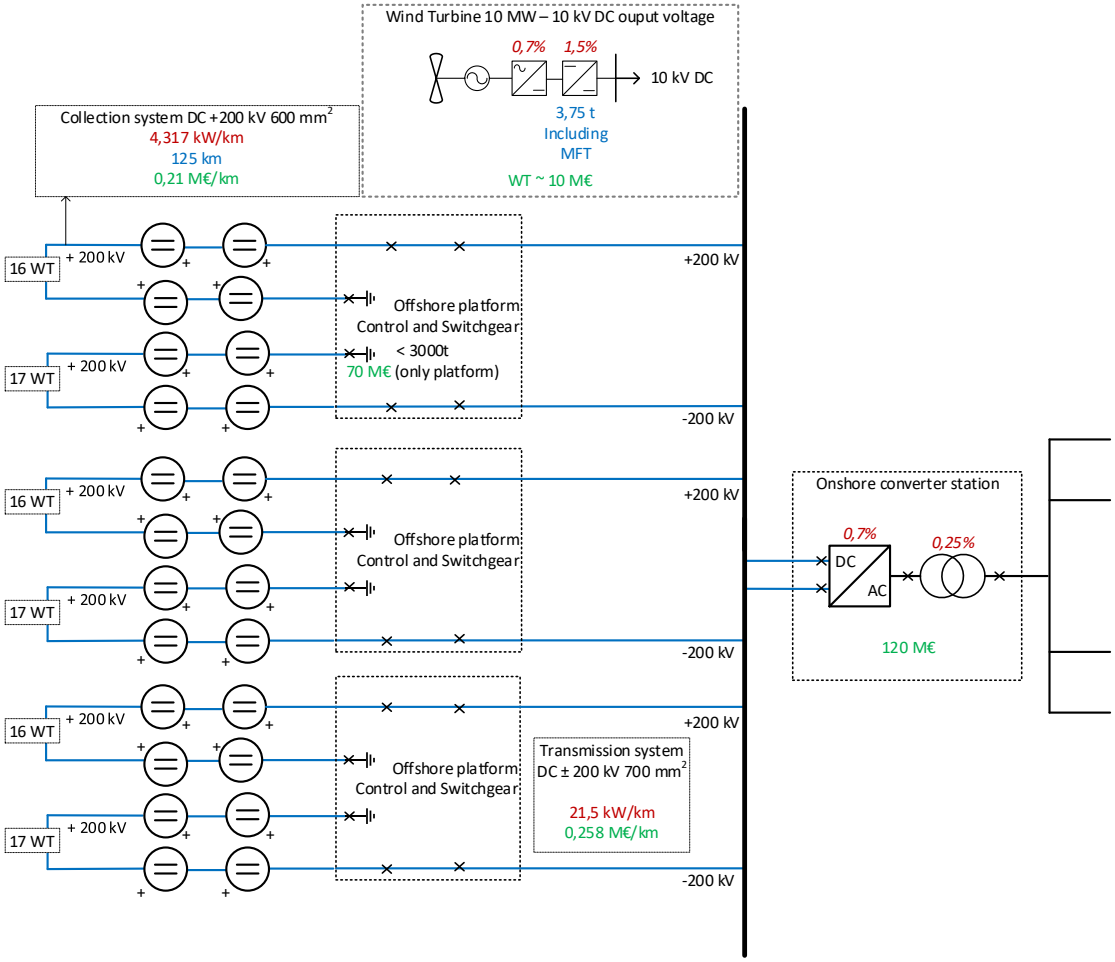

Figure 6-2. A detailed cost/Loss data of an DC Series 1GW park having 100 WTs of 10 MW capacity [137]

6.1 Real scale transformer basic design

With the above-mentioned background, an important research questions have to be answered: For a real-scale turbine, what are the approximate resulting size and weight for a real converter unit? Is it feasible? What is the possible energy efficiency of a real-scale unit specially at low wind condition? Does it compete with the traditional wind turbine generating system?

A real scale prototype transformer for such a DC/DC converter is herewith proposed. A 10 MW, 1.8/18 kV 5 kHz AC, 250 kV DC prototype, with a ferrite core.

First the basic design is introduced.

- Rated primary current, I_{T1} (r.m.s.) = 10 MW/1.8 kV = 5555 A
- Number of turns, N_1 and N_2 = 12 and 120
    - (For the winding type demonstrated in Figure 4-3, the highest voltage difference between two adjacent discs of 6 turns/disc will be 18 kV/120 x 6 x 2 = 1800 V and this means that a vertical distance should be considered between two discs which are selected as 3 mm in this design.)
- Magnetic core cross-section, calculated from (2-30) as 23437 mm^2 for the case of using Ferrite material where
    - V_{rms1} is the rated voltage of the primary winding = 1800 V
    - K_c is the core filling factor ≈ 1 for the Ferrite cores
    - N_1 is the number of turns of the primary winding = 12
    - B_m is the maximum working flux density of the core ≈ 0.32 T for the Ferrite
    - f is the switching frequency = 5 kHz
- By switching from 125 kV for the prototype to 250 kV the electrical field in the core window will be much higher. The isolation distances shall be increased, compared with the prototype case. As explained in Section 2.2.3, this means a higher number of barriers and oil gaps. The oil gap distances, the OIP barriers thicknesses and the number of barriers were increased. Using the developed method earlier demonstrated in Section 4.2, after a series of simulations, the oil gap distances of 6 mm, the OIP barrier thicknesses of 6 mm and a number of barriers of 4 are selected.
- As the AC voltage levels are 4 times higher than for the prototype MFT case, the core area is selected similar to the prototype with 2 times increase in the dimensions. The core will have 40 x 56 = 2240 mm^2 as physical core area and similar to the prototype case, 10 core stacks including 20 U cores is found to be suitable for the real scale design.
- A litz wire 8869 x 0.2 mm having the physical dimension of 26.6 × 17.5 mm^2 is assumed to be used. This is a 7 x 7 wires combination of the previously used 3.8 x 2.5 litz wires.
- For the primary layer type winding, considering 5555 A as the rated r.m.s. current, the space that the primary winding occupy in the core window will have a height of 851 mm (consisting of eight 26.6 mm parallel wires on top of each other) and the width of 130 mm (consisting of four 17.5 mm layers having a 20 mm oil gap between the layers for the cooling purpose). Considering 3 turns of the 8 parallel 26.6 × 17.5 mm^2 litz wires on the top of each other, the ideal magnetic height of the winding will be 638 mm. For eight parallel 9000 x 0.2 mm litz wire the actual current density will be 2.5 A/mm^2.
- For the secondary disc type winding, considering 555.55 A as rated r.m.s. current, the space that the secondary winding occupy in the core window need a height of 589 mm (consisting of

twenty 26.6 mm discs having a 3 mm oil gap between the discs for the electrical isolation and for cooling purpose) and a width of 115 mm (consisting of six 17.5 mm wires on the side of the each other having 2 mm gaps for the cooling purpose between turns). The actual current density will be 1.97 A/mm^2 which is less than the maximum permissible 3 A/mm^2 presented by the litz wire supplier [106].

The dimensions of the real scale HVDC MFT are presented in Figure 6-3.

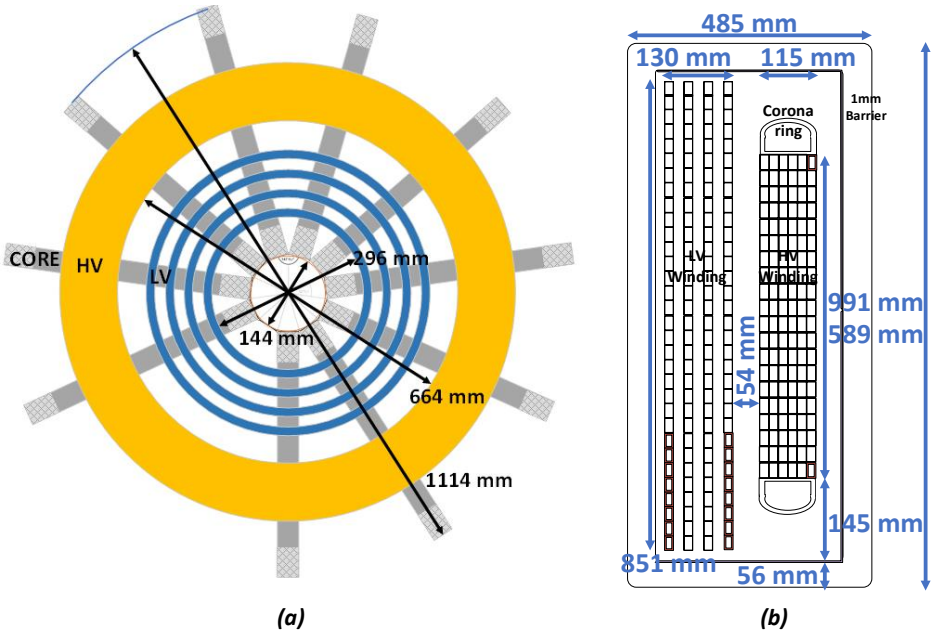

Figure 6-3. Dimensions of the real scale Ferrite 1.8 kV/18 kV, 0.32 T, 5555 A/555 A, 12/120 Turns, 5 kHz MFT

6.2 Real scale transformer insulation design

Since both conductivity measurement data, both for the mineral oil and ester oil are available in this stage, Comsol simulations are performed to consider insulation strength if the same mechanical design is filled with mineral or with ester oil. Figure 6-4 shows the electric field level in the different areas of the transformers for different times at 50 °C. Referring to the simulation results presented in Section 3.1.4.3 the ester transformer has reached to the final steady state situation after 10 seconds while for the mineral oil this time was less than 1 seconds.

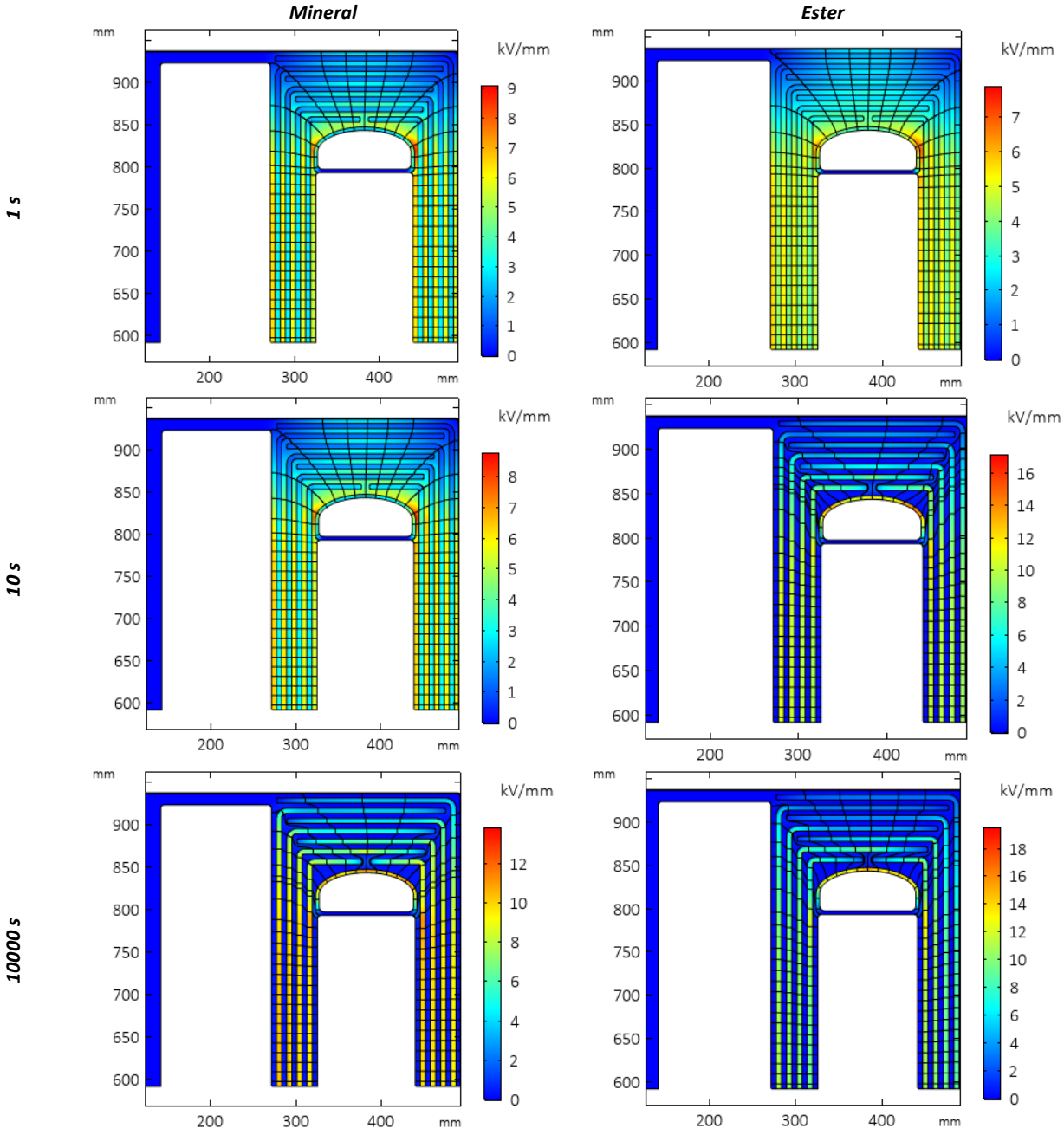

Figure 6-4. Electric filled in the mineral and ester filled real scale transformers after 1, 10 and 10000 seconds at 50 °C

The summary of the simulations performed to detect the weak areas in the oil gaps and OIP barriers is presented in Table 6-1.

Table 6-1. A summary of the insulation design simulation for the electric field in the oil gaps and OIP

	Temperature (°C)	Maximum E-field in OIP (kV/mm)	Minimum SF in oil gaps
Mineral oil and OIP	30	16.3	1.88
	50	13.7	1.88
	90	7.4	1.88
Ester oil and OIP	30	17.4	2.14
	50	18.2	2.15
	90	17.8	2.19

The table shows that in case of the maximum Electric field (E-field) in the OIP barriers, the transformer filled with the mineral oil is safer; however, the variation of the E-field with temperature is higher and

this means that the stress in the oil gaps will be changing with the loading and unloading of the transformer which can be interpreted as an unfavourite feature. Regarding the Safety Factor (SF) the situation is not the same and the ester oil gaps are under lower stress compared to the mineral oil. It should be mentioned that, as the maximum oil gap strength curves were not available for the ester oil case, based on the similar AC breakdown test levels reported in literature [136, 143, 144], the same maximum oil gap strength curves are used both for the mineral and ester oils. Figure 6-5 shows the regions with the lowest SF or the highest E-field detected for the mineral and ester oil field transformers.

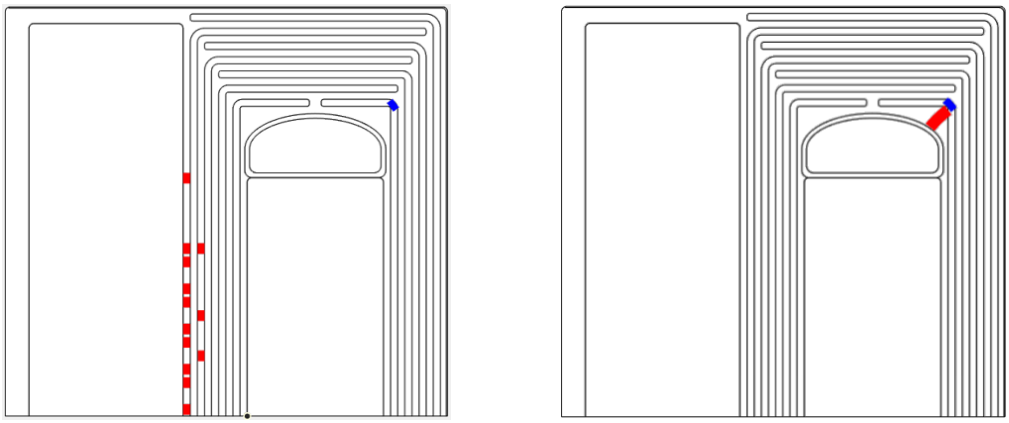

(a) *(b)*

Figure 6-5. The critically stressed regions in the oil (red) and in the OIP barriers: the transformer filled with the mineral oil (a), and the ester oil (b)

Figure 6-6 shows the regions with the lowest SF detected for the creepage fields in the mineral and ester oil transformers occurred. The summary of the simulations performed to detect the weak creepage areas in the oil-OIP interfaces is presented in Table 6-2.

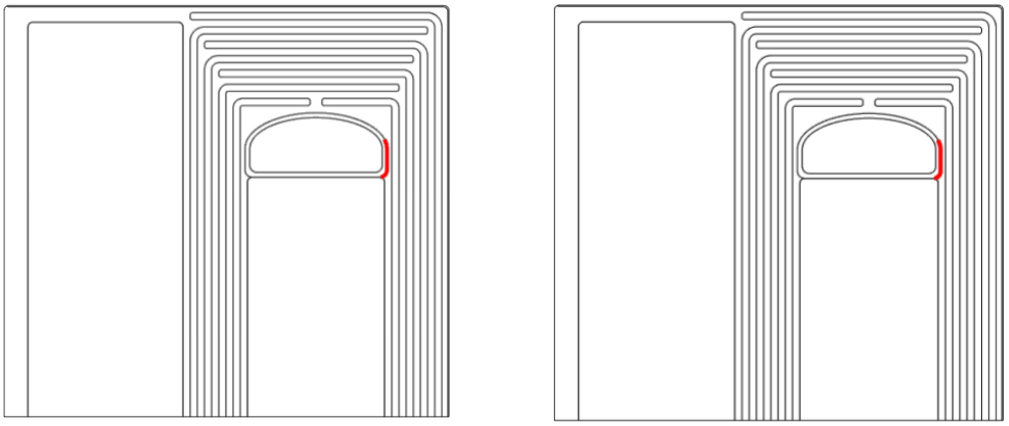

(a) The transformer filled with the mineral oil ***(b) The transformer filled with the ester oil***

Figure 6-6. The critically stressed regions in the oil/OIP interfaces (red): the transformer filled with the mineral oil (a), and the ester oil (b)

Table 6-2. A summary of the insulation design simulation for the creepage electric field in the oil-OIP interfaces

	Temperature (°C)	Minimum SF on the creepage paths
Mineral oil and OIP	30	2.17
	50	2.15
	90	2.44
Ester oil and OIP	30	2.13
	50	2.18
	90	2.24

At the same time the leakage inductance dictated from the converter side shall be considered. This makes a restriction for the dimensions of the windings and their distance from each other. In addition, the issue of cooling for the windings should be investigated. The windings have higher current densities in case of the real scale transformer. The thermal design is not covered by this thesis, but it is natural that before the placements of the insulation barriers and the oil gaps, is made, the flow of the cooling transformer oil inside the active part shall be investigated.

6.3 Real scale transformer leakage inductance

The calculation is made by the method presented in Section 2.4.4. The calculated leakage inductance is 29.74 μH.

6.4 Real scale transformer losses

The real scale transformer's core losses can directly be calculated based on the cores' W/kg value and the weight of the core. As for the series DC concept application it is assumed that the voltage will be kept at the rated voltage of 1.8 kV at the primary side, the maximum working flux density of the core, B_m will be 0.32 T. The W/kg value at this flux density and the room temperature is 11.65 W/kg according to the information presented under Section 5.1.3. As the weight of the cores are 297.6 kg, the core losses will be nearly 3467 W at room temperature. It should be noted that the Ferrite core losses reduces to 2/3 of its value when its temperature increases from ambient temperature of 20 to the operating temperature of 75 °C [104].

To calculate the winding losses the method presented in Section 4.6 is used. Figure 6-7 demonstrates the FEMM 2D axisymmetric simulation performed to calculate the winding losses. The calculated loss for the HV winding is 5.66 kW and for the LV winding is 3.87 kW at 20 °C. At 75 °C the same losses are 6.93 kW and 4.74 kW for HV and LV respectively.

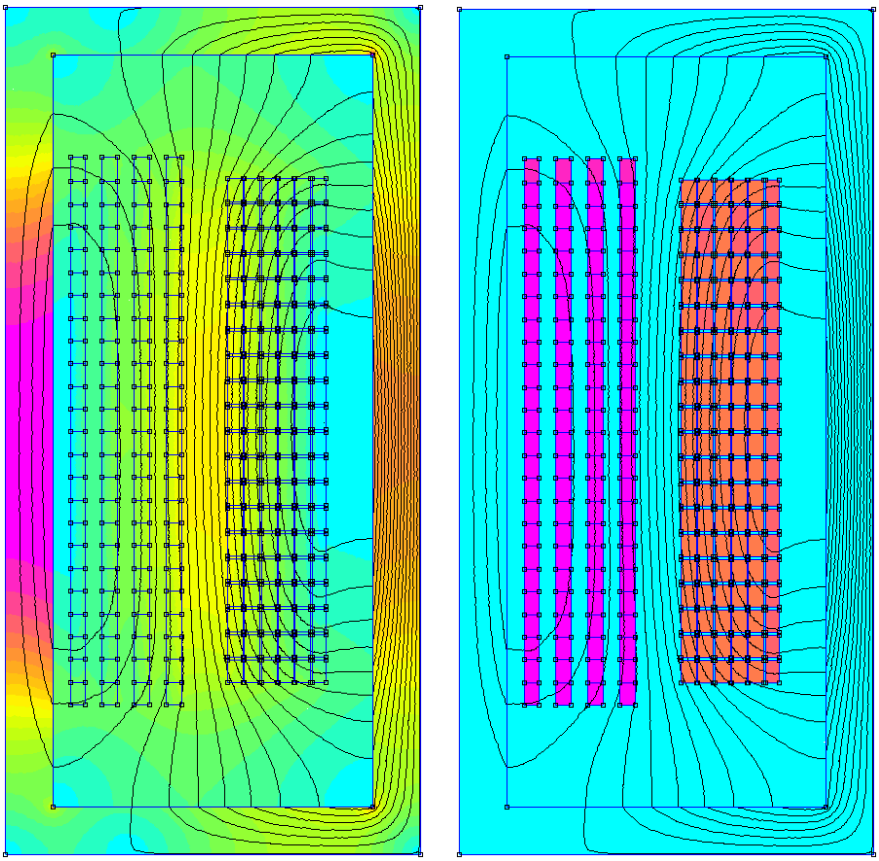

(a) (b)

Figure 6-7. Winding losses analysis of the MFT with equivalent material representation for 5 kHz: the flux density distribution (a), and the current density distribution (b)

Figure 6-8 demonstrates the transformer loss versus the transferred power. The resistivity of copper at 20 °C is 1.74×10^{-8} and at 75 °C is 2.13×10^{-8} Ωm. The winding losses are calculated for both temperatures, and it is higher at elevated temperature. The figure shows that the system has an acceptable performance even at very low losses when the transformer is not fully loaded.

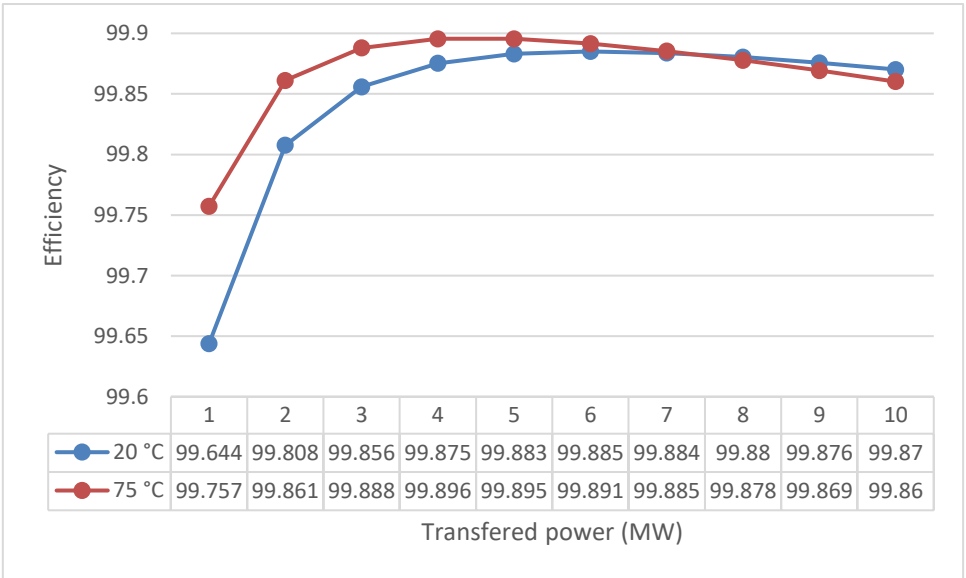

	1	2	3	4	5	6	7	8	9	10
20 °C	99.644	99.808	99.856	99.875	99.883	99.885	99.884	99.88	99.876	99.87
75 °C	99.757	99.861	99.888	99.896	99.895	99.891	99.885	99.878	99.869	99.86

Figure 6-8. The real scale MFTs efficiency vs transferred power at ambient and operating temperature

6.5 Real scale transformer weight and volume

Table 6-3 presents the weights and volumes of the designed real scale transformer. The fill factor is 0.6 for the litz wire and the density of the copper wire is 8.96 g/cm^3. The density of the core is 4870 kg/m^3.

Table 6-3. The weights and volumes of the designed real scale MFT

Parameter	Real scale MFT	kV
Tank diameter	1.10	m
Tank height	0.99	m
Tank volume	0.94	m^3
Core volume	0.061	m^3
Core weight	297.59	kg
Copper volume	0.245	m^3
Copper weight	1319.1	kg
Oil volume	0.63	m^3
Oil weight	571.3	kg
Total weight	2.188	Tons

For a quick comparison, a sample three phase 10 MVA, 50 Hz, 6.3/33 kV transformer can have a dimension of L2.9 x W1.4 x H2.2 m^3 and a weight of 26 tons. More examples are presented in Table 6-4.

Table 6-4. Examples of 50 Hz 3-phase transformers in a similar range to the designed real scale MFT

Voltage (kV)	6.6/20	20/20	6.3/33
Weight (Ton)	20.6	22.3	21.2
Length (m)	3.5	3.3	3.4
Width (m)	2.4	2.2	2.8
Height (m)	2.8	3.0	2.9
Tank volume (m^3)	23.5	21.8	27.6

6.6 Offset DC voltage versus isolation thickness, weights, and volumes

6.6.1 Isolation thickness versus the offset HVDC voltage

To complete the task, here the developed methods are utilized to give a comparative isolation thickness, weight, and volume table. It is assumed that a transformer with the same power rating is designed to withstand higher offset voltages, up to 400 kV DC.

Previously, a complete comparison between the mineral and ester oil is presented. As it is the objective of this study to utilize an environmentally friendly oil for the transformer design, for the real scale designs, only ester oil is investigated.

For this comparison, the dimensions of the LV winding and the height of the core window is kept unchanged. The dimensions of the HV winding and the number of insulation barriers are changed to make the smallest possible core window dimension which in turn, means lower weight and volume of the transformer. It is obvious that every design could have different height of LV winding and core but, the goal is to present a clearer comparison picture of the effect of a changing offset DC voltage on the insulation design in the core window and, to not struggle with the magnetic design aspects.

Four designs are investigated: Designs benefiting from two pressboard barriers, three, four and five. To manage a uniform insulation thickness around the HV winding as well as the minimum core window

area, the number of discs is selected as 24, 20, 20 and 15 consequently to satisfy the constant constraint of 120 turns. All other magnetic design aspects are kept constant.

The minimum resistible DC voltage is extracted by repetitive simulations, based on restrictions earlier presented as the acceptance criteria for a successful insulation design. It is obvious that the selection of a lower operating voltage will mean a higher safety factor for the design. The flowchart which is followed for each design is presented in Figure 5-31 [132].

In addition to the oil gaps and the OIPs, for every design the electric field is investigated on each oil-OIP interface (for 4, 6, 8 and 10 times) and on each shield surface. 50 streamlines are studied to find the maximum electric field in OIPs (where the streamline passes through OIPs or the lowest safety factor (where it passes the oil gaps). This is performed for 81 time points (in four time-intervals of 1-10, 10-100, 100-1000 and 1000-10000 seconds). For example, nearly 5000 repetitions were performed to investigate the suitability of the 5-barrier design. The results of the simulations are depicted in Table 6-5. In this table the limiting parameter for the applicable offset DC voltage to the transformer is given based on worst case scenarios. The minimum safety factor for the oil gap is assumed to be 1.5 and the maximum stress on the OIP equal to 20 kV/mm.

Table 6-5. The worst-case scenarios for four insulation design

Number of pressboards		2	3	4	5
Limiting parameter	Temp.				
Max electric field in OIP (kV/mm)	30˚C	19.5 @ sec. 22.0	19.5 @ sec. 25.1	19.5 @ sec. 25.1	19.7 @ sec. 31.6
	50 ˚C	19.4 @ sec. 6.0	19.2 @ sec. 7.9	19.3 @ sec. 7.9	19.2 @ sec. 8.9
	90 ˚C	19.0 @ sec. 1.8	18.9 @ sec. 2.0	18.9 @ sec. 2.2	18.9 @ sec. 2.2
Min. total isolation thickness		44 mm	68 mm	92 mm	116 mm
Max. safe operating voltage		200 kV	275 kV	325 kV	385 kV

Table 6-6 presents the worst cases of stress applied to the oil gaps, oil-paper interfaces, and the combined path streamlines.

Table 6-6. The worst cases of stress applied to the oil gaps, oil-paper interfaces, and the combined path streamlines

Worst cases of Oil Gaps			
200 kV – 44 mm			
temp.	30 ˚C	50 ˚C	90 ˚C
min. SF	1.5	1.5	1.5
time	1.0 s	1.0 s	1.0 s
275 kV – 68 mm			
temp.	30 ˚C	50 ˚C	90 ˚C
min. SF	1.5	1.5	1.6
time	1.0 s	1.0 s	1.0 s
325 kV – 92 mm			
temp.	30 ˚C	50 ˚C	90 ˚C
min. SF	1.6	1.6	1.7
time	1.0 s	1.0 s	1.0 s
385 kV – 116 mm			
temp.	30 ˚C	50 ˚C	90 ˚C
min. SF	1.5	1.6	1.6
time	1.0 s	1.0 s	1.0 s

-

Worst cases of Creepage Surface			
200 kV – 44 mm			
temp.	30 ˚C	50 ˚C	90 ˚C
min. SF	2.0	2.0	2.1
time	12.6 s	4 s	1.4 s
275 kV – 68 mm			
temp.	30 ˚C	50 ˚C	90 ˚C
min. SF	2.1	2.2	2.2
time	12.6 s	4.0 s	1.4 s
325 kV – 92 mm			
temp.	30 ˚C	50 ˚C	90 ˚C
min. SF	2.1	2.2	2.2
time	12.6 s	2.5 s	1.3 s
385 kV – 116 mm			
temp.	30 ˚C	50 ˚C	90 ˚C
min. SF	2.0	2.0	2.1
time	1.4 s	1.0 s	1.0 s

-

Worst cases of Combined Oil Gaps-Creepage Surface			
200 kV – 44 mm			
temp.	30 ˚C	50 ˚C	90 ˚C
min. SF	1.5	1.5	1.5
time	1.0 s	1.0 s	1.0 s
275 kV – 68 mm			
temp.	30 ˚C	50 ˚C	90 ˚C
min. SF	1.5	1.5	1.5
time	1.4 s	1.0 s	1.0 s
325 kV – 92 mm			
temp.	30 ˚C	50 ˚C	90 ˚C
min. SF	1.4	1.4	1.5
time	1.0 s	1.0 s	1.0 s
385 kV – 116 mm			
temp.	30 ˚C	50 ˚C	90 ˚C
min. SF	1.4	1.4	1.4
time	1.0 s	1.0 s	1.0 s

Figure 6-9 present a simplified demonstration of the relation between the transformer offset DC design voltage and the required isolation thickness between the HV winding and the LV and grounded core.

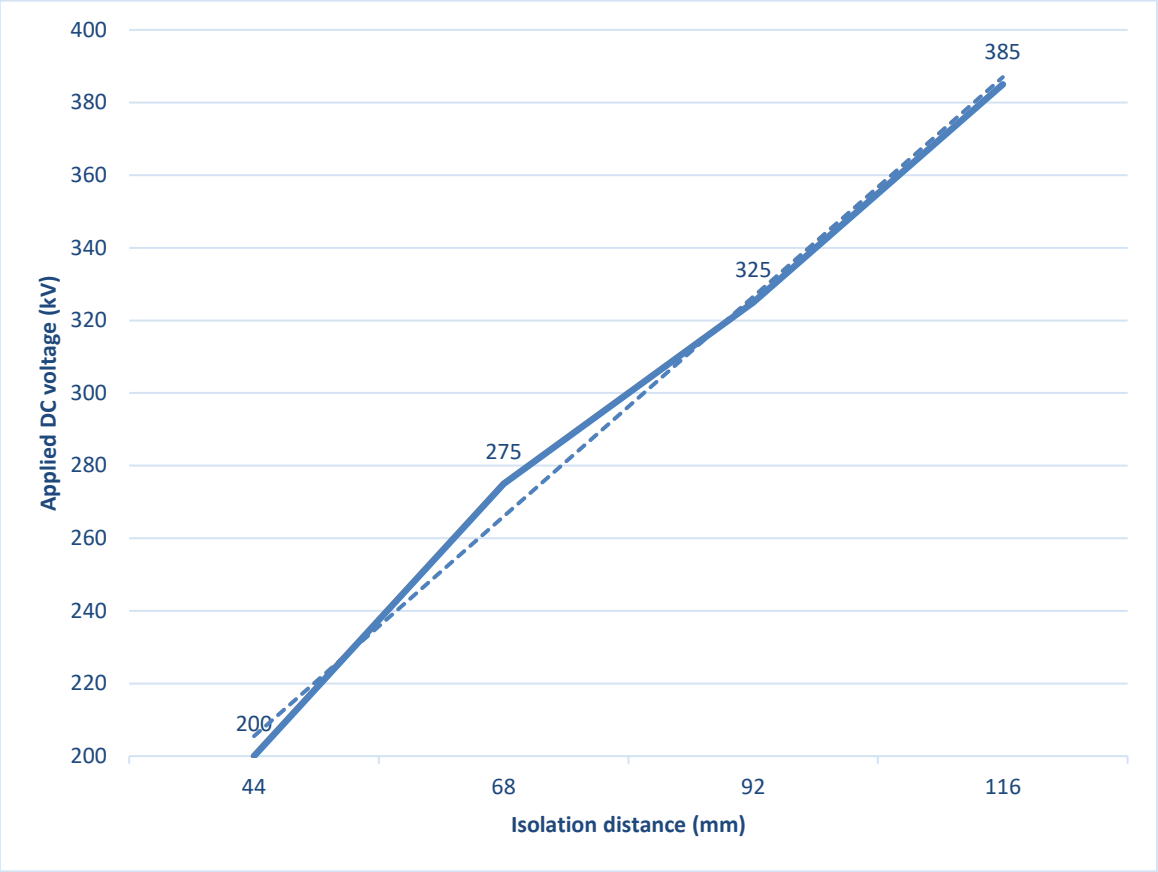

Figure 6-9. The relation between the transformer offset DC design voltage and the required isolation thickness between the HV winding and the LV and grounded core

6.6.2 Weight and volume versus the offset HVDC voltage

The weights of the transformers are calculated as the sum of the weights of windings, oil, and the cores. The fill factor and the density of the copper wire as well as the density of the core are as it mentioned previously in this section. Table 6-7 presents the summary of the results.

Table 6-7. The weights and volumes of the designed real scale MFTs versus applied offset DC voltage

Parameter	200	275	325	385	kV DC
Tank diameter	0.98	1.07	1.12	1.24	m
Tank height	0.99	0.99	0.99	0.99	m
Tank volume	0.74	0.89	0.97	1.20	m^3
Core volume	0.058	0.060	0.061	0.064	m^3
Core weight	282.43	292.79	298.03	311.77	kg
Copper volume	0.229	0.254	0.246	0.289	m3
Copper weight	1231.1	1366.2	1323.7	1552.2	kg
Oil volume	0.45	0.58	0.66	0.85	m^3
Oil weight	407.3	518.8	598.5	766.0	kg
Total weight	1.921	2.178	2.220	2.630	Tons

6.7 Integration to DC/DC converter

6.7.1 Real scale DC/DC converter losses versus transferred power

To calculate the DC/DC converter losses the equivalent circuit of the transformer is inserted inside a DAB using Matlab Simulink (Figure 6-10).

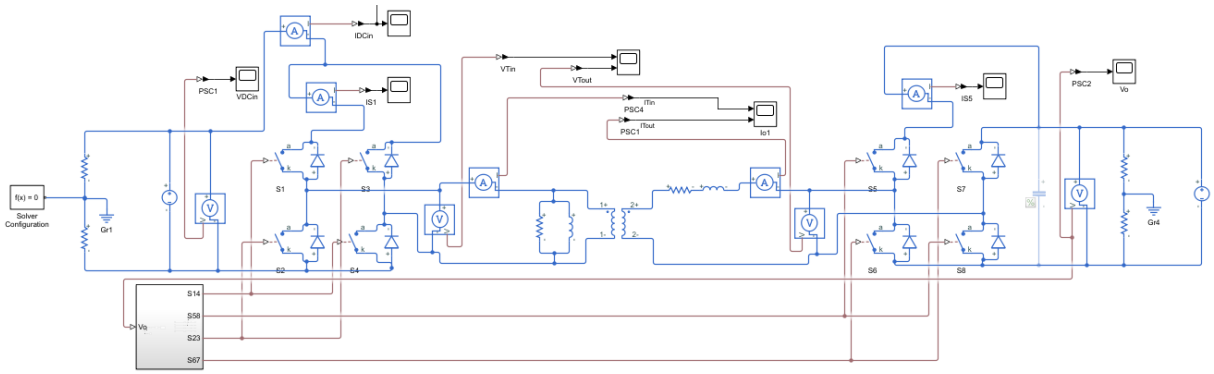

Figure 6-10. Equivalent circuit of the transformer inserted inside a DAB in Simulink

An advantage of utilizing the series DC concept can be the lower losses compared to the conventional parallel systems, especially during low wind condition. In this condition the produced power is low, and a high efficiency can be a major benefit.

To adopt the power electronic units to the rated current and voltage of the MFT, 6 parallel 1500 A, 3300 V, 5SNA 1500E330305 are used on the LV side and, 2 parallel and 5 series combination of 6500 V, 500 A, 5SNA 0500J650300 ultra low-loss ABB HiPak IGBTs are used. In this way, the aggregated IGBT at the LV side is rated to 9000 A and 3300 V, and at the HV side to 1000 A and 32500 V while, the transformer rating is 5555 A and 1800 V for the LV side and 555 A and 18000 V for the HV side. The aggregated IGBTs with a max voltage rating of 3300 V, is sufficient for an 1800 V usage and a rated current of 9000 A is sufficient for 5555 A operation.

The equations for calculations are presented in Section 2.7. Figure 6-11 presents the transformer's primary side voltage and current, and switch currents at primary and secondary side when 6 MW power is transferred by the DAB.

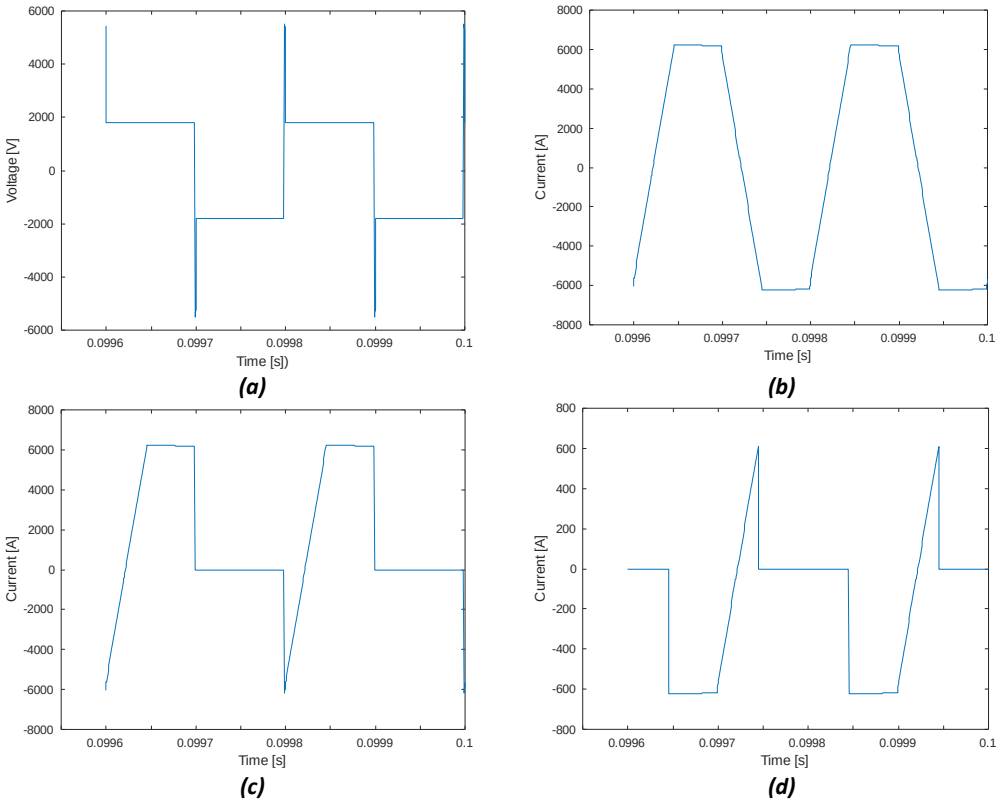

Figure 6-11. Sample transformer primary side voltage and current, and switch currents at primary and secondary sides: the transformer primary side voltage (a) and current (b), the primary side S1 switch current (c), and the secondary side S5 switch current (d)

Figure 6-12 demonstrates the rate of change in the transferred power and current while the voltage is kept constant, and the phase shift of DAB is changing.

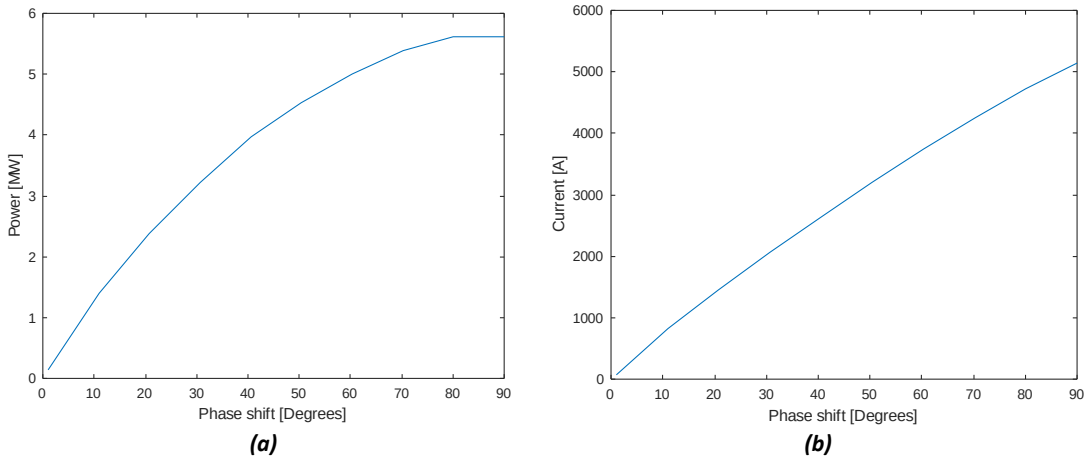

Figure 6-12. The transferred power from transformer and its input current while adjusting the DAB's phase shift: The transformer input power (a), and the transformer primary side r.m.s. current (b)

Table 6-8 presents the input data, extracted from the semiconductors' specifications used for the calculation of the semiconductor losses. The forward voltage and the resistance values representing the on-state losses of the IGBTs and diodes are presented in the table.

Table 6-8. V_F and R_{on} of the used IGBTs and diodes

	V3300 I1500	LV side diode	V6500 I500	HV side diode
V_F (V)	1.0	1.2	1.2	1.6
Extracted R_{on} (Ω)	0.0016	0.0006	0.0052	0.0044

Table 6-9 demonstrates the losses when the real scale transformer inserted in a DAB and a maximum active power of 6 MW transmitted from transformer. It has been assumed that soft switching was achievable in all operating points, and accordingly has the switching losses been ignored.

Table 6-9. The losses of the components of a real scale DC/DC converter when it delivers up to 6 MW power

MW	Temp (°C)	PSDL	PSTL	SSDL	SSTL	Total DAB Semiconductor Loss(W)	Total transformer (W)	Total Converter (W)	Efficiency
6	75	1729	18834	15524	1729	38439	6512.2	44951.2	99.251
5		738	12326	10015	738	23923	5228.6	29151.6	99.417
4		371	8425	6733	371	15972	4178.4	20150.4	99.496
3		141	5378	4339	141	10044	3361.6	13405.6	99.553
2		50	3067	2487	50	5698	2778.1	8476.1	99.576
1		13	1286	1027	13	2340	2428.0	4768.0	99.523

In the table the following abbreviations are used:

- PSDL, Primary Side Diode Loss
- PSTL, Primary Side Transistor Loss
- SSDL Secondary Side Diode Loss
- SSTL Secondary Side Transistor Loss

Figure 6-13 demonstrates the change in the converter efficiency with the change in transferred power.

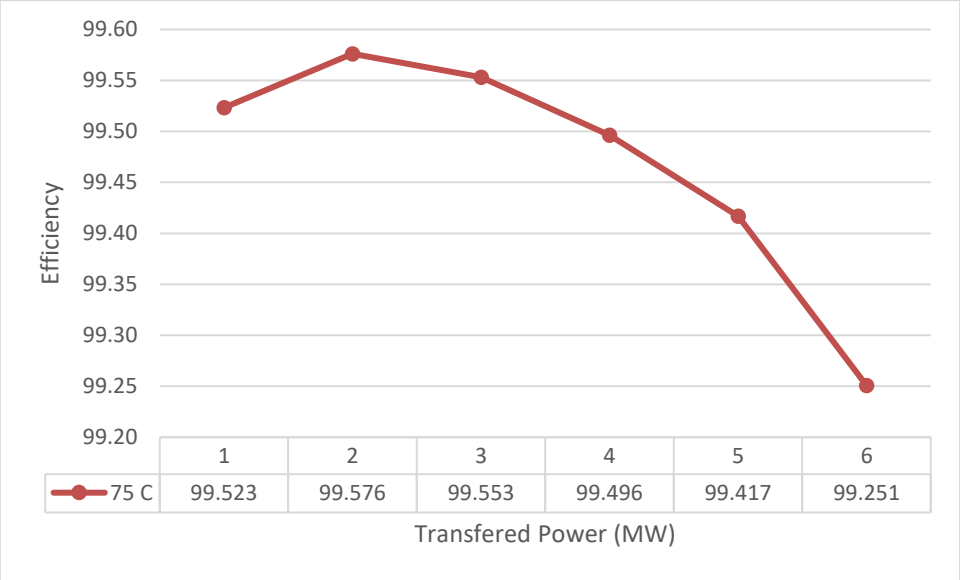

Figure 6-13. The change in the converter efficiency with the change in transferred power

6.7.2 Packaging

The designed MFT shall be integrated into a power electronic converter. The MFT is dimensioned for 1.8/18 kV, 5.5/0.55 kA, 250 kV DC offset voltage. Figure 6-14 demonstrates a proposal of a circuit diagram of such an integration. The power electronic unit consists of active bridges at both sides of the MFT with the aggregated IGBTs.

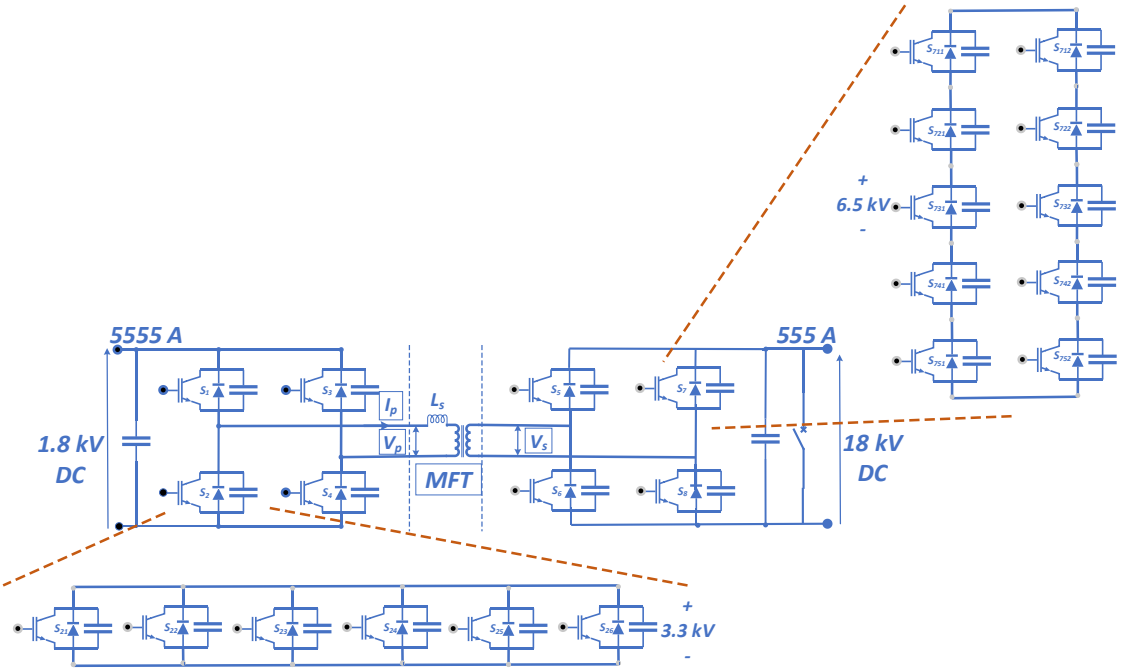

Figure 6-14. The circuit diagram of MFT integrated in a DAB with series The aggregated IGBT packs on HV side and parallel on the LV side of the MFT

Each aggregated IGBT of the H is proposed to consist of five IGBTs (two 500 A in parallel), each having a rated voltage of 6.5 kV. The physical dimensions of a sample IGBT pack and the suggested physical arrangements of the packs are displayed in Figure 6-15.

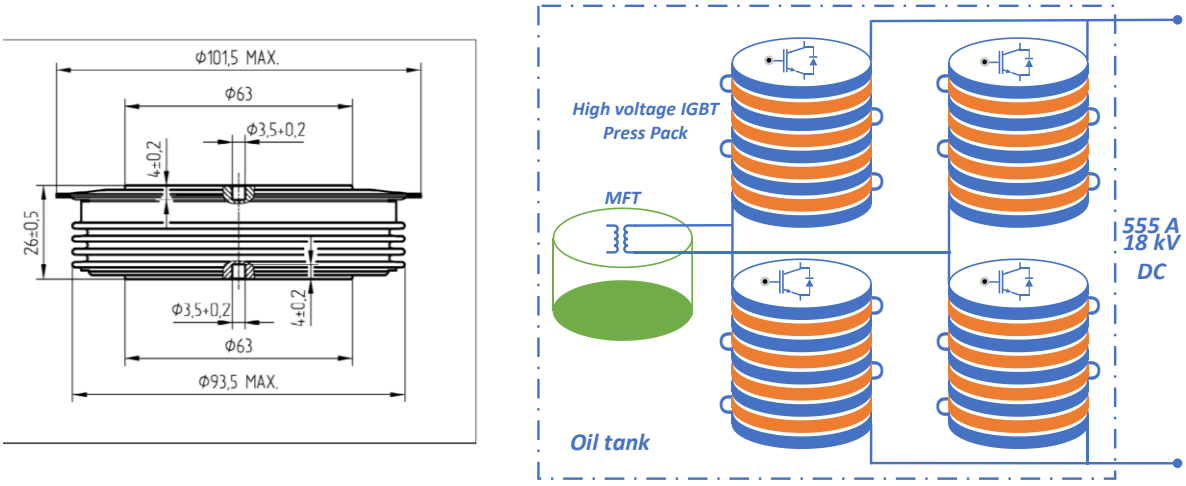

(a) ***(b)***

Figure 6-15. The physical dimensions of a sample IGBT pack (a), and the suggested physical arrangements of the packs (b)

A schematic drawing of a real scale MFT with the high voltage series connected IGBTs of the secondary side (HV side) of the DAB H bridge is demonstrated in Figure 6-16.

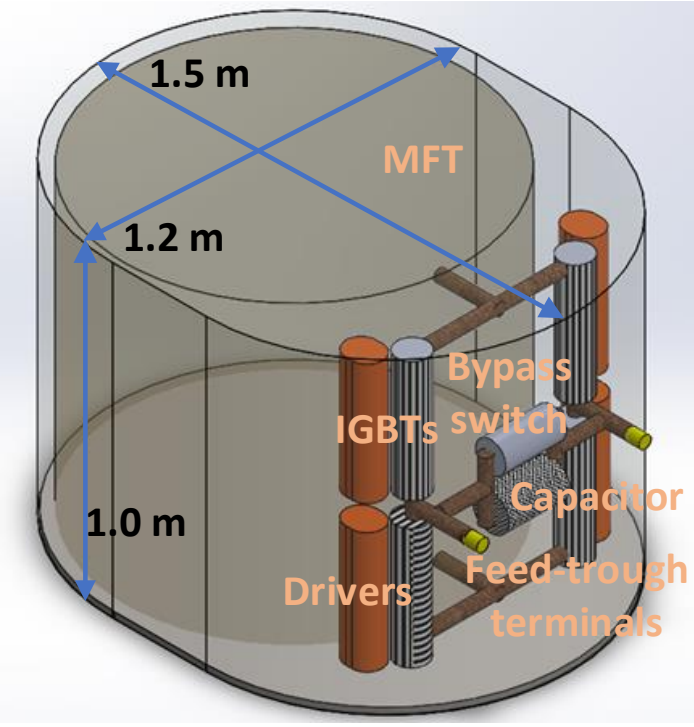

Figure 6-16. A schematic drawing of a real scale MFT with the high voltage series connected IGBTs of the DAB H bridge

In Figure 6-16, the big cylinder inside is the MFT, the grey patterned cylinders are IGBT stacks, the brown parallel cylinders are IGBT drivers, one of the horizontal cylinders is a capacitor and the other one is a switch to short circuit the bridge in case of a failure. Each column of IGBTs includes cooling surfaces between each pair of IGBTs which is cooled down by a forced oil circulation as it is the case for the MFT. The Converter is housed in a metal tank, filled with a biodegradable oil. Required isolation distances for the elements to the tank walls are <100mm which will be filled with oil gap-OIP combinations as was done for the MFT's HV winding.

A direct cable connection to the metal transformer tank shall be used. An example is a set of HV-CONNEX separable connectors, size 6, which are designed to work with an AC voltage up to 170 kV and a current up to 2500 A. Special components with corresponding material properties suitable for offshore applications can be ordered. In this case, there will be no need for external clearances in air as a shielded cable is connected directly to a grounded transformer tank (Figure 6-17).

(a) *(b)*

Figure 6-17. A HV-CONNEX separable connectors schematic [145] the female coupling on metal transformer tank (a), and the cable termination directly pluggable to the tank (b)

The metal tank can be placed inside a monopile tubular turbine steel foot which is the most common foundation for offshore wind turbines and normally have a diameter bigger than 6 metres or in a

container of W3.0×D2.0×H2.0 m which will have enough space for feedthrough cable connections and maintenance operations. (Figure 6-18).

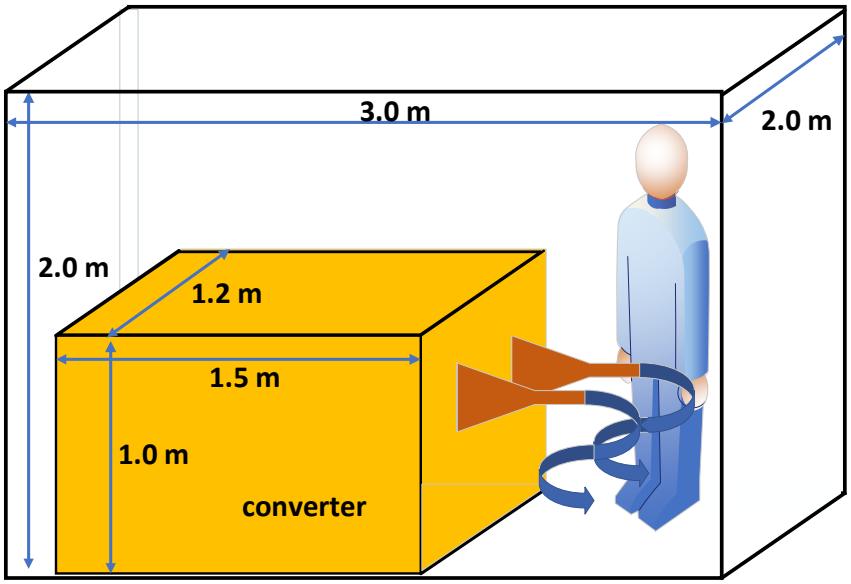

Figure 6-18. A 1.8/18 kV, 5555/555 A DC/DC converter having a 250 kV DC offset isolation to ground

To use a metal tank is a more professional solution but the feed-trough terminals are very expensive. In case, the innovative solution of using a tank made of insulation material as it is proposed for the MFT in this study, the insulation distance of the high voltage outputs from ground shall be selected as 1.5 m. According to IEC 60071-1 [146], for a case of applying a 250 kV DC step, the highest voltage (U_m, r.m.s. value) of 170 kV (≈250/√2) can be selected which dictates a clearance higher than 1.5 m. This is true in the case of standard reference atmospheric conditions [146], where the temperature is 20 °C, the pressure is 1013 mbar and the absolute humidity is 11 g/m^3. In addition, the ambient air shall not be polluted by dust, vapours, or salt. These means that, in case a construction like the prototype transformer is selected at reference atmospheric condition the minimum dimensions of a container carrying the transformer will not be smaller than 3.2 x 3 x 3 m^3 (Figure 6-19). It is clear that this is a safety clearance distance, and no one can enter this area when the transformer is energized.

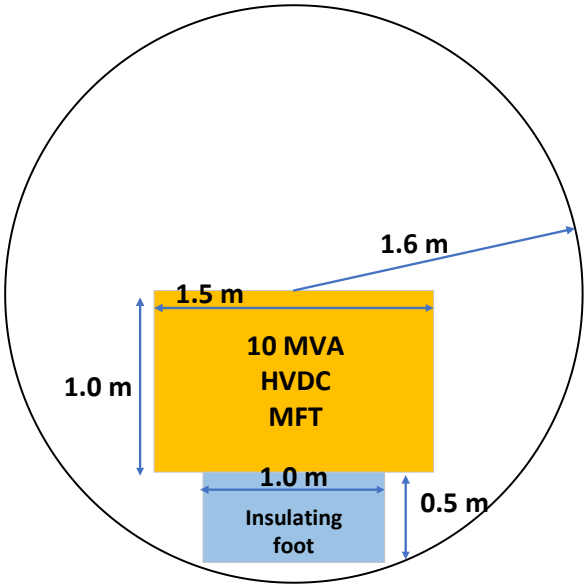

Figure 6-19. Clearances required for a DC/DC converter in an insulating tank when it is placed in a metallic container

7 Thermal Simulations

As for the fulfilling the withstand criterion of a very high DC voltage, the windings are covered by oil impregnated pressboards (Figure 4-4), it is very important to check that with which oil velocity the maximum of the following Max temps reaches 80 °C (353 K):

- Maximum HV winding surface temperature
- Maximum LV winding surface temperature
- Maximum Core surface temperature
- Maximum oil temperature in the tank

For the ferrite core, 100 °C is taken as a normal operating temperature [104]. The oil and paper insulating materials have their own limits of temperature which can be found in their specification sheets. For conventional mineral oil type power transformers with a normal use of life expectancy, the top oil temperature is limited to 105 °C and the hot spot temperature to 95 °C, all considering the ambient temperature of 30 °C [104]. In this case study, 80 °C is a selection considering the safe side, both for insulating material and for plexiglass tank and pressing plates.

In case of using ester as insulating oil, the operating temperature can considerably be increased [147]. However, thermally upgraded paper insulation materials should also be used. Synthetic ester oil like Midel 7131 has a higher viscosity compared with the mineral oil (Figure 7-1) which makes it less favourable regarding the cooling capability [148]. However, because of an excellent fire resistance property and especially due to its biodegradability [147] it is very suitable for offshore remote platforms. Therefore, the cooling capability of the prototype transformer is investigated considering the ester oil as the insulating oil. It is obvious that if the cooling system design demonstrates a good performance having the ester oil in circulation, it will perform excellent with a mineral oil. However, the flow distribution might change fundamentally, and performance must be checked prior to application.

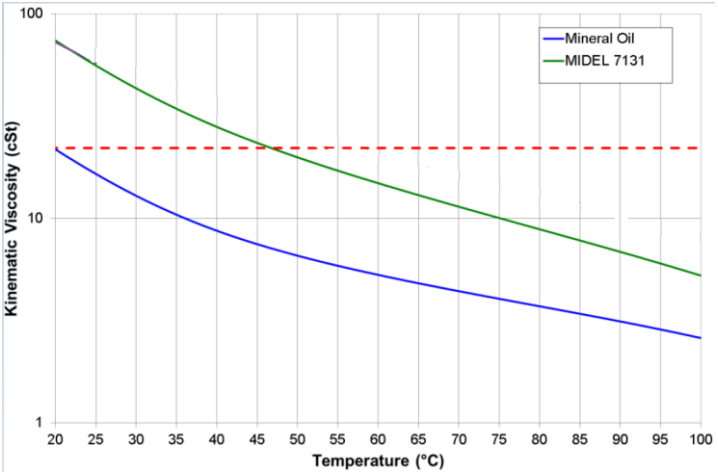

Figure 7-1. Comparison curves of ester and mineral oil viscosity (obtained from Midel Company)

In the following parts, innovative improvements are presented to enhance the performance of the cooling system and to limit the temperatures to the above-mentioned constraints. The thermal simulations are based on the ester oil.

The thermal capacity (specific heat) of the oil is set to 1.9 kJ/kg°C and it is assumed that it circulates with the speed of 0.2 kg/s. The forced input oil is assumed to have a constant temperature of 25 °C. As

it is calculated, 120 W is assumed to be produced by cores (12 W for each core stack) and 96 W by windings (48 W for each winding).

For thermal dimensioning, an open-source Computational fluid dynamics (CFD) software, OpenFOAM is used for computation, and ParaView, an open-source visualization application is used for flow field visualization. The BuoyantBoussinesqSimpleFoam solver with the OpenFOAM fork Helyx with momentum and energy equation is used to solve the model. The volume meshing and computations are parallelized on multiple CPUs. The parameters presented in Table 7-1 are used as input to the simulations.

Table 7-1. The parameters are used as input to the simulation process

	ester	mineral
λ Thermal conductivity (W/m.K)	0.141	0.1462
Cp Specific heat capacity (J/kg.K)	1990	1968.4
μ Dynamic viscosity (Pa.s)	13.174	3.67
Nu Nusselt Number (-)	14×10^{-3}	4.34×10^{-3}
Pr Prantl Number (-)	40	40
ρ Fluid Density (kg/m^3)	941	845.7
p reference (Pa)	101325.0	
T reference (K)	300.0	
Beta (1/K)	3×10^{-4}	

Efficient cooling on wall bounded flows is related to the momentum of the flow. A preliminary control of the design showed a wasted momentum of the coolant in the channels between the cores (Figure 7-2). Iterative design and verification steps are chosen to improve the coolant momentum distribution on warm surfaces of the transformer.

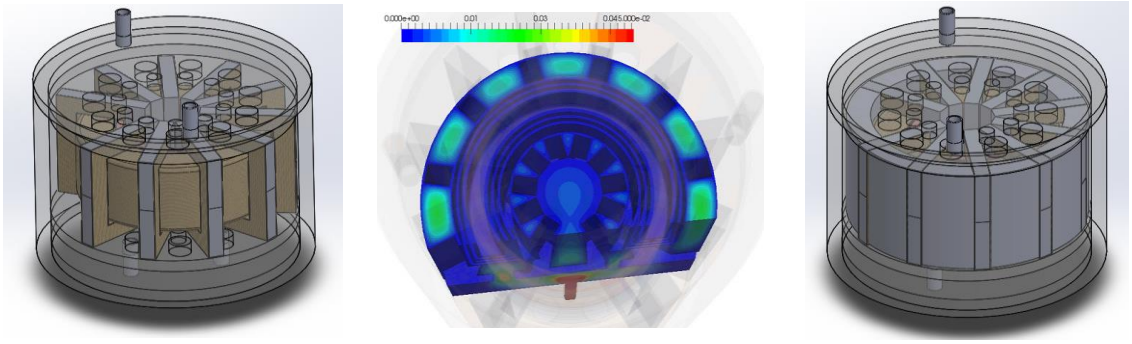

(a) ***(b)*** ***(c)***

Figure 7-2. A modification in the design for the purpose of the improvement of the thermal performance of the transformer: the preliminary design (a), the wasted high velocity magnitude (m/s) between the cores (b), and the improved design including added obstructions to channel the momentum into active part (c)

The results of first run of the thermal evaluation of the preliminary design showed the results reported in Table 7-2. The table demonstrates that the thermal design of the transformer is not skilfully performed, and the results overrides the mentioned limits.

Table 7-2. The temperatures for the preliminary design (°C)

	min	average	max
HV winding	39.6	159.1	269.0
LV winding	28.3	71.9	241.4
Core	28.3	66.8	285.8
oil	-	-	284.8

Figure 7-3 demonstrates that there is an improvement from blocking the free space between the core legs near the tank wall, but the middle channel should also be blocked in an effective way so that the cooling effect of oil on the cores is not undermined too much.

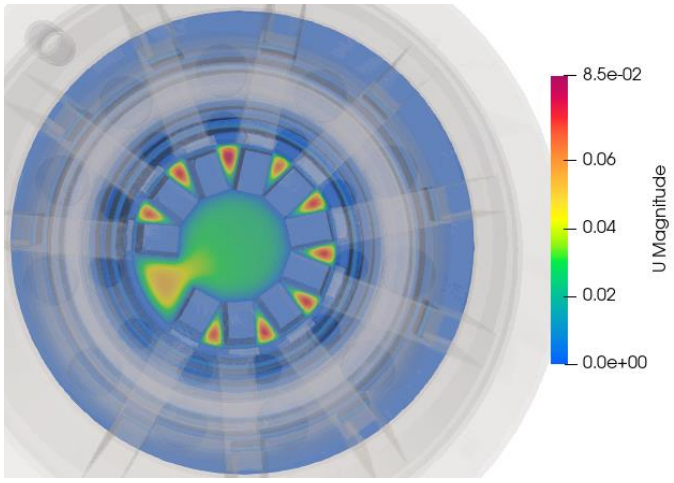

Figure 7-3. The wasted high velocity magnitude (m/s) of oil in the middle channel (a), and the improved oil flow by blocking the middle channel

The calculation showed a hot surface temperature for the cores in Kelvin:

- HV winding: min = 300.3, average = 307.5, max = 314.5
- LV winding: min = 300.4, average = 303.2, max = 346.0
- Core: min = 300.7, average = 309.9, max = 431.7

The result of core surface temperature dictated a decrease of 10% in the middle plug size (Figure 7-4).

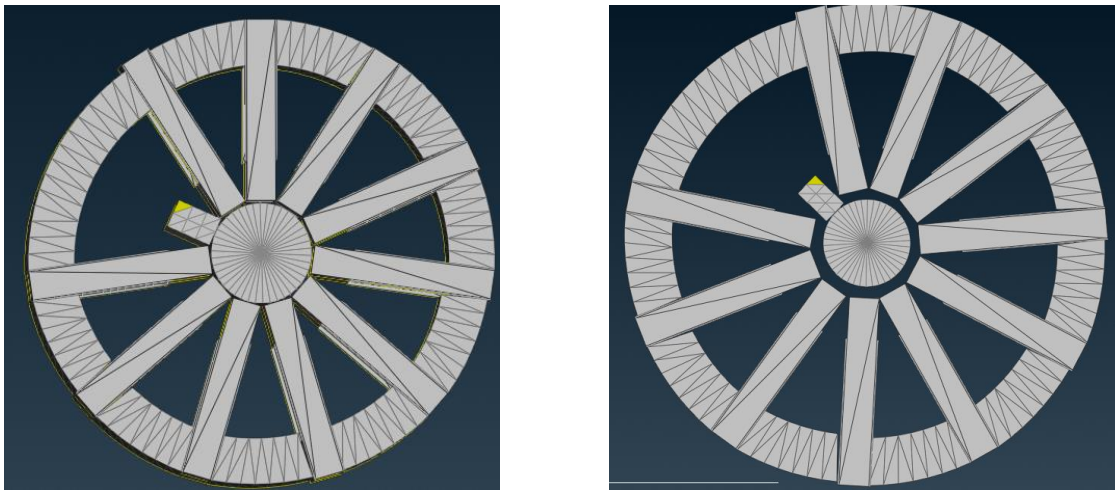

(a) ***(b)***

Figure 7-4. A totally blocked middle column (a), and an improved design to help better cooling of the core material (b)

To have a control on the oil flow direction and to lead the oil to pass the round openings between the formed OIP insulations on the top and the bottom of the active part, one natural improvement was to change the design of the upper and lower pressing plates, from having several holes, to a round opening in the middle (Figure 7-5).

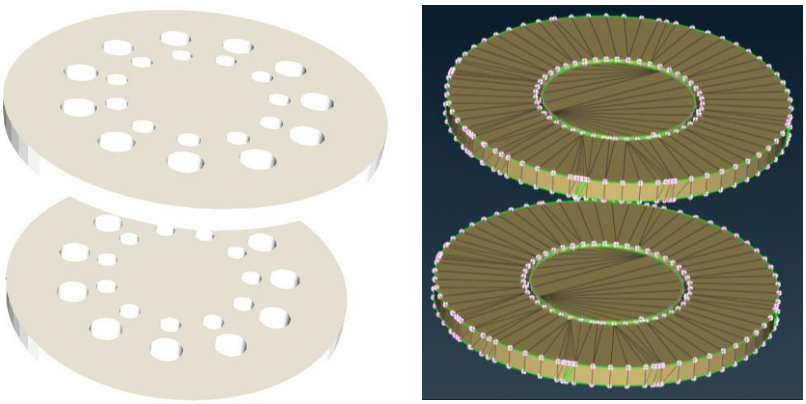

(a) *(b)*

Figure 7-5. The preliminary design of pressing plates of the prototype (a), and an effective improvement (b)

Another improvement is made to cool down the cores on their surfaces facing the transformer tank by making oil jet channels on the top and bottom press plates (Figure 7-6).

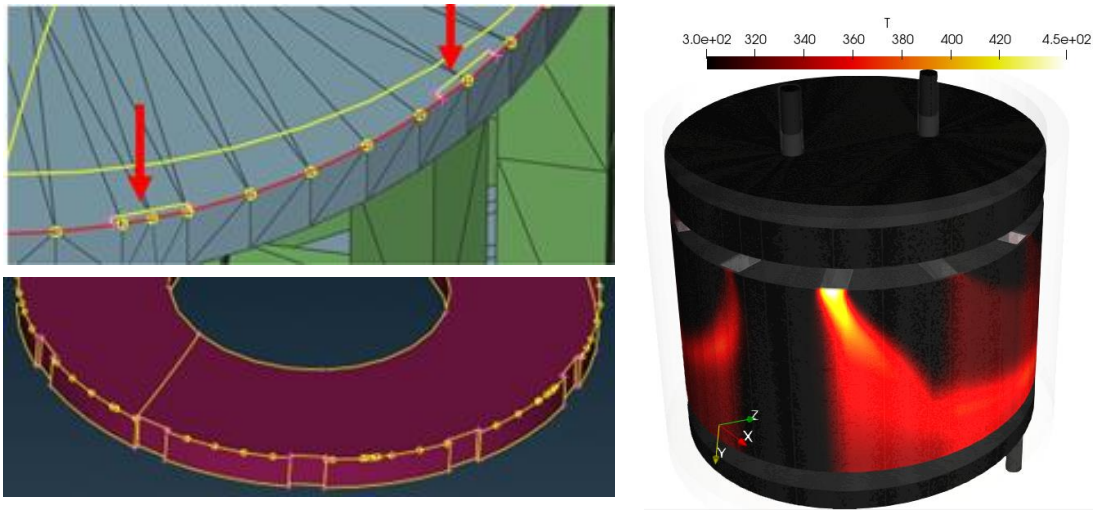

(a) *(b)*

Figure 7-6. Improved core surface cooling by creating oil jet channels on the top and bottom press plates (a), and the resulting temperature distribution diagram (b)

This improvement reduced the maximum core temperature form max = 431.7 to 390.6 K.

Figure 7-7a demonstrates a 2D velocity field of the oil inside the improved design. However, some more improvements can be made. There are two pipes as the oil outlet on the bottom of the oil tank. A laminar flow analysis in Figure 7-7b shows that the second oil outlet on the bottom of the tank (on the left) is not used effectively, as the coolant is channelled mostly toward one outlet (on the right) to leave the transformer tank. This leads to a less uniformly distributed flow and the loss of efficiency of the cooling system.

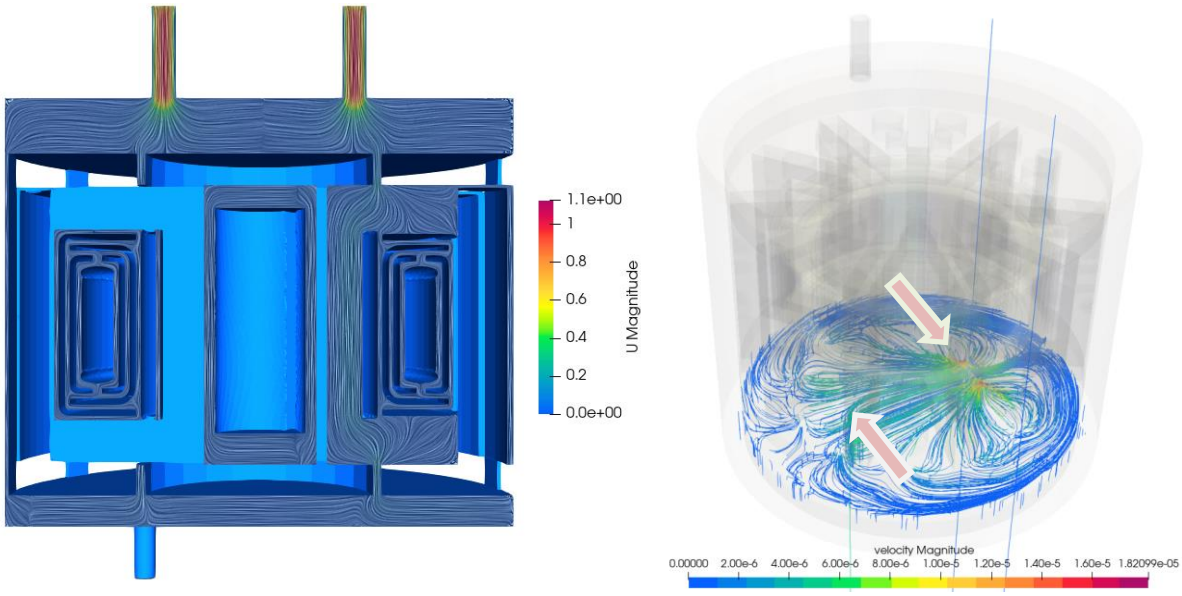

(a) ***(b)***

Figure 7-7. A 2D velocity magnitude (m/s) of the oil inside the improved design (a), and the ineffective second oil outlet on the left side of the tank bottom plate (b)

Figure 7-8 demonstrates that another improvement is the distance between the oil inlet pipes on the tank top cover. In this way, as it can be seen from Figure 7-7a also, the oil flow will directly enter from the top opening of the insulation system to the isolation channel between the windings. Oil inlets are placed at the top to let the oil weight help the flow circulation.

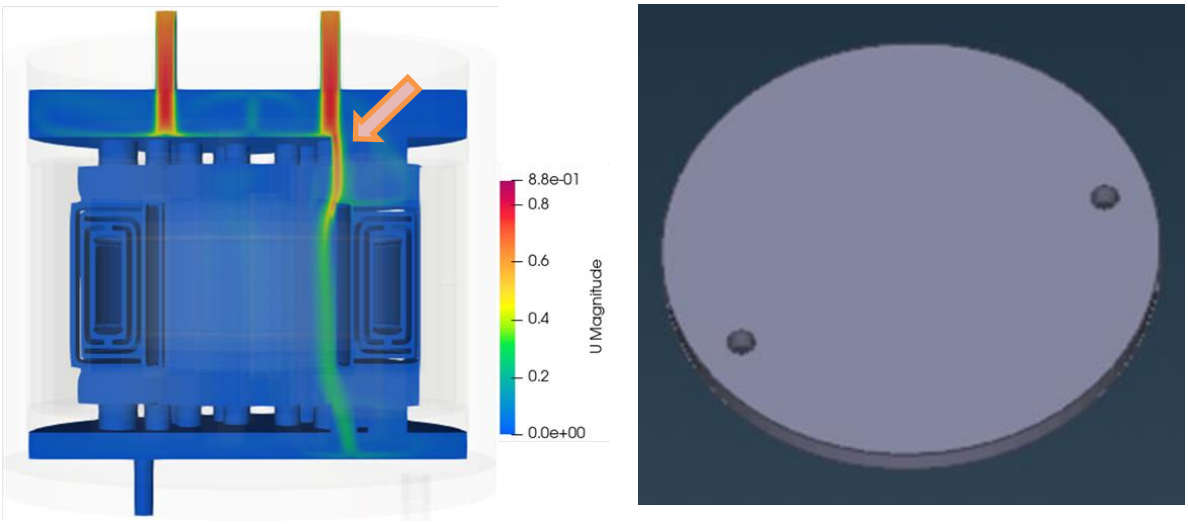

(a) ***(b)***

Figure 7-8. An improvement for the place of oil inlet pipes on the transformer's top cover is required: the top cover holes (a), and the deviation in the flow root of the oil (b)

The final results are demonstrated in Figure 7-9 where it is obvious that the hottest point on the active part has no temperature higher than 80 °C.

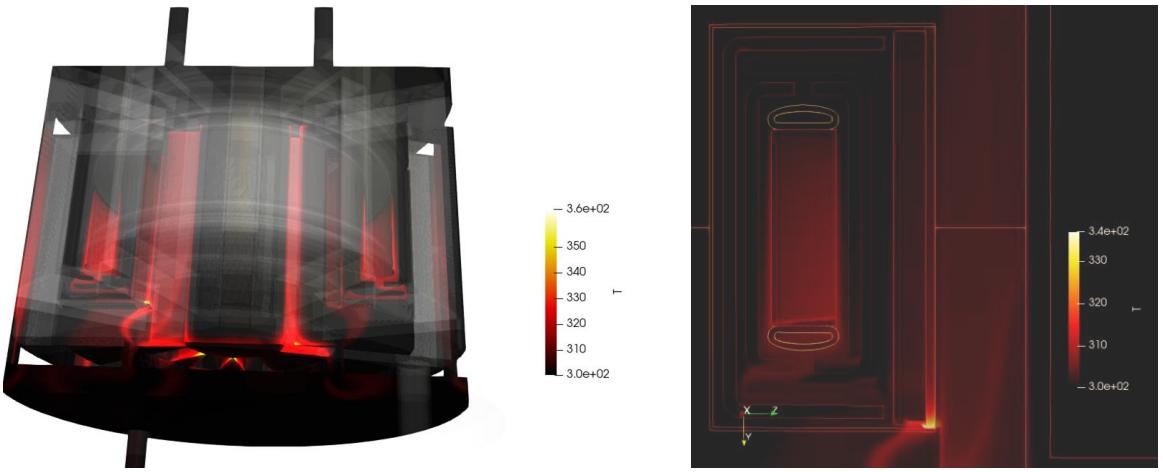

(a) *(b)*

Figure 7-9. A 3D temperature (K) distribution diagram in the active part (a), and a 2D picture of the hottest points on the active part (b)

After the simulations the heat transfer coefficients are extracted to check that the model is built on correct assumptions (Table 7-3).

Table 7-3. Heat transfer coefficients extracted after simulations

	Core	HV	LV
Convective heat flux (W)	120	48	48
Wall temp (K)	305	307.7	303.3
Tw-Tref (K)	7.4	9.6	5.2
Reference convective heat transfer coefficient (W/m^2K)	79.7	61.6	79.9

Table 7-4 demonstrates that the final results of simulations after improvements are satisfying.

Table 7-4. The final results after improvements (°C)

	min	average	max
HV winding	27.1	34.5	41.5
LV winding	27.3	30.1	74.9
Core	27.5	32.1	117.4
oil	-	-	116.3

Figure 7-10a demonstrates a monitor which shows that the resulted temperatures are stabilized after enough number of iterations and are correctly determined. It is made sure that the error in the computations is lying below an accepted limit line. In Figure 7-10b shows that all the field variable residuals are less than 1e-4.

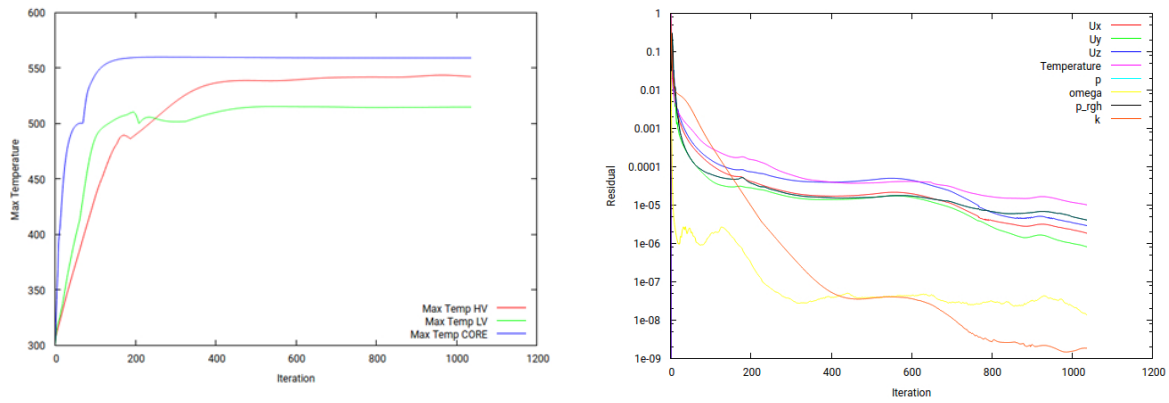

(a) *(b)*

Figure 7-10. Temperature convergence monitor curves for the final temperature results (a), and the error in the computations (b)

8 Conclusions and Future Work

8.1 Conclusions

The knowledge generated during this research contributes to building data which in the long run should lead to making a solution possible, which realizes a technology for the direct connection of offshore wind farms to land, without a need for a very large and expensive 50 Hz transformer station. The technology is based on the use of DC/DC converters individually for each offshore wind turbine and to connect them in series in order to feed an HVDC transmission cable for the energy transport to the grid. The key element of the convertors is a Medium Frequency Transformer (MFT). The design principles of such transformer have been the focus of the present research. It is proven that the insulation of the MFT is capable of withstanding a high DC offset voltage, also combined with high frequency oscillations, which can only be realized by an oil-immersed system.

- As a fundamental input to the insulation design, electrical characterization (specifically, measurements of DC conductivity) of used insulation materials, including mineral and ester oils and OIP, has been performed. A low sensitivity towards noise, high voltage setup with a controlled temperature is designed and built. A proper precondition method is established, and several measurements are performed. The conductivity values were calculated in the range of the applied electric field of (1-6) kV/mm and (1-12) kV/mm for oil and OIP, respectively, and for a temperature range of (30-90) °C. The obtained results have been verified against (a limited set of) published data that confirmed their validity as well as the accuracy and efficiency of the measuring methods used. In comparison to previous methods introduced in literature, reliable and repeatable measurements for synthetic ester oil and OIP are investigated, implemented and proposed. Although the setup delivered reliable and repeatable results, still more work is needed to automatise the measurement process and to reduce the huge man-hour investment which has been done in this work for performing the measurements.
- The data on temperature and field dependent electric conductivities of mineral and synthetic ester oil as well as OIP, were obtained for the HVDC application. The results for the ester OIP are unique and were not publicly available earlier, they are now published and accessible for all stakeholders. The results appear promising, however due to lack of evidence from other works, it was at this stage not possible to validate the conductivity values of synthetic ester OIP, but hopefully more research on the subject will come up, making this possible.
- The measurements have demonstrated that the conductivities of transformer oil and OIP exhibit strong nonlinear dependencies on the temperature and the electric field, that makes the design and performance of the insulation of the MFT dependent on specific operation conditions. The acquired data are used as input for electrostatic FEM simulations. Based on the measurement results, a non-linear Maxwell Wagner model is developed and applied in the Comsol software. The developed method worked well, and the program outputs were both visually and numerically presented. However, it was more desirable that the program be used for designing several combined samples of different forms subjected to various voltage and temperature conditions and the results are validated later by experimental breakdown tests. Later, the research is concentrated on the elements which are affected by the insulation design and are relevant for the performance of the converter, namely, the leakage inductance,

parasitic capacitances and losses. Finally, a prototype has been built and tested to verify the key results.

- An innovative combined-path methodology for designing oil-paper insulation system of a MFT operating at high DC offset based on is developed. It is shown that the *E* curve of the combined-path is greater than the *E* curves of the oil gap and creepage paths. This, consequently, will lead to a lower SF for the combined-path with respect to the SFs of its forming oil gap and creepage paths. Therefore, using the combined-path method results in a safe and more reliable design. In order to confirm the theory findings and to establish the validity limits of the combined-path method more experiments have to be performed.
- A parametric field and temperature dependent stress investigation, focusing on all the weak points of the transformer insulation are performed which is strongly recommended for a reliable HVDC oil paper insulation system design process. The nonlinear dependency of the oil and OIP on the applied voltage and temperature, is considered. This is crucial for an accurate calculation of the dynamic electric fields in the insulation system of the transformer. A procedure, as a sequential flowchart that ensures the voltage withstand at all points during the energization until a full loaded steady-state phase has been proposed. The results found on the investigated design were promising, however, further experimental validation would have been desirable. It is an industry routine that for oil-filled transformers, the long oil gaps are divided by several solid barriers. In this study, it is verified that, for a DC design, the thickness of solid barriers shall be precisely determined based on the voltage drop over their thickness. It is explained how the position, form and the overlapping of the solid barriers shall be considered. What definitely would have been desirable would have been to conduct more experimental verification of the theoretically found results.
- It is demonstrated how the leakage inductance constraint can be realized on the insulation design stage. An analytical method has been established for the computing the leakage inductance. The final expressions are simple and allow for quick accurate (with errors below 1%, which was considered to be a very good achievement) calculations thus eliminating the need for time-consuming 3D FEM simulations. The scope of the study was limited to medium frequency applications in the ranges lower than 20 kHz. However, for frequencies higher than 100 kHz the effect of winding loss on the reduction of the leakage inductance should be investigated further.
- At high switching frequencies, parasitic capacitances of the transformer cause unwanted oscillations at the sharp rising or falling occasions of the square wave shape of a DAB due to resonances with the inductive elements of the circuit. In the thesis, innovative methods are presented to achieve a high frequency equivalent circuit of a high power, high voltage, medium frequency transformer for power electronic applications. The criteria employed for the validation of the method is the comparison of the resonance frequencies of the *Z* curves. The curves are measured from a prototype transformer or the developed equivalent circuits, under both open and short circuit conditions. It is shown that the error level of the introduced Medium frequency (MF) model is less than 5 % and in the case of Extended model, is less than 2 %. The result was considered to be quite acceptable. In addition, the introduced MF model is more accurate compared with the method presented in literature even for conventional transformers with one grounded terminal. The scope of this research did not include the nonlinear nature of the core and a variable magnetising inductance on the resonance frequencies of the model, which of course would have been a valuable contribution. The effect of a nonlinear core modelling on low-frequency behaviour of a transformer is investigated

earlier, for example in [149]. To increase the accuracy of the capacitive equivalent circuit model, this would have been a valuable further research step.

- The effective numerical method proposed by Meeker [111] was utilized for calculation of eddy current losses in medium frequency transformer windings made by litz wires. The numerical method is based on the equivalent permeability and conductivity of stranded copper conductors. The proposed method is effective and quick. It was found that this methodology worked well also for the transformer case investigated in this work. However, as it is stated in [111] the method has used assumptions and estimations which can lead to a lower accuracy for special cases.
- The data sheets for transformer wires or insulation materials are normally presented for power frequency applications. The presented results of the high frequency breakdown tests performed during this study show that the characterization of the insulation of the delivered materials like litz wires or insulation tapes is a vital step before the design of a medium frequency transformer. A test with a standard setup showed that, increasing the insulation test frequency from DC to 5 kHz can cause at least 5 times reduction in the withstand strength of a litz wire isolation. This experiment shows how important is to characterize the components precisely based on the parameters related to the stress type that the object will experience under the operation condition. It has to be admitted that the experiments should have included more samples and much better controlled environment to produce more secure results with a lower standard deviation. In addition, to fully establish the limits, the theoretical findings shall be verified by experimental results. For example, the corona or partial discharge shall be properly removed, and a stable square wave source should have been used for the tests. In addition, the reliability of the results can be improved by repeating the same tests on different samples and isolation types.
- The research conducted on the various subtasks. The study is successfully utilised and implemented for the design of a unique 50-kW prototype oil-paper type transformer having a very small core window size (70×126 mm^2) which should withstand 125 kV offset DC voltage. The prototype has been manufactured by in-house tools and equipment and has successfully passed the related verification tests. No such a prototype's construction or design procedure have been reported earlier in literature. Based on the developed and verified design method, an indicative curve, suggesting the relation between the required withstand strength of the transformer to the offset DC voltage and the isolation distances inside the core window is presented. Although the prototype has successfully passed the DC insulation test, the formation of surface charge on the transformer's tank body was noticed. Also, here it would have been great to investigate the performance of the transformer further to build more knowledge about the real limits in terms of insulation, losses, temperature etc.
- A comparison of the achieved conductivity values of ester and mineral oil/OIP highlights that the conductivity ratio of the ester oil/OIP (which is in the range of 15-25) are not as much temperature and voltage stress dependent, as the conductivity ratio of mineral oil/OIP (in the range of 1-294) is. In a unique judgement, this means a reduced dynamic stress level of the transformer design in case of using ester oil and OIP. It is also shown that the ester oil/OIP conductivities are approximately 100-1000 times higher than mineral oil/OIP conductivities. This results in a much shorter time (in the range of few decades of second) for the ester-insulated transformer to reach the steady state condition compared with the mineral oil insulated transformer, which demands more than 2.5 h to reach a steady state condition. Although the initial results were considered as a substantial success, the operational condition

change of a same transformer in case its oil is changed from mineral to ester, can be an interesting comparison.

- A main result of the research was that it brought knowledge about the DC series system moving it a step closer to a feasible concept. For the investigated oil-insulated transformer topology, it appeared that it seems realistic to reach a DC offset voltage of ±350 kV. The volume of a 10 MVA, 250 kV DC transformer is less than 1 m^3 and its weight is limited to 2.2 Tons. The efficiency of transformer is 99.86 % and not less than 99.76 % even in a low wind condition when the transferred power is limited to 1 MW. For a sample 6 MW DC/DC converter, the study shows that the efficiency of the converter remains at a level of higher than 99.25 %. The volume of the converter is less than 1.8 m^3 which means that there is a good possibility of installing it in a container fixed to the structure of a wind turbine, or even inside the turbine. The ratings can be compared with a conventional 50 Hz transformer platform where the weight and volume of the transformer only, can reach up to 20 Tons and 25 m^3. It would have been valuable to investigate the insulation and cooling system design of the power electronic parts with the same detail as was done for the transformer. Even though, the efficiency and weight and volume data of the converter in total is approximate, the results are considered to be an important step towards a realisation of the series DC wind turbine concept.

To sum up, the concept of the medium frequency transformer with a high DC insulation to ground thought to be used in DC/DC converters for a series high voltage DC integration of offshore wind farms, has been proven viable, and no obstacle to further progress have been identified. This cross disciplinary research introduces new solutions for power-electronic researchers, and a new application for high-voltage designers. The developed method in this work can be easily implemented for more complicated designs of HVDC MFTs and facilitates the application of these step-up transformers for power electronic engineers where higher isolation levels are required.

8.2 Outlook and Future work

This research effort has been one step towards building knowledge for the realisation of a series DC wind park. There are a number of issues which requires further work.

- One of the fundamental questions about insulation is ageing. For transformer insulation based on impregnated cellulose, it is accelerated by moisture and temperature. Thus, development of a method for conductivity measurements under ageing with controlled humidity is highly desirable.
- To take one of the advantages of ester oil, which is its withstand to a higher operation temperature, the other high temperature tolerant solid insulation materials can be considered and their compatibility are studied. This includes investigation on high temperature insulation materials like Nomex paper. Research on plastic based solid insulation materials like Teflon, PE, POM or Plexiglas inside oil and the wetting effect of oil on the surface of them is also desirable.
- To optimize the oil-paper DC insulation design, Multiphysics simulations need to be conducted to account for transport of charge carries and their deposition on materials interfaces. A classical design tools based on constant conductivity values of the materials are not capable to implement such features, and the proposed non-linear MW model is thus a good starting point for further development. As a scientific method for verification of the performed experiments in this study, a Kerr effect setup can be built and measurements on different ester

oil – PB barrier arrangements be performed. Charge transfer and accumulation simulations in ester oil and OIP and between the covered or bare electrodes would be very useful to conduct.

- More work is required regarding the nonlinear dependency of the conductivities to temperature change. This aspect is more important when a natural oil flow is established inside the transformer which contributes to temperature differences at different positions of the insulation system at one moment of time. Here the results of this research should be perceived as a very initial step, and an investigation on temperature gradient inside the transformer tank would be desirable to conduct and a combined Multiphysics thermal and electrical insulation design simulation and analysis as well.
- As it is mentioned in conclusion, using the combined-path method results in a more reliable design. Therefore, it would be of highly desirable to perform experiments in order to confirm the theory findings and to establish the validity limits of the combined-path method.
- Insulation design curves for mineral oil insulation systems are established and published decades ago. For ester oil, there is very limited access to sources in this regard. Undoubtedly a comprehensive work effort is of very high value in order to extract these curves with a high confidence.
- It would be of great value to investigate the effect of winding losses on the reduction of the leakage inductance. This is especially important if a frequency range of higher than 100 kHz is under consideration for a study.
- To investigate the nonlinear nature of the core and a variable magnetising inductance on the resonance frequencies of the MFTs and on the parasitic capacitance equivalent circuits, is another important topic for further work.
- An establishing of the validity limits of the Continuum representations of wound coils method, for calculation of winding loss is definitely worth a research effort.
- To continue with the research on high voltage breakdown of the insulation materials under high frequency stress, AC breakdown tests can be performed on insulation materials using a voltage source having a square wave shape and with a secured removal of the external PD, negatively affecting the test results. In addition, high frequency induced over voltage test could be performed on the manufactured prototypes. For a design with a metal tank where a plug-in high voltage cable termination is used, the effect of a high HV AC fast rising square wave on the HVDC feedthrough, the cable to tank bushing can be investigated.
- To eliminate a need for a big and expensive high voltage DC bushing, in this work a novel tank design is presented. For the prototype, an available off-the-shelf plexiglass cylinder is used. The high voltage DC test demonstrated the accumulation of charges and local minor surface discharges. This disadvantage must be tackled. This can also be the case if we use glass. By applying a semiconductor coating on the surface of the tank, this effect might be eliminated, but further research is needed.
- As mentioned in the conclusion, to perform comparisons to investigate the changes that shall be applied to the operational condition of a same oil type MFT in case its oil is changed from mineral to ester oil, is a valuable effort.
- This research focused on the transformer, however, insulation and thermal studies of the other components, e.g., the power semiconductors is definitely a topic worthy of further research. Moreover, the DC/DC converter's weight, volume, and efficiency was crudely estimated, and here undoubtedly more research is needed, to drive the concept further on towards realisation.

9 Publications Summary

In this Chapter the summaries of the published articles during this research work are presented.

Journal articles

1. A Novel Oil-Immersed Medium Frequency Transformer for Offshore HVDC Wind Farms
   M. Kharezy, H. R. Mirzaei, Y. Serdyuk, T. Thiringer, and M. Eslamian
   IEEE Power Delivery, 2021
   https://ieeexplore.ieee.org/document/9247458
   Offshore wind farms pose the challenge of transmission of produced energy in an economic and effective way over long distances, justifying investments in High Voltage Direct Current (HVDC) systems. A solution to surmount the need for an expensive and large power transformer station is to connect each wind turbine to a DC/DC converter in which a Medium Frequency Transformer (MFT) is utilized to reduce the size of the station. Further, the DC outputs of the converters of the wind turbines can be connected in series to create a high DC voltage. In this solution, the MFTs are required to be insulated against a high DC voltage to ground in a limited compartment. This contribution presents a prototype of a 50 kW oil-paper insulated MFT operating at biased 422/4500 V/V AC 5 kHz and 125 kV DC test voltage, which has been manufactured and subjected to verification HV tests. The dielectric design of the prototype MFT based on finite element solution of non-linear Maxwell-Wagner equations is introduced and the acceptance criteria and practical design considerations are discussed.

2. Green Solution for Insulation System of a Medium Frequency High Voltage Transformer for an Offshore Wind Farm
   M. Kharezy, H. R. Mirzaei, Y. Serdyuk, and T. Thiringer
   MDPI Energies, 2022
   https://www.mdpi.com/1996-1073/15/6/1998
   High Voltage Direct Current (HVDC) transmission represents the most efficient way for transporting produced electrical energy from remotely located offshore wind farms to the shore. Such systems are implemented today using very expensive and large power transformers and converter stations placed on dedicated platforms. The present study aims at elaborating a compact solution for an energy collections system. The solution allows for a minimum of total transformer weight in the wind turbine nacelle reducing or even eliminating the need for a sea-based platform(s). The heart of the project is a Medium Frequency Transformer (MFT) that has a high DC voltage insulation towards ground. The transformer is employed in a DC/DC converter that delivers the energy into a serial array without additional conversion units. The insulation design methodology of an environmentally friendly HV insulation system for an MFT, based on pressboard and biodegradable oil, is introduced. The measurement method and results of the measurements of electrical conductivities of the transformer oil and Oil Impregnated Pressboard (OIP) are reported. The measurements show that the biodegradable ester oil/OIP conductivities are generally higher than the mineral oil/OIP conductivities. Numerical simulations reveal that the performance of the insulation system is slightly better when ester oil is used. Additionally, a lower temperature dependency for ester oil/OIP conductivities is observed, with the result that the transformer filled with ester oil is less sensitive to temperature variations.

3. An Accurate Method for Leakage Inductance Calculation of Shell-Type Multi Core-Segment Transformers with Circular Windings
   M. Eslamian, **M. Kharezy**, and T. Thiringer
   IEEE Access, 2021
   https://ieeexplore.ieee.org/document/9509430

The leakage eld in shell-type transformers is strongly affected by the boundary conditions introduced by the core walls and thus the effect of the core should be considered properly in the leakage inductance calculation. In this paper, a new method for accurate calculation of the leakage inductance of shell-type multi core-segment transformers with circular windings is presented. For this purpose, first, the expressions for self and mutual inductances are derived in cylindrical coordinates considering the core walls as the flux-normal boundary condition. Then, a new approach is proposed for calculating the leakage inductance considering the number and dimensions of the used core segments. The method is developed at first for single and double core-segment transformers (known also as E-core and U-core transformers) and then adopted for shell-type segmented-core transformers. The method is verified by 3-D FEM simulations. The comparisons with the previous analytical methods demonstrate the superiority of the proposed method. A transformer prototype has been built and verification tests have been conducted. The comparisons show that the leakage inductance can be estimated with an error less than 1%, demonstrating a very high accuracy with the proposed method.

4. Determination of Parasitic Capacitance of High- Power Medium Frequency Transformers: Case study of a high voltage DC biased transformer for wind power application
   M. Kharezy, M. Eslamian, T. Thiringer, Y. Serdyuk, and B. Khanzadeh
   IEEE Power Delivery, 2023
   https://ieeexplore.ieee.org/document/10226221
   Determination of parasitic capacitances is a necessary step in the design process of transformers to be used in power electronic devices. At high switching frequencies, these capacitances together with inductive elements of the circuit cause unwanted oscillations during fast transients such as sharp fronts of square voltage waves appearing in a dual active bridge converter. In the paper, parasitic capacitances of high-power transformers supposed to operate at frequencies up to several kHz and high DC offset voltages (100 kV and higher) are analyzed. Two methods based on the equivalent circuit approach are suggested. To validate the methods, they are used to determine the parameters of an equivalent circuit of a prototype transformer developed earlier. The capacitances are calculated using the results of 3D FEM simulations performed based on the structure of the transformer as input. Furthermore, another set of data used for validation of the proposed calculation methods was obtained from the conducted direct measurements of frequency dependent impedance of the transformer. The accuracy of the proposed methods is discussed. It is concluded that the methods can be used for quick estimations of the parameters of transformers designed for power electronic applications.

5. An Accurate Analytical Method for Leakage Inductance Calculation of Shell-Type Transformers with Rectangular Windings
   M. Eslamian, **M. Kharezy**, and T. Thiringer
   IEEE Access, 2021
   https://ieeexplore.ieee.org/document/9430546
   This paper presents an accurate analytical method for calculating the leakage inductance of shell-type E-core transformers with rectangular windings. For this purpose, first, an expression for calculating the leakage inductance per unit length inside the core window considering the core walls as the flux-normal boundary condition is derived. Then, a new accurate method for determining the Mean Length of Turns (MLT) based on the total stored energy is presented. The MLT is needed for the leakage inductance calculation using 2-D methods. By dividing the MLT into three partial lengths and calculating the corresponding leakage inductances using three different core window arrangements, the effect of core structure on the total leakage inductance is considered. The method is verified by 3-D FEM simulations as well as the leakage

inductance measurements on two different fabricated transformer prototypes. The superiority of the method is also confirmed by comparisons with the previous analytical approaches. The proposed method enables the leakage inductance calculation with an error less than 1%, compared to the 3-D FEM results. Using the presented method, the leakage inductance calculations can be performed rapidly and accurately in the design stage without the need for time-consuming 3-D FEM simulations.

6. Multilevel Dual Active Bridge Leakage Inductance Selection for Various DC-Link Voltage Spans
   B. Khanzadeh, T. Thiringer, and **M. Kharezy**
   MDPI Energies, 2023
   https://www.mdpi.com/1996-1073/16/2/859
   The leakage inductance of the transformer in a dual active bridge (DAB) DC/DC converter directly impacts the ac current waveforms and the power factor; thus, it can be considered a design requirement for the transformer. In the existing literature, a choice is made to either ensure soft switching in nominal power or to minimize the RMS current of the transformer. The inductance is typically obtained using optimization procedures. Implementing these optimizations is time consuming, which can be avoided if a closed-form equation is derived for the optimum leakage inductance. In this paper, analytical formulas are derived to estimate the desired leakage inductance such that the highest RMS value of the current in the operation region of a DAB is kept to its minimum value. The accuracy and sensitivity of the analytical solutions are evaluated. It is shown that in a large design domain, the solution for the YY-connected MFT has a less than 3% error compared to the results obtained from an optimization engine. As an example of the importance of selecting the leakage inductance correctly, it is shown that for 11% deviations in the dc link voltages, a 10% deviation from the desired leakage inductance value can cause 2% higher RMS currents in the converter.

7. Design Methodology and Optimization of a Medium-Frequency Transformer for High-Power DC–DC Applications
   A. Bahmani, T. Thiringer and **M. Kharezy**
   IEEE Transactions on Industry Applications, 2016
   https://ieeexplore.ieee.org/document/7496932
   The medium-frequency power transformer (MFPT) is one of the key elements of an isolated bi-directional DC/DC converters in applications such as future all-dc offshore wind farms, traction, and solid-state transformers. This paper describes a design methodology taking into account loss calculation, isolation requirements, and thermal management. Incorporating this design methodology, an optimization process with a wide range of parameter variations is applied on a design example to find the highest power density while the efficiency, isolation, thermal, and leakage inductance requirements are all met.

Conference articles

8. Core Loss Evaluation of MFTs with Square-wave Voltage Excitation
   M. Kharezy, M. Eslamian, and T. Thiringer
   SMM, 2023
   Submitted in April 2023
   A Medium Frequency Transformer (MFT) inside a Dual Active Bridge (DAB) normally operates under a square voltage waveform. Many publications have stated that the empirical equations based on measurements and the formulation contributed by Steinmetz are the most appropriate relation for the estimation of core losses under non-sinusoidal excitation of MFTs. However, to obtain Steinmetz parameters one should rely on characterization curves supplied by core manufacturers which normally are acquired at the operation conditions far from the targeted transformer's design prerequisites. The objective of this article is to present an

experimental method to estimate the Steinmetz parameters for the loss estimation under medium frequency non-sinusoidal excitation at the actual operational conditions of flux density, temperature, and frequency.

9. Insulation Design of a Medium Frequency Power Transformer for a Cost-Effective Series High Voltage DC Collection Network of an Offshore Wind Farm
   M. Kharezy, M. Eslamian, and T. Thiringer
   ISH, 2019
   Proceedings of the 21st International Symposium on High Voltage Engineering,
   https://link.springer.com/chapter/10.1007/978-3-030-31680-8_134
   DC can be used advantageously in transmission of power from offshore wind farms, utilizing series connection of the individual turbines' outputs. Employing individual wind turbine converters, operating at high frequency, the advantage of DC can be achieved without the need for a large central converter. This solution obviates the need of expensive, bulky and heavy 50 Hz transformer or centralized DC/DC converter platforms. Power electronic converters are among the enabling technologies to establish a series DC intertie system. The most important advantage of a DC/DC converter using a Medium Frequency Power Transformer (MFPT) is its compact size in comparison with a normal grid frequency transformer. The function of a MFPT is to provide voltage step up and isolation between generators and the HVDC link. The need for a compact structure dictates further design constraints. A MFPT should have a high-power transmission capability from a small volume as well as minimal internal insolation distances. Furthermore, in the series DC integration circuit, DC/DC converters can experience a very high offset DC voltage depending on the converter's position with respect to earth (in the range of one or two hundred kilovolts), while the primary side (wind turbine generator side) is only exposed to a few kV. Due to its promising features, many research activities have been devoted to the design and optimization of MFPTs. However, only a few activities specifically addressed the insulation requirements for them. In this article, the challenges of the high DC voltage insulation design of a MFPT are presented.

10. Performance of Insulation of DC/DC Converter Transformer for Offshore Wind Power Applications
    M. Kharezy, H. R. Mirzaei, J. Rastamo, M. Svensson, Y. Serdyuk, and T. Thiringer
    IEEE CEIDP, 2020
    https://ieeexplore.ieee.org/document/9437501
    High voltage direct current transmission is an effective way of energy transportation from offshore wind farms to the grid. One of the most economical solutions to realize it is based on a series connection of the wind turbines. This technology requires implementation of a DC/DC converter incorporating a special transformer operating at high DC voltages with superimposed high frequency components. To design the high voltage insulation of such a transformer, the dielectric properties of the materials constituting the insulation are to be known in a wide range of variations of the electric field and temperature. In the present study, results of the measurements of field and temperature dependencies of the electric conductivities of a typical high-quality mineral transformer oil and oil-impregnated pressboard are reported. The measurements were performed at different combinations of voltage-temperature stresses reflecting the insulation's operation condition. The obtained data are used for performance evaluation of the insulation system of a prototype of the transformer.

11. Estimation of the winding losses of Medium Frequency Transformers with Litz wire using an equivalent permeability and conductivity method
    M. Kharezy, M. Eslamian, and T. Thiringer
    IEEE EPE, 2020
    https://ieeexplore.ieee.org/document/9215900

To achieve the highest efficiency of a Dual Active Bridge converter, it is crucial to accurately calculate the winding losses of the Medium Frequency Transformer (MFT) situated inside it. In this article, an effective numerical method for calculation of the copper losses in MFTs with rectangular-shaped windings made up of litz wire, is utilized and practically verified.

12. Calculation of the Leakage Inductance of Medium Frequency Transformers with Rectangular-Shaped Windings using an Accurate Analytical Method
    M. Eslamian, **M. Kharezy**, and T. Thiringer
    IEEE EPE, 2019
    https://ieeexplore.ieee.org/document/8915036
    To achieve the lowest loss by the Zero-Voltage Switching of a Dual Active Bridge converter, it is crucial to precisely calculate the embedded Leakage Inductance of the used Medium Frequency Transformer (MFT). An effective analytical method is proposed for calculation of the leakage inductance of the MFT with rectangular-shaped windings.

13. Optimization and Experimental Validation of Medium-Frequency High Power Transformers in Solid-State Transformer Applications
    M. A. Bahmani, T. Thiringer, and **M. Kharezy**
    IEEE Apec, 2016
    https://ieeexplore.ieee.org/document/7468297
    High power isolated DC-DC converters are likely to provide solutions for many technical challenges associated with power density, efficiency and reliability in potential applications such as offshore wind farms, inter-connection of DC grids, MVDC in data centres and in future solid state transformer applications. The high-power medium frequency transformer (HPMFT) is one of the key elements of such a converter to realize the voltage adaption, isolation requirements, as well as high power density. This paper describes a design and optimization methodology taking into account the loss calculation, isolation requirements and thermal management. Incorporating this design methodology, an optimization process with a wide range of parameter variations is applied on a 50 kW, 1 / 3 kV, 5 kHz transformer to find the highest power density while the efficiency, isolation, thermal and leakage inductance requirements are all met. The optimized transformers are then manufactured and will be presented in this paper.

14. Optimum Leakage Inductance Determination for a Q2L-Operating MMC-DAB with Different Transformer Winding Configurations
    B. Khanzadeh, T. Thiringer, and **M. Kharezy**
    IEEE Ee, 2019
    https://ieeexplore.ieee.org/document/8923224
    This paper discusses the procedure for the determination of the optimum leakage inductance of a medium frequency transformer (MFT) for a quasi-two-level (Q2L) operating three-phase modular multilevel converter dual-active bridge (MMCDAB) considering the effects of the MFT winding configuration. Three different winding configurations—namely, Y-Y, D-D, and Y-D—are considered for the connection of the MFT windings. The optimum leakage inductance requirement of the MFT, the currents total harmonic distortion (THD), and the transformer utilization factor (TUF) are compared for the three winding configurations. It is found that the Y-Y and the D-D configurations have similar optimum leakage inductance patterns, which are different from the Y-D configuration. Furthermore, it is established that an optimized leakage inductance value for a conventional DAB, can be utilized for the Q2L-operating MMCDAB for a wide range of transition time with the Y-Y and the D-D winding configurations if less than a 5% error could be tolerated in its value. A comparison with respect to the TUF and the currents THD revealed that the Y-Y and the D-D configurations result in a higher TUF compared to the

Y-D configuration; However, the Y-D configuration has approximately two times lower currents THD compared to the other two configurations.

15. Design Methodology and Optimization of a Medium Frequency Transformer for High Power DC-DC Applications
    M. A. Bahmani, T. Thiringer, and **M. Kharezy**
    IEEE Apec, 2015
    https://ieeexplore.ieee.org/document/7104707
    The high-power medium frequency transformer (HPMFT) is one of the key elements of an isolated, bi-directional DC-DC converters in applications such as future all-DC offshore wind farms, traction and solid-state transformers. This paper describes a design methodology taking into account the loss calculation, isolation requirements and thermal management. Incorporating this design methodology, an optimization process with a wide range of parameter variations is applied on a design example to find the highest power density while the efficiency, isolation, thermal and leakage inductance requirements are all met.

16. Challenges with the design of cost-effective series DC collection network for offshore wind-farm
    M. Kharezy, and T. Thiringer
    Wind Integration Workshop, 2018
    https://research.chalmers.se/publication/507667/file/507667_Fulltext.pdf
    This article summarizes a current PhD research project at Chalmers University of Technology financed by the Swedish Energy Agency and with the contribution of RISE Research Institutes of Sweden. The aim is to study the size of a high-power DC/DC converter which is fit into a container outside a wind turbine for direct integration of an offshore DC series connected wind power plant. This becomes possible using an isolation transformer having a medium frequency high voltage withstand as well as a very high HVDC insulation level. Both obtainable voltage strength levels, as well as lifetime of the insulation system are issues that are going to be investigated carefully.

Bibliography

[1] IEA. "IEA Press Release, Offshore wind to become a $1 trillion industry." https://www.iea.org/news/offshore-wind-to-become-a-1-trillion-industry (accessed 2023-02-24).

[2] U. S. D. o. Energy. "Independent Statistics & Analysis. Assessing HVDC Transmission for Impacts of Non-Dispatchable Generation." https://www.eia.gov/analysis/studies/electricity/hvdctransmission/pdf/transmission.pdf (accessed 2023-02-24).

[3] M. A. Bahmani, "Design and Optimization Considerations of Medium-frequency Power Transformers in High-power DC-DC Applications," Chalmers University of Technology, 2016. [Online]. Available: https://books.google.se/books?id=XG8CkAEACAAJ

[4] M. Kharezy, "Constructional Design, Manufacturing and Evaluation of High Power Density Medium Frequency Transformer Prototypes ", Chalmers University of Technology, 2014. [Online]. Available: http://publications.lib.chalmers.se/records/fulltext/211818/211818.pdf

[5] L. Heinemann, "An actively cooled high power, high frequency transformer with high insulation capability," in *APEC. Seventeenth Annual IEEE Applied Power Electronics Conference and Exposition (Cat. No.02CH37335)*, 2002 2002, vol. 1, pp. 352-357 vol.1, doi: 10.1109/APEC.2002.989270.

[6] M. Steiner and H. Reinold, "Medium frequency topology in railway applications," in *2007 European Conference on Power Electronics and Applications*, 2-5 Sept. 2007 2007, pp. 1-10, doi: 10.1109/EPE.2007.4417570.

[7] Spezial-Transformatoren-Stockach. "MF Transformer for Traction." https://sts-trafo.de/en/transformers (accessed 2023-02-24).

[8] M. Jaritz, S. Blume, and J. Biela, "Design procedure of a 14.4 kV, 100 kHz transformer with a high isolation voltage (115 kV)," *IEEE Transactions on Dielectrics and Electrical Insulation,* vol. 24, no. 4, pp. 2094-2104, 2017, doi: 10.1109/TDEI.2017.006279.

[9] T. B. Gradinger, U. Drofenik, and S. Alvarez, "Novel insulation concept for an MV dry-cast medium-frequency transformer," in *2017 19th European Conference on Power Electronics and Applications (EPE'17 ECCE Europe)*, 11-14 Sept. 2017 2017, pp. P.1-P.10, doi: 10.23919/EPE17ECCEEurope.2017.8099006.

[10] P. Huang, C. Mao, and D. Wang, "Electric field simulations and analysis for high voltage high power medium frequency transformer," *Energies,* vol. 10, no. 3, p. 371, 2017.

[11] G. Ortiz, "High-power DC-DC converter technologies for smart grid and traction applications," ETH Zurich, 2014.

[12] D. Dujic and M. Mogorovic, "High Power MFT Design Optimization," École Polytechnique Fédérale de Lausanne, 2017.

[13] M. A. Bahmani, T. Thiringer, and M. Kharezy, "Optimization and experimental validation of medium-frequency high power transformers in solid-state transformer applications," in *2016 IEEE Applied Power Electronics Conference and Exposition (APEC)*, 20-24 March 2016 2016, pp. 3043-3050, doi: 10.1109/APEC.2016.7468297.

[14] U. Gäfvert, A. Jaksts, C. Tornkvist, and L. Walfridsson, "Electrical field distribution in transformer oil," *IEEE Transactions on Electrical Insulation,* vol. 27, no. 3, pp. 647-660, 1992, doi: 10.1109/14.142730.

[15] U. Gäfvert, O. Hjortstam, Y. Serdyuk, C. Tornkvist, and L. Walfridsson, "Modeling and Measurements of Electric Fields in Composite Oil/Cellulose Insulation," in *2006 IEEE Conference on Electrical Insulation and Dielectric Phenomena*, 15-18 Oct. 2006 2006, pp. 154-157, doi: 10.1109/CEIDP.2006.312084.

[16] L. Yang, S. M. Gubanski, Y. V. Serdyuk, and J. Schiessling, "Dielectric properties of transformer oils for HVDC applications," *IEEE Transactions on Dielectrics and Electrical Insulation,* vol. 19, no. 6, pp. 1926-1933, 2012, doi: 10.1109/TDEI.2012.6396949.

[17] K. Kato, H. Okubo, F. Endo, A. Yamagishi, and K. Miyagi, "Investigation of charge behavior in low viscosity silicone liquid by kerr electro-optic field measurement," *IEEE Transactions on Dielectrics and Electrical Insulation,* vol. 17, no. 4, pp. 1214-1220, 2010, doi: 10.1109/TDEI.2010.5539692.

[18] M. Wakamatsu, K. Kato, N. Inoue, H. Koide, and H. Okubo, "DC field measurement in Oil/Pressboard composite insulation system by electro-optic Kerr effect," *IEEE Transactions on Dielectrics and Electrical Insulation,* vol. 10, no. 6, pp. 942-947, 2003, doi: 10.1109/TDEI.2003.1255770.

[19] H. Okubo, "HVDC electrical insulation performance in oil/pressboard composite insulation system based on Kerr electro-optic field measurement and electric field analysis," *IEEE Transactions on Dielectrics and Electrical Insulation,* vol. 25, no. 5, pp. 1785-1797, 2018, doi: 10.1109/TDEI.2018.007187.

[20] Y. Ebisawa, S. Yamada, S. Mori, and T. Teranishi, "DC creepage breakdown characteristics of oil-immersed insulation," *IEEE Transactions on Dielectrics and Electrical Insulation,* vol. 16, no. 6, pp. 1686-1692, 2009, doi: 10.1109/TDEI.2009.5361590.

[21] R. Nakane, H. Okubo, and K. Kato, "HVDC electrical insulation performance based on charge activity in oil-pressboard composite insulation structures," *IEEE Transactions on Dielectrics and Electrical Insulation,* vol. 26, no. 2, pp. 576-583, 2019, doi: 10.1109/TDEI.2019.007682.

[22] M. Yea, K. J. Han, J. Park, S. Lee, and J. Choi, "Design optimization for the insulation of HVDC converter transformers under composite electric stresses," *IEEE Transactions on Dielectrics and Electrical Insulation,* vol. 25, no. 1, pp. 253-262, 2018, doi: 10.1109/TDEI.2018.006629.

[23] T. Gabler, K. Backhaus, S. Großmann, and R. Fritsche, "Dielectric modeling of oil-paper insulation systems at high DC voltage stress using a charge-carrier-based approach," *IEEE Transactions on Dielectrics and Electrical Insulation,* vol. 26, no. 5, pp. 1549-1557, 2019, doi: 10.1109/TDEI.2019.008175.

[24] H. P. Moser and V. Dahinden, *"Transformerboard II, Properties and application of transformerboard of different fibers"*. Weidmann AG, 1987.

[25] M. J. P. Jeroense and F. H. Kreuger, "Electrical conduction in HVDC mass-impregnated paper cable," *IEEE Transactions on Dielectrics and Electrical Insulation,* vol. 2, no. 5, pp. 718-723, 1995, doi: 10.1109/94.469968.

[26] Waslström, "Cigré, Electra, ELT_046_1, working group A2.12, "Voltage tests on transformers and smoothing reactors for HVDC transmission"," 978-2-85873-213-5, 1976.

[27] Beletsky, "Cigré, working group A2.12, Session paper "Insulation problems in power transformers for HVDC transmissions"," 978-2-85873-213-5, 1976.

[28] "Cigré working group A2/D1.41, "Technical Brochure 646: HVDC transformer insulation: Oil conductivity"," 978-2-85873-349-1, 2016.

[29] M. Khanali, "Effects of Distorted Voltages on the Performance of Renewable Energy Plant Transformers," UWSpace, 2017. [Online]. Available: http://hdl.handle.net/10012/12368

[30] T. L. Koltunowicz, "Accelerated Insulation Aging Due to Thermal and Electrical Stresses in Future Power Grids," Boxpress, 2014. [Online]. Available: https://books.google.se/books?id=Pnx0rgEACAAJ

[31] T. Koltunowicz, A. Cavallini, D. Djairam, G. C. Montanari, and J. Smit, "The influence of square voltage waveforms on transformer insulation break down voltage," in *2011 Annual Report Conference on Electrical Insulation and Dielectric Phenomena*, 16-19 Oct. 2011 2011, pp. 48-51, doi: 10.1109/CEIDP.2011.6232593.

[32] R. C. Kiiza, M. G. Niasar, R. Nikjoo, X. Wang, and H. Edin, "Change in partial discharge activity as related to degradation level in oil-impregnated paper insulation: effect of high voltage impulses," *IEEE Transactions on Dielectrics and Electrical Insulation,* vol. 21, no. 3, pp. 1243-1250, 2014, doi: 10.1109/TDEI.2014.6832271.

[33] P. H. Morshuis, "Degradation of solid dielectrics due to internal partial discharge: some thoughts on progress made and where to go now," *IEEE Transactions on Dielectrics and Electrical Insulation,* vol. 12, no. 5, pp. 905-913, 2005.

[34] M. A. Bahmani and T. Thiringer, "Accurate Evaluation of Leakage Inductance in High-Frequency Transformers Using an Improved Frequency-Dependent Expression," *IEEE Transactions on Power Electronics,* vol. 30, no. 10, pp. 5738-5745, 2015, doi: 10.1109/TPEL.2014.2371057.

[35] E. Agheb, M. A. Bahmani, H. K. Høidalen, and T. Thiringer, "Core loss behavior in high frequency high power transformers—II: Arbitrary excitation," *Journal of Renewable and Sustainable Energy,* vol. 033113, no. 4, 2012. [Online]. Available: https://doi.org/10.1063/1.4727917.

[36] S. A. K. S.V. Kulkarni, *"Transformer Engineering Design, Technology, and Diagnostics"*. CRC Press is an imprint of Taylor & Francis Group, an Informa business, 2013.

[37] K. Karsai, D. Kerényi, and L. Kiss, *Large Power Transformers*. Elsevier, 1987.

[38] R. M. D. Vecchio, B. Poulin, P. T. Feghali, D. M. Shah, and R. Ahuja, *Transformer Design Principles: With Applications to Core-Form Power Transformers, Second Edition*. Taylor & Francis, 2010.

[39] X. Guo, C. Li, Z. Zheng, and Y. Li, "General Analytical Model and Optimization for Leakage Inductances of Medium-Frequency Transformers," *IEEE Journal of Emerging and Selected Topics in Power Electronics,* vol. 10, no. 4, pp. 3511-3524, 2022, doi: 10.1109/JESTPE.2021.3062019.

[40] A. Boyajian, "Leakage Reactance of Irregular Distributions of Transformer Windings by the Method of Double Fourier Series [includes discussion]," *Transactions of the American Institute of Electrical Engineers. Part III: Power Apparatus and Systems,* vol. 73, no. 2, pp. 1078-1086, 1954, doi: 10.1109/AIEEPAS.1954.4498933.

[41] A. L. morris, "The influence of various factors upon the leakage reactance of transformers," *Journal of the Institution of Electrical Engineers*, vol. 86, no. 521*,* pp. 485-495. [Online]. Available: https://digital-library.theiet.org/content/journals/10.1049/jiee-1.1940.0068

[42] E. Billig, "The calculation of the magnetic field of rectangular conductors in a closed slot, and its application to the reactance of transformer windings," *Proceedings of the IEE - Part IV: Institution Monographs*, vol. 98, no. 1*,* pp. 55-64. [Online]. Available: https://digital-library.theiet.org/content/journals/10.1049/pi-4.1951.0007

[43] P. Hammond, "Roth's method for the solution of boundary-value problems in electrical engineering," *Proceedings of the Institution of Electrical Engineers*, vol. 114, no. 12*,* pp. 1969-1976. [Online]. Available: https://digital-library.theiet.org/content/journals/10.1049/piee.1967.0373

[44] M. Eslamian, M. Kharezy, and T. Thiringer, "Calculation of the Leakage Inductance of Medium Frequency Transformers with Rectangular-Shaped Windings using an Accurate Analytical Method," in *2019 21st European Conference on Power Electronics and Applications (EPE '19 ECCE Europe)*, 3-5 Sept. 2019 2019, pp. P.1-P.10, doi: 10.23919/EPE.2019.8915036.

[45] M. Lambert, F. Sirois, M. Martinez-Duro, and J. Mahseredjian, "Analytical Calculation of Leakage Inductance for Low-Frequency Transformer Modeling," *IEEE Transactions on Power Delivery,* vol. 28, no. 1, pp. 507-515, 2013, doi: 10.1109/TPWRD.2012.2225451.

[46] X. Margueron, A. Besri, P. O. Jeannin, J. P. Keradec, and G. Parent, "Complete Analytical Calculation of Static Leakage Parameters: A Step Toward HF Transformer Optimization," *IEEE Transactions on Industry Applications,* vol. 46, no. 3, pp. 1055-1063, 2010, doi: 10.1109/TIA.2010.2045327.

[47] I. Hernandez, F. d. Leon, and P. Gomez, "Design Formulas for the Leakage Inductance of Toroidal Distribution Transformers," *IEEE Transactions on Power Delivery,* vol. 26, no. 4, pp. 2197-2204, 2011, doi: 10.1109/TPWRD.2011.2157536.

[48] R. Schlesinger and J. Biela, "Comparison of Analytical Models of Transformer Leakage Inductance: Accuracy Versus Computational Effort," *IEEE Transactions on Power Electronics,* vol. 36, no. 1, pp. 146-156, 2021, doi: 10.1109/TPEL.2020.3001056.

[49] O. W. Andersen, "Transformer Leakage Flux Program Based on the Finite Element Method," *IEEE Transactions on Power Apparatus and Systems,* vol. PAS-92, no. 2, pp. 682-689, 1973, doi: 10.1109/TPAS.1973.293773.

[50] P. Silvester and A. Konrad, "Analysis of Transformer Leakage Phenomena by High-Order Finite Elements," *IEEE Transactions on Power Apparatus and Systems,* vol. PAS-92, no. 6, pp. 1843-1855, 1973, doi: 10.1109/TPAS.1973.293564.

[51] M. Nazmunnahar, S. Simizu, P. R. Ohodnicki, S. Bhattacharya, and M. E. McHenry, "Finite-Element Analysis Modeling of High-Frequency Single-Phase Transformers Enabled by Metal Amorphous Nanocomposites and Calculation of Leakage Inductance for Different Winding Topologies," *IEEE Transactions on Magnetics,* vol. 55, no. 7, pp. 1-11, 2019, doi: 10.1109/TMAG.2019.2904007.

[52] W. G. Hurley and W. H. Wölfle, *"Transformers and Inductors for Power Electronics: Theory, Design and Applications"*. Wiley, 2013.

[53] L. Rabins, "Transformer reactance calculations with digital computers," *Transactions of the American Institute of Electrical Engineers, Part I: Communication and Electronics,* vol. 75, no. 3, pp. 261-267, 1956, doi: 10.1109/TCE.1956.6372526.

[54] R. A. G. Jimenez, G. G. Oggier, D. P. Fernandez, and J. C. Balda, "Analysis of Current Resonances due to Winding Parasitic Capacitances in Medium-Voltage Medium-Frequency Transformers," in *2022 IEEE Applied Power Electronics Conference and Exposition (APEC)*, 20-24 March 2022 2022, pp. 939-943, doi: 10.1109/APEC43599.2022.9773427.

[55] B. Cogitore, J. P. Keradec, and J. Barbaroux, "The two-winding transformer: an experimental method to obtain a wide frequency range equivalent circuit," *IEEE Transactions on Instrumentation and Measurement,* vol. 43, no. 2, pp. 364-371, 1994, doi: 10.1109/19.293449.

[56] C. Liu, L. Qi, X. Cui, and X. Wei, "Experimental Extraction of Parasitic Capacitances for High-Frequency Transformers," *IEEE Transactions on Power Electronics,* vol. 32, no. 6, pp. 4157-4167, 2017, doi: 10.1109/TPEL.2016.2597498.

[57] J. Biela and J. W. Kolar, "Using Transformer Parasitics for Resonant Converters—A Review of the Calculation of the Stray Capacitance of Transformers," *IEEE Transactions on Industry Applications,* vol. 44, no. 1, pp. 223-233, 2008, doi: 10.1109/TIA.2007.912722.

[58] L. Dalessandro, F. d. S. Cavalcante, and J. W. Kolar, "Self-Capacitance of High-Voltage Transformers," *IEEE Transactions on Power Electronics,* vol. 22, no. 5, pp. 2081-2092, 2007, doi: 10.1109/TPEL.2007.904252.

[59] L. Deng *et al.*, "Modeling and Analysis of Parasitic Capacitance of Secondary Winding in High-Frequency High-Voltage Transformer Using Finite-Element Method," *IEEE Transactions on Applied Superconductivity,* vol. 28, no. 3, pp. 1-5, 2018, doi: 10.1109/TASC.2018.2794476.

[60] N. Abeywickrama, Y. V. Serdyuk, and S. M. Gubanski, "High-Frequency Modeling of Power Transformers for Use in Frequency Response Analysis (FRA)," *IEEE Transactions on Power Delivery,* vol. 23, no. 4, pp. 2042-2049, 2008, doi: 10.1109/TPWRD.2008.917896.

[61] M. Kharezy and T. Thiringer, "Challenges with the design of cost-effective series DC collection network for offshore wind-farms," presented at the 17th Wind Integration Workshop on Large scale Integration of Wind Power into Power Systems as well as on Transmission Networks for Offshore Wind Power Plants, Stockholm, Sweden, 2018.

[62] M. Kharezy, H. R. Mirzaei, J. Rastamo, M. Svensson, Y. Serdyuk, and T. Thiringer, "Performance of Insulation of DC/DC Converter Transformer for Offshore Wind Power Applications," presented at the CEIDP2020, Conference on Electrical Insulation and Dielectric Phenomena, NJ, USA, 2020.

[63] M. A. Bahmani, T. Thiringer, and M. Kharezy, "Design Methodology and Optimization of a Medium-Frequency Transformer for High-Power DC-DC Applications," *IEEE Transactions on Industry Applications,* vol. 52, no. 5, pp. 4225-4233, 2016, doi: 10.1109/TIA.2016.2582825.

[64] C. R. Sullivan, "Computationally efficient winding loss calculation with multiple windings, arbitrary waveforms, and two-dimensional or three-dimensional field geometry," *IEEE Transactions on Power Electronics,* vol. 16, no. 1, pp. 142-150, 2001, doi: 10.1109/63.903999.

[65] F. Tourkhani and P. Viarouge, "Accurate analytical model of winding losses in round Litz wire windings," *IEEE Transactions on Magnetics,* vol. 37, no. 1, pp. 538-543, 2001, doi: 10.1109/20.914375.

[66] M. A. Bahmani, T. Thiringer, and H. Ortega, "An Accurate Pseudoempirical Model of Winding Loss Calculation in HF Foil and Round Conductors in Switchmode Magnetics," *IEEE Transactions on Power Electronics,* vol. 29, no. 8, pp. 4231-4246, 2014, doi: 10.1109/TPEL.2013.2292593.

[67] E. Agheb, "Medium Frequency High Power Transformers for All-DC Wind Parks," Norwegian University of Science and Technology, 2017. [Online]. Available: http://hdl.handle.net/11250/2448642

[68] M. Eklund, N. Naphthenics, P. Jarman, and M. Edwall, *"Transformer Oil Handbook"*. Nynas AB, 2010.

[69] K. L. R. Fritsche, F. Trautmann, T. Hammer, "Transformers for High Voltage Direct Current Transmission - Challenge, Technology and Development," (in DE), 2016. [Online]. Available: https://www.researchgate.net/publication/315657537.

[70] R. Asano and S. A. Page, "Reducing Environmental Impact and Improving Safety and Performance of Power Transformers With Natural Ester Dielectric Insulating Fluids," *IEEE Transactions on Industry Applications,* vol. 50, no. 1, pp. 134-141, 2014, doi: 10.1109/TIA.2013.2269532.

[71] I. Fofana, "50 years in the development of insulating liquids," *IEEE Electrical Insulation Magazine,* vol. 29, no. 5, pp. 13-25, 2013, doi: 10.1109/MEI.2013.6585853.

[72] T. G. Aakre, T. A. Ve, and Ø. L. Hestad, "Conductivity and permittivity of midel 7131: effect of temperature, moisture content, hydrostatic pressure and electric field," *IEEE Transactions on Dielectrics and Electrical Insulation,* vol. 23, no. 5, pp. 2957-2964, 2016, doi: 10.1109/TDEI.2016.7736858.

[73] P. J. Rumpelt, F., "Oil Impregnated Pressboard Barrier Systems Based on Ester Fluids for an Application in HVDC Insulation Systems," (in EN), *MDPI Energies,* 2017, Art no. 10122147. [Online]. Available: https://www.mdpi.com/1996-1073/10/12/2147#cite.

[74] *IEC 62770: Fluids for electrotechnical applications - Unused natural esters for transformers and similar electrical equipment*, STD-572432, 2013.

[75] *IEC 63012: Insulating liquids - Unused modified or blended esters for electrotechnical applications*, ICS 29.040.10, 2019.

[76] H. P. Moser, *"Transformerboard"*. Weidmann AG, 1979.

[77] A. Küchler, *"High Voltage Engineering: Fundamentals-Technology-Applications"*. Springer, 2017.

[78] M. Kharezy, M. Eslamian, and T. Thiringer, "Insulation Design of a Medium Frequency Power Transformer for a Cost-Effective Series High Voltage DC Collection Network of an Offshore Wind Farm," in *Proceedings of the 21st International Symposium on High Voltage Engineering*, Cham, B. Németh, Ed., 2020// 2020: Springer International Publishing, pp. 1406-1417.

[79] H. Okubo, T. Sakai, T. Furuyashiki, K. Takabayashi, and K. Kato, "HVDC electric field control by pressboard arrangement in oil-pressboard composite electrical insulation systems," in *2016 IEEE Conference on Electrical Insulation and Dielectric Phenomena (CEIDP)*, 16-19 Oct. 2016 2016, pp. 35-39, doi: 10.1109/CEIDP.2016.7785513.

[80] M. Liebschner, *Interaktion von Ölspalten und fester Isolation in HVDC-Barrierensystemen*. VDI-Verlag, 2009.

[81] K. B. T. Gabler, J. Speck, R. Fritsche and S. Großmann, "Experimental Validation of the Charge Carrier-based Modelling of Oil-Paper Insulations at High DC Voltage Stress," *Conference: 20th International Symposium on High Voltage EngineeringAt: Buenos Aires, Argentina,* 2017.

[82] K. Backhaus, J. Speck, M. Hering, S. Großmann, and R. Fritsche, "Nonlinear dielectric behaviour of insulating oil under HVDC stress as a result of ion drift," in *2014 ICHVE International Conference on High Voltage Engineering and Application*, 8-11 Sept. 2014 2014, pp. 1-4, doi: 10.1109/ICHVE.2014.7035453.

[83] K. B. T. Gabler, T. Goetz, T. Linde, S. Grossmann and R. Fritsche, "Investigation on the breakdown behaviour of oil-paper insulations at superimposed DC and lightning impulse

voltage stress," *Conference: VDE-Hochspannungstechnik 2018 - ETG-Fachtagung, Berlin, Germany,* 2018.
[84] F. Schober, S. Harrer, A. Kuchler, F. Berger, W. Exner, and C. Krause, "Transient and steady-state dc behavior of oil-impregnated pressboard," *IEEE Electrical Insulation Magazine,* vol. 32, no. 4, pp. 8-14, 2016, doi: 10.1109/MEI.2016.7528985.
[85] F. Vahidi, S. Tenbohlen, M. Rösner, C. Perrier, and H. Fink, "Influence of electrode material on conductivity measurements under DC stresses," in *2014 IEEE 18th International Conference on Dielectric Liquids (ICDL)*, 29 June-3 July 2014 2014, pp. 1-5, doi: 10.1109/ICDL.2014.6893133.
[86] T. Gabler, K. Backhaus, T. Götz, S. Groβmann, and R. Fritsche, "Effect of the Non-Linear Electric Conductivity of Mineral Insulating Oil on the Dielectric Strength at High DC Voltage Stress," in *2018 IEEE Conference on Electrical Insulation and Dielectric Phenomena (CEIDP)*, 21-24 Oct. 2018 2018, pp. 54-57, doi: 10.1109/CEIDP.2018.8544845.
[87] *IEC 62631-3-1: Determination of resistive properties (DC methods) – Volume resistance and volume resistivity – General method*, ICS 17.220.99; 29.035.01, 2016.
[88] M. Lisowski and R. Kacprzyk, "Changes proposed for the IEC 60093 Standard concerning measurements of the volume and surface resistivities of electrical insulating materials," *IEEE Transactions on Dielectrics and Electrical Insulation,* vol. 13, no. 1, pp. 139-145, 2006, doi: 10.1109/TDEI.2006.1593412.
[89] *ASTM D 257-14: Standard test methods for dc resistance or conductance of insulating materials*, ASTM, 2014.
[90] Küchler. (2006). Cigré, Study Comittee A2, Session paper "Condition Assessment of Aged transformer Bushing Insulation".
[91] Z. Ouyang, J. Zhang, and W. G. Hurley, "Calculation of Leakage Inductance for High-Frequency Transformers," *IEEE Transactions on Power Electronics,* vol. 30, no. 10, pp. 5769-5775, 2015, doi: 10.1109/TPEL.2014.2382175.
[92] K. Zhang *et al.*, "Accurate Calculation and Sensitivity Analysis of Leakage Inductance of High-Frequency Transformer With Litz Wire Winding," *IEEE Transactions on Power Electronics,* vol. 35, no. 4, pp. 3951-3962, 2020, doi: 10.1109/TPEL.2019.2936523.
[93] A. Fouineau, M. A. Raulet, B. Lefebvre, N. Burais, and F. Sixdenier, "Semi-Analytical Methods for Calculation of Leakage Inductance and Frequency-Dependent Resistance of Windings in Transformers," *IEEE Transactions on Magnetics,* vol. 54, no. 10, pp. 1-10, 2018, doi: 10.1109/TMAG.2018.2858743.
[94] P. L. Dowell, "Effects of eddy currents in transformer windings," *Proceedings of the Institution of Electrical Engineers,* vol. 113, no. 8, pp. 1387-1394, 1966, doi: 10.1049/piee.1966.0236.
[95] J. A. Ferreira, "Improved analytical modeling of conductive losses in magnetic components," *IEEE Transactions on Power Electronics,* vol. 9, no. 1, pp. 127-131, 1994, doi: 10.1109/63.285503.
[96] M. Eslamian, M. Kharezy, and T. Thiringer, "An Accurate Analytical Method for Leakage Inductance Calculation of Shell-Type Transformers With Rectangular Windings," *IEEE Access,* vol. 9, pp. 72647-72660, 2021, doi: 10.1109/ACCESS.2021.3080242.
[97] M. Eslamian, M. Kharezy, and T. Thiringer, "An Accurate Method for Leakage Inductance Calculation of Shell-Type Multi Core-Segment Transformers With Circular Windings," *IEEE Access,* vol. 9, pp. 111417-111431, 2021, doi: 10.1109/ACCESS.2021.3103541.
[98] M. Mogorovic and D. Dujic, "Sensitivity Analysis of Medium-Frequency Transformer Designs for Solid-State Transformers," *IEEE Transactions on Power Electronics,* vol. 34, no. 9, pp. 8356-8367, 2019, doi: 10.1109/TPEL.2018.2883390.
[99] M. Kharezy, H. R. Mirzaei, Y. Serdyuk, T. Thiringer, and M. Eslamian, "A Novel Oil-Immersed Medium Frequency Transformer for Offshore HVDC Wind Farms," *IEEE Transactions on Power Delivery,* vol. 36, no. 5, pp. 3185-3195, 2021, doi: 10.1109/TPWRD.2020.3035718.
[100] Comsol. "Capacitance Matrix of Two Sphares." Comsol. https://www.comsol.com/model/capacitance-matrix-of-two-spheres-49751 (accessed 2023-02-21).

[101] Comsol. "Inductance Matrix Calculation PCB Coils." Comsol. https://www.comsol.com/model/inductance-matrix-calculation-of-pcb-coils-89921 (accessed 2023-02-21).
[102] W. Shen, "Design of High-density Transformers for High-frequency High-power Converters," Virginia Polytechnic Institute and State University, 2006. [Online]. Available: https://books.google.se/books?id=XG8CkAEACAAJ
[103] C. P. Steinmetz, "On the Law of Hysteresis," *Transactions of the American Institute of Electrical Engineers,* vol. IX, no. 1, pp. 1-64, 1892, doi: 10.1109/T-AIEE.1892.5570437.
[104] TDK. "SIFERRIT material N87." https://www.tdk-electronics.tdk.com/download/528882/71e02c7b9384de1331b3f625ce4b2123/pdf-n87.pdf (accessed 2023-02-24).
[105] Hitachi. "FINEMET F3CC Series Cut Cores." https://www.hilltech.com/pdf/Hitachi/Datasheets/SA1_FT3_Cut_Core.pdf (accessed 2023-02-24).
[106] Elektrisola. "LITZ WIRE." https://www.elektrisola.com/en/Litz-Wire/Info (accessed 2023-01-20).
[107] R. W. A. A. D. Doncker, D. M. Divan, and M. H. Kheraluwala, "A three-phase soft-switched high-power-density DC/DC converter for high-power applications," *IEEE Transactions on Industry Applications,* vol. 27, no. 1, pp. 63-73, 1991, doi: 10.1109/28.67533.
[108] Vonroll. "Winding Wires and Litz Wires." https://sibel.bg/upl_doc/Wire_EN_20120516_(2).pdf (accessed 2023-02-24).
[109] O. Moreau, L. Popiel, and J. L. Pages, "Proximity losses computation with a 2D complex permeability modelling," *IEEE Transactions on Magnetics,* vol. 34, no. 5, pp. 3616-3619, 1998, doi: 10.1109/20.717854.
[110] J. Gyselinck and P. Dular, "Frequency-domain homogenization of bundles of wires in 2-D magnetodynamic FE calculations," *IEEE Transactions on Magnetics,* vol. 41, no. 5, pp. 1416-1419, 2005, doi: 10.1109/TMAG.2005.844534.
[111] D. Meeker. "Continuum Representation of Wound Coils via an Equivalent Foil Approach." https://www.femm.info/examples/prox/notes.pdf (accessed 2023-02-24).
[112] N. Mohan, T. M. Undeland, and W. P. Robbins, "Power Electronics - Converters, Applications, and Design (3rd Edition)," ed: John Wiley & Sons.
[113] *IEC 60076-3: Power transformers - Insulation levels, dielectric tests and external clearances in air* 978-2-83220-830-4, 2013.
[114] *IEC 61251: Electrical insulating materials and systems - A.C. voltage endurance evaluation*, ICS 17.220.99; 29.035.01, 2015.
[115] G. C. Stone, R. G. v. Heeswijk, and R. Bartnikas, "Investigation of the effect of repetitive voltage surges on epoxy insulation," *IEEE Transactions on Energy Conversion,* vol. 7, no. 4, pp. 754-760, 1992, doi: 10.1109/60.182659.
[116] D. R. Johnston, J. T. LaForte, P. E. Podhorez, and H. N. Galpern, "Frequency Acceleration of Voltage Endurance," *IEEE Transactions on Electrical Insulation,* vol. EI-14, no. 3, pp. 121-126, 1979, doi: 10.1109/TEI.1979.298211.
[117] *IEC 60034-18-41: Rotating electrical machines - Part 18-41: Partial discharge free electrical insulation systems (Type I) used in rotating electrical machines fed from voltage converters - Qualification and quality control tests*, ICS 29.160, 2014.
[118] *IEC 60156: Insulating liquides - Determination of breakdown voltage at power frequency - Test method*, 1995.
[119] *IEC 60851-5: Winding wires - Test methods - Part 5: Electrical properties*, ICS 29.060.10, 2008.
[120] S. M. Hasheminezhad, E. Ildstad, and A. Nysveen, "Breakdown strength of solid|solid interface," in *2010 10th IEEE International Conference on Solid Dielectrics*, 4-9 July 2010 2010, pp. 1-4, doi: 10.1109/ICSD.2010.5568229.
[121] *IEC 60243-1: Electric strength of insulating materials -Test methods - Part 1: Tests at power frequencies*, ICS 17.220.99; 29.035.01, 2013.

[122] *ASTM D149-97a: Standard test method for dielectric breakdown voltage and dielectric strength of solid electrical insulating materials at commercial power frequencies*, 2004.
[123] T. Hammarström, "Partial Discharges at Fast Rising Voltages," Chalmers University of Technology, 2014. [Online]. Available: http://publications.lib.chalmers.se/publication/200974-partial-discharges-at-fast-rising-voltages
[124] Küchler. (2010). Cigré, Study Comittee D1, Session paper "Evaluation of Conductivities and Dielectric Properties for Highly Stressed HVDC Insulating Materials".
[125] G. Steeves. ""Vapor phase transformer drying – Part I," Transformer Magazine, Volume3, Issue 2, April 2016." www.transformers-magazine.com (accessed 2016-05-23).
[126] *IEC 60641-2: Pressboard and presspaper for electrical purposes - Part 2: Methods of tests*, ICS 17.220.99, 2004.
[127] F. Vahidi, S. Tenbohlen, M. Rösner, C. Perrier, and H. Fink, "The investigation of the temperature and electric field dependency of mineral oil electrical conductivity," *Conference: VDE-Hochspannungstechnik 2013 - ETG-Fachtagung, Dresden, Germany,* 2013.
[128] Y. Li, K. Zhou, G. Zhu, M. Li, S. Li, and J. Zhang, "Study on the Influence of Temperature, Moisture and Electric Field on the Electrical Conductivity of Oil-Impregnated Pressboard," (in EN), *MDPI Energies,* 2019, Art no. 12163136 [Online]. Available: https://www.mdpi.com/1996-1073/12/16/3136#cite.
[129] P. Rumpelt and F. Jenau, "Investigation on DC conductivity of alternative insulating oils as an application for HVDC converter transformers," in *2017 IEEE 19th International Conference on Dielectric Liquids (ICDL)*, 25-29 June 2017 2017, pp. 1-6, doi: 10.1109/ICDL.2017.8124607.
[130] C. Daran-Daneau, D. É, M. F. Fréchette, and S. Savoie, "Influence of the surrounding medium on the dielectric strength measurement of LLDPE/clay nanocomposites," in *2012 IEEE International Symposium on Electrical Insulation*, 10-13 June 2012 2012, pp. 654-658, doi: 10.1109/ELINSL.2012.6251553.
[131] Y. Ohki, "News from Japan," *IEEE Electrical Insulation Magazine,* vol. 29, no. 6, pp. 71-74, 2013, doi: 10.1109/MEI.2013.6648759.
[132] M. Kharezy, H. R. Mirzaei, T. Thiringer, and Y. V. Serdyuk, "Green Solution for Insulation System of a Medium Frequency High Voltage Transformer for an Offshore Wind Farm," *Energies*, vol. 15, no. 6, doi: 10.3390/en15061998.
[133] H. Yongtao, W. Eberle, and L. Yan-Fei, "New measurement methods to characterize transformer core loss and copper loss in high frequency switching mode power supplies," in *2004 IEEE 35th Annual Power Electronics Specialists Conference (IEEE Cat. No.04CH37551)*, 20-25 June 2004 2004, vol. 2, pp. 1695-1701 Vol.2, doi: 10.1109/PESC.2004.1355681.
[134] Imperix. "Imperix PEB 8038 - Half-bridge SiC power module." https://imperix.com/products/power/half-bridge-module/ (accessed 2023-02-24).
[135] "Cigré working group D1.12, "Technical Brochure 520: Material properties of solid HVDC Insulation systems"," 978-2-85873-213-5, 2012.
[136] B. Dolata, H. Borsi, and E. Gockenbach, "Comparison of Electric and Dielectric Properties of Ester Fluids with Mineral Based Transformer Oil," presented at the Proceedings of the 15st International Symposium on High Voltage Engineering, Ljubljana, Slovenia, 2007.
[137] O. Guillén Sentís, "Feasibility of sea based wind park," Chalmers University of Technology, 2020. [Online]. Available: https://hdl.handle.net/20.500.12380/301473
[138] T. C. Estate. "The Crown Estate, Guide to an offshore wind farm " https://www.thecrownestate.co.uk/media/2860/guide-to-offshore-wind-farm-2019.pdf (accessed 2023-02-24).
[139] NorthSeaGrid. "Offshore electricity grid implementation in the north sea, Technical report." https://www.windguard.de/veroeffentlichungen.html?file=files/cto_layout/img/unternehmen/veroeffentlichungen/2015/NorthSeaGrid-Offshore%20Electricity%20Grid%20Implementation%20in%20the%20North%20Sea.pdf (accessed 2023-02-24).

[140] Entsoe. "Offshore Transmission Technology " https://eepublicdownloads.blob.core.windows.net/public-cdn-container/clean-documents/pre2015/publications/entsoe/SDC/European_offshore_grid_-_Offshore_Technology_-_FINALversion.pdf (accessed 2023-02-24).

[141] P. Härtel, T. K. Vrana, T. Hennig, M. v. Bonin, E. J. Wiggelinkhuizen, and F. D. J. Nieuwenhout, "Review of investment model cost parameters for vsc hvdc transmission infrastructure," *Elsevier Electric Power Systems Research,* vol. 151, pp. 419-431, 2017. [Online]. Available: https://doi.org/10.1016/j.epsr.2017.06.008.

[142] DNV.GL. "66 kV Systems for Offshore Wind Farms, Report No.: 113799-UKBR-R02, Rev. 2, Document No.: 74107077-1, Date: 2015-03-05 " https://www.tennet.eu/fileadmin/user_upload/Our_Grid/Offshore_Netherlands/Consultatie_proces_net_op_zee/Technical_Topics/4_T1._Enclosure_nr_1b_-_66_kV_systems_for_Offshore_Wind_Farms_by_DNV_GL.pdf (accessed 2020-06-01).

[143] M. Lashbrook, A. Gyore, and R. Martin, "A review of the fundamental dielectric characteristics of ester-based dielectric liquids," *Elsevier Science Direct Procedia Engineering,* vol. 202, pp. 121-129, 2017. [Online]. Available: https://doi.org/10.1016/j.proeng.2017.09.699.

[144] M. Lashbrook, A. Gyore, R. Martin, R. Cselko, and B. Nemeth, "Design considerations for the use of ester-based dielectric liquids in transmission equipment," in *2017 IEEE 19th International Conference on Dielectric Liquids (ICDL)*, 25-29 June 2017 2017, pp. 1-6, doi: 10.1109/ICDL.2017.8124734.

[145] Pfisterer. "Cable systems, cable fittings for high voltage networks." https://www.pfisterer.com/fileadmin/pfisterer/downloads_en/CableSystemHV-CT-EN.pdf (accessed 2023-02-24).

[146] *IEC EN 60071-1:2006 "Insulation co-ordination – Part 1: Definitions, principles and rules*, 2006.

[147] P. Rozga, A. Beroual, P. Przybylek, M. Jaroszewski, and K. Strzelecki, "A Review on Synthetic Ester Liquids for Transformer Applications," *Energies,* vol. 13, no. 23, p. 6429, 2020. [Online]. Available: https://www.mdpi.com/1996-1073/13/23/6429.

[148] J. W. a. C. P. W. B. PAHLAVANPOUR "Cooling Ability of Insulating Liquids," presented at the e-ARWtr2016 Advanced Research Workshop on Transformers, Spain, 3-5 October 2016, 2016.

[149] S. Jazebi *et al.*, "Duality Derived Transformer Models for Low-Frequency Electromagnetic Transients—Part I: Topological Models," *IEEE Transactions on Power Delivery,* vol. 31, no. 5, pp. 2410-2419, 2016, doi: 10.1109/TPWRD.2016.2517327.

CHALMERS UNIVERSITY OF TECHNOLOGY
Gothenburg, Sweden
www.chalmers.se

A green High voltage DC-biased oil type Medium Frequency Transformer

Electric energy generated by offshore wind parks is transported to the consumer with HV (High Voltage) submarine cables using AC (Alternating Current=växelspänning), the same as we have in our sockets at home. AC transmission is realized today by collecting the energy produced by several wind turbines in a bulky and expensive transformer, placed on a dedicated platform. Installation and maintenance costs could be reduced by eliminating such platforms using DC (Direct Current=likspänning), i.e., the same energy form that a battery gives out. Equipping each wind turbine with an individual DC/DC converter and connecting them in series to reach the required DC voltage level makes efficient HVDC energy transportation to the shore possible. The converter can be made sufficiently small to be placed on the wind turbine tower or even in its nacelle by implementing special MFTs (Medium Frequency Transformers), which operate at voltages comprising of a high-frequency component superimposed onto a high DC offset voltage. DC insulation design of such transformers and investigation of the effects of high DC insulation level on other electromagnetic properties of the transformer is the subject of the present research. A solution is presented, and a prototype is constructed. The unit has the rated power of 50 kW and rated voltages of 0.4/5 kV including DC offset of 125 kV and square-shaped oscillations with the frequency of 5 kHz. To reduce size and allow for efficient cooling, the transformer's active part is immersed in an environmentally friendly oil, and cellulose-based materials is used for insulation. The approach is extended and the design of a full-scale DC/DC converter with rated parameters of 6 MW, 1.8 kV having a 250 kV offset DC voltage is presented, enabling installation of converters weighing 2.2 tons with volumes of 1.8 m3 at the bottom of the wind turbine towers.